Engineering Nano-Assemblies of Inorganic Particles

by

Yefeng Li

Submitted in accordance with requirements for the degree of
Doctor of Philosophy

The University of Leeds
The School of Chemical and Process Engineering

Sep 2019

Acknowledgements

I have a long list of people who have made contributions to this project and thesis. First, I would like to express my acknowledgements to my supervisors Prof Andrew Bayly and Dr David Harbottle for their academic supervision and supports throughout my PhD study.

I would like to give special thanks to my industry supervisors Dr Stephen Sutcliffe and Dr John Edwards who managed my project at Venator UK. Many thanks for their help with setting up the project, sharing the manufacturing process information, supplying materials, providing ideas and feedback, and all other forms of supports to my study.

I would like to give thanks to my colleague Karrar AI-Dirawi for his help with the creative method for estimating the hollowness of spray-dried granules. I also thank Wael Ebrahim for his supports with all single droplet drying experiments, and data analysis.

I would like to thank Mr Stuart Micklethwaite from Leeds Electron Microscopy and Spectroscopy Centre (LEMAS) for all my SEM, FEI and TEM studies. Same thanks to Dr Ben Douglas from SCAPE for colloidal characterisations, Mr Martin Fuller from Biological Science School for microtome sectioning analysis and to all other colleagues for all your generous help, encouragements, ideas and all forms of contributions.

I also appreciate the funding sources from the EPSRC Centre for Doctoral Training in Complex Particulate Products and Process (CDT-CP3) at Chemical and Process Engineering School of the University of Leeds. This substantial support allows me to focus on my study over years without any financial distraction.

At last, I would like to thank my family for being understanding with my decision for undertaking this PhD study, and their encouragements when I was experiencing a difficult time. Many thanks for being supportive in past 5 years.

Abstract

Ultrafine particles, with particle size less than 1 µm, tend to be difficult for users to handle. Therefore, they are often assembled into larger granules for ease of handling and to allow controlled delivery in their desired functions. Engineers who manufacture granules want to be able to control and predict the structures formed and ultimately predict the functional performance of the granular products. The overall aim of this project is to engineer structure for TiO_2 (titanium dioxide) type pigments using a controlled spray drying method. It is also important to gain a detailed understanding of the morphology control techniques and the associated properties of spray-dried granules.

The project first considers the colloidal characterisations of two distinctive TiO_2 slurry systems in order to develop an overall understanding of the feed materials for the subsequent spray drying experiments. The morphology, size and surface of primary particles from two slurries system were examined using SEM, TEM and EDX analysis. The surface charge measurements were performed to identify the iso-electric point (IEP) at which system start to aggregate for two systems. The slurries were re-formulated with controlled colloidal stability by adjusting pH of system to IEP and to non-IEP conditions. The following particle size, particle settling, and rheology measurements confirmed the difference between slurry at IEP and non-IEP condition in terms of colloidal structure.

Initial drying work was performed using a pilot-plant scale ProCepT spray drying using an ultrasonic at 120ºC. It has been found the variations in colloidal structure of a droplet is responsible for the assemblies of primary particles during the drying process. For the spray drying of alumina-coated TiO_2 system at all three concentration levels, spherical morphology was found from drying of slurries at IEP condition, whereas a buckled morphology was seen from drying of slurries at non-IEP condition. The Morphologi G3 image analysis indicated a size range of 10-100 µm for all spray-dried granules, regardless of their external morphology. For the spray drying of non-coated TiO_2 system at all three concentration levels, constant spherical morphology was obtained from drying of slurries at both IEP and non-IEP conditions. In fact, a buckled morphology was expected from drying a “well-dispersed” system. The colloidal stability was not proved to affect the morphology in spray drying of the non-coated TiO_2 system.

The subsequent drying work was conducted at 200ºC using the same ultrasonic nozzle to investigate the temperature effect and were conducted at 120ºC using a 0.6 mm bi-fluid nozzle to investigate the atomisation effect to the product. The revised drying process conditions were found to have minor effect on the spray-dried morphology for both two TiO_2 systems. The obtained morphologies were same as the ones prepared from 120ºC drying using an ultrasonic nozzle.

The 20%wt slurries at both IEP and non-IEP conditions from two TiO_2 particles systems were dried at 120ºC using a more controlled single droplet drying rig to verify the morphologies from spray drying experiment. For alumina-coated system, the morphologies obtained from single droplet drying were consistent from spray drying work. However, a buckled morphology was obtained from drying of non-coated system at non-IEP condition which was different from its spherical morphology obtained from spray drying study. The morphology forming mechanism was proposed based on the experimental results and calculated Péclet number, and the key driving force for structure buckling was identified to be capillary force. The droplet size effect on morphology was studied by drying the “well-dispersed” droplets with varied size from two TiO_2 systems. Through the estimation of central void of spray-dried granule, the morphology was proved to be dependent on the hollowness of granule and particle-particle interaction in shell of droplet.

It was found the investigated spray drying process conditions cannot affect the porosity, internal structure, surface area, moisture adsorption and desorption, and the density of the spray-dried granule, whereas the alumina-coating layer on particle surface exhibited a significant effect on these properties. As the colloidal stability was proved to be important to morphology control, it allows a more research gaps for slurry formulation development.

Table of Contents

List of Figures

List of Tables

Nomenclature

A	Hamaker Constant
$A_{combined}$	combined Hamaker constant
$A_{particle}$	Hamaker constant of a particle
A_{medium}	Hamaker constant of medium
A, B, C	Antoine constants for water
a	particle radius
a_{tube}	radius of capillary tube
C_i	concentration of solute i
$C_{s,I}$	surface concentration of component i
$C_{m,I}$	average concentration of component i in a droplet
c_0	molarity of monovalent electrolyte
D	diffusion rate of particles suspended in a droplet
D_i	diffusivity of solute i in liquid phase
D_g	diffusion coefficient of gas phase
D_0	initial droplet diameter
$D_{(t)}$	droplet diameter at time t
$D(50)$	particle size up to which 50% of total volume of particles (population)
D_{sep}	separation distance between two particles suspended in medium
d	diameter of particle
E	Young’s modulus
e	the charge of electron
F	surface force
F_{vdw}	Van der Waals force
g	gravity of Earth
h	shell thickness
h_{cap}	height of pulled water in capillary tube
K_B	Boltzman constant
k	evaporation rate of a droplet

k_p	permeability of shell
k_{De}	Debye screening parameter
k_{De}^{-1}	Debye length
P_{cap}	water capillary pressure
P_{Darcy}	Dary's pressure
Pe	Péclet number
Pe_i	associated Péclet number of component *i*
R	droplet radius
R_{pore}	radius of pore between adjacent particles (or radius of capillary curvature)
T	Kelvin temperature
T_{wb}	wet bulb temperature
T_G or T_g	drying gas temperature
T_b	liquid phase boiling temperature
T_{in}	inlet temperature for spray drying process
T_{out}	outlet temperature for spray drying process
t	time
W	potential energy
W_{vdw}	Van der Waals interaction energy
W_{net}	net energy interaction between two particles
W_{EDL}	electrical double layer (repulsive) energy interaction between two particles
Y_s	mass fraction of solvent at droplet surface
Y_∞	mass fraction of solvent far at infinite distance
ε	relative permittivity of medium
ε_0	permittivity of free space
Ψ_0	surface potential or zeta-potential
τ_D	droplet drying time
ρ_g	density of gas
ρ_l	density of liquid feed
η	liquid viscosity

υ	relative velocity between liquid and shell
$\emptyset_c$	volume fraction of a packing of particles (shell)
γ	water-air interfacial tension

Chapter 1 Introduction

1.1 Introduction

Nano-particles, of size less than 1 µm, have drawn great scientific attention due to their superior surface areas, mechanical stability, chemical reactivity, optical and other physical characteristics. These ultrafine particles play a very important role in many industrial applications, such as pharmaceuticals, food, ceramics, catalysts, electronics, pigments, cosmetics, agriculture, automotive, printing, and construction (Rhodes, 2008, Faure et al., 2010, Nandiyanto and Okuyama, 2011, Iskandar, 2009). The fabrication of structured particles via controlled approaches is of great interest in both industry and academia. Many techniques have been utilised for controllable morphologies, such as wet synthesis, emulsion-assisted self-assembly method, attrition or milling to bulk materials, freeze-drying, spray drying, and pyrolysis method (Cho, 2016, Iskandar et al., 2001, Velev et al., 2000, Iskandar et al., 2009, Nandiyanto and Okuyama, 2011).

Spray drying method has been extensively employed for particles production because this technique is trusted in practice and has advantages of simple continuous and rapid process, economy and capability of scale-up (Masters, 1972, Mujumdar, 2006, Niessen, 2010, Nandiyanto and Okuyama, 2011, Li et al., 2010). In recent years, using a spray drying method to engineer particles with controllable structures has drawn tremendous attention. This rapid granulation technique allows people to have certain control of final product morphology and size in order to meet desired functional application purposes and to minimise the inhalation hazard when working with fine powder (potential cause of serve health damage). Furthermore, the properties of nano-scaled primary particles can be retained in the drying formed macroscopic granules (Vehring, 2008).

1.2 Background

In the pigment industry, the common synthesis routes for titanium dioxide (TiO_2) manufacturing are either the sulfuric acid and the chlorine route (Middlemas et al., 2015). More information about these two synthesis processes will be given in the literature review chapter. Globally only a few companies can manufacture rutile type TiO_2 pigments using the chlorine process. Venator UK (supplier for the materials used in this project) is one of such specialist that focuses on manufacturing high-quality titanium dioxide pigments. In Venator's TiO_2

manufacture process, the synthesized pigments will be subsequently subjected to a series of post-synthesis treatments to improve the mechanical and the optical properties of the final product and to deliver an acceptable physical form. The block diagram (Figure 1) below briefly outlines Venator's post-treatments to TiO_2 pigments. A schematic diagram that describes the same process in depth is shown in Figure 2 (Sutcliffe et al., 2015).

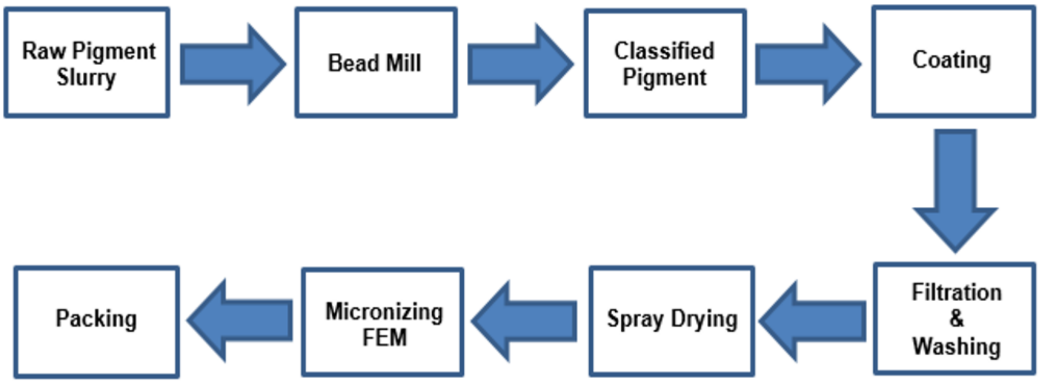

Figure 1 Block diagram of Venator's post-synthesis process of TiO_2 production (Sutcliffe et al., 2015)

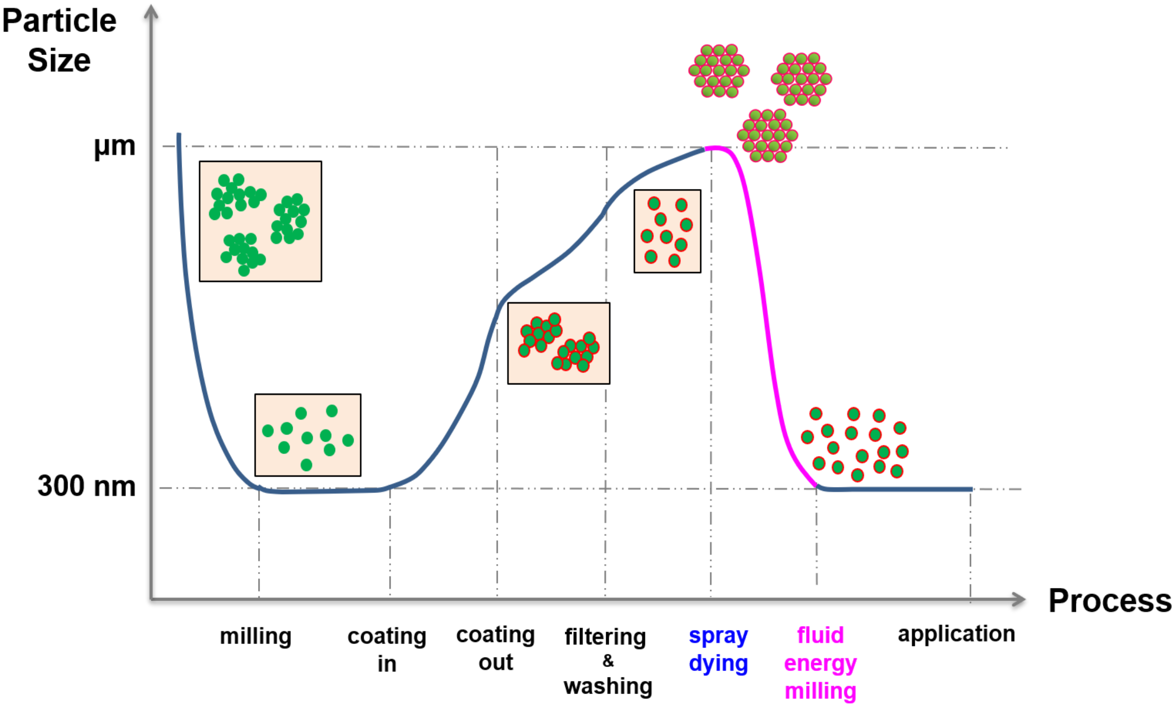

Figure 2 Schematic diagram of the post-manufacture process of TiO_2 production (Sutcliffe et al., 2015)

In Figure 2, the manufactured pigments are first dispersed in water and filled into a bead mill for size reduction to approx. 300 nm diameter (primary particle size). Sodium hexametaphosphate is added as a dispersing agent (to anchor onto pigments surface) before the milling step to assist the subsequent coating process. The resulting TiO_2 slurry is allowed to settle for the removal of oversized pigments. Aluminum sulphate ($Al_2(SO_4)_3$) solution is added to the slurry followed by sodium hydroxide (NaOH) solution to form insoluble AlO(OH) (boehmite type alumina). The boehmite will precipitate and then fall onto TiO_2 pigments surface to form surface coating layers. Subsequently, sulphuric acid (H_2SO_4) is added for neutralising the excessive NaOH and lowering the system pH to 8 which is close to the iso-electric point of boehmite alumina. The coated TiO_2 pigments start to flocculate due to weakened electrical double-layer force at pH = 8. These large flocculates are filtered and then washed with a plenty of deionised water over several times to remove the residual salt (Na_2SO_4) from the system. The key reaction schemes of alumina coating formation are shown in Figure 3.

$$NaOH + AI_2(SO_4)_3 \rightarrow Na_2SO_4 + AIO(OH) \downarrow$$

$$H_2SO_4 + NaOH \rightarrow Na_2SO_4 + H_2O$$

Figure 3 Reaction schemes of alumina coating formation (Sutcliffe et al., 2015)

The washed filter cakes are re-dispersed into the water to remake a “clean” TiO_2 slurry. Subsequently, the slurry is spray dried to form larger TiO_2 granules. These granules will be ground using a Fluid Energy Mill (FEM) to reduce the size down to approx. 300 nm. The 300 nm size is beneficial for users as these small pigments can be easily dispersed into their matrices to fit different end applications. However, it is difficult to handle ultra-fine powder due to high cohesivity, poor flowability and potential to cause of dust hazards. A high energy-consuming FEM step is used to break the spray-dried granules into small particles for customers as they prefer to input less energy for mixing or agitating process. However, this FEM step adds a high cost to the current production process.

Venator UK addressed this costly FEM process issue and showed interest in developing the ability to predict particle structure forming. A controlled spray drying solution is proposed to assemble the primary particles in a slurry into larger granules for ease of powder handling. It is important to understand the structure formation mechanisms and identify the key parameters responsible for the product morphology control. It was also required to develop an understanding of the correlation between the drying formed morphologies and the corresponding internal structures and associated mechanical properties. This can help Venator to further optimise the FEM step from the current process.

There has been recent progress in the understanding of spray drying of a colloid system. Recent reports[1] revealed the relationship between some drying process variables and the final product morphology. In particular, some models have been developed for morphology prediction (Bayly, 2014, Handscomb et al., 2009a, Handscomb et al., 2009b, Vehring, 2008). However, those studies were limited to the use of various single droplet drying techniques rather than use of a real spray dryer. Many complex phenomena involved in the spray drying process, such as atomisation, rapid heat transfer, and mass transfer, etc. were not completely covered. Furthermore, understanding of the correlation between material properties, drying process conditions, spray-dried particle morphology, and structure still remains out of reach. Therefore, many research gaps and challenges remained. There is still a need to develop this state of the art to highlight the key mechanisms driving the structural transformation in a colloidal droplet during a spray drying process. Because of this, both largely experimental work and empirical models are highly demanded.

1.3 Aims and Objectives

The overall aim of this project is to engineer any possible structures for TiO_2 pigment systems using a controlled spray drying method. It is also important to gain a detailed understanding of the morphology control techniques and the associated properties of spray-dried products. The project first considers the colloidal characterisations of two distinctive TiO_2 slurry systems. The interaction forces between primary particles in a suspension have a significant effect on the drying behaviour of system. It has been found the variations in colloidal structure of a droplet can lead to a dramatic change to the assemblies of primary particles during the drying process (Lintingre et al., 2015, Lintingre et al., 2016, Lyonnard et al., 2002, Takahashi et al., 1995, Tsapis et al., 2005). Therefore, the

---

[1] See literature review chapter for details

techniques for controlling the final product morphologies are initially explored via manipulating the particle-particle interaction in a slurry feed. Subsequently, the morphology is investigated by the variation of spray drying process conditions, including the drying temperature and the atomisation conditions.

The drying behaviours of two TiO_2 systems are further studied using a more controlled single droplet drying technique to verify the morphology observations from spray drying work and to study the structure transformation (evolution of a single droplet) throughout a drying process. It is also expected to identify the morphology forming mechanisms and the key parameters responsible for driving the morphology control. Finally, the internal structure of spray-dried TiO_2 granules needs to be assessed and correlated with the spray-dried morphology and associated mechanical properties to gain an insight into overall engineering control through a spray drying approach. The ultimate goal of this research is the development of relationship(s) between the slurry characteristics, processing aspects of spray drying and the morphologies of the produced granules.

1.4 Thesis Structure

The main text of this thesis comprises seven chapters, with the first being the background and the objectives of this project.

Chapter 2 Covers the literature review on the information about titanium dioxide (including manufacture routes and post-synthesis process), the particle-particle interactions in a colloidal suspension, introduction to spray drying principles, structure development in a spray drying process, achievements and limitations made in morphology control of spray-dried particles.

Chapter 3 Focuses on the colloidal characterisation of two TiO_2 slurry systems received from Venator UK used in this study. One TiO_2 system has alumina coating covered on particle surface, and the other system has phosphate type dispersants anchored to TiO_2 particle surface[2]. The particle-particle interaction in a colloidal system plays a significant role in the spray-dried granule structure. Therefore, it is very important to understand the characteristics of the material being dried. In this chapter, the colloidal characteristics of two systems were

---

[2] More information about two TiO_2 slurry system are given in Chapter 3

assessed in terms of primary particle morphology and size, coating structure, particle surface charge, particle size, particles settling behaviour, and rheology of slurries.

Chapter 4 In this chapter, slurries prepared with different solid concentration and aggregation levels were dried using a pilot-plant scale ProCepT spray dryer. The influences of slurry formulation and the spray drying process conditions on the product morphology were studied. The initial drying studies were conducted at 120ºC with an ultrasonic type nozzle for atomisation. The experiment was extended to 200ºC drying temperature with the same atomisation condition to explore the high-temperature effect on resulting morphology. Finally, a bi-fluid nozzle was used to investigate the influence of different atomisaiton on product morphology.

Chapter 5 Drying was repeated (same slurry formulation) using a more controlled single droplet drying rig to verify the morphologies observed from the spray drying experiment. The single drying experiment allows a constant monitor of droplet evolution over time. Thus, the morphology forming mechanisms were studied through the calculation of drying associated Péclet number. The mechanism drives the buckling of spray-dried structure was proposed. The influence of droplet size on buckling behaviour was studied through the granule hollowness estimation. To mimic the particle-particle interaction at a droplet gelation condition, the yield stress values of highly concentrated slurries were measured using a rheometer.

Chapter 6 This chapter shows the internal structure analyses of spray drying formed granules through the microtome sectioning, BET specific surface area, dynamic vapour sorption, and porosity determination experiments. The morphologies were correlated with their internal structures and the associated mechanical properties (compressibility and flowability) to provide a vision of overall engineering control of product.

Chapter 7 General conclusions from this project research and some suggestions for future work.

Chapter 2 Literature Review

2.1 Introduction

In this chapter, background information about two commonly used industry TiO_2 manufacture routes is given first. As the TiO_2 particles are processed in wet (water slurry) for both synthesis and post-manufacture treatments (including spray drying), the surface interaction forces between particles in such a colloidal system are detailed as well. Fundamental concepts of spray drying technique, a droplet drying stages, and the associated structure evolution during the drying process are discussed in depth. Several particle morphology control studies by using different drying techniques are reviewed to present recent progress in particle engineering. Finally, the limitation and shortage of those studies and the remained opportunities in this field are addressed.

2.2 Titanium Dioxide

2.2.1 Introduction

As a predominant whitening pigment, titanium dioxide is an inorganic compound and has been widely used in a variety of industries since the 20th century. Titanium dioxide occurs naturally in three main crystalline forms: anatase, rutile, and brookite. The high refractive index (2.7) imparts TiO_2 a greater level of opacity and superior colour hiding power. TiO_2 also has excellent UV light absorbing capability, good chemical resistance, nontoxicity, strong resistance to discolouration (by solar exposure), high thermal stability, selective range of particle size, and the "whitest of while" colour" (McNulty, 2007, Middlemas et al., 2015, Hess et al., 1995). The current annual pigmentary TiO_2 consumption is over 4.5 million tons all over the world, and this figure is still rising. The main uses cover pharmaceuticals, personal care, cosmetics, coatings, plastics, printing and food applications. For example, the TiO_2 is used by the dairy industry to improve the whiteness and sensory acceptance of semi-skimmed milk (Winkler, 2003, Koleske, 1995, McNulty, 2007).

2.2.2 Titanium Dioxide (TiO_2) Manufacture Processes

The overall chemistry manufacture process of titanium dioxide is to convert the impure TiO_2 mineral feed into another intermediate chemical, followed by the separation of impurities. Finally, convert the intermediate chemical back to pure TiO_2. The common commercial manufacture methods include the sulfuric acid process and the high-temperature chloride process (McNulty, 2007).

The sulphate acid process is usually used for pigment grade TiO_2 manufacture, and it accounts for about 40% of world TiO_2 pigment production. The commonly used feedstocks for sulphate route process are titania slag and mineral ilmenite which contain 79-86% and 45-65% TiO_2 respectively. The overall considerations for the choice of feedstocks include the operation costs, plant configuration, feedstock cost, waste discharge, and EHS (Environment, Health & Safety) requirements (McNulty, 2007). In the sulphate process, the ilmenite or titania slag feedstock is digested with concentrated sulfuric acid to produce titanyl sulphate. For mineral ilmenite based feedstocks, ferric iron is converted to a ferrous form in a reduction step which further results in hydrogen dispersion. All undigested materials are removed in the following clarification step. For ilmenite based feedstock, copperas is separated out in a crystallisation process. The titanyl sulphate is treated with a hydrolysis step to precipitate a hydrous TiO_2 compound. This is followed by a filtration and washing step and forward to a calcination treatment. Finally, the resulting product is treated with coating, milling, and drying operation. The schematic diagram of the overall sulphate manufacture process is shown in Figure 4 (McNulty, 2007, Middlemas et al., 2015).

The chloride process has rapidly grown since the 1970s. The changeover from sulphate to chlorination process was because the latter one is a more compact, more clean and continuous operational process. Efficient recycling of chlorine can be achieved due to a high level of chlorine recovery. Furthermore, considerably fewer by-products are generated from the chlorine process (Hess et al., 1995). In chloride process route, impure TiO_2 feedstock (which usually contains rutile and synthetic rutile) is contacted with petroleum coke in the presence of chloride gas at 1000ºC in a fluidised bed reactor where chlorination process occurs. All resulting products from chlorination process are presented in vapour form, and include titanium tetrachloride ($TiCl_4$), oxides of carbon (CO and CO_2) and all impure metals from stockfeed in the form of metal chlorides (McNulty, 2007). In next setp, the gas stream is cooled down by contacting with liquid $TiCl_4$. At this cooling level, the $TiCl_4$ contained in gas steam remained its gas form, whereas, all metal chlorides vapours are restored to their solid form and are separated out and treated with limestone for impurity waste disposal. The $TiCl_4$ (gas form) is further condensed to liquid form under cooling and then reacted with oxygen at 1500ºC in a high temperature oxidation reactor to reform pure TiO_2. The released chloride gas from this oxidation process is recycled back to the chlorination step at the beginning of process. Similar to the sulphate process, the resulting TiO_2 product is further treated with a coating, milling and drying process to form a final product (Hess et al., 1995, McNulty, 2007, Middlemas et al., 2015). The schematic diagram of the overall chloride process is shown in Figure 5 (McNulty, 2007).

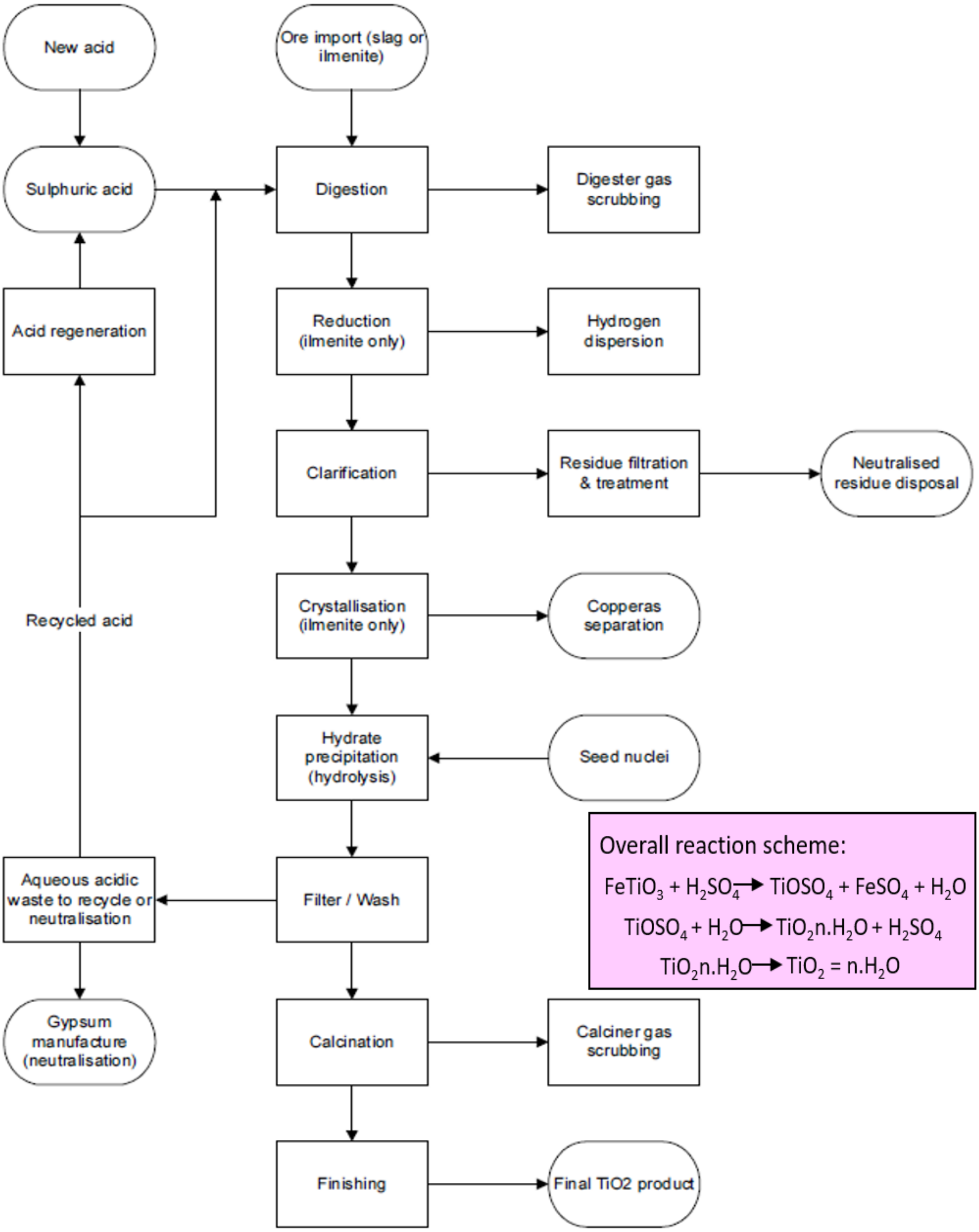

Figure 4 Schematic diagram of the sulphate process and the overall reaction scheme.

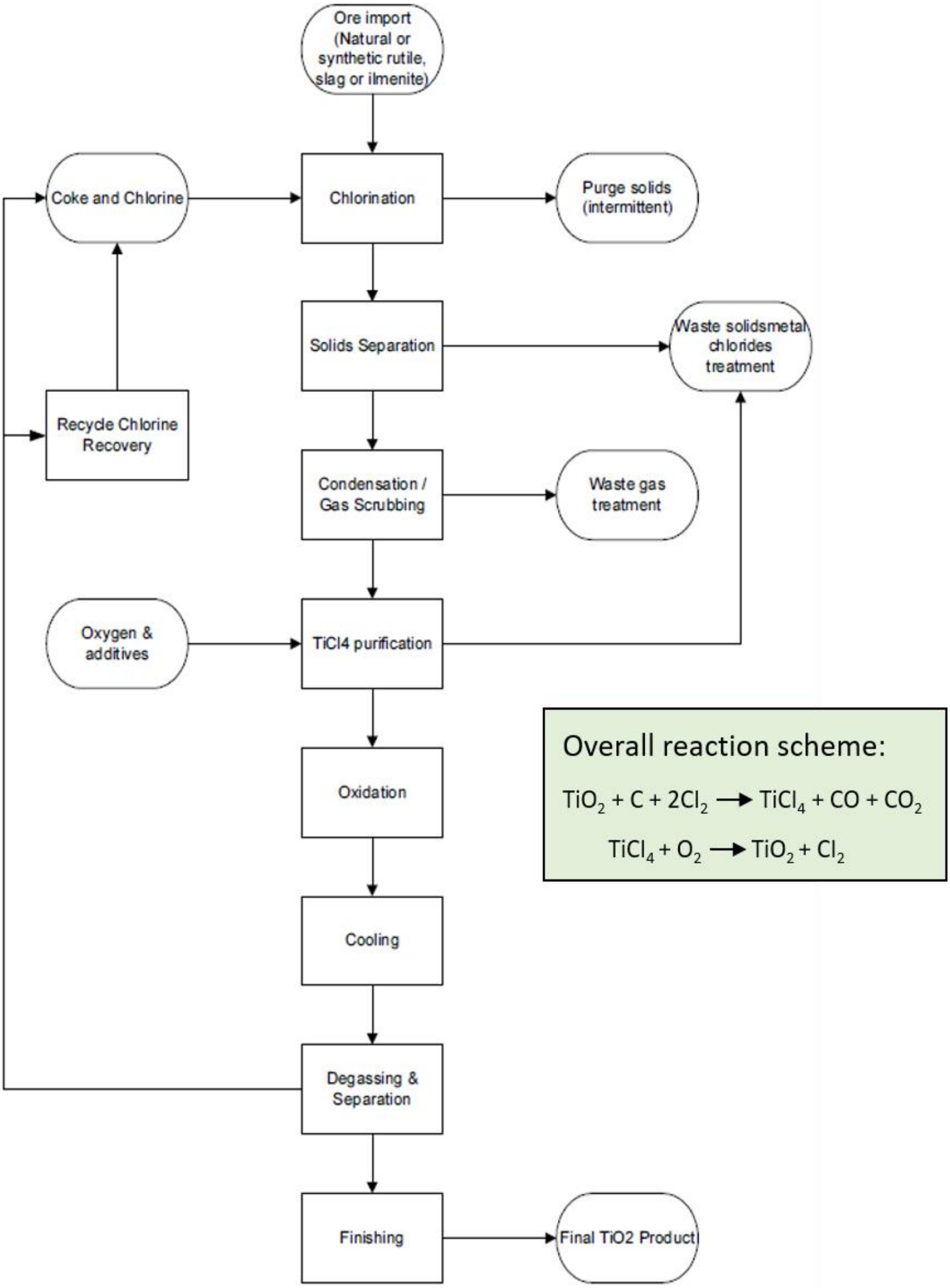

Figure 5 Schematic diagram of the chloride process route and the overall reaction scheme.

2.2.3 Coating Process on TiO_2 pigments

There is yellow colouration issue to titanium dioxide pigments. When they are used as whiteners in paint formulation, the chemical reaction between the titanium dioxide and any any polystyrene based polymeric component will form impurities that impart yellow colour to product. The titanium dioxide itself is inherent in semi-conductivity property which will releases electrons under UV. This process also results in formation of undersiable yellow colouration (Brand, 1982). Therefore, TiO_2 pigments are commonly subjected to a surface coating treatment in manufacture process to improve the durability and to lessen the yellowing problem. The coating process involves milling the crude pigments in water by using a ball mill or a sand mill. The resulting pigment dispersion is allowed to settle for removal of oversized particles. Commonly selected coating agents are hydrous silica or alumina materials. By adjusting the pH of dispersion, the oxide precipitates out of water and fall onto the pigment surface to form a coating layer. This is followed by filtration and washing process to remove excessive salts. The clean pigments are re-dispersed in water to reform slurry and is spray-dried to form granular products (Hess et al., 1995).

2.3 Colloidal Particle-Particle Interaction

2.3.1 Introduction

In a colloidal system, the surface forces between particles are derived from the electromagnetic interactions and can be computed by summing all the interaction forces between all the molecules or atoms in the particles across the intervening medium. The nature of surface forces existing between two adjacent particles can be either attractive or repulsive. The factors that influence the surface forces include the material type of particle, the medium and the separation distance between particles. Mathematically, the surface force (F) can be express by Equation (2.1), where (W) is potential energy and (D_{sep}) is separation distance between particles. The common mechanisms that drive surface forces between particles include van der Waals interaction, electrical double layer, and adsorbing polymers that lead to bridging, steric and depletion forces (Rhodes, 2008, Israelachvili, 2011).

$$F = -\frac{dW}{dD_{sep}} \tag{2.1}$$

2.3.2 Van der Waals Forces

Van der Waals force is derived from electrodynamic interactions, and it is operative between neighbouring molecules or atoms in a short-range distance. The van der Waals force consists of three types of forces with different interaction mechanisms (Shaw, 1980, Van Oss et al., 1980, Nic et al., 2005).

- Keesom: the force between two molecules or atoms both with permanent dipoles.
- Deby: the force between one molecule or atom with a permanent dipole and the other molecule or atom with an induced dipole.
- London Dispersion: the force between two molecules or atoms with instantaneous dipoles induced by fluctuations in the charged distribution of a molecule or an atom.

In the case of two spherical particles with an equal diameter (*d*). When the separated distance between particles (D_{sep}) is much smaller than the diameter, the van der Waals interaction and force can be express by Equation (2.2) and (2.3), where (W_{vdw}) and (F_{vdw}) are van der Waals interaction energy and force separately, and (*A*) denotes the Hamaker constant (Rhodes, 2008).

$$W_{vdw} = -\frac{A\,d}{24\,D_{sep}} \tag{2.2}$$

$$F_{vdw} = -\frac{A\,d}{24D_{sep}^2} \tag{2.3}$$

Hamaker constant, which is a function of the electric polarizability and the density of the material, can be understood as a numerical value to express the magnitude and attribute of the interaction for a given particular pair of particles acting across the intervening medium. For the case of two particles (denoted as material 1 and 2) immersed in a medium (denoted as material 3), the system configuration can be illustrated in Figure 6. When the material (1 and 2) are the same, the combined Hamaker constant ($A_{combined}$) for a system with the same type of spherical particles (with relatively smooth surface) immersing in a medium can be expressed in Equation (2.4) (Cosgrove, 2005, Rhodes, 2008).

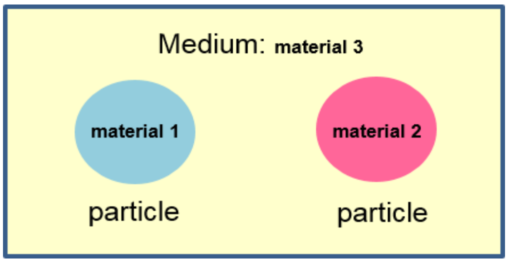

Figure 6 Schematic diagram of the type of materials for particles and intervening medium (Rhodes, 2008).

$$A_{combined} = \left(\sqrt{A_{particle}} - \sqrt{A_{medium}}\right)^2 \quad (2.4)$$

2.3.3 Electrical Double Layer

The majority of particles in a suspension have electrical charge on their surfaces. There are various mechanisms of surface charge developments, such as surface groups, ionisation, dissolution of ionic solids, isomorphous substitution and adsorption of the charged species, etc. (Cosgrove, 2005, Malvern, 2015b). An example of how does a metal oxide particle becomes charged on the surface as a result of surface groups ionisation is demonstrated here in order to better understand the concept. Titanium dioxide particle is used for illustration as it is firmly associated with this project.

In open-air, the TiO_2 particle is comprised of equal number of titanium atoms with positive charges and oxygen atoms with negative charges (Figure 7 a for illustration). When being dispersed in water, the titanium atoms (Ti) and oxygen atoms (O) will react with water molecules separately to produce unsatisfied (Ti-OH) and (O-H) groups (Figure 7 b) via the reaction schemes shown in (Figure 7 c). At an acidic pH condition, the surface of particle is mainly comprised of positively charged (Ti-OH_2^+) and (O-H_2^+) species (Figure 8 a) which are created via reactions between surface groups (Ti-OH) and (O-H) with (H^+) ions in water (scheme shown in Figure 8**Error! Reference source not found.** c). Likewise, at a basic pH condition, the surface of particle acquires negative charges as a result of (Ti-O^-) and (O^-) species (Figure 8 b) which are created via reactions between surface groups (Ti-OH and O-H) with (OH^-) ions in water (Figure 8 d) (Rhodes, 2008, Hunter, 2001).

For a metal oxide based colloidal system, there is a pH at which the particle surface has electrical neutrality indicating a zero surface net charge. This specific pH point is known as the iso-electric point (IEP) for this particle material. As a result of acid solution addition, the system pH is below the IEP and the particle surface becomes positively charged. As a result of alkali addition, the pH of the system pH is above the IEP, leaves a negative charge on particle surface (Rhodes, 2008, Hunter, 2001).

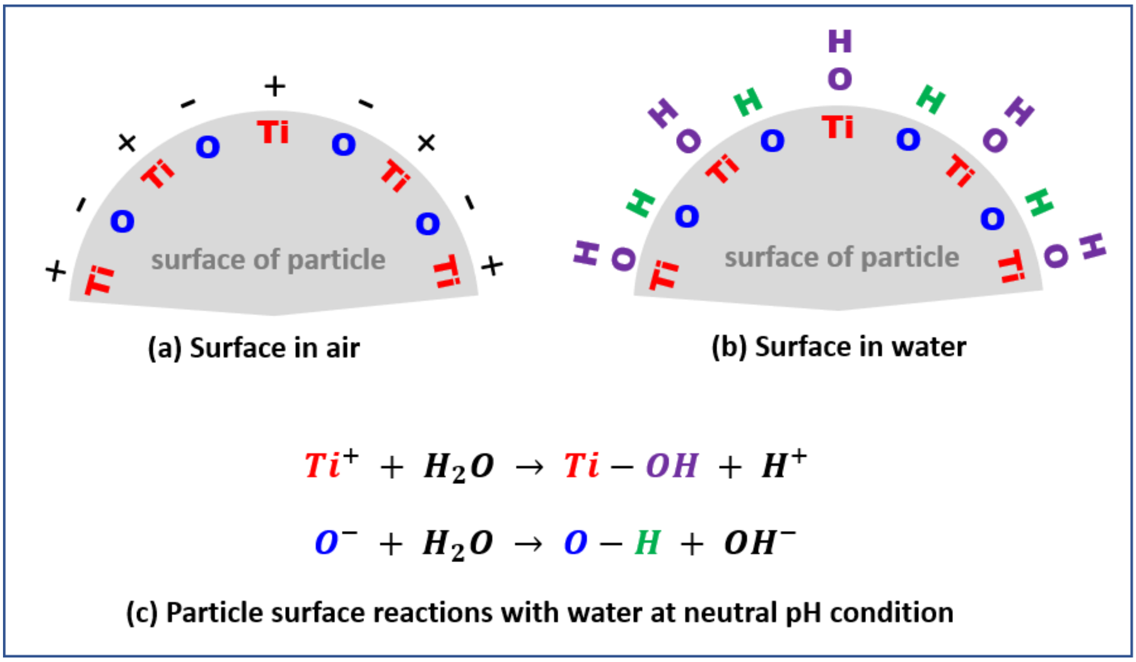

(a) Surface in air

(b) Surface in water

$$Ti^+ + H_2O \rightarrow Ti - OH + H^+$$

$$O^- + H_2O \rightarrow O - H + OH^-$$

(c) Particle surface reactions with water at neutral pH condition

Figure 7 Schematic diagram of TiO_2 particle surface: (a) in air; (b) in water; (c) particle surface reactions with water at neutral pH condition (Rhodes, 2008).

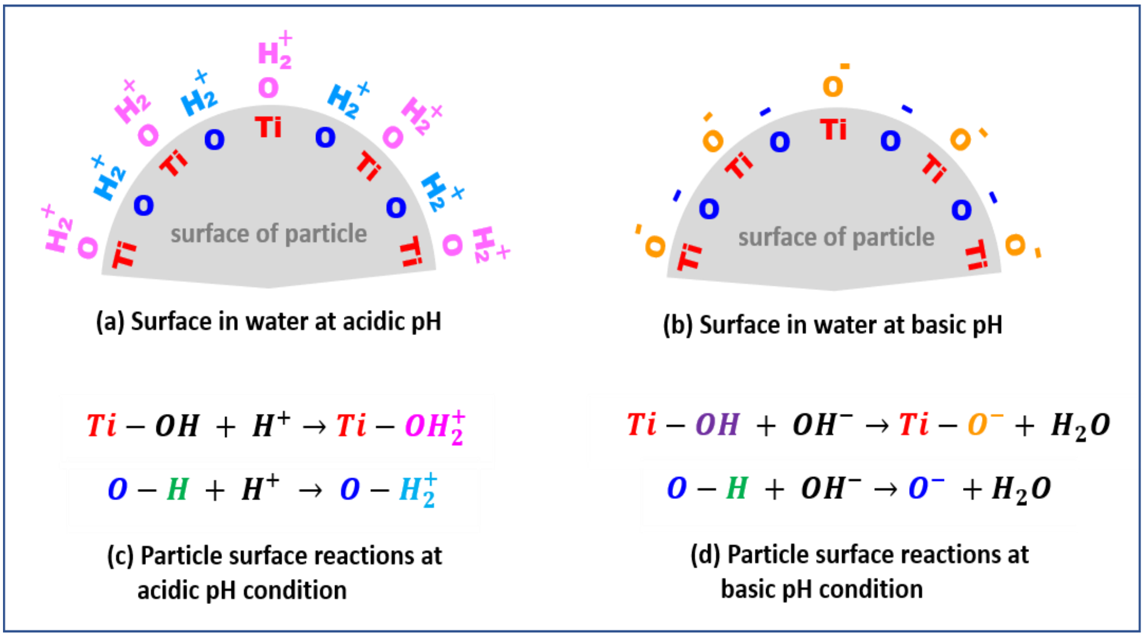

(a) Surface in water at acidic pH

(b) Surface in water at basic pH

$$Ti - OH + H^+ \rightarrow Ti - OH_2^+$$

$$O - H + H^+ \rightarrow O - H_2^+$$

(c) Particle surface reactions at acidic pH condition

$$Ti - OH + OH^- \rightarrow Ti - O^- + H_2O$$

$$O - H + OH^- \rightarrow O^- + H_2O$$

(d) Particle surface reactions at basic pH condition

Figure 8 Schematic diagram of TiO_2 particle surface: (a) at acidic pH; (b) at basic pH; (c) surface reactions at acidic pH condition; (d) surface reactions at basic pH condition (Rhodes, 2008).

The charge acquired on particle surface can result in a diffuse cloud of oppositely charged ions from the surrounding medium (denoted as counter-ions) shrouding the particle surface in order to maintain the entire colloid system electrically neutral. The concept of electrical double layer (EDL) is used to describe the distribution of counter-ions in the interfacial region surrounding the particle surface. The electrical double layer is derived from: i) an inner Stern layer where immobile counter-ions are strongly bound to the charged particle surface; and ii) a Diffuse layer in outer region, which is comprised of less firmly associated ions (Figure 9). Within the Diffuse layer, there is another notional boundary layer located adjacent to the Stern layer. Due to the Brownian motion or other external forces, a colloid particle in water is under a random movement. The ions within the notional boundary layer will follow the movement of the particle, and this notional layer is usually defined as Shear lane. The rest of ions existing beyond this Shear plane will remain in the bulk of solution rather than following the movement of particle (Rhodes, 2008, Hunter, 2001, Hoath, 2016, Malvern, 2015b, Holdich, 2002).

With respect to the potential of the layers defined above, the difference in potential between the charged particle surface and the bulk solution is the surface potential (Ψ_0). The potential on the Stern layer and the Shear plan are known as the Stern potential and Zeta potential (ξ) respectively. Technically, the measurement of particle surface potential is difficult because there are immobile ions strongly bonded to the surface. In practice, it is easier to directly determine the zeta potential of system by measuring the velocity of particles in an applied electric field. Thus, the terms of surface potential and zeta potential have often been used interchangeably for calculation (Israelachvili, 2011, Rhodes, 2008). When two particles approach on another under external force(s), their electrical double layers (EDL) overlap, and leading to a high concentration of ions midway between the two particles. If both particles are carrying same charge, the osmotic pressure of counterions and the Columbic interaction between two particles are acting to force the two particles to repel, which is known as EDL repulsion (Rhodes, 2008, Holdich, 2002, Cosgrove, 2005).

The electrical double layer (EDL) is characterised by its thickness which is termed as Debye length (k_{De}^{-1}), where (k_{De}) is Debye screening parameter. For a colloidal system with monovalent type electrolyte background, Equation (2.5) can be used for calculation, where (c_0) is the molarity of monovalent electrolyte, K_B the Boltzman constant, T the Kelvin temperature, e the charge of electron, ε and ε_0 the relative permittivity of medium and permittivity of free space (Israelachvili, 2011, Rhodes, 2008). It is noted that the Debye length (k_{De}^{-1}) is dependent to system temperature T. In the case of ambient condition, the Deby length calculation for a monovalent electrolyte based system can be simplified by using Equation (2.6)

Both the addition of electrolyte and the electrolyte valency have effect on the thickness of EDL. In general, high ionic concentration and ionic valent can compress the EDL. As a result, the van der Waals attraction will play an important role in interacting adjacent particles as the range of EDL repulsion is greatly weakened.

$$\frac{1}{k_{De}} = \left(\frac{\varepsilon\ \varepsilon_0\ K_B\, T}{e^2\, C_0}\right)^{1/2}\ (nm) \tag{2.5}$$

$$k_{De} = 3.29\sqrt{[C_0]}\ (nm^{-1}) \tag{2.6}$$

For the case of two similar spherical particles with smooth surface and same type of charge, the EDL interaction energy can be calculated by Equation (2.7) where

(d), (Ψ_0), (ε), (ε_0) and (D) are the diameter of particle, the surface potential (or zeta potential), the relative permittivity of medium, the permittivity of free space (8.854 x 10^{12} C^2/J/m) and the separation distance between two particles (Rhodes, 2008, Cosgrove, 2005, Verwey, 1947).

$$W_{EDL} = \pi\ \varepsilon\ \varepsilon_0\ d\ \varphi_0^2\ exp(-kD) \tag{2.7}$$

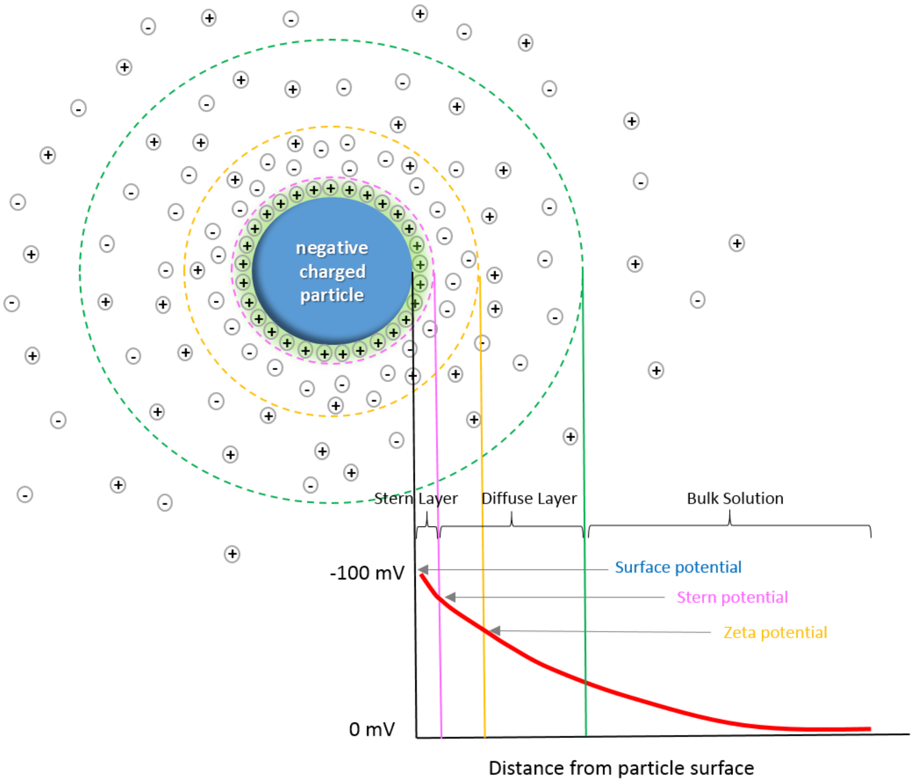

Figure 9 Schematic diagram of EDL double layer for a negatively charged particle (Malvern, 2015b)

2.3.4 Net Interaction Force

The net interaction between two particles in water can be determined by combing the energy from the attractive van der Waals interaction and the repulsive interaction Equation (2.8). The theory of net interaction was first developed by Derjaguin, Landau, Verwey, and Overbeek in the 1940s, and known as DLVO theory (Hoath, 2016, Malvern, 2015b). This theory predicts the aggregation of a colloid system at a specific pH in terms of describing the change in energy interaction between adjacent particles with charges in a medium. Figure 10 demonstrates that the changes in interaction between two charged particles as the separation varies (Hoath, 2016). The green and blue dot lines represent electrical double layer interaction and van der Waals interaction respectively. It clearly shows as particle separation distance becomes smaller, both attractive and repulsive interactions are getting larger in magnitude with different rates. The combined effects of double layer and van der Waals interaction is expressed by a red curve seen in Figure 10. When two particles are very close in distance, the net energy falls into a primary minima region where van der Waals mostly dominates. As the separation between particles increases, the repulsive energy dominates, indicating the particles are well dispersed in medium. At this moment the system stability can be assessed by the height of energy barrier whose amplitude should be at least 10 K_BT (where K_B is the Boltzman constant and T is the Kelvin temperature) to maintain sufficient colloidal stability (Hoath, 2016, Rhodes, 2008, Lintingre et al., 2016, Lintingre et al., 2015). As the distance further increases, the net energy falls into the secondary minima region. Particle flocculation is seen, but the process is reversible if an external force is applied, such as mixing or stirring. In real work, the DVLO model is often used to predict the aggregation of a colloidal suspension at specific pH of interest. This can be achieved by the comparison of the net interaction curves obtained at different pH.

$$W_{net} = W_{vdw} + W_{EDL} \qquad (2.8)$$

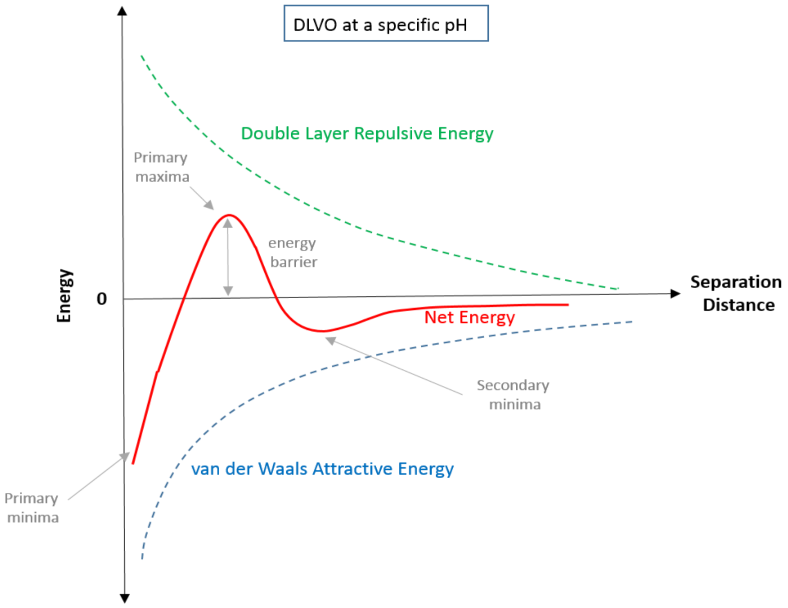

Figure 10 Schematic diagram of DLVO theory for two spherical particles (Hoath, 2016)

2.4 Spray Drying

2.4.1 Introduction

Spray drying is a method of producing dry powder by rapidly drying the liquid feed in a heated gas flow. This effective transformation method is a one-step continuous process, and it has been used in a wide range of applications including pharmaceuticals, food, polymer, detergents, and colorants (Masters, 1972). The liquid feeds for spray drying are usually thermal sensitive type solution, suspension, slurry, and even paste. Depending upon the properties of the liquid feed and the design of spray dryer, the resulting product varies in physical form, possibly: fine powder, granules or large agglomerates. Air is typically used as hot drying gas for an aqueous-based system. Nitrogen gas is used when the liquid feed is an oxygen-sensitive or flammable organic solvents based system (Mujumdar, 2006, Niessen, 2010).

The primary process of spray drying consists of three steps: atomisation, droplet-to-droplet conversion, and particle product collection. Spray drying is a complex process that covers a rapid removal of water from atomised small droplets using heated gas flow. The heat and mass transfer phenomena are occurring simultaneously on droplet surface, coupled with phase change and droplet structure transformation. In spray drying, the formulated solution is or slurry is fed into a drying chamber through an atomiser where liquid feed can be atomised into small droplets. Meanwhile, heated gas is introduced to the drying chamber through a disperser to contact with those droplets to induce evaporation. The spray drying process can be controlled via both liquid feed formulation and the drying processing conditions. Finally the spray-dried particulate product is separated from the exhaust gas and collected by a cyclone, a filter bag or an electric field precipitator (Masters, 1972, Mujumdar, 2006, Nandiyanto and Okuyama, 2011). The schematic diagram of a spray drying process is illustrated in Figure 11.

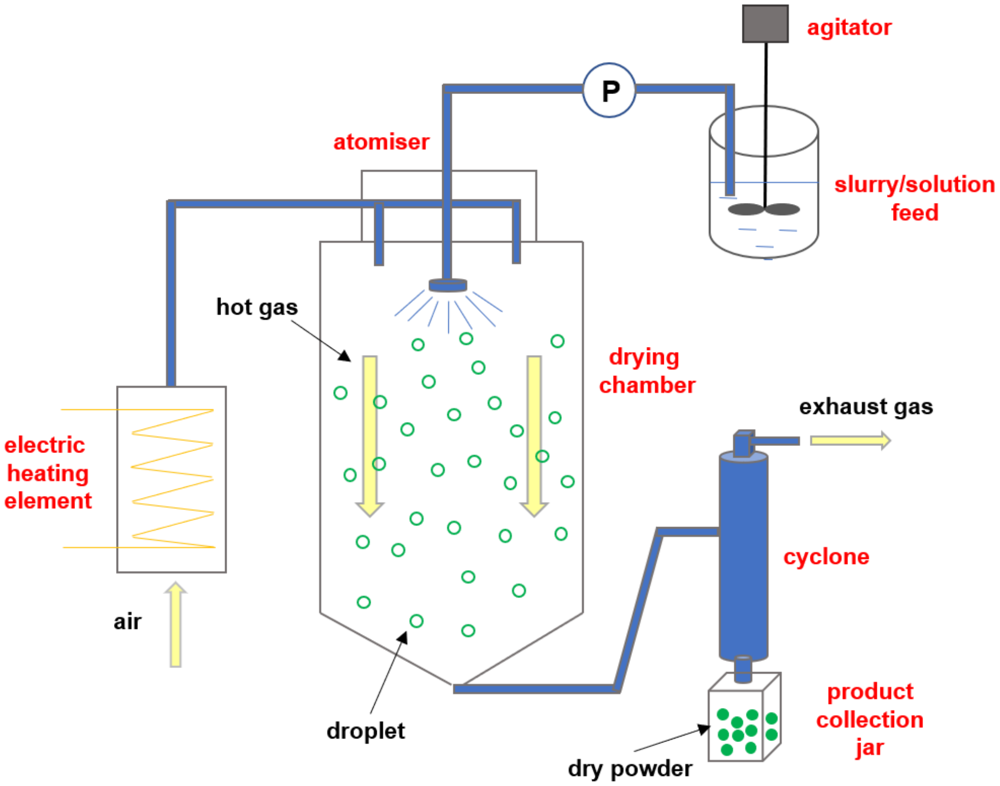

Figure 11 schematic illustration of a spray drying process

2.4.2 Atomisation

The atomisation process plays an important role in determining the uniformity of the final dried product (Masters, 1972). In the atomisation step, the initial bulk precursor is fed into an atomiser that locates on top of the drying chamber to convert the liquid feed into discrete droplets with a small size (1-1000 μm). Because the subsequent drying evaporation is directly related to the surface area of atomised droplet, homogeneous sprays can ensure an identical heat transfer rate, mass transfer rate and drying time to all droplets. Therefore, a good atomisation is critical to an efficient drying process and physical properties of spray-dried powder (O'Sullivan et al., 2019). Based on the type of driving force installed, the commonly used atomisers include rotary disk, two-fluid nozzle, electrospray, and ultrasonic nozzle (Nandiyanto and Okuyama, 2011). The selection of appropriate atomiser depends on the operation process, the spray dryer configuration, the physicochemical properties of the liquid feed (such as formulation, surface tension, viscosity, volatility, and volume) and the required droplet size (O'Sullivan et al., 2019, Schuck et al., 2016). In principle, the droplet size distribution generated from an atomiser is determined by the input energy, liquid feeding rate, liquid viscosity, and surface tension. Higher atomisation energy leads to smaller droplets with a narrow distribution which further results in fine product powder. For a liquid with high viscosity, more energy input is required to produce sprays with acceptable droplet size for the following evaporation process (Filkova and Mujumdar, 1995, Hall et al., 2011).

The commonly used atomisaiton techniques for a lab-scale or a pilot-scale spray dryer are usually bi-fluid nozzle and ultrasonic nozzle (Jackson and Lee, 1991). A bi-fluid nozzle (also known as pneumatic nozzle) utilises a compressed gas flow (usually air for a water-based system and N_2 for a solvent-based system) to shear the liquid stream into small droplets which form a conical spray pattern. Depending on the nozzle design, the compressed gas flow can contact with the liquid feed either within the nozzle body or near the exit of the nozzle tip (Písecký, 2012, Jackson and Lee, 1991, O'Sullivan et al., 2019). A ProCepT bi-fluid type nozzle with internal gas-liquid mixing is illustrated in Figure 12. The maximum atomisation airflow from such a nozzle from ProCepT is approximate. 50 L/min (ProCepT, 2014b). A bi-fluid nozzle is commonly used for viscous liquids which are challenges to other types of nozzles. With a constant atomisation gas flow rate, higher solid content and higher viscosity of liquid feed lead to larger droplets with broader distribution. However, smaller droplets are still achievable by increasing the gas flow rate for atomisation (Jackson and Lee, 1991).

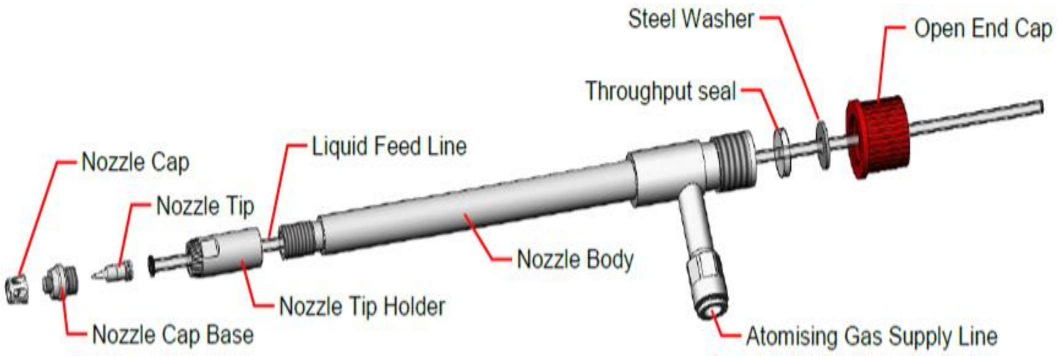

Figure 12 A bi-fluid type nozzle from ProCepT 4M8-TriX spray dryer (with internal gas-liquid mixing design) (ProCepT, 2014b)

An ultrasonic atomiser utilises the ultrasound vibration to produce droplets. The key component in nozzle is a piezoelectric transducer (made of either quartz or lithium zirconate titanate material) that can convert the input electrical energy to mechanical vibration. Acoustic waves can be generated as a result of the mechanical vibration to atomise the liquid feed into droplets. A schematic diagram of an ultrasonic atomiser is shown in Figure 13 (O'Sullivan et al., 2019). Different frequencies can be installed onto the atomiser, and each frequency generates a specific drople size range. For a 25 kHz ultrasonic nozzle from ProCepT 4M8-Trix spray dyer, a droplet size range of 20 -150 µm can be achieved. In principle, lower frequency can result in larger droplets, and the droplet sizes created by an ultrasonic atomiser is larger than the ones generated by a bi-fluid atomiser (ProCepT, 2014a). The ultrasonic atomiser is usually employed for lab-scale spray drying only. It is not economical for full-scale production due to the high energy consumption of this atomisation technique (Klaypradit and Huang, 2008, O'Sullivan et al., 2019).

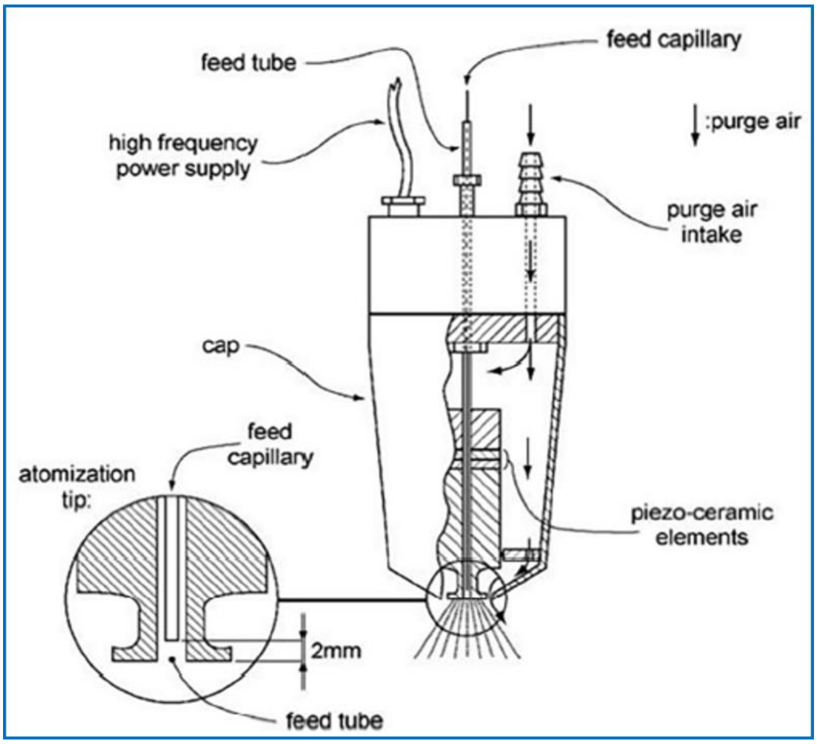

Figure 13 Schematic diagram of an ultrasonic atomiser (Freitas et al., 2004, O'Sullivan et al., 2019)

2.4.3 Evaporation

The droplets generated from the atomisation process will be carried with the heated gas flow to travel through the spray dryer chamber. The droplets will undergo a rapid water evaporation process, resulting in solute condensation within the droplet (Nandiyanto and Okuyama, 2011, Masters, 1972). The driving force of droplet evaporation is the difference between the water vapour pressure and its partial pressure in the air. From the energy perspective of view, the total energy required for vaporisation is transported from the heated gas. Therefore, the heat transfer rate from gas to droplet surface will determine the evaporation rate (Vehring, 2008, Vehring et al., 2007).

In spray drying, the evaporation process mainly consists of two periods. The evaporation initially takes place from the saturated vapour layer established at the surface of the droplet. As the evaporation further progresses, the droplet surface can reach a saturated point. The surface saturation remains due to the diffusion of moisture from the droplet, replenishing the moisture loss at the surface. The evaporation rate for this first drying period is considered to be constant. In the second drying period, as the surface moisture content is further reduced, there is insufficient water diffusing from the droplet to replenish the surface moisture (to maintain its saturation). When the surface moisture content drops down to a critical level, the solute starts to precipitate out to form a shell (crust) at the droplet surface. The evaporation rate is then determined by the diffusion rate of water through the formed surface shell. Typically the dried surface shell becomes thicker with time, resulting in a decrease in evaporation rate (Masters, 1972). The evaporation rate (*k*) for the first constant evaporation period follows a linear relationship with droplet size and can be expressed in Equation (2.9), where D_0 is the initial droplet diameter, *t* is the evaporation time and *D(t)* is the droplet diameter at time *t* (Vehring et al., 2007, Vehring, 2008, Fuchs, 2013):

$$D^2(t) = D_0^2 - kt \tag{2.9}$$

The droplet drying time (τ_D) can be derived from Equation (2.9) when the droplet diameter at time *t*, *d(t)* = 0. The expression is shown in Equation (2.10) (Vehring, 2008):

$$\tau_D = \frac{D_0^2}{k} \tag{2.10}$$

Droplet evaporation rate determination in a realistic spray dryer is not straight forward because there are difficulties in obtaining the droplet size information. Vehring et al. recommended a method for evaporation rate approximation without the need for droplet size information. The approximation is shown in Equation (2.11). The D_g, ρ_g, and ρ_l are diffusion coefficient of the gas phase, density of gas at wet bulb temperature, and density of the liquid feed. Y_s and Y_∞ are the mass fraction of the solvent at the droplet surface and the mass fraction of the solvent far from the surface at equilibrium temperature (Vehring, 2008, Finlay, 2001).

$$k = 8D_g \frac{\rho_g}{\rho_l} (Y_s - Y_\infty) \tag{2.11}$$

The mass fraction of the solvent at the droplet surface (Y_s) can be calculated by dividing the solvent vapour pressure at equilibrium temperature by the atmospheric pressure. The solvent vapour pressure (P) can be determined by using the Antoine Equation (2.12) or tabulated data, where A, B, and C are Antoine constants for water (Vehring et al., 2007).

$$P = 10^{\left(A - \frac{B}{C + T_{wb}}\right)} \tag{2.12}$$

The equilibrium temperature at droplet surface can be approximated to its associated wet bulb temperature (T_{wb}) which can be estimated using an empirical correlation shown in Euqation (2.13), where T_G is the drying gas temperature and T_b is the liquid phase boiling temperature (Vehring, 2008, Miller et al., 1998).

$$T_{wb} = 137 \left(\frac{T_b}{373.15}\right)^{0.68} \log(T_G) - 45 \tag{2.13}$$

2.4.4 Particles Recovery

Following the drying process that occurred in the spray dryer chamber, the spray-dried particles will pass through a separation unit that recovers the granules from the drying gas. The selection of such a unit depends upon the separation efficiency, processing cost, material type and the nature of product. Commonly used units include cyclone, filter bag, electrostatic precipitator, and wet scrubber. Different separation techniques are compared in Table 1 (Nandiyanto and Okuyama, 2011, Rhodes, 2008).

Table 1 Different types of product recovery technique (Nandiyanto and Okuyama, 2011)

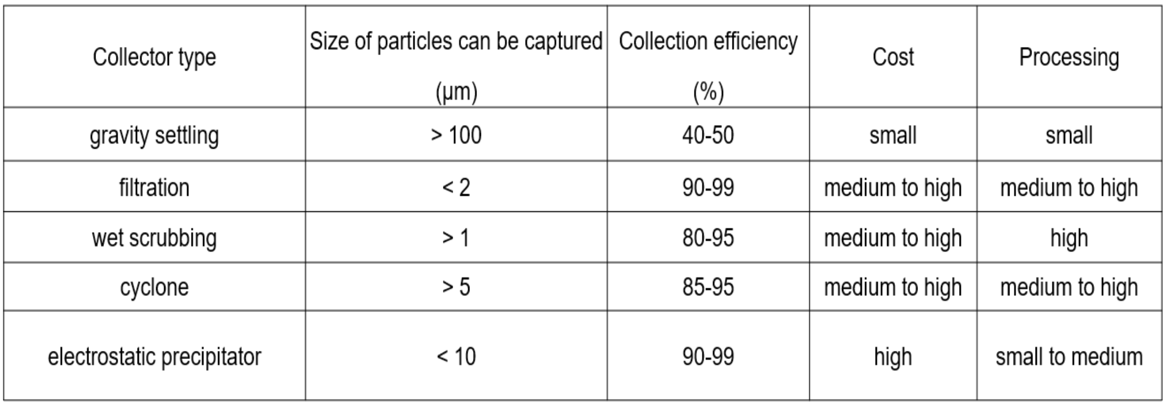

Collector type	Size of particles can be captured (μm)	Collection efficiency (%)	Cost	Processing
gravity settling	> 100	40-50	small	small
filtration	< 2	90-99	medium to high	medium to high
wet scrubbing	> 1	80-95	medium to high	high
cyclone	> 5	85-95	medium to high	medium to high
electrostatic precipitator	< 10	90-99	high	small to medium

2.5 Structure Development during Drying Process

2.5.1 Introduction

A single droplet involved in spray drying can transform into various possible structures. The morphology achieved is determined by the material formulation, spray dryer design and the drying process conditions. Examples of spray-dried particles are given in Figure 14, Figure 15 and Figure 16. These particles were all prepared by using a spray drying method. The SEM images in Figure 14 show a few spray-dried silica granules, the morphology varies from spherical to toroidal shape by changing the primary particle size (Iskandar et al., 2003). In Figure 15, the morphology of glycoprotein granules has changed significantly by varying the drying temperature (Bayly, 2014). Figure 16 exhibits more complex morphologies for spray-dried NaCl and pharmaceutical pulmosphere solid foam particles (Vehring, 2008).

This section first introduces the category of materials commonly used for spray drying and then provides an overview of morphologies which were summarised by pioneers. The following section looks at the evolution of droplet as a function of drying temperature based on different drying process stages. Several lab-scaled single droplet drying techniques for studying the drying behaviour and structure formation are presented in the last section.

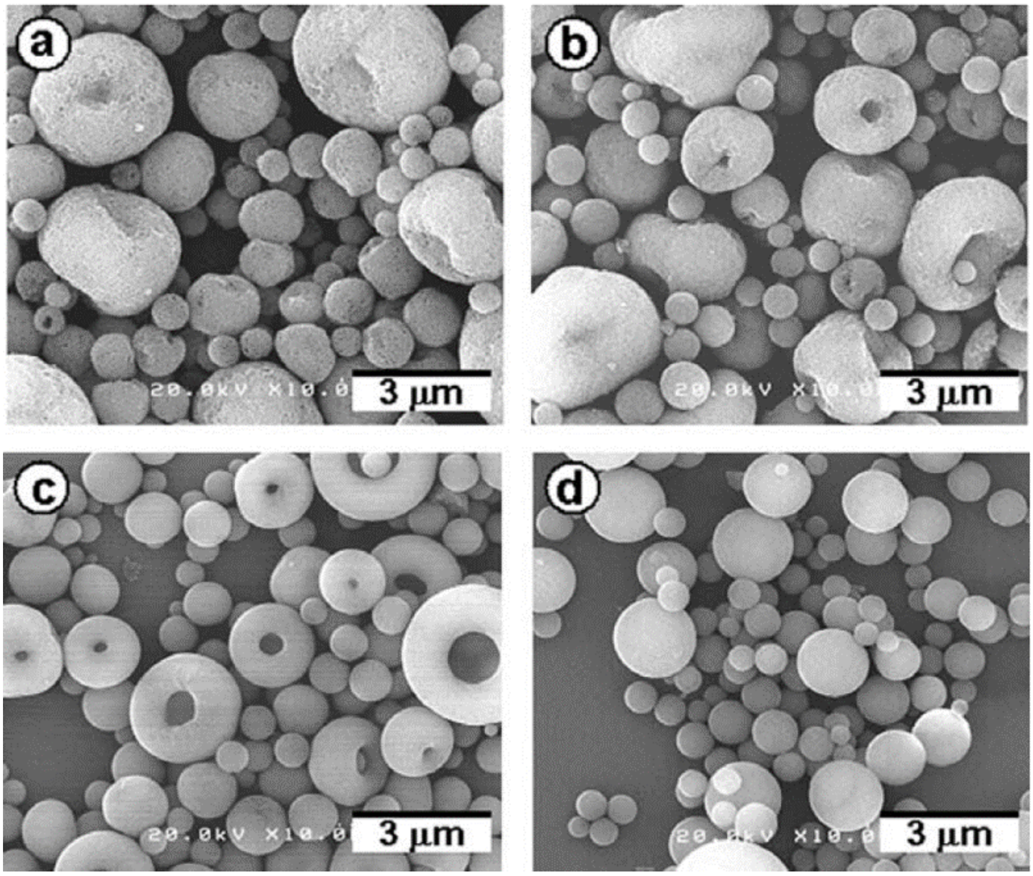

Figure 14 Effect of primary particle size (d_p) on the morphology of silica granule prepared from (a) dp=75 nm; (b) d_p= 50 nm; (c) d_p=25 nm; (d) d_p=5 nm (Iskandar et al., 2003).

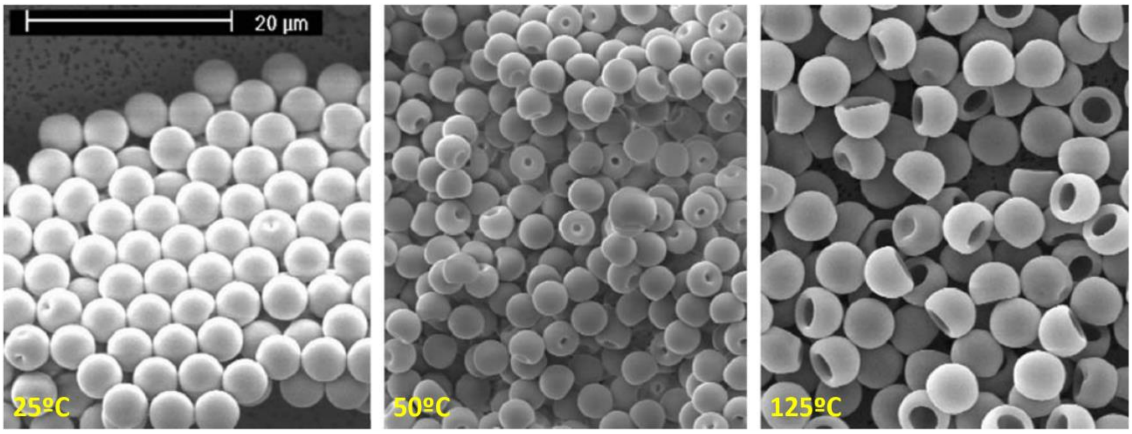

Figure 15 Influence of spray drying temperature on glycoprotein particle morphology. The drying temperature is 25ºC, 50ºC and 125ºC from left to right and the scale bar is consistent for all three images (Vehring, 2008).

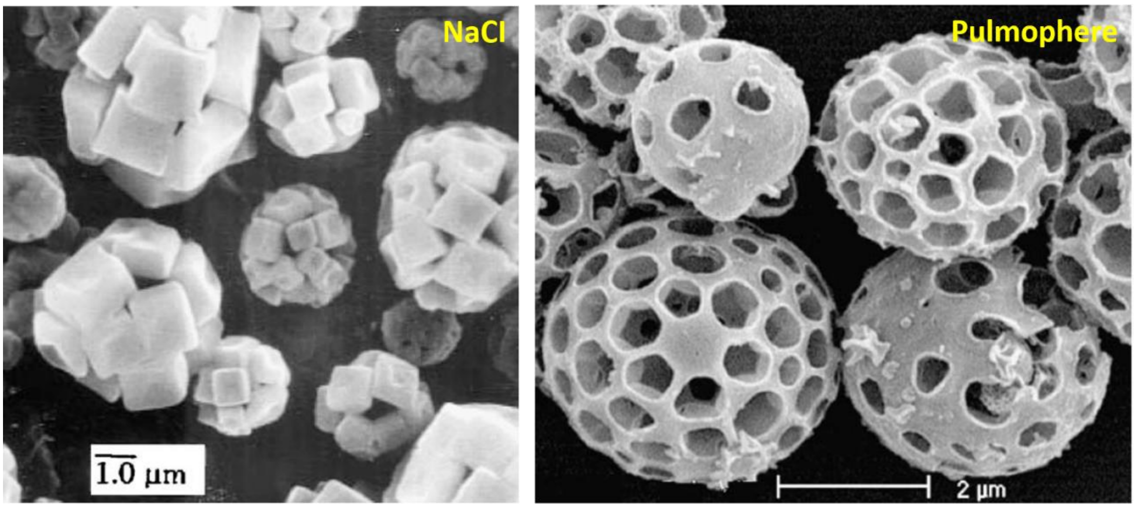

Figure 16 Spray-dried NaCl particles and pulmospheres for inhalable pharmaceuticals (Vehring, 2008)

2.5.2 Materials Types

This section focuses on the droplet evolution and particle structure development during a drying process. According to the drying behaviours, phase change over a drying process and the morphological structure formation, the materials for drying were categorised into three systems by Walton et al. These systems are referred as colloidal suspension (or agglomerate), crystallization and skin forming material (Bayly, 2014, Walton and Mumford, 1999).

Crystallization System: contains soluble molecules dissolved in the droplet being dried. The phase transition occurs when the equilibrium saturation limit is reached. The crystals precipitation is controlled by the size of nucleus and the nucleation kinetics (Bayly, 2014). Typically, amorphous morphology is observed after drying because the rapid drying rate does not allow the formulation of nuclei before the droplets become dried. Furthermore, the increased super-saturation may also contribute to the rapid nucleation rate which leads to an amorphous state (Walton and Mumford, 1999). The impact of these effects on the overall morphology can be investigated by comparing the time difference between crystallization and nuclei formation (Leong, 1987).

Skin Forming System: when drying materials, such as polymers and carbohydrates, an amorphous skin can be formed. Temperature plays an important role in changing the final granule structure. The formed skin with pliable and visco-elastic properties can impact the final granule morphology by slowing the drying rate. This leads to an increase in the droplet surface temperature. When the temperature reaches the boiling point, a rapid inflation stream can puff the granule structure. As slow progress has been made to the skin forming system, there are opportunities to develop models and understandings to explain the observed phenomena in these fields (Walton and Mumford, 1999, Bayly, 2014).

Colloidal Dispersion System: Significant progress has been achieved in drying of suspensions, slurries, and emulsions. Many experiments, quantitative analyses, and models have been completed and reported in this field to develop understandings of structure formation and tools for morphology prediction. In these studies, the structure evolution was linked with the material, the drying conditions, the associated physicochemical properties of droplet, and the corresponding forces that occur during drying (Bayly, 2014).

2.5.3 An Overview of Morphologies

In many early cases, the studies of spray drying were more or less related to specific material and application. The learning of material drying characteristics, spray-dried particle properties, morphology forming mechanisms and liquid feed formulation are limited as people simply dry a material and only measure the bulk properties of particles (Bayly, 2014).

In 1960, Charlesworth *et al*. (1960) summarised all morphologies, shown in Figure 17, they achieved by spray drying a droplet containing dissolved solid at different temperatures. The correlation between material’s drying behaviour and drying temperature was first systematically studied by pioneers (Bayly, 2014, Charlesworth and Marshall, 1960). This milestone was soon followed by Mumford from Aston University and other pioneers from world wild who further developed the morphology map, made contributions to this spray drying field and categorised the materials into three systems according to their different drying behaviours (Walton, 2000, Walton and Mumford, 1999, Hassan and Mumford, 1996, Bayly, 2014).

A comprehensive review of pharmaceutical particle engineering via spray drying was represented by Vehring (2008). This review provides fundamental concepts and frameworks for particle engineering and structure prediction. Vehring (2008) also highlighted the effect of spray drying process conditions upon the resulting morphology based on the calculation of dimensionless Péclet number (Vehring, 2008, Bayly, 2014). The detailed definition for Péclet number and its importance to morphology predication is given in section 2.6.1. More recently, Nandiyato & Okuyama published a review of over 15 years studies on morphology creation via spray drying method (shown in Figure 18). This review presents techniques for morphology engineering via control of droplet size and formulation of liquid precursor. Some morphology formation mechanisms are outlined in Figure 18 and Figure 19. These spray drying techniques were commented as “an art rather than science” (Bayly, 2014, Okuyama et al., 2006, Okuyama and Lenggoro, 2003).

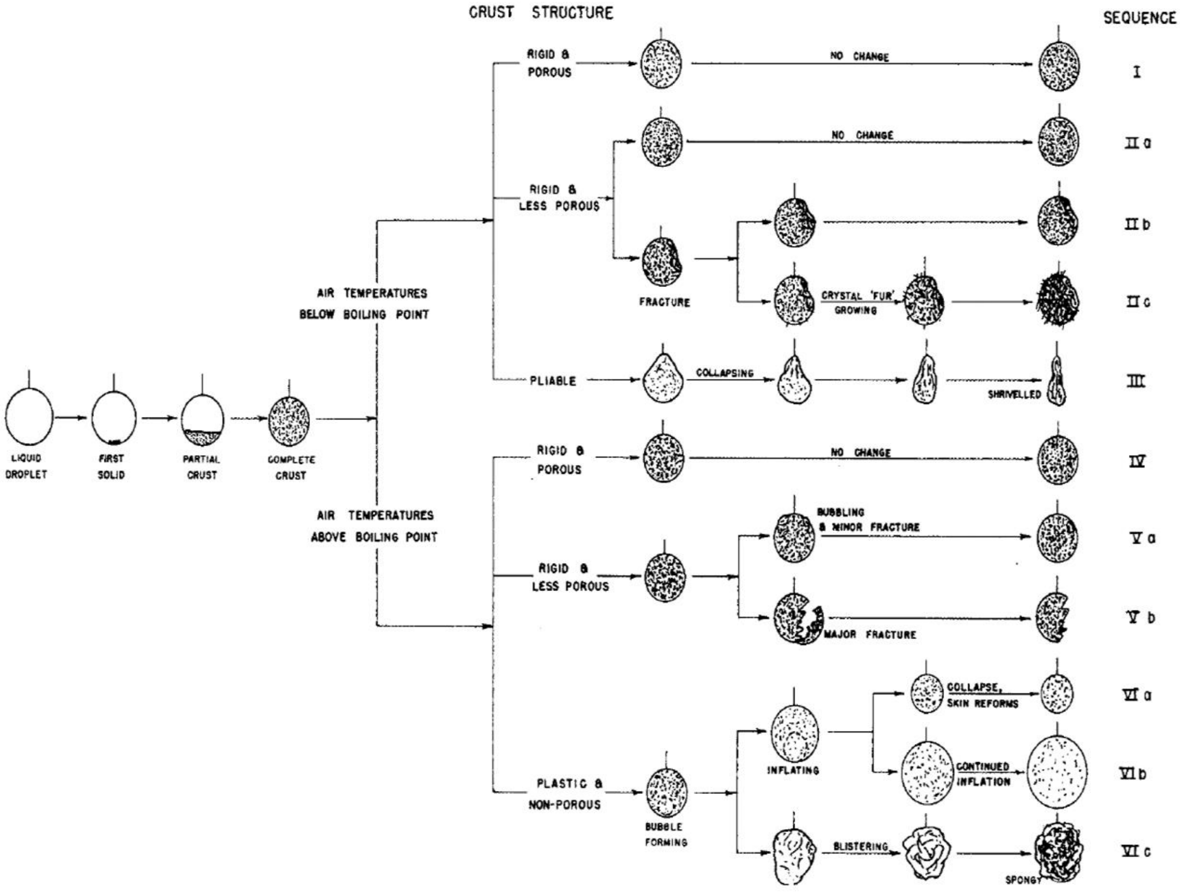

Figure 17 The morphology map of spray-dried particles developed by Charlesworth (Charlesworth and Marshall, 1960)

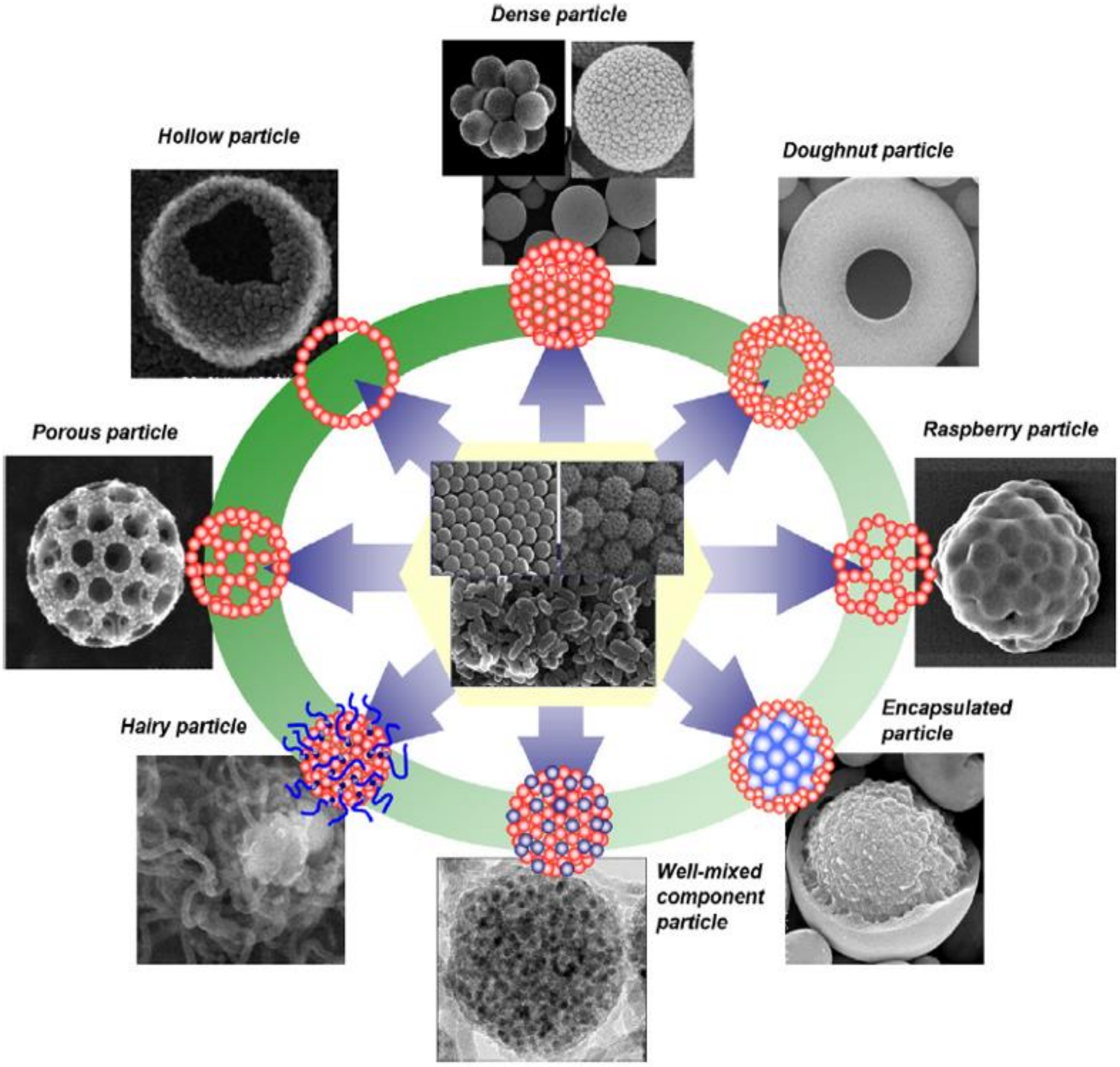

Figure 18 Various particle morphologies prepared using the spray drying method (Nandiyanto and Okuyama, 2011)

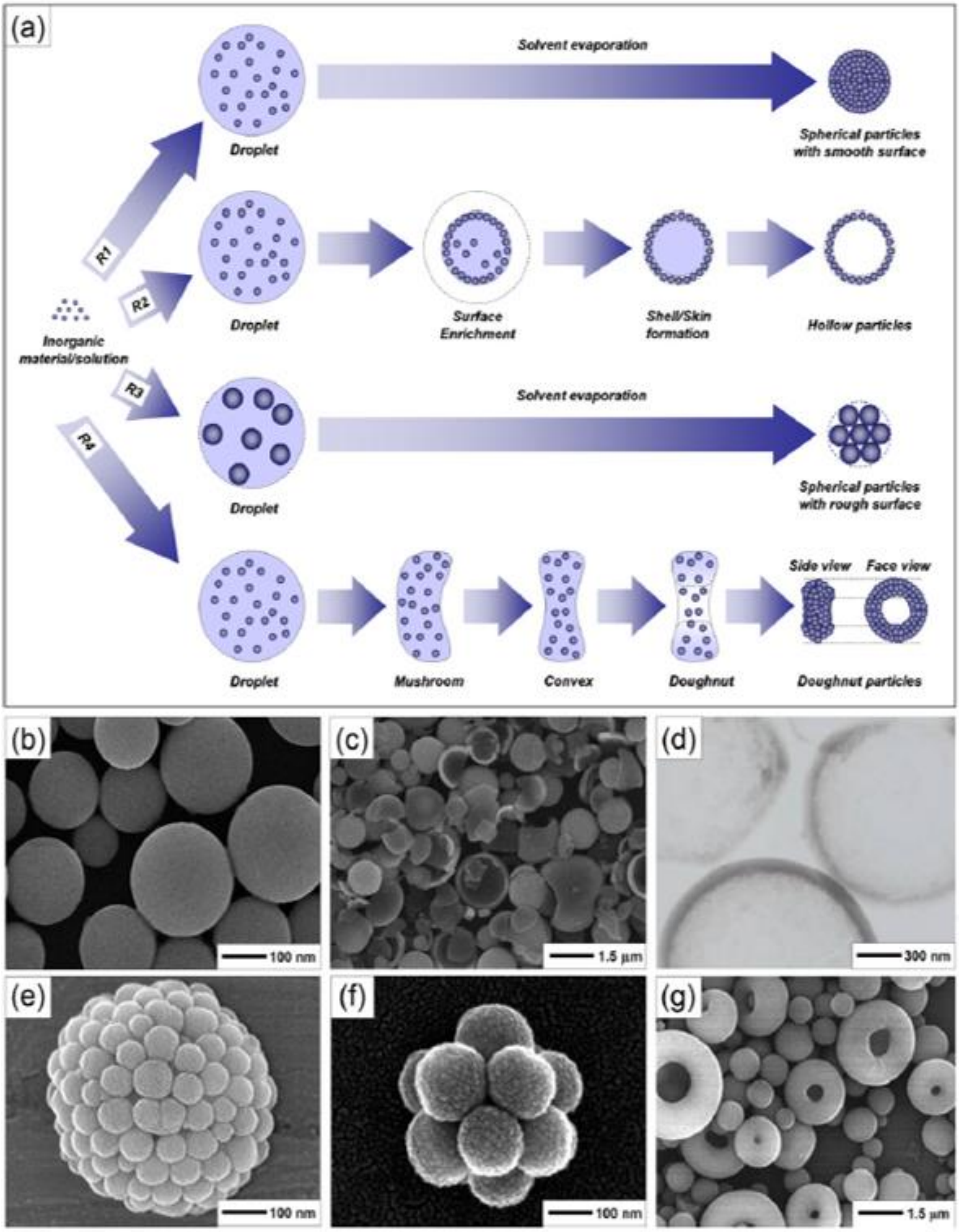

Figure 19 Schematics of morphology formation mechanisms and example particles: (a) formation routes; (b) SEM image of alkoxide particles; (c) broken ZrO_2 particles; (d) hollow ZrO_2 particles; (e) silica granule prepared from 70nm nanoparticles; (f) silica granule prepared from 120nm nanoparticles; (g) doughnut shaped silica granules (Nandiyanto and Okuyama, 2011).

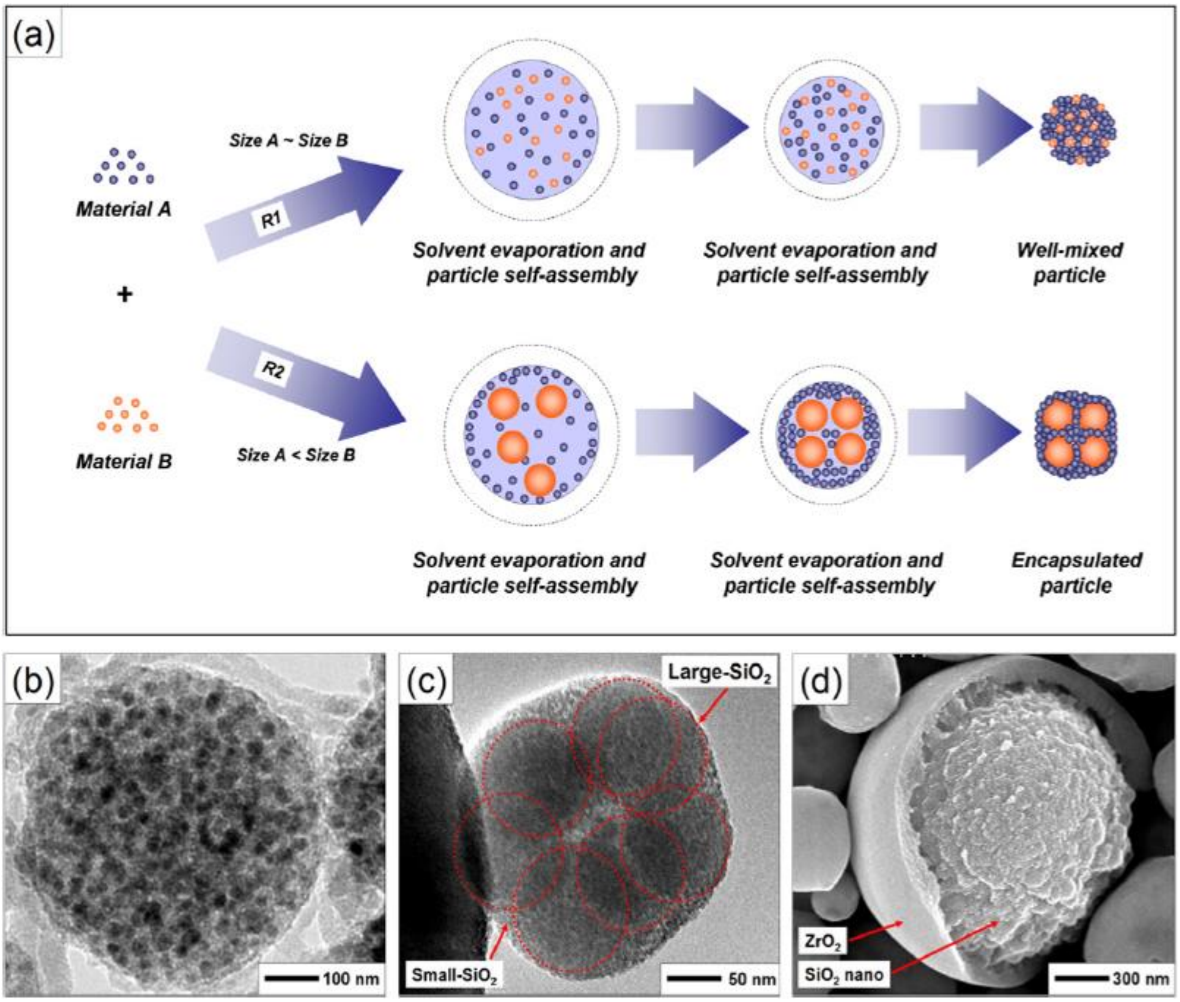

Figure 20 Schematics of morphology formation mechanisms and SEM example images: (a) formation routes; (b) spherical granule with a composition of two materials; (c) microencapsulated SiO_2 granule; (d) microencapsulated SiO_2 granule with ZrO_2 shell (Nandiyanto and Okuyama, 2011)

2.5.4 Drying Stages and Relationship to Evolving Structure

The drying process of a single droplet can be divided into 5 stages which clearly describe the structure and temperature evolution as drying time (Nešić and Vodnik, 1991). The schematic diagram of temperature evolution as a function of drying stages is shown in Figure 21 (Handscomb et al., 2009a, Bayly, 2014).

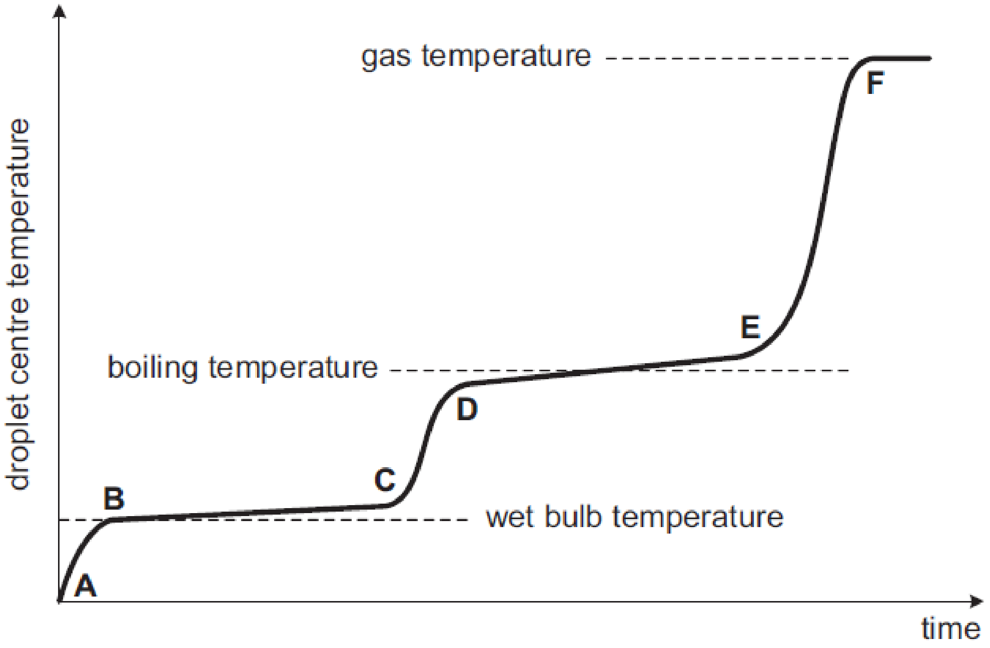

Figure 21 Schematic diagram of temperature evolution as a function of 5 drying stages: (A-B) initial period; (B-C) constant rate period; (C-D) crust formation; (D-E) boiling period; (E-F) final period (Handscomb et al., 2009a)

Stage 0 (Initial period): the droplet starts to contact with heated gas in a drying chamber where rapid heat transfer and mass transfer occur simultaneously at this stage. The droplet temperature increases sharply initially and then reaches its equilibrium state (which is its wet-bulb temperature) at the end of this stage. The total amount of heat needed for droplet evaporation is transferred from the heated gas (Bayly, 2014, Nešić and Vodnik, 1991).

Stage 1 (constant rate period): the droplet surface is saturated with solvent vapour, and the droplet temperature remains to its wet-bulb temperature. The drying rate for this period is constant, and the droplet size keeps shrinking as drying processes. The surface of the droplet becomes enriched with either solute or suspended particles as a result of fast evaporation. The component (dissolved solute or suspended solids) gradient within a droplet can be determined by drying rate. This constant rate period is very short in a real spray drying system due to a high drying rate normally applied (Nešić and Vodnik, 1991, Bayly, 2014).

Stage 2 (crust formation): as drying further progresses, solid like crust is increasingly formed as a result of enriched droplet surface. The drying rate is slowed due to the growth of this crust shell. Depending on the drying characteristics and the structure-forming behaviour, the materials for drying were categorised into three systems (suspension, crystallization and film formation) which are described above (Walton and Mumford, 1999). At this stage, the droplet size continues to reduce until its surface can build sufficient strength to withstand the shrinkage. Depending on the nature of crust and pressure evolution within the droplet, the drying formed morphology varies. Handscomb et al. outlined a map of possible morphologies that evolved from the drying of droplets containing dissolved solute or suspended solids (Figure 22) (Handscomb et al., 2009a, Bayly, 2014).

Stage 3 (boiling): the droplet surface solidification slows the drying rate. This causes a resistance to water evaporation and the droplet temperature consequently increases towards drying gas temperature. If the external drying gas has a high temperature, the droplet will reach its boiling point at which an increase in pressure within the droplet can be seen. Consequently, the drying formed structure may inflate, deflate or rupture at the end of this stage (Bayly, 2014).

Stage 4 (final): after the completed evaporation of residual water, the temperature of the resulting granular product becomes close to the drying air temperature. There is no further change to the solid product structure although cracking may occur on the granule surface due to thermal stresses (Bayly, 2014).

2.5.5 Single Droplet Drying Method

In experimental studies, different approaches have been explored to investigate the drying kinetics, material formulation and the morphology formation of a droplet. The most common method is to collect the dried particle and exam the morphology using a microscope (Bayly, 2014, Nuzzo et al., 2015). The single droplet drying studies were first initiated by Fuchs (1934) and Frossling (1938), followed by Langstroth *et al.* (1950) to explore the evaporation phenomena of pure liquid droplets (Walton, 2000, Walton and Mumford, 1999). Ranz et al. further extended studies to systems containing small dissolved molecules or suspended particles (Ranz and Marshall, 1952). Popular used single droplet drying methods include acoustic levitation, aerodynamic levitation, Leidenforsot effect, drying a droplet deposited on a hydrophobic surface and drying a droplet hanged on a filament (Lintingre et al., 2015, Lintingre et al., 2016, Yamamoto and

Sano, 1992a, Perdana et al., 2011b, Toei et al., 1978, Yarin et al., 1997, Gandhi et al., 1996). However, none of these techniques is perfect for mimicking a spray drying process because the droplet size involved (in a range from few hundred micrometres to few millimetres) is much larger than the size of the atomised droplet from a real spray dryer. However, these techniques were still emphasised by many researchers as the complex interactions encountered in a real spray dryer can be avoided to simplify the practical means of observing droplet drying behaviours. A carefully controlled single droplet drying technique can still reproduce the main characteristics of a spray drying process and provide useful in situ information on the droplet evolution and structure formulation (Bayly, 2014, Walton and Mumford, 1999). An example of a suspending droplet drying method is illustrated in (Walton and Mumford, 1999).

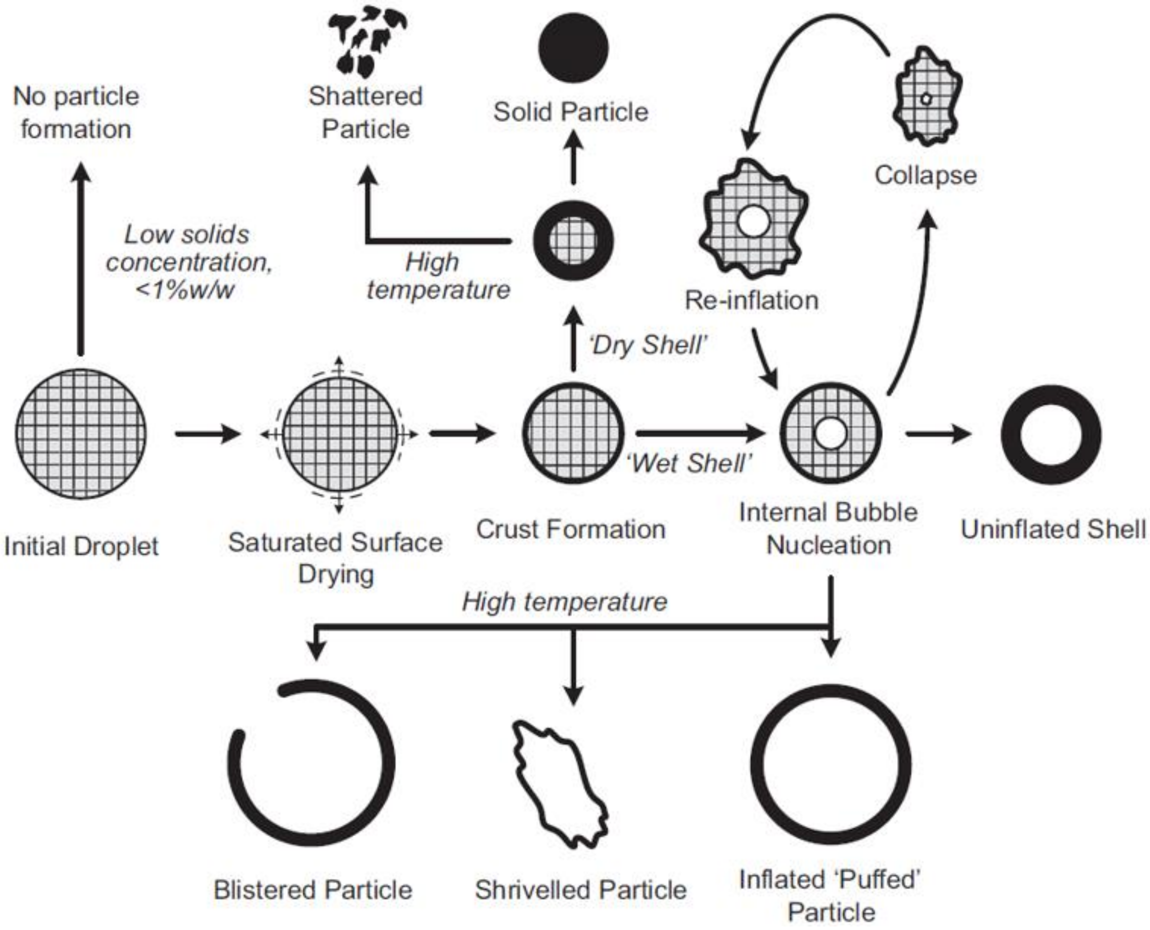

Figure 22 Various morphologies obtained as a result of drying droplets containing dissolved solute or suspended solids (Handscomb et al., 2009a)

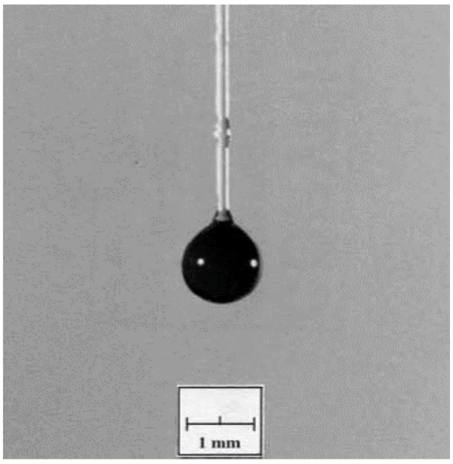

Figure 23 Illustration of suspending single droplet drying method (Walton and Mumford, 1999)

2.6 Morphology Control of Spray-dried particles

2.6.1 Evolution of Concentration Gradients and Péclet Number

To understand the structure formation in a spray drying process, it is important to look at the concentration gradient change in a droplet. When a droplet dries, there is an increase in the concentration of component(s) on its surface. This causes a phase transformation across the droplet surface in a system with dissolved solid(s) or surface gelation in a colloidal suspension system. Figure 24 outlines two distinctive structure formation routes. At the extreme of a droplet with a fast evaporation rate, the rapid receding air/liquid interface can collect solutes due to its slow diffusion action toward the droplet centre. At the extreme of solutes with a faster diffusion rate, the solid concentration within a droplet remains constant (Bayly, 2014).

A dimensionless Péclet number is introduced as a useful tool for predicting the shell formation during a droplet drying process. Péclet number is known as the ratio of a droplet evaporation rate to the solute diffusion within the droplet (Bayly, 2014, Vehring, 2008, Cho, 2016). In the case of droplet surface evaporation rate is faster than the solute diffusion rate, the associated Péclet number becomes greater than 1 (Figure 24 a). The rapid receding surface leads to solutes accumulation which further forms a shell or a crust. Consequently, a hollow sphere with decreased density is formed. This is often followed by a subsequent structure deformation, such as buckling or crumpling under the effect of external force or gravity (schematically shown in Figure 25). In the case of the evaporation rate is slower than the diffusion rate, the associated Péclet is smaller than 1 (Figure 24 b). There is no surface enrichment because solutes diffuse fast toward to droplet center. As a result, the droplet continues to shrink isotropically to form a solid sphere (Bayly, 2014, Mosén et al., 2005).

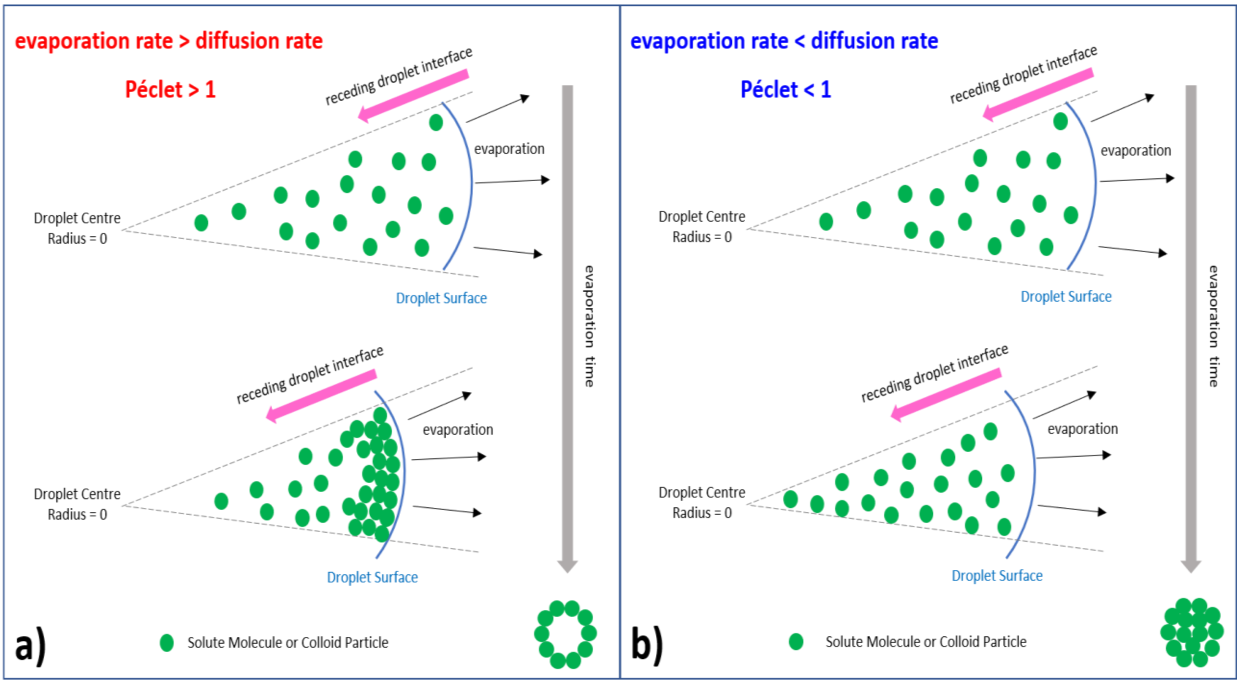

Figure 24 Schematic diagram of structure formation: a) droplet evaporation rate faster than solute diffusion rate; b) solute diffusion rate faster than droplet evaporation rate (Bayly, 2014)

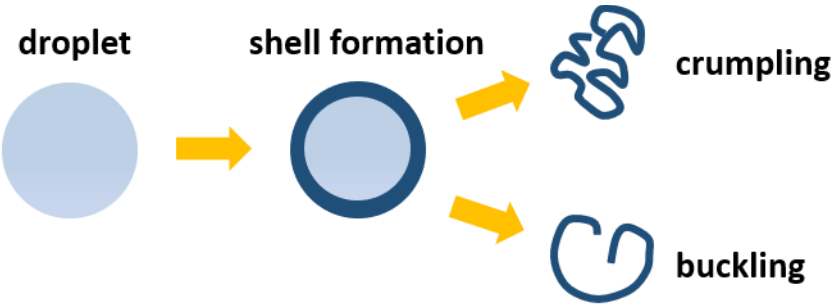

Figure 25 Proposed particle formation process for component with high Péclet number

Many numerical models that describe the distribution of solute components in an evaporating droplet have been presented. For a small droplet with a constant diffusion rate, a low Reynolds and a low Sherwood number, the solute concentration variation can be expressed using a Fick's second law of diffusion

(Bird, 2002, Vehring, 2008) shown in Equation (2.14). The parameters C_i, t, D_i, and R are the concentration of solute i, time, the diffusivity of solute i in the liquid phase and droplet radius (Leong, 1987, Bayly, 2014).

$$\frac{\partial C_i}{\partial t} = D_i \frac{\partial^2 C_i}{\partial R^2} + \frac{2\, \partial C_i}{R\, \partial R} \qquad (2.14)$$

Leong *et al*. (1987) presented a solution to the diffusion equation above under the assumption of a constant evaporation rate (Leong, 1987). The solution was re-arranged by Vehring *et al*. (2007) to derive a new dimensionless quantity of surface enrichment of component i, E_i (Vehring et al., 2007). The expression is shown in Equation (2.15), the $C_{s,i}$, $C_{m,i}$, and Pe_i are the surface concentration of component i, the average concentration of component i in a droplet, and associated Péclet number of component i. β_i is a function that requires integrations for calculating each Péclet number. The E_i can be approximated using following Equation (2.16) if Pe < 20 (Vehring, 2008, Vehring et al., 2007). These dying models numerically demonstrate the formation of a shell or a crust in drying a droplet with higher Péclet number. This is consistent with the schematic proposal shown in Figure 24 (Bayly, 2014).

$$E_i = \frac{C_{s,i}}{C_{m,i}} = \frac{exp(0.5Pe_i)}{3\beta_i} \qquad (2.15)$$

$$E_i = \frac{C_{s,i}}{C_{m,i}} = 1 + \frac{Pe_i}{5} + \frac{Pe_i^2}{100} - \frac{Pe_i^2}{4000} \qquad (2.16)$$

2.6.2 Achievement in Colloidal System Drying

Drying of a colloidal system has drawn much attention recently, and studies in this field thrive. The most frequently reported spray-dried morphology is a spherical shape. Ths morphology is formed as a result of the isotropical size reduction of a droplet containing particles. However, more reports focused on the use of spray drying to prepare hollow or buckled particles. Iskandar *et al*. (2003) presented a morphology control study via spray drying of silica sol. The study indicated both the droplet stability and the hydrodynamic effect on a droplet (exerted by air) have an impact on the morphology. The hydrodynamic effect was correlated with droplet size, droplet density, and surface tension. The hydrodynamic effect can be controlled by the carrier gas velocity and drying temperature. The experiments indicated a spherical morphology can be obtained by drying smaller sized droplets, and a doughnut-shaped morphology can be produced by drying larger droplets with addition of surfactant at a high drying temperature (Figure 26) and at high drying gas velocity (Iskandar et al., 2003). A schematic diagram of parameters responsible for different morphology is shown in Figure 27.

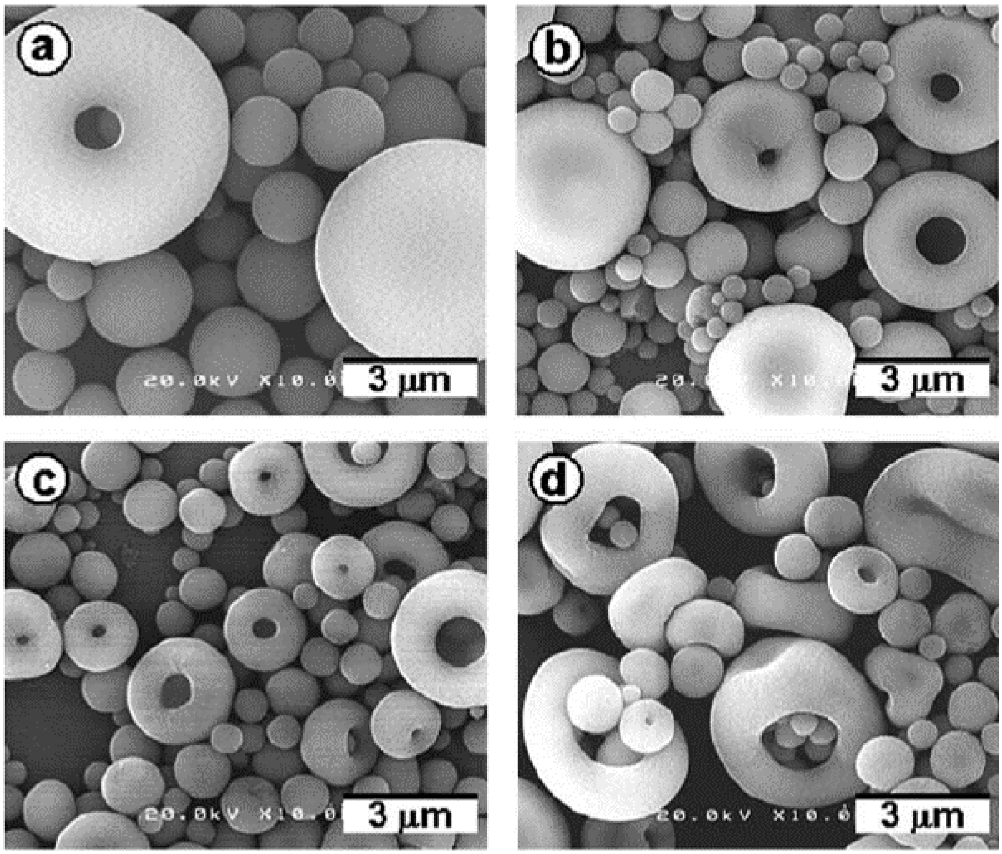

Figure 26 Effect of drying temperature on the morphology of silica particle: a) 200ºC; b) 400ºC; c) 600ºC; d) 1000ºC (Iskandar et al., 2003)

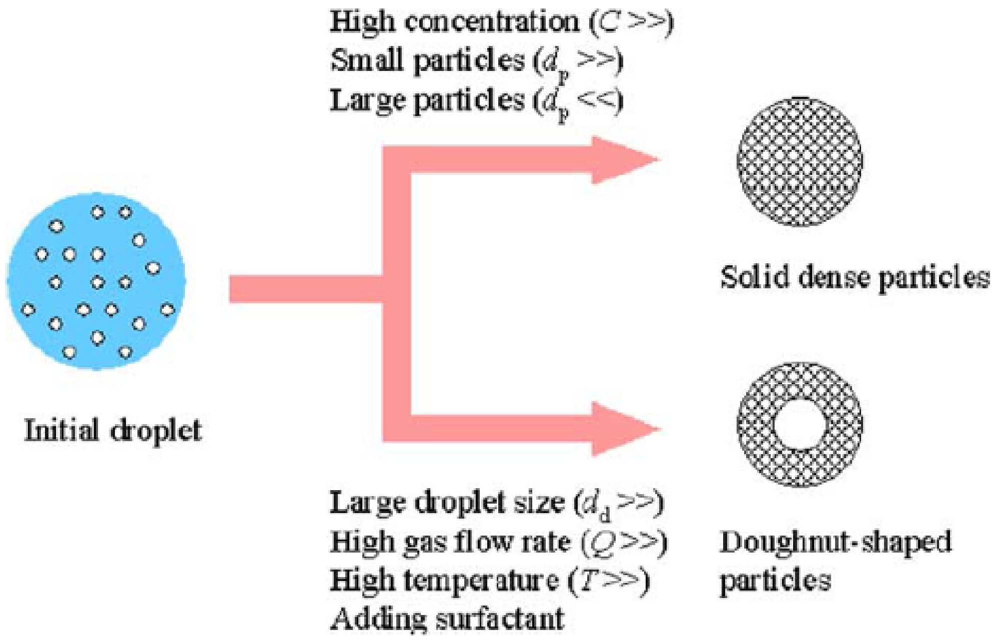

Figure 27 Schematic diagram of the parameters responsible for a spherical and a toroid morphology (Iskandar et al., 2003)

The toroidal or doughnut-shaped morphology has also been reported by other researchers. Sen *et al*. (2009) found a droplet transformation from sphere to toroidal shape when drying an alumina dispersion with a high mass fraction of primary particles (Figure 28). However, the morphology remained spherical when drying same alumina system but with a low mass fraction of primary particles. The colloidal dispersion content was found to be responsible for the morphology change. The toroidal structure was proposed by the onset of buckling of the sphere droplet with low solid content (Sen et al., 2009). Saha *et al*. (2011) and Miglani *et al*. (2015) noted similar toroidal morphology when drying a silica colloid using an acoustic levitator (Saha et al., 2012, Miglani and Basu, 2015). Cho (2016) also observed particles with different hollowness extent from spray drying of silica nano-colloid. The drying temperature was proved to impact the morphology. A less hollow morphology (sphere a dimple on surface) was observed when the drying was performed at 160ºC and very hollow particles were obtained at 200ºC drying temperature (Figure 29). Cho (2016) also mentioned the observation of perfect spherical morphology when drying temperature was decreased to 120º, but no image evidence was given (Cho, 2016).

Different hypotheses for toroidal morphology formation had been proposed. Iskander *et al*. (2003) postulated the surface deformation of a droplet is caused by the aerodynamic effect by air. Sen *et al*. (2009) postulated the droplet buckling to be responsible for the hollow morphology. Miglani *et al*. (2015) proposed the deformation occurs on one side of the droplet first, then moved on to the other side. As droplet dries, these two defective regions met to form a toroidal structure. Cho (2016) contributed the droplet hydrodynamic instability at high drying temperature to the formation of hollow particles. The variations in hollowness were explained by the calculation of Péclet number at different drying temperature (Cho, 2016). Walker *et al*. (1999) presented the rheological yield stress of slurry to be responsible for a distorted morphology from drying (Walker et al., 1999). Some other researchers considered the formation of toroidal shaped particles was possibly caused by the break-up droplets from atomisation process in spray drying (Bayly, 2014).

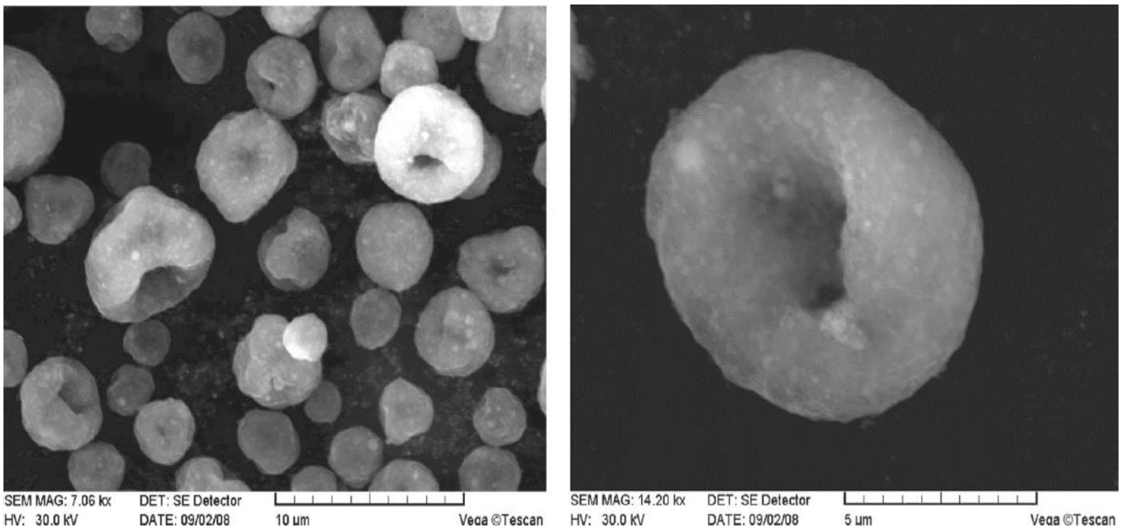

Figure 28 SEM of spray-dried alumina particles with toroidal morphology (Sen et al., 2009)

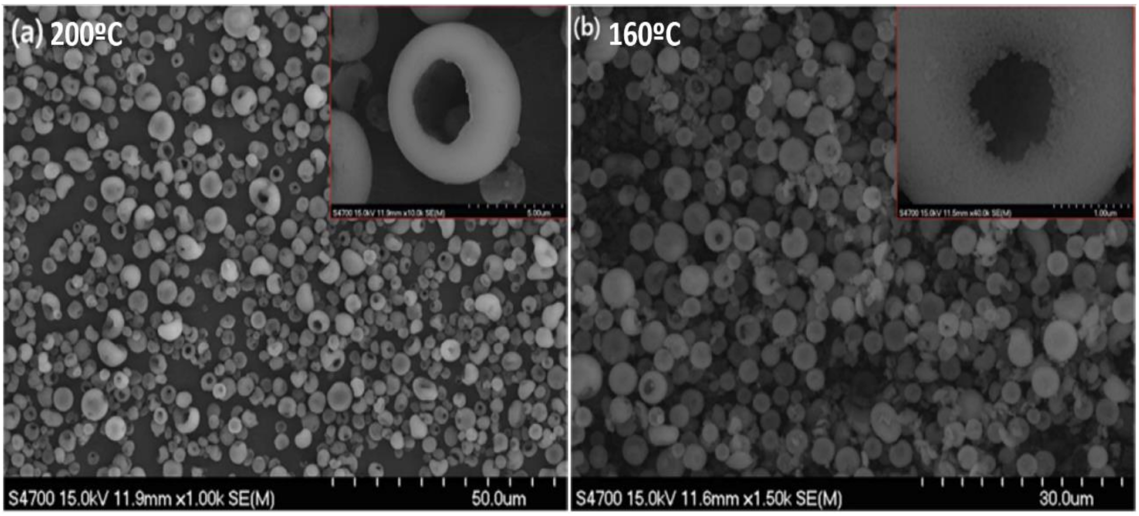

Figure 29 Silica particles prepared at a different temperature: a) hollow morphology obtained at 200ºC; b) less hollow particles obtained at 160ºC (Cho, 2016)

However, recent studies argued that there is no strong correlation between a hollow or buckled morphology and hydrodynamic effect and/or Péclet number under common spray drying conditions. Lintingre *et al*. (2015) used a dimensionless Weber number[1] to describe the process of liquid droplet deformation and formation. Through a series of quantitative analyses, they demonstrated that the instability effect on a droplet caused by the gas pressure can sustain for time less than 10 ms, after which a paid recovery into spherical shape can complete. Numerically, a droplet characteristic drying time was identified to be at least one order of magnitude larger than the time needed for recovery to a spherical shape. Therefore, the buckled morphology was proven not to be caused by the hydrodynamic effect. The schematic diagram of liquid injection from a spray dryer nozzle is shown in Figure 30 (Lintingre et al., 2016, Lintingre et al., 2015, Tsapis et al., 2005).

Lintingre *et al*. (2016) have also proven the ineffectiveness of Péclet number for morphology prediction from a single droplet drying of zirconia suspension. They demonstrated that in drying of a 100 µm diameter droplet containing 100 nm diameter particles, the associated Péclet number was found to be high (>> 1), which indicates the droplet evaporation rate is at least three orders of magnitude larger than particle diffusion rate. In fact, particle diffusion can be negligible if their size is above 1 µm, whose size is much smaller than the droplets usually seen in

---

[1] Weber number is the ratio of hydrodynamic pressure exerted by air (on droplet) to the Laplace pressure on droplet/air interface (Lintingre *et al*. (2015)).

most spray dryers. This means the Péclet will always remain greater than 1 when drying a colloidal droplet. Considering those findings, Lintingre *et al*. (2016) concluded that neither hydrodynamic effect nor the Péclet is responsible for the droplet buckling behaviour (Tsapis et al., 2005, Lintingre et al., 2015, Lintingre et al., 2016).

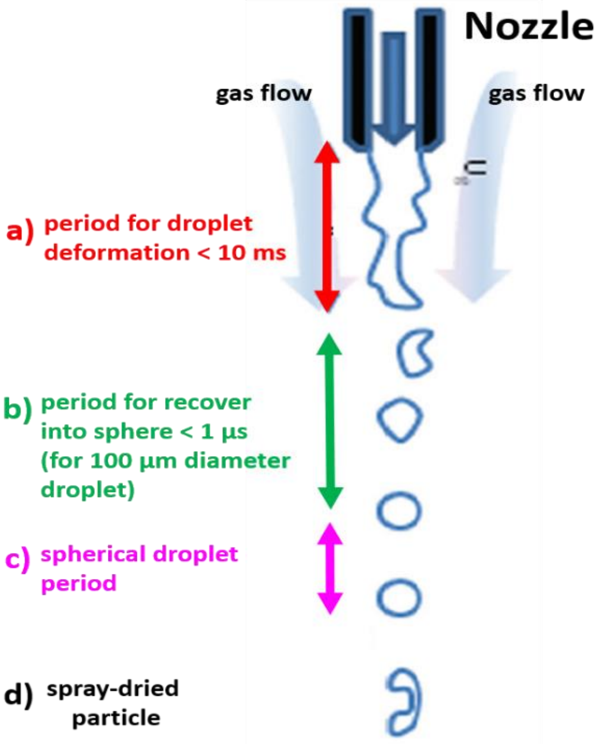

Figure 30 Schematic diagram of liquid injection from a spray dryer nozzle: a) droplet initially deforms due to drying gas pressure; b) liquid recovers into spherical shape; c) spherical droplet drying; d) spray-dried particle (Lintingre et al., 2016)

2.6.3 Research Gaps and Opportunities

The relevance of those literature reviews to this research study is high. There has been much progress in understanding the structural transformation in drying of a colloidal system. In particular, the review of Nandiyanto *et al*. (2011) highlighted engineering methods to create various morphology. However, the methods outlined by Nandiyanto were only applicable to sub-micrometer scale particle preparation. There has been no clear evidence to show these “state of the art” can be used to produce spray-dried particles in a micrometer size range, which is usually preferred by industries due to the powder handling issue. Furthermore, the descriptions of the mechanical performance and internal structure of various particle morphologies from these reviews were very limited, the importance of different morphology on the mechanical performance was not highlighted. Many predictive models have been reported to allow spray-dried structure prediction. However, these studies were based on either different single droplet drying techniques or a small benchtop spray dryer. In a real spray dryer system, the use of these models still challenges. The driving force responsible for the morphology formation may differ when looking at varied droplet scale for drying. Therefore, many research gaps and challenges still remained.

None of the previous studies has provided a comprehensive correlation between material properties, drying process conditions, spray-dried particle morphology, associated internal structure and mechanical properties. This research is based on drying of specific industrial TiO_2 materials utilising both a real pilot scale spray dryer and a single droplet drying rig. The study covers the impacts of formulation aspects (such as, different type of TiO_2 pigments, solid content loaded in slurry, and pH variation), drying process aspects (such as, different drying temperature, and atomisation), and droplet scale (drying using varied sized droplets) to the properties of spray-dried particles. All become novelty for this research.

Chapter 3 Slurry Characterisations

3.1 Introduction

In a colloidal system, particle-particle interaction plays a significant role in determining the structure of a spray-dried granular product. Variation in the formulation of a colloidal suspension can result in a dramatic change to the assemblies of primary particles during spray drying process (Bayly, 2014, Handscomb et al., 2009a, Handscomb et al., 2009b, Tsapis et al., 2005, Vehring, 2008). Therefore, it is very important to understand the characteristics of the material being dried. This chapter focuses on the colloidal characterisation of two distinctive TiO_2 slurry systems received from Venator UK. One system has alumina coated on particle surface, and the other system has phosphate type dispersants anchored to particle surface. The morphology and surface of the primary particles from two TiO_2 systems were accessed using a Scanning Electron Microscope (SEM) and Transmission Electron Microscopy (TEM) techniques. The surface charge of particles was measured as a function of system pH. The aggregation level of a slurry was carefully controlled by tuning the pH of system and the corresponding slurry particle size, particle settling behaviour and rheology were also characterised step by step. All measured results are used to understand the colloidal behaviour of the two systems at different aggregation levels and to serve as a guide on slurry formulation for the subsequent spray drying studies. The key outcomes from this work can further assist the investigation of formulation aspect effects on spray-dried granules shown in Chapter 4 and the understanding of mechanisms driving the structure transformation throughout the drying process discussed in Chapter 5.

3.2 Experimental

3.2.1 Slurries Preparation

Two types of TiO_2 slurries received from Venator UK were used in this study. The first type is TiO_2 pigments dispersed in water to form an aqueous slurry (referred to as non-coated TiO_2). There are sodium hexametaphospahte $(NaPO_3)_6$ (with trade name of Calgon, Univar UK) dispersants[1] anchored throughout the

---

[1] Sodium hexametaphosphate (also known as Graham salt) added at level of 0.2% wt/wt on neat TiO_2 particle

pigments surface in order to assist the subsequent coating process (details of the coating process are shown in the literature review chapter). In the other system, the TiO_2 pigments (uncoated pigments, same as described for non-coated particles) are coated with 3%wt alumina matter and then dispersed in water (referred to as alumina-coated TiO_2). Both two types of slurries were from the same TiO_2 synthesis (production) batch and the particle coating process was conducted by Venator UK. All received slurries were vigorously agitated using an overhead stirred to achieve a homogenous suspension and then diluted to three solid concentration levels[2] (10%wt, 20%wt and 30%wt) with deionised water for the subsequent characterisations.

3.2.2 Characterisation Methods

Crystalline Phase Analysis

X-ray powder diffraction (XRD) technique (D8 Bruker, Germany) which utilises Cu Kα X-ray source was used for identifying the crystalline phase of TiO_2 pigments contained in non-coated slurries. 20 ml non-coated TiO_2 slurry (30%wt solid) was completely dried in an oven. The dried powder was collected and finely ground by using a mortar and pestle. The resulting fine powder was carefully deposited into a silicon holder. The sample surface was flattened to level with the top edge of silicon holder. The sample was scanned between 2θ angle of 10º to 70ºC at 0.05º increment (300 ms per step). The obtained pattern was matched against standard rutile crystal structure. Alumina-coated particle was not analysed because the TiO_2 particle under the coating layer is the same as the non-coated particle.

Particle Morphology

Particles from two types of slurries were characterised for morphology and size by using a Hitachi SU8230 Scanning Electron Microscope (SEM). For the SEM sample preparation, the diluted TiO_2 slurry (to 0.1%wt by using de-ionised water) was dropped on a wafer and dried in front of a fan heater (Figure 31). The dried TiO_2 particles were coated with a carbon layer (10 nm thickness) to minimise the charing effect during SEM scanning. The morphology of particle was analysed with collected images and the size of primary particles was measured by looking at the Feret diameter.

---

[2] Solid content levels were consistent with Venator's research. 30%wt is the maximum limitation that the feed line and the pump of spray dryer can handle.

The morphology and the surface of alumina-coated TiO_2 pigment surface were further studied using a FEI Titan Themis Cubed 300 Transmission Electron Microscopy (TEM) fitted with a Gtan OneView 16 Megapixel CMOS digital camera for imaging collection. The imaging work was operated at 300 kV in a bright field scanning condition. For sample preparation, the dried TiO_2 powder was mixed in ethanol and dropped onto a copper grid coated with a carbon film. The TiO_2-ethanol mixture was left to dry in a fumehood before sending into TEM chamber for imaging. Energy Dispersive X-ray spectroscopy (EDX) was used to to identify the elements distributed across the particle surface to verify the presence of alumina coating on TiO_2 particle surface. The EDX analysis was conducted using a super-X EDX system with windowless 4-detector design fitted on same TEM unit. The STEM probe current for mapping was set to 420 pA.

Figure 31 Fan heater dried TiO_2 particles on SEM wafers

Particle Surface Charge

The zeta-potential of slurries at pH values of interest were measured with a ZetaProbe Analyzer (Colloidal Dynamics, USA). The measurement was conducted on diluted TiO_2 slurry (to 1%wt) with addition of 10^{-3} M NaCl as electrolyte background which allows a safe pH adjustment between the range of 3 to 10. The prepared slurry was split into two equal portions. The pH of one slurry portion was decreased from neutral to acid with 1 M HCl solution. The pH of the other slurry portion was increased to basic with pH=12 NaOH solution. The slurry was kept mixing with a built-in mechanical stirrer, and the zeta-potential values at different pH point were measured. At each pH point, a total of 5 repeat measurements were collected and averaged. The measured zeta-potential values were plotted against the corresponding pH to identify the iso-electric (IEP) point of two types of TiO_2 particles.

Based on the obtained IEP curves, for each TiO_2 system, slurry formulation was prepared at two different pH to represent different colloidal structure. The pH of one slurry was controlled at iso-electric point (to represent an aggregated system), and the other slurry was controlled at a pH with high zeta-potential value (to represent a colloid stable system). The subsequent particle size, particle settling and rheology characterisation were all based on the aggregated slurry and stable slurry from each TiO_2 system. The purpose of these characterisation is to verify the system difference between two types of TiO_2 particles, as well as the colloidal structure difference between IEP and the non-IEP slurries.

Slurry Particle Sizing

The particle size distribution (PSD) of slurry from each system was characterised using a Malvern Masterszier 2000 equipped with a wet measurement unit and a built-in online ultrasonic bath. The standard operation procedure (SOP) was set for 10 repeated measurements with 5 seconds delay time between measurements. An averaged PSD result from 10 repeats was collected. The diluted slurry (to 1%wt solid content) at pH of interest was fed into the wet measurement unit which was filled with de-ionised water at same pH value[3] for immediate sizing. The resulting PSD was collected and referred to as “0 min size”. Subsequently, the slurry remained in the chamber was sonicated using the online ultrasonic function for 20 minutes and was sized again to investigate the effect of applied ultrasound to the strength of aggregation may present in the slurry. The measured PSD result was referred to as “after 20 mins ultrasound size”. For each TiO_2 slurry system, the PSDs at different pH were plotted together to compare the colloidal structure difference in terms of size.

Particle Settling

The particle settling rate was assessed using a Turbiscan Analyser (Formulaction, France). The slurry sample at different concentration level was carefully filled in a glass vial (to the mark of 42 mm height) using a plastic pipette. The glass vial was then transferred to the measurement chamber with temperature controlled at 22ºC. A detection head that emits near-infrared light is moving up and down along the glass sample cell to scan the entire sample height. A transmission detector and a backscatter detector will receive the light pass through the cell and backward by sample respectively. The schematic diagram of

---

[3] The pH of de-ionised water in the wet measurement unit was adjusted to the same pH point as the slurry using either NaOH or HCI solution.

Turbiscan working mechanism is shown in Figure 32 (Formulaction, 2009). The scan was set for every 1 min with a total length of 60 mins.

For comparison purpose, the slurry stability was also assessed by looking at the particle/air interface change on the shelf over the same period of time (3600 s) at room temperature of 20.5ºC. The slurries used for shelf-life assessment were same as the slurries used for Turbiscan test. The same method was used for filling slurry into a glass cell. A ruler was placed by the sample cell for an indication of particle interface height change. Photo evidence was taken at different time intervals. The thickness of the particle bedding formed from visual shelf life assessment was compared against the results obtained from the Turbiscan test to verify the consistency in particle settling behaviour. To better understand the results obtained from both visual assessments and dynamic Turbiscan tests, the gelation point of different TiO_2 slurries were calculated. The method for calculation was shown in the settling behaviour section of results and discussion.

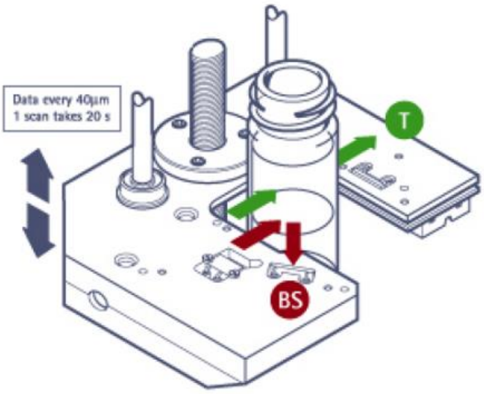

Figure 32 Measurement principle of the Turbiscan stability analyser (Formulaction, 2009)

Rheology

The rheology of slurries with a solid content of 10%wt, 20%wt, and 30%wt from each TiO_2 system was characterised using a MCR-301 rheometer (Anton Paar Process Instruments, Austria) with a concentric cylinder geometry. The slurry under test was pre-sheared at 600 s^{-1} for 120 s and then rested for 60 s prior to measurement. The shear rate was ramped from 900 to 1 s^{-1} in logarithm way over 5 mins, and the corresponding viscosity was recorded throughout the shearing process. All rheological measurements were controlled at 22ºC to minimise the temperature effect to shearing.

3.3 Results and Discussions

3.3.1 Structure of Primary Particles and Surface Coating

Figure 33 presents the XRD pattern of the non-coated TiO_2 sample received from Venator. The detected peaks matched the rutile powder diffraction pattern (Okrusch et al., 2003). There are no other peaks observed in this pattern, further confirming the rutile phase and sample purity.

SEM analysis of non-coated TiO_2 slurry shown in Figure 34 shows an elliptical particle shape for primary particles with a size range of 300±100 nm (Ferret diameter measured using a SEM measuring tool). The observed morphology and size is consistent with the results of same rutile type TiO_2 particles (surface uncoated) reported by other researchers (Li et al., 2012). The elliptical morphology for primary particle was formed from the milling step (after rutile TiO_2 are synthesized) at which the particles are shaped by shearing and impacting forces for size reduction purpose (Elliott et al., 2019, Sutcliffe et al., 2015). The Venator's post-manufacture process for rutile type TiO_2 pigment is described in background section of Chapter 1.

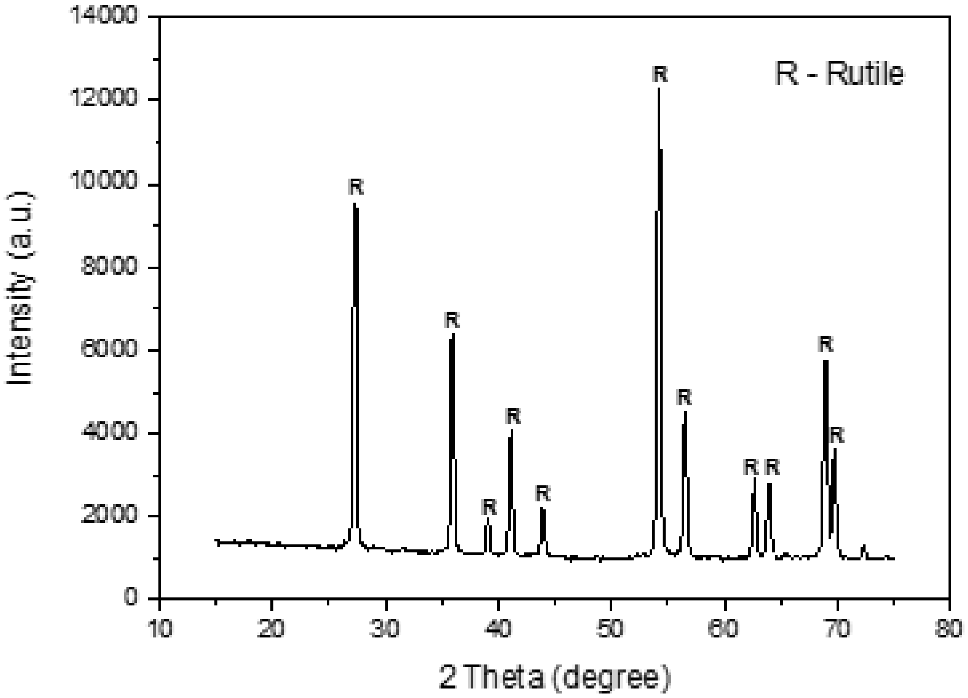

Figure 33 XRD phase diagram of received non-coated TiO_2 particles. All peaks matched rutile diffraction pattern are marked as "R".

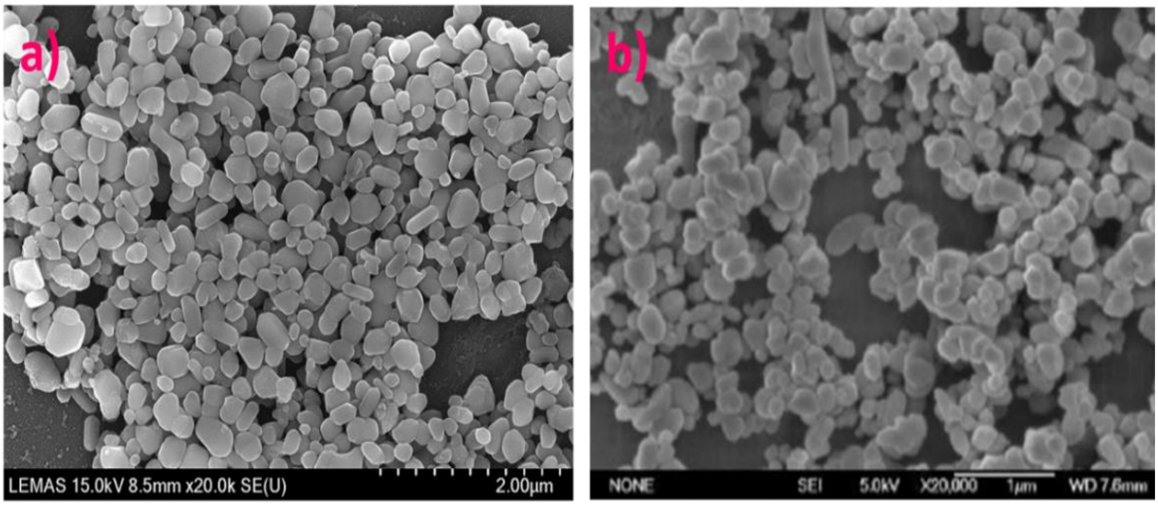

Figure 34 SEM of non-coated TiO_2 particles: a) Venator rutile TiO_2 particles with ellipsoidal shape and 300±100 nm size; b) Rutile TiO_2 particles reported by Li. *et al*. (2012) with similar morphology and size.

By contrast, the alumina-coated TiO_2 system exhibit some different particle structure. Figure 35 shows these coated particles are irregularly shaped aggregates[4] with a size range of 2-10 µm under SEM. The observed particle structure from SEM was further confirmed with the TEM images (Figure 36 a)

---

[4] Refers to as an primary particles assembly with strong bonding.

which note the aggregation of primary particles. Figure 36 a) also outlines the ellipsoidal shape for individual coated particles. The zoomed-in image shown in Figure 36 a) demonstrates the presence of loose flocculant layer on TiO_2 pigment surface. Li *et al.* (2012) presented similar TEM results for similar alumina-coated TiO_2 pigments (the same un-coated TiO_2 particles, the same type of alumina coating material, but with slightly different coating process condition), which is shown in Figure 36 b). Li et al. (2012) and other researchers identified this loose flocculant layer on particle surface was assigned to the boehmite type alumina (with a structure of AlO(OH)) through XPS spectra of O 1s at the peak of 531.2 eV (Li et al., 2012, Siwinska-Stefanska et al., 2008, Wu et al., 2006). The high quality TEM images also indicate the alumina coating on pigment surface is not uniform due to its loose flocculant morphology. The coating thickness is estimated to be between 5-10 nm using TEM measurement tool.

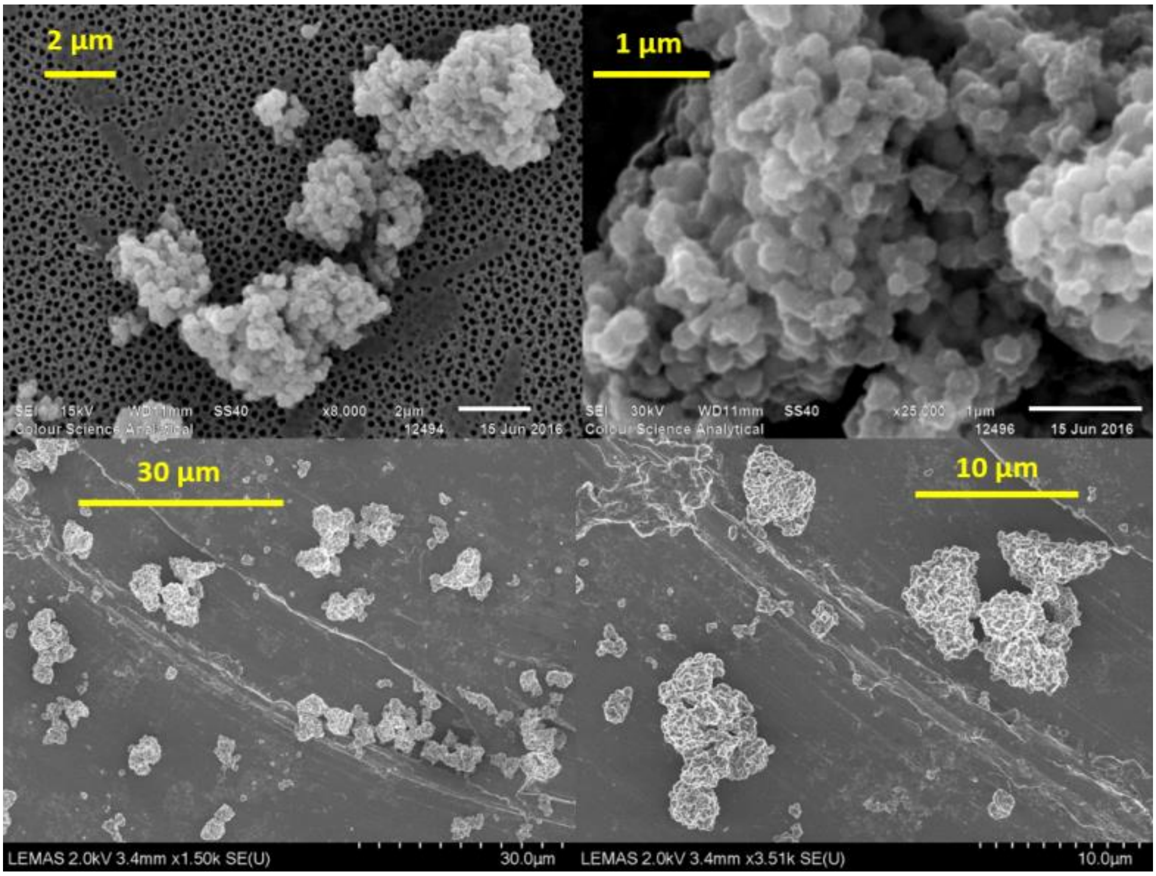

Figure 35 SEM of alumina-coated TiO_2 particles.

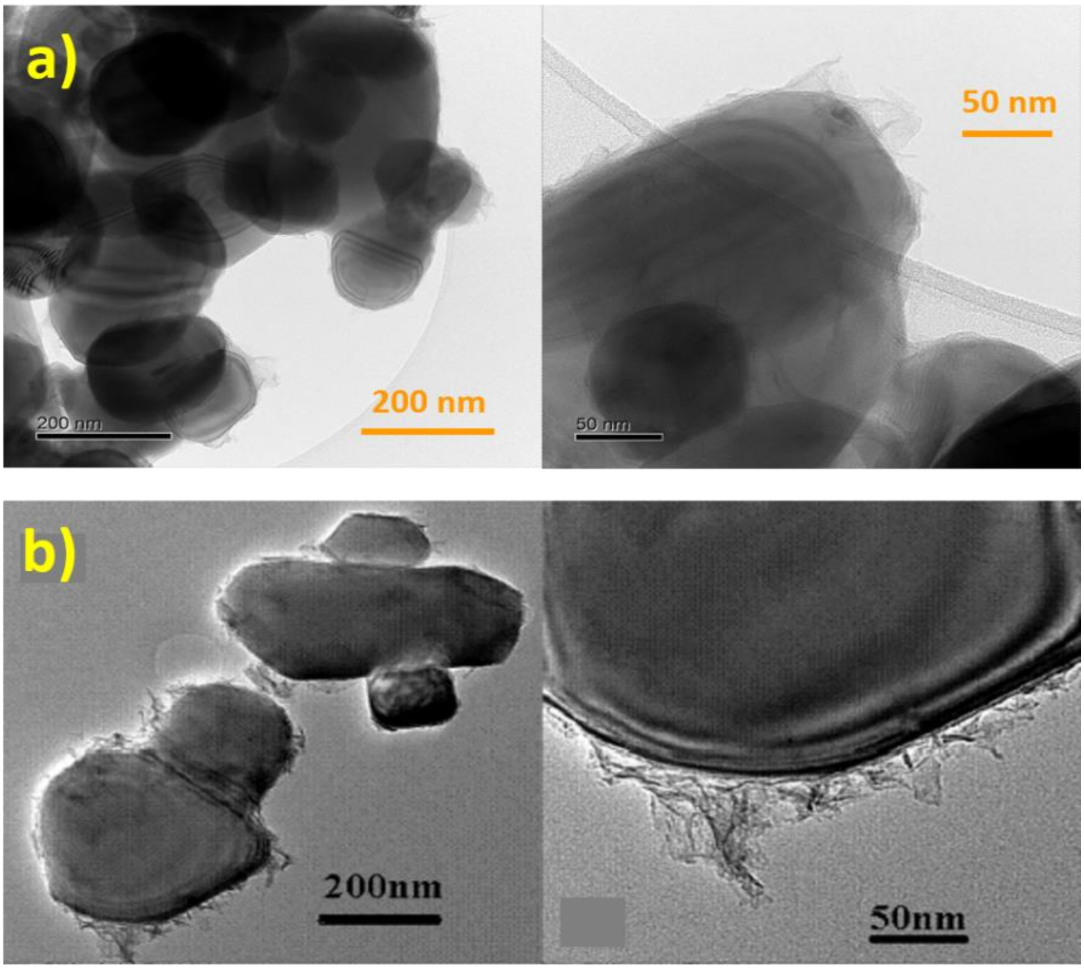

Figure 36 TEM images of coated particles: a) alumina-coated TiO_2 particles prepared by Venator with aggregated structure; b) alumina-coated TiO_2 particles reported by Li. *et al*. (2012). The same type of alumina coating was prepared at similar process conditions onto same rutile type TiO_2 particles. All TEM images note the presence of loose flocculant layer on pigments surface.

The elements distribution across alumina coating on TiO_2 particles surface was quantitatively determined using an EDX analysis. Figure 37 outlines the element mapping for aluminium, titanium and oxygen. The mass fraction calculation based on Figure 37 a) indicates the fraction of aluminium and titanium presented in the coating is 3.97% and 96.03% respectively. This is in a good agreement with Venator's claim about coating formulation and results presented by other researchers (Sutcliffe et al., 2015, Li et al., 2012).

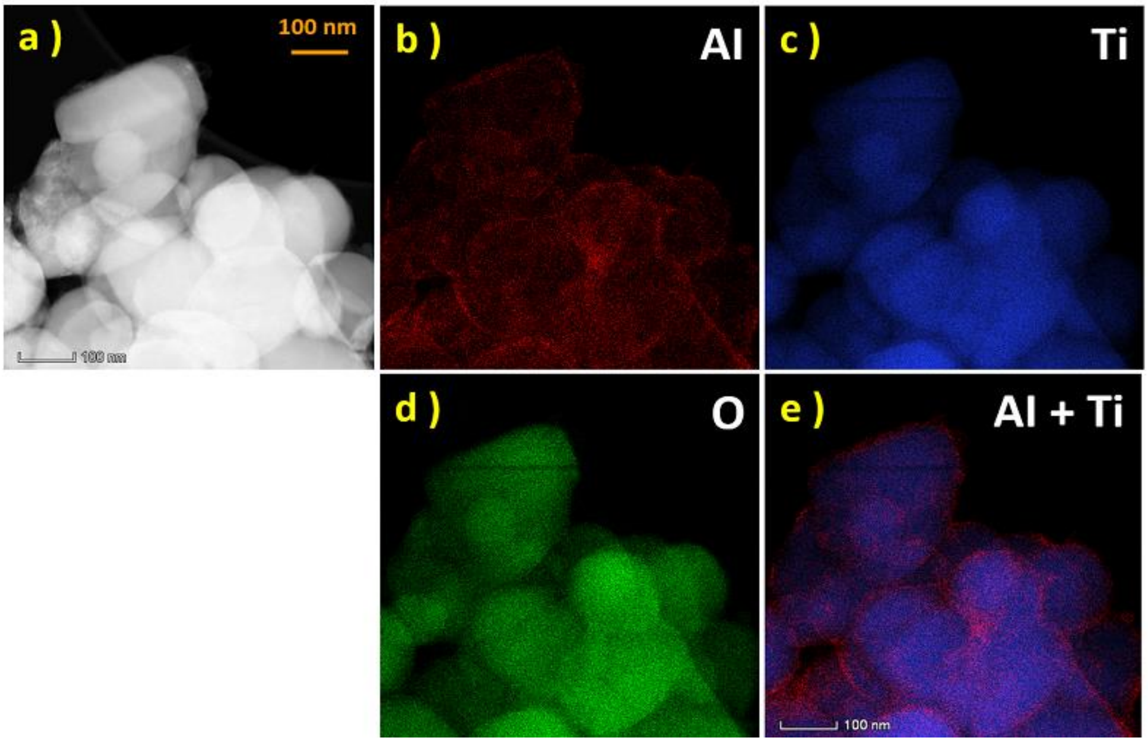

Figure 37 EDX analysis of alumina coating: a) TEM of alumina-coated TiO_2 particles; b) Element mapping of aluminium; c) Element mapping of titanium; d) Element mapping of oxygen; e) Element mapping of aluminium and titanium. All elements mapping are based on TEM image a).

3.3.2 Particles Surface Charge

The surface charge plays an important role in the control of particle-particle interaction in a colloidal system. In this study, the IEP (iso-electric point) of two types of TiO_2 systems were determined by measurement of zeta-potential as a function of pH values. Figure 39 shows the IEP for non-coated TiO_2 particle and alumina-coated TiO_2 particle is at pH=4.5 and pH=8.4 respectively. The nature of the surface charge on the non-coated TiO_2 system is shown schematically in Figure 38. At a pH below IEP, the particle surface becomes positively charged due to the presence of ($Ti\text{-}OH_2^+$) and ($O\text{-}H_2^+$) species, whereas a negatively charged surface at pH above IEP due to the presence of ($Ti\text{-}O^-$) and (O^-) (Rhodes, 2008).

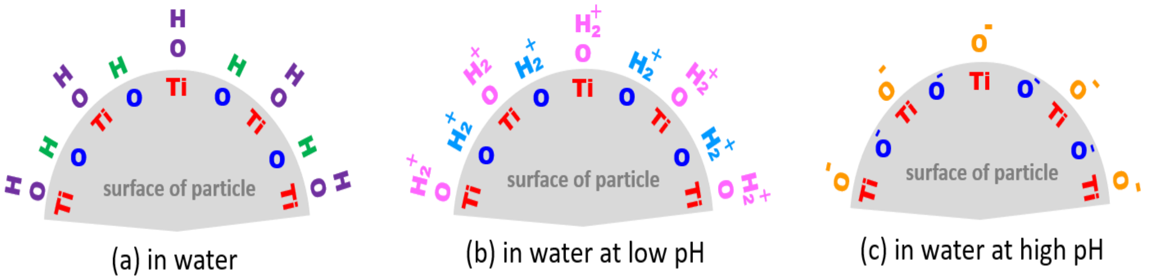

(a) in water

(b) in water at low pH

(c) in water at high pH

$Ti^+ + H_2O \rightarrow Ti-OH + H^+$

$O^- + H_2O \rightarrow O-H + OH^-$

$Ti-OH + H^+ \rightarrow Ti-OH_2^+$

$O-H + H^+ \rightarrow O-H_2^+$

$Ti-OH + OH^- \rightarrow Ti-O^- + H_2O$

$O-H + OH^- \rightarrow O^- + H_2O$

Figure 38 Schematic diagram of TiO_2 particle surface: (a) in neutral water; (b) in water at low pH (acidic) condition; (c) in water at high pH (basic) condition.

The measured IEP values for two particles systems are highly consistent with recent literature reports. Li *et al.* (2012) measured the zeta-potential value as function of pH for rutile type TiO_2 with various surface coating (graphical results shown in Figure 40). Their work indicates the IEP for uncoated TiO_2 is pH=4.6 which is same as the value from this study. The result also demonstrates the pH=8.5 as IEP for boehmite coated TiO_2. This is highly consistent with pH=8.4 measured in this study and results measured by other researchers (Li et al., 2012, Siwinska-Stefanska et al., 2008, Wu et al., 2006, Mikulasek et al., 1997). However, latest research demonstrate the actual IEP for neat boehmite alumina material is at about pH=11 (Kaledin et al., 2019, Kaledin et al., 2016). It reveals the boehmite alumina coated on Venator's TiO_2 surface is "patchy" rather than uniformly distributed. This conclusion can be further confirmed by the mapping of aluminium and titanium elements from EDX analysis (shown in Figure 37).

The determined IEP can provide a guide for manipulating the colloidal structure of prepared slurry. A schematic diagram is outlined in Figure 41 to show the effect of pH on flocculation level of particles. In principle, particle starts to strongly aggregate due to the neutralised surface charge at the IEP. In contrast, a well-dispersed system can be observed if the pH is adjusted away from IEP (refers as non-IEP). This is because the electric repulsive double-layer becomes dominant between neighbouring particles at non-IEP condition (Malvern, 2015b, Rhodes, 2008, Hoath, 2016). There is a plateau on each of the curves shown in Figure 39 which means the system is colloidal stable at the corresponding pH range due to increased absolutely zeta-potential values. The repulsive force becomes dominant between particles, preventing aggregation caused by Brownian motion or gravity. For the alumina-coated system, this plateau falls between pH 3 to pH

4.5 with corresponding zeta-potential of 60 to 70 mV. For the non-coated system, the plateau is between pH 7 to pH 8.5 with corresponding zeta-potential of -50 to -45 mV.

Based on the obtained IEP curves and, for each TiO_2 system, slurry formulation was prepared at two different pH to represent different colloidal structure. For the non-coated TiO_2 system, pH 4.5 (IEP) was used to represent an “aggregated” slurry and pH 7.4 (non-IEP) was used to represent a “well-dispersed” slurry. For alumina-coated TiO_2 system, pH 8.4 (IEP) and pH 4.5 (non-IEP) are selected for an “aggregated” and a “well-dispersed” slurry respectively.

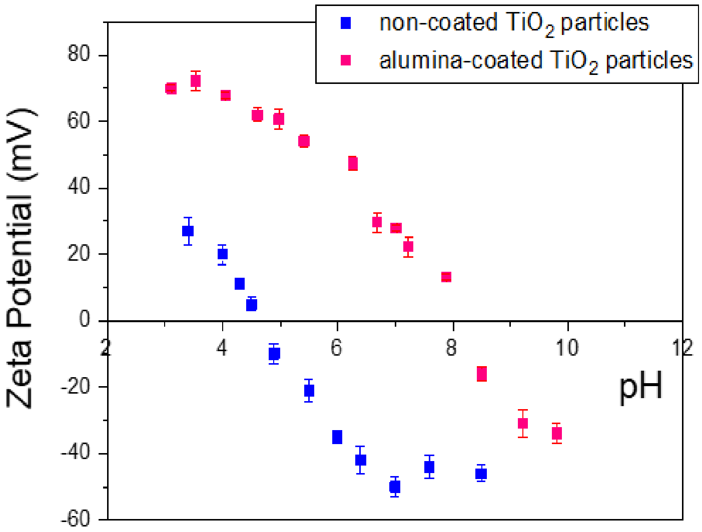

Figure 39 Zeta-potentials of two types of TiO_2 particles as a function of pH: the iso-electric point for non-coated particle is pH 4.5; the iso-electric point for alumina-coated particle is pH 8.4

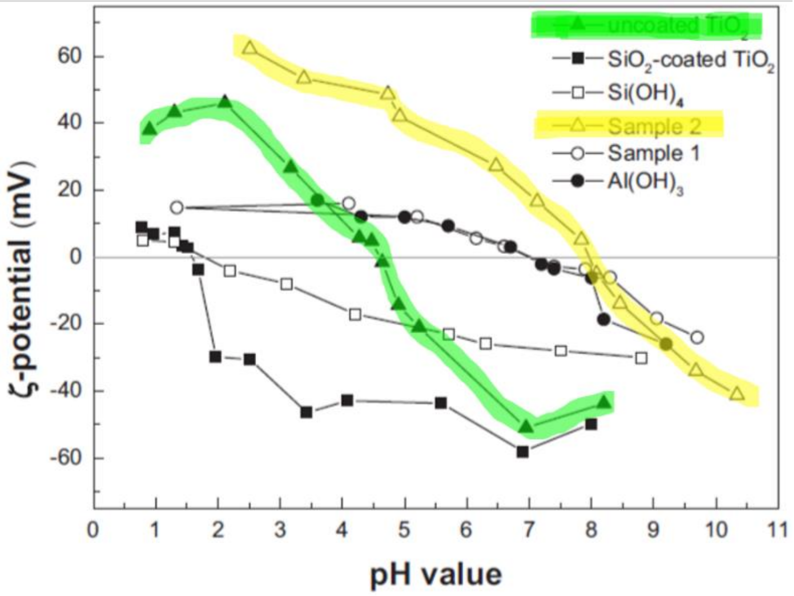

Figure 40 The zete-potential of pure substances and coated rutile TiO_2 particles. The green highlighted curve represents for neat TiO_2, while the yellow highlighted curve represent for boehmite alumina coated TiO_2.

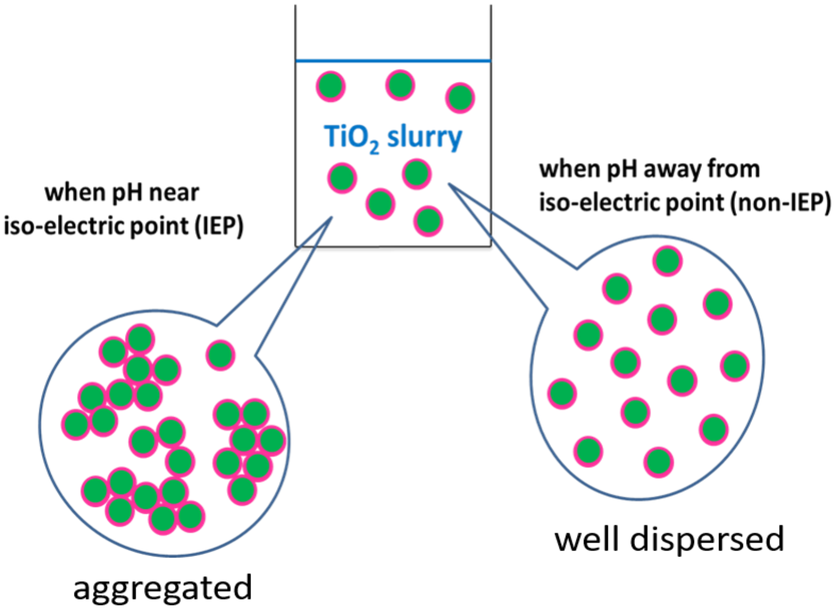

Figure 41 Schematic diagram of pH effect on the aggregation of a colloidal system. When the system pH is near IEP, particles strongly aggregate; when the system pH is far away from IEP, all particles are well dispersed by dominating repulsive force

3.3.3 Particle Size Analysis

Figure 42 a) and b) show the particle size distribution change as a function of applied ultrasonic treatment for non-coated TiO_2 slurry at non-IEP (pH 7.4) and

IEP (pH 4.5). To compare the sizing results measured at IEP and non-IEP at t = 0 min (prior to the ultrasound treatment), the IEP slurry was found to have a mode value of approx. 5 µm, whereas the value for non-IEP one was as small as 0.4 µm. Figure 42 b) clearly indicates there was a formation of large aggregates as a result of neutralised particle surface charge at IEP condition. The change in size distribution caused by applied ultrasound demonstrates a weak structure for formed aggregates at IEP. For non-IEP one, the size distribution was independent of applied ultrasound, indicating 0.4 µm (volume equivalent diameter) is its primary particle size which is in good agreement with SEM observations. The detailed D(50) particle size results are provided in Table 2.

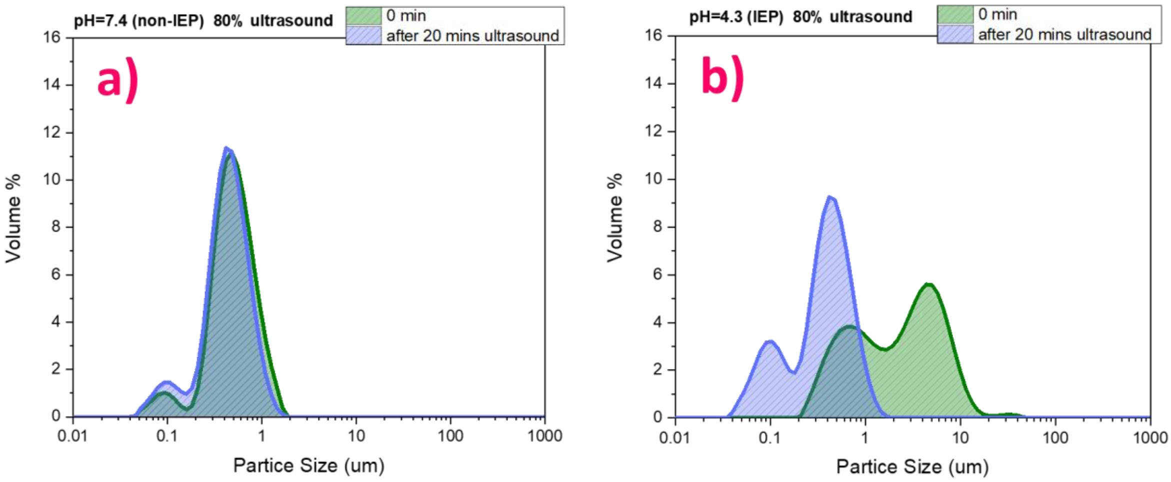

Figure 42 Particles sizing results of non-coated TiO_2 slurry: a) non-IEP; b) IEP. "0 min" represents for immediate sizing result; "after 20 mins ultrasound" refers to sizing results measured after 20 mins ultrasound treatment.

The sizing results for alumina-coated TiO_2 slurry are shown in Figure 43. The non-IEP slurry was found to have a bimodal distribution, whose narrow peak accounts for high volume fraction weighing in small size region. The size distribution shift as a result of applied ultrasonic treatment implies the presence of particle aggregates. This finding is consistent with SEM and TEM observations of alumina-coated particles shown in Figure 35. The formation of aggregates at IEP condition was caused by the neutralised particle surface charge (attractive van der Waals became dominant). While, the formation of aggregate at non-IEP condition was believed as the consequence of adhesive alumina coating layer between particles (Faure et al., 2010, Siwinska-Stefanska et al., 2008). Prior to ultrasound treatment, the IEP slurry exhibited high volume weighting in large particle size region when compared to the non-IEP slurry. This caused by the combination of weakened repulsive force and glueing effect of alumina coating layer.

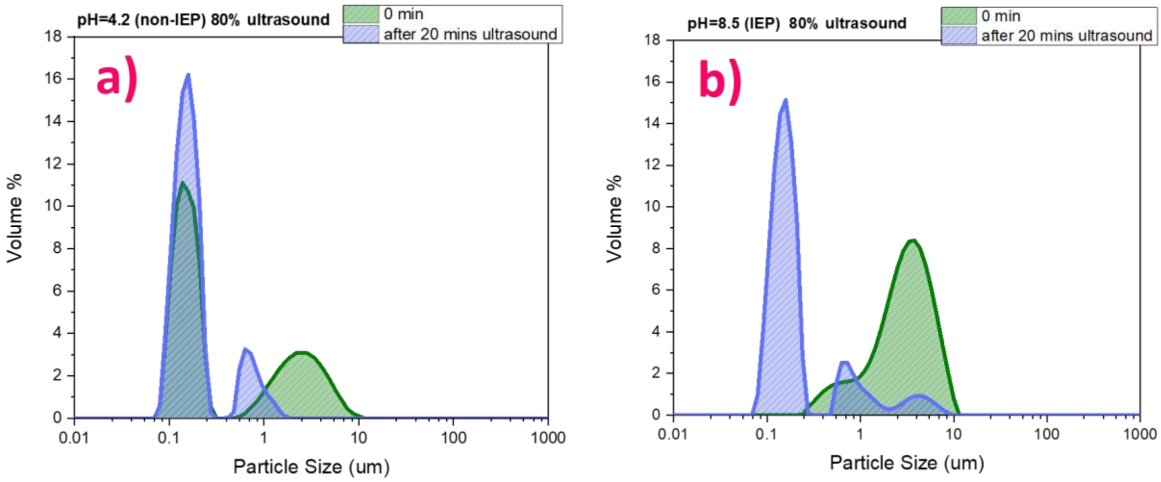

Figure 43 Particles sizing results of alumina-coated TiO_2 slurry: a) non-IEP; b) IEP. "0 min" represents for immediate sizing results; "after 20mins ultrasound" refers to sizing results measured after 20 mins ultrasound treatment.

Table 2 Summary of TiO_2 particle D(50) size measured at 0 min.

D(50) µm	non-IEP	IEP
non-coated TiO_2 slurry 0 min	0.472	2.360
alumina-coated TiO_2 slurry 0 min	0.558	2.934

3.3.4 Settling Behaviour

The particles settling behaviour was initially assessed by filling slurry with different pH and varied concentration into a 6 mm tall Turbiscan glass tube and monitoring the particle/water interface change over a period of 3600 s. Figure 44 indicates the settling behaviour of non-coated TiO_2 particles at non-IEP condition (pH=7.5) at three different solid content. After 3600 s settling time, the height of particles bedding increased from 8 mm to 20 mm as concentration increased from 20%wt to 30%wt. However, there was no clear sign of sediment for 10%wt slurry after 3600 s settling. In order to gain a better understanding of these observations, a similar test was executed on slurries with increment in solid concentration over extended settling time (24 hrs). A similar particle settling behaviour was identified after 24 hrs and is shown in Figure 45, which indicates the formation of closely packed particle bedding for the 20%wt to 50%wt slurries. Both Figure 44 and Figure 45 show a cloud of diffusive fine in 10%wt slurry, implying existing of a number of fine particles at this concentration level. However, the bedding thickness for this 10%wt slurry was not visually clear due to the presence of those fine particles.

Figure 46 verifies the formation of particles bedding by monitoring the height of particle/water interface as a function of time using a Turbiscan. The length of the scan was set to 3600 s which was a used in the visual assessments. The last data point of each Turbiscan curve shown in Figure 46 represents for final particles bedding height. The measured height for 20%wt (12 mm) and 30%wt (20 mm) slurries were found in good agreement with observations in Figure 44 and Figure 45. Turbiscan test indicated a formation of bedding with a thickness of 5 mm in 10%wt slurry. This complies with the trend of bedding height gradient as a function of slurry concentration increment see in Figure 45 and also demonstrates the observed cloud to be diffusive fine particles at 10%wt level.

Figure 44 Sedimentation of 10%wt, 20%wt and 30%wt non-coated TiO_2 slurries at non-IEP condition (pH=7.5) after different time intervals.

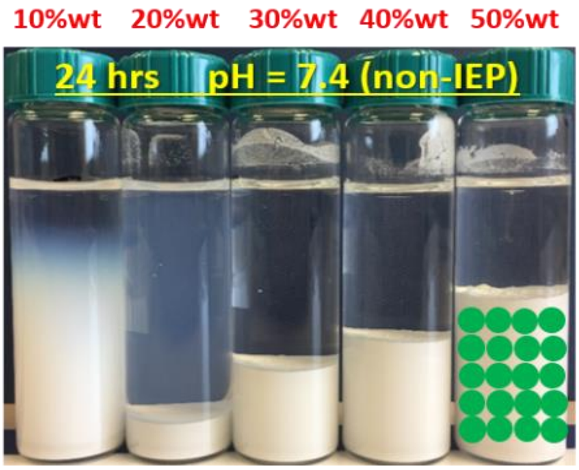

Figure 45 Repeated sedimentation test on non-coated TiO_2 slurries at non-IEP condition (pH=7.4) with extended solid concentration after 24 hrs. A taller 8 mm glass tube was used to for a better visual assessment of 10%wt slurry.

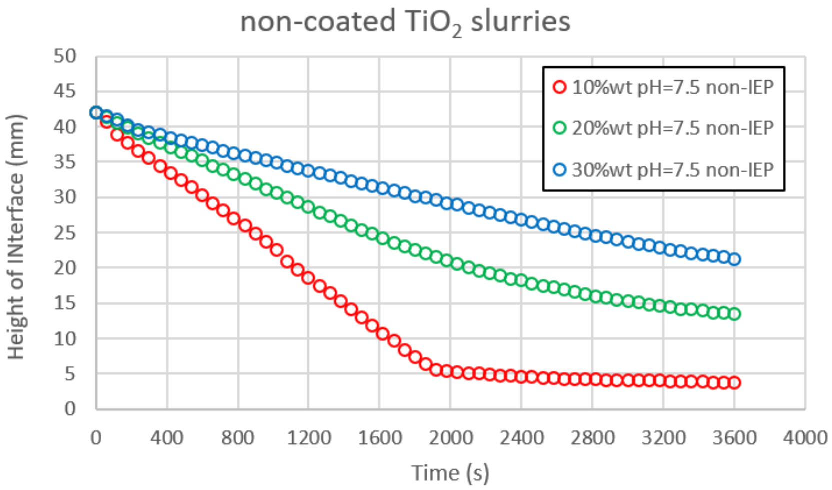

Figure 46 Turbiscan results of 10%wt, 20%wt and 30%wt non-coated TiO_2 slurries at non-IEP condition (pH=7.5) over 3600 s

The particles settling behaviour of non-coated TiO_2 slurries with a solid content of 10%wt, 20%wt and 30%wt at IEP condition (pH=4.5) is shown in Figure 47. At 10%wt concentration level, the particles at IEP condition were found to have a fast settling rate with thicker settled bedding height due to their larger particle size which was confirmed by PSD results shown in Figure 42. However, as the particle concentration increased (to approx. 20%wt), these particles at IEP condition formed a gel net-working which stabilised the entire structure (the gel point is calculated and shown in Table 3). Therefore, the particle settling from 20%wt and 30%wt slurry was hindered due to their gelled structure. The visual assessments were backed up with the Turbiscan measurement shown in Figure

48 which also suggests a fast interface decreasing for 10%wt slurry, and minor interface changes for 20%wt and 30%wt slurries. In comparison with non-IEP slurries, higher bedding was found in IEP slurry over three concentration levels, which indicates that the bedding consisted of a loosely packed aggregates.

Figure 47 Sedimentation of 10%wt, 20%wt and 30%wt non-coated TiO_2 slurries at IEP condition (pH=4.5) at different time intervals

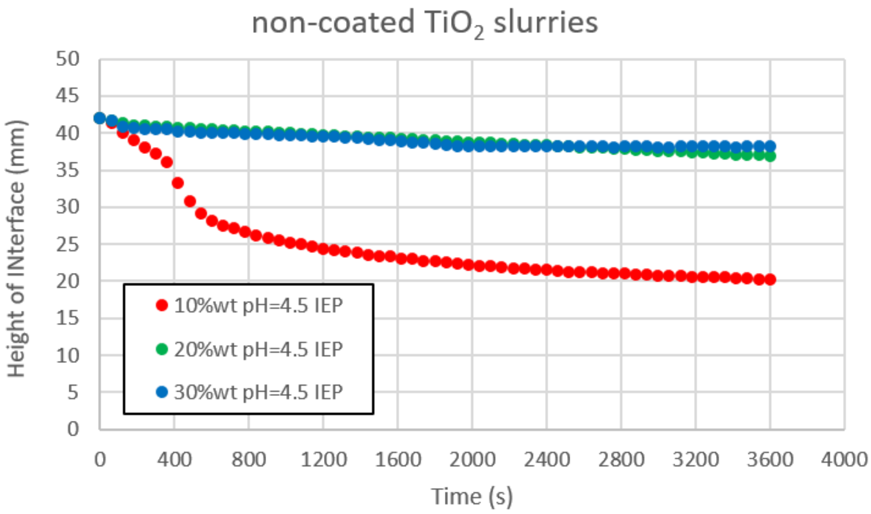

Figure 48 Turbiscan results of 10%wt, 20%wt and 30%wt non-coated TiO_2 slurries at IEP condition (PH=4.5) over 3600 s

The gel point of a colloidal system plays an important role in particles settling behaviour. It is known as the minimum solid content at which a network is developed between neighbouring particles. When a system reaches its gel point, the yield stress caused by the particle-particle interactions can support the network weight. This means all particles or flocs involved in this system are becoming stiff/stable due to entirely networked structure. Despite direct measurement of gel point is not possible, accurate sedimentation method invented by DeKretser has been widely used for determination of this critical point (De Kretser et al., 2003, Franks et al., 2004). In this method, a suspension with low solid content is prepared and filled into several batch columns that decreases in initial height. After 5 days settling time, the final sediment height of different batch is recorded (a schematic diagram of the gel point calculation is shown in Figure 49). Due to mass conservative of solid particles in each batch, the gel point of system can be determined by calculation of fitting straight line slope, *k* from the plot of *y* (product of the initial height and initial concentration) against *x* (final sediment height). The calculated gel point of two TiO_2 slurries systems at non-IEP and IEP are shown in Table 3 below.

For non-coated TiO_2 particles at non-IEP condition, high gel point was found (> 60%wt) which was beyond the range of slurry concentrations used for sedimentation study. The exact gel point was not identified because it was difficult to take the reading for 10%wt slurry due to the presence of fine particle cloud. This system was colloidal stable due to high surface charge effect, but these particles still settle as time elapses due to its relatively higher density (compared with water). For non-coated TiO_2 at IEP, 22%wt was determined as the point that the system structure starts to become stiff which was consistent with the observations of 20%wt and 30%wt slurries shown in Figure 47.

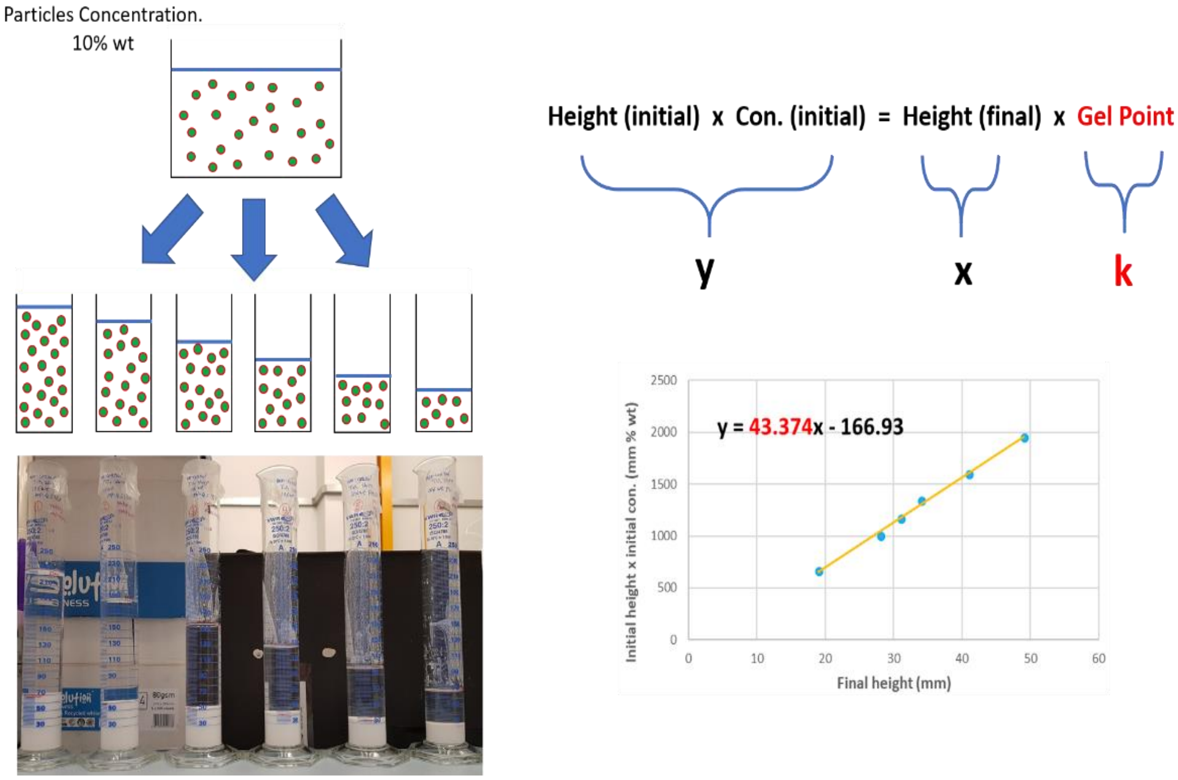

Figure 49 The illustration of gel point calculation method

Table 3 Summary of the calculated gel point of different slurries

	Gel Point %wt
non-coated TiO_2 slurry pH=7.5 non-IEP	> 60
non-coated TiO_2 slurry pH=4.5 IEP	22
alumina-coated TiO_2 slurry pH=4.5 non-IEP	10
alumina-coated TiO_2 slurry pH=8.4 IEP	43

The particles settling behaviour of alumina-coated TiO_2 slurries with solid content of 10%wt, 20%wt and 30%wt at non-IEP condition (pH=4.5) is shown in Figure 50. The particle/water interface was found to be independent of solid content and settling time, which was confirmed by the Turbiscan results shown in Figure 51. These alumina-coated slurries at non-IEP condition were found to contain aggregates from SEM, TEM and PSD measurements. However, no obvious settling was observed from the visual assessment shown in Figure 50 due to the formation of a gel structure above 10%wt (see Table 3). Therefore, stable interfaces were observed from theTurbiscan results for these slurries (Figure 51).

Figure 50 Sedimentation of 10%wt, 20%wt and 30%wt alumina-coated TiO_2 slurries at non-IEP condition (pH=4.5) at different time intervals

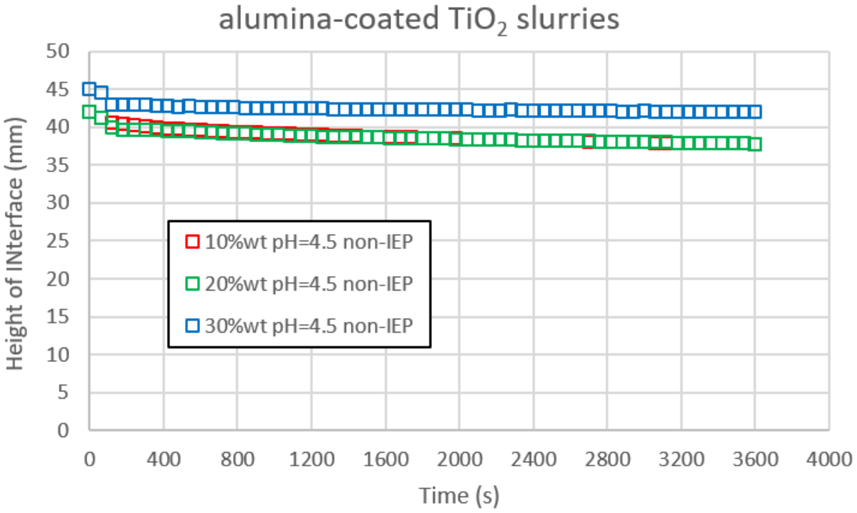

Figure 51 Turbiscan results of 10%wt, 20%wt and 30%wt alumina-coated TiO_2 slurries at non-IEP condition (pH=4.5) over 3600 s.

The particles settling results of alumina-coated TiO_2 slurries with varied solid content at IEP condition (pH=8.4) are shown in Figure 52 and Figure 53. The settling behaviour of these coated particles (aggregates) at IEP condition looked similar to those of non-coated aggregates formed at IEP condition. There was an increase in particles bedding height as solid loading increased from 10%wt to 30%wt. Table 3 indicates the gel point for this system is above 43%wt which means this system will only become stiff when high solid content is loaded. It is also noted there was diffusive cloud existing in the top part of slurry at all solid concentration. This demonstrated the presence of a large portion of fines in alumina-coated slurry and further confirmed the high volume-weighted PSD peak observed in small particle size region from Figure 43.

Figure 52 Sedimentation of 10%wt, 20%wt and 30%wt alumina-coated TiO_2 slurries at IEP condition (pH=8.4) at different time intervals.

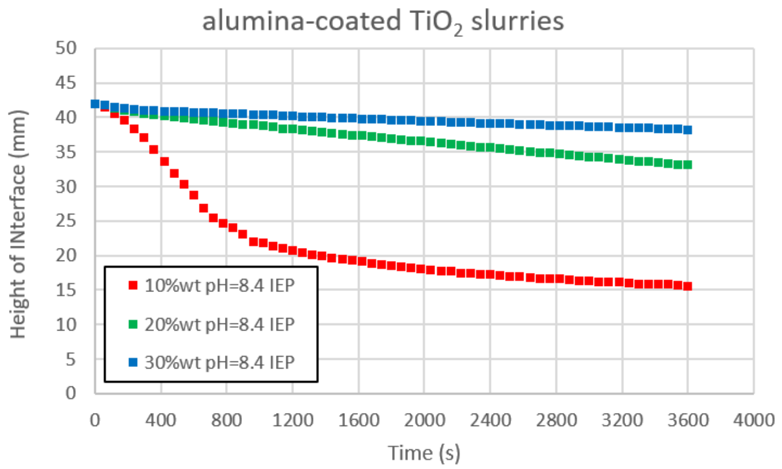

Figure 53 Turbiscan results of 10%wt, 20%wt and 30%wt alumina-coated TiO_2 slurries at IEP condition (pH=8.4) over 3600 s

3.3.5 Rheology

The rheological properties are the reflection of system microstructure which is dominated by the interaction between neighbouring particles within the system at pH of interest (Mikulasek et al., 1997, Biggs et al., 2009). Therefore, the effect of pH on rheological properties of two TiO_2 slurry systems was studied and shown in Figure 54. A similar rheological trend was found in two TiO_2 systems. In general, there was a clear difference in apparent viscosity between IEP and non-IEP slurries at 10%wt, 20%wt and 30%wt levels. Furthermore, the system viscosity was found to increase as solid content increased. The rheological performances of all non-IEP slurries from two TiO_2 systems were similar to neat de-ionised water, showing more or less Newtonian behaviour. There was unexpected shear thickening in non-IEP slurries when shear rate exceeded 100 s^{-1}. This was caused by the vortex of secondary flow formed under high shearing condition (Liddell and Boger, 1994, Morris et al., 1999, Yang et al., 2001).

All slurries at IEP condition from two TiO_2 systems showed shear thinning behaviour. At IEP condition, the viscosity of 20%wt and 30%wt non-coated slurries were found to be higher than the 20%wt and 30%wt alumina-coated slurries. This is because the higher particle-particle interaction caused by the gelled structure for non-coated slurries at 20%wt and 30%wt levels (Table 3). At IEP condition, the 10%wt slurries from two TiO_2 systems exhibited similar rheological behaviour due to their similar particle settling performance (shown in Figure 47 and Figure 52).

At IEP condition, both two TiO_2 systems exhibited shearing thinning behaviour which is the result of micro-structural rearrangement under applied shear or force. At low shear rates, these aggregated slurry systems tend to maintain an irregular order with a relatively high viscosity resulting from particle-particle interaction. At higher shear rate, the aggregated structure were broken down to primary particles and rearranged into string-like layers. As a result of rearrangements, particle-partilce interaction is weakened which contributed to a drop in viscosity (shear thinning curves observed). In addition, the particle size analysis shown above already indicated the aggregates (from either TiO_2 system) can break to its primary particle size under applied ultrasonic sound. This finding further demonstrated that the occurrence of shear thinning behaviour (as consequence of particles arrangement) observed in rheology studies for aggregated systems at high shear rates.

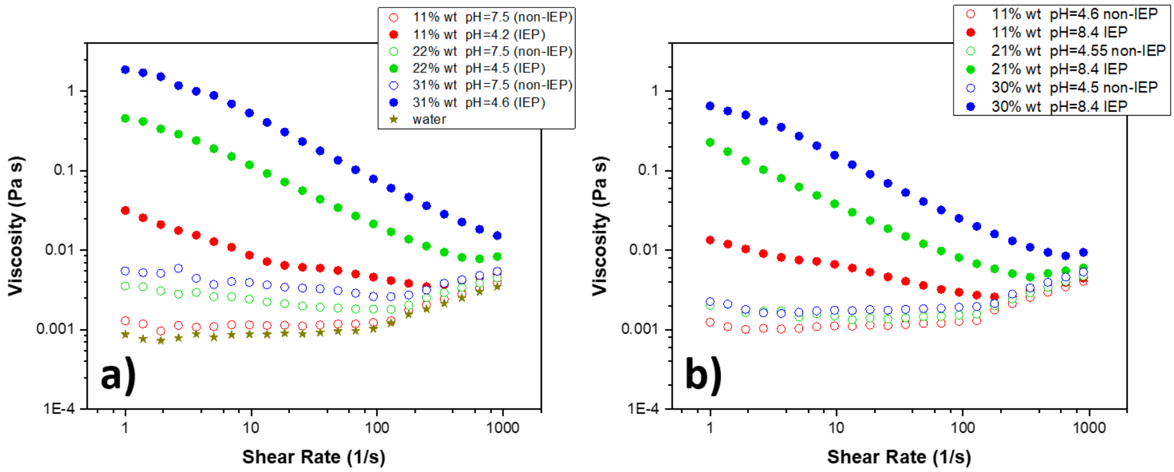

Figure 54 Rheological flow curves of 10%wt, 20%wt and 30%wt slurries at non-IEP and IEP conditions for: a) non-coated TiO2 system; b) alumina-coated system. Flow curve for de-ionised water is shown in a) with star symbols

3.4 Conclusion

In summary of slurry characterisation work, The non-coated TiO_2 samples were analysed using X-ray powder diffraction for crystalline phase identification. The peaks obtained in the diffraction pattern confirmed its rutile phase and high sample purity.

SEM analysis was used to investigate primary particle size and shape for two TiO_2 systems. The SEM images showed a large portion of primary particles are ellipsoidal shaped with a size range of 300±100 nm (Ferret diameter) for the non-coated TiO_2 particles. By contrast, the alumina-coated TiO_2 pigments are irregular shaped aggregates with a size range of 2-10 µm under SEM. The observed particle structure from SEM was further confirmed using more powerful TEM. The TEM images also showed the presence of loose flocculant layer on pigment surface. The EDX analysis of elements distribution across the particle surface and the XPS spectra measured by other researchers identified the loose surface layer to be boehmite type alumina (Li et al., 2012).

The surface charge measurements indicated the iso-electric point at which particles start to strongly aggregate are pH 4.5 and pH 8.4 for the non-coated and the alumina-coated system respectively. These results provided a guide for manipulating the particle-particle interaction in two colloidal systems. In the non-coated TiO_2 system, pH 4.5 (IEP) was used to represent a well-dispersed slurry and pH 7.4 (non-IEP) was used to represent an aggregated slurry. For alumina-coated TiO_2 system, pH 8.4 (IEP) and pH 4.5 (non-IEP) are selected for a well-dispersed and an aggregated slurry respectively. The purpose of formulating slurries in this way is to distinguish between IEP and non-IEP slurries in terms of colloidal stability.

The particle size distribution (PSD) of non-coated TiO_2 system indicated the presence of a large aggregates at IEP with D(50) = 2.3 µm. The formed aggregates was found to break by the applied ultrasonic treatment, resulting a PSD similar to non-coated particles at non-IEP pH condition. The particle size D(50) of non-coated TiO_2 at non-IEP was found to be 0.4 µm which was consistent with the size observed from SEM images (300±100 nm). It is also noted the applied ultrasonic treatment is not able to change the PSD at non-IEP condition. This further confirmed the PSD with D(50) of 0.4 µm is the actual size for non-coated TiO_2 particles. For alumina-coated system, the PSD shift a result of applied ultrasonic treatment implies the presence of particle aggregates in both IEP and non-IEP slurries. This finding is consistent with SEM and TEM observations. The formation of aggregates at IEP was caused by the neutralised particle surface charge, while aggregates formed at non-IEP was caused by the adhesive alumina coating layer between particles.

In non-coated TiO_2 system, at 10%wt concentration level the particles at IEP condition were found to have a faster settling rate with thicker settled bedding height due to its particle (aggregate) size. As particle concentration exceed above 20%wt, these particles at IEP condition formed a gel net-working which stabilised the entire structure. Therefore, the particle settling of 20%wt and 30%wt slurries were hindered due to the gelled structure. The non-coated particles at non-IEP condition exhibited an increased sediment bedding height as concentration increased from 10% to 30%wt. The gelation point for this system was found to be high (above 60%wt), but the exact value was difficult to identify as the reading of interface height cannot be taken due to the presence of fine cloud. The particle settling test for non-coated system confirmed the presence of large aggregate at IEP condition shown in PSD measurement.

In alumina-coated TiO_2 system, it was found the particle at non-IEP condition barely settled at all concentration levels. This was because its gelation point was as low as 10%wt, indicating a strong particle-particle interaction. At the IEP condition, fast particle settling behaviour was found due to large aggregates (confirmed by PSD results). It was also noted there was diffusive cloud in slurries at IEP condition. This demonstrated the presence of a large portion of fine particles seen in PSD results of alumina-coated particles.

The rheological performance of slurries at non-IEP condition from two TiO_2 systems showed water like Newtonian behaviour. All slurries at IEP condition exhibited higher viscosity due to increased particle size due to aggregation. At IEP condition, the viscosity of 20%wt and 30%wt non-coated slurries were higher than that of alumina-coated slurries. This is caused by the increased particle-particle interaction as a result of structure gelation.

Chapter 4 Influence of Slurry Formulation and Processes on Dried Granules Properties

4.1 Introduction

In the last chapter, the colloidal performance of two TiO_2 slurries systems was assessed. For each system, the differences between “well dispersed” slurry and “aggregated” slurry were identified in terms of colloidal properties. Literature review shown in Chapter 2 revealed the progress achieved in drying of a colloidal dispersion. There are many reports on the influences of drying process conditions and colloidal stability on the spray-dried morphology. Various particle morphologies were obtained from drying studies of different colloidal material systems with different drying techniques. Different hypotheses for morphology formation had been proposed, such as aerodynamic effect by air, Péclet number, droplet breakup, rheological yield stress of slurry and drying temperature (Iskandar et al., 2003, Sen et al., 2009, Miglani and Basu, 2015, Bayly, 2014, Cho, 2016, Walker et al., 1999, Okuyama et al., 2006, Lintingre et al., 2015, Lintingre et al., 2016, Nandiyanto and Okuyama, 2011, Vehring, 2008). In this chapter, in order to explore the key parameters that may affect the morphology of Venator’s TiO_2 materials. Slurries drying work was performed using a commercial pilot-plant scale spray dryer. The study focused on investigating the effects of slurry formulation (colloidal stability) and spray drying process conditions on the morphology, size, density and residual moisture content of the spray-dried granules[1].

4.2 Experimental

4.2.1 Materials

The TiO_2 particles used for spray drying work were same as the ones used in slurries characterisation studies shown in Chapter 2. For each type of the two TiO_2 systems, 10%wt, 20%wt and 30%wt slurries with addition of 10^{-3} M NaCl electrolyte at both IEP and non-IEP conditions were prepared for subsequent

---

[1] In this research, term of “granule” is referred as to the discharged product from drying or assembly of primary particles (from slurry) caused by drying. In literatures, agglomerate, spray-dried particle and spray-dried powder are often used interchangeably.

spray drying work. For non-coated TiO_2 slurry system, at each solid content level, the formulation was controlled at non-IEP condition (pH 7.4) to represent a well-dispersed system and was also controlled at IEP condition (pH 4.5) to represent a flocculated system. For the alumina-coated TiO_2 system, pH for non-IEP and IEP formulation was controlled 4.5 and 8.4 at each solid content level respectively. In this project, the maximum solid content studied was 30%wt, because the ProCepT spray dryer pump capability and feed tube diameter is struggle to handle slurry with higher concentration[2].

4.2.2 Drying Facilities and Method

A 4M8Trix lab scale spray dyer from ProCepT Belgium was employed for all spray drying studies. The spray dryer was set up with a 3 drying columns, which is totally 3 m height and 0.4 m width (see Figure 55). The atomisation nozzle is positioned in the centre of hot air dispenser which is located on the top of the drying tower for co-current drying initiation. For initial formulation effect study, all drying studies were conducted at 120ºC with drying air velocity of 0.4 m^3/min, and a 25 kHz ultrasonic nozzle was employed for droplets atomisation. The slurry feed in the beaker was being stirred continuously with a magnetic bar to avoid particle settle and the slurry feed rate was controlled at 2.0 to 2.5 g/min throughout the drying process. A large cyclone was fitted for effective separation of granules from drying air. The pressure drop over cyclone was controlled at 10 mbar by tuning the additional airflow (through transport tube and cyclone) to 80 to 100 ml/min.

In order to investigate the effects of drying processing conditions on the final product morphology, the subsequent drying work was conducted at 200ºC with a same ultrasonic nozzle for atomisation and was also conducted at 120ºC with a 0.6 mm bi-fluid nozzle for atomisation. All spray-dried granules were assessed and compared in terms of morphology using a HITACHI SU8230 SEM and a HITACHI Tabletop TM4000 SEM. The particle size of granules was characterised using a Malvern Morphologi G3S image analysis technique which scans every individual particle dispensed onto a glass slide. The particles were dispensed at an air pressure of 0.5 bar (minimum setting value) and 5 bars (maximum setting value) to investigate the breakage behaviour of those drying formed granules (Malvern, Malvern, 2015a). The residual moisture content of spray drying formed

---

[2] Drying of higher concentrated slurries attempted, but the liquid feed tube was frequently blocked due to the high viscosity of material.

granules were accessed by using a TGA (Thermal Gravimetric Analysis) with a programme of temperature ramp from ambient to 200ºC at increment rate of 5ºC/min and followed by a hold at 200ºC for 15 mins for removal of any organics.

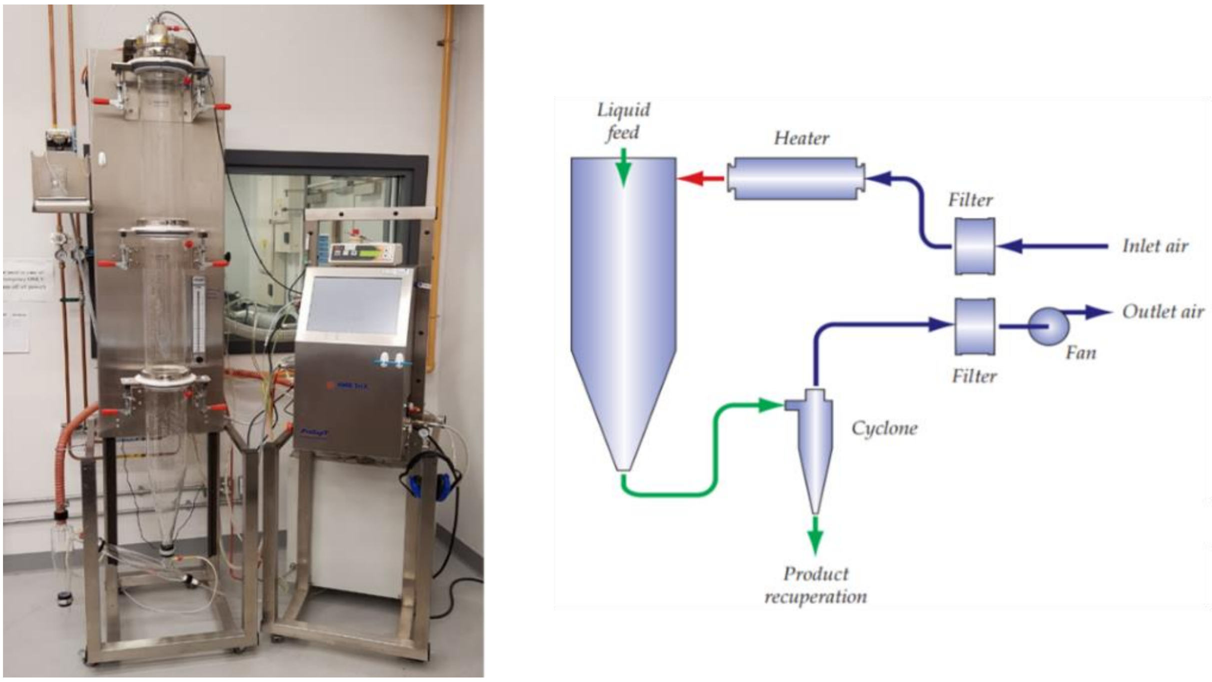

Figure 55 ProCepT 4M8Trix spray dryer with 3 drying chambers (columns) setup and its schematic process diagram (ProCepT, 2019)

4.3 Results and Discussions

4.3.1 Formulation Effect on Morphology

4.3.1.1 Alumina-coated TiO_2 System

The initial spray drying results of alumina-coated TiO_2 slurry with 10%wt, 20%wt and 30%wt solid content at IEP and non-IEP conditions are shown in Figure 56, Figure 57 and Figure 58 respectively. Regardless of slurry solid content, drying of IEP slurries all resulted in beautiful spherical granules. Furthermore, some broken granules shown in SEM clearly demonstrated a solid internal structure for those spherical granules. In the drying of “well-dispersed” non-IEP slurries, distorted and buckled morphology was formed at all slurry solid content levels. Similar “doughnut” and “mushroom” like morphologies were previously reported when drying of well-dispersed TiO_2 and ZrO_2 sol, silica nano-colloids, and zirconia suspensions by different researchers (Sizgek et al., 1998, Iskandar et al., 2003, Cho, 2016, Walker et al., 1999, Lyonnard et al., 2002). Furthermore, similar spherical and buckled morphology was reported when spray drying of more flocculated and less flocculated slurries (Walker et al., 1999). Those pioneers postulated the formation of non-spherical morphologies is caused by either the instability of droplet which is caused by hydrodynamic effect or the collapse of granule surface. In fact, the colloidal properties of slurry/suspension being dried play an important role in final product morphology. None of those literature provided any strong convincing evidence to support their hypotheses. In order to shed a light on the mechanism of morphology formation, a detailed discussion along with the results from sing droplet drying experiment is given in Chapter 5.

alumina-coated TiO_2 slurry 10%wt pH= 8.4 (IEP) Spherical Morphology

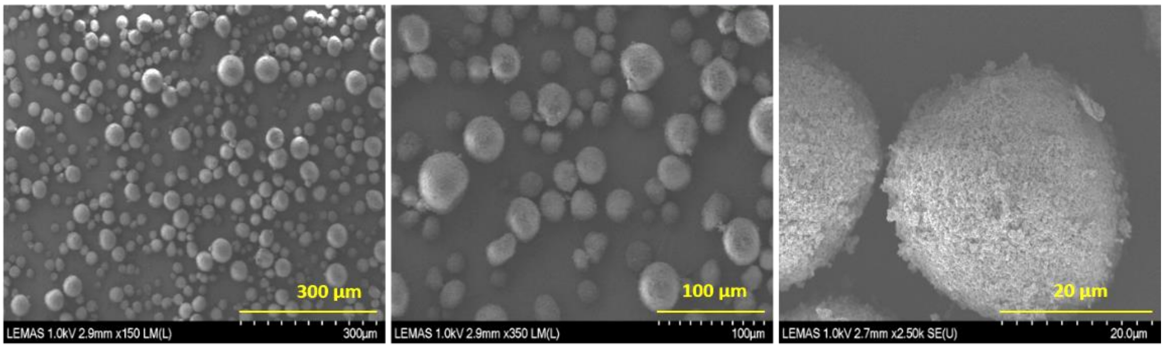

alumina-coated TiO_2 slurry 10%wt pH= 4.5 (non-IEP) Buckled Morphology

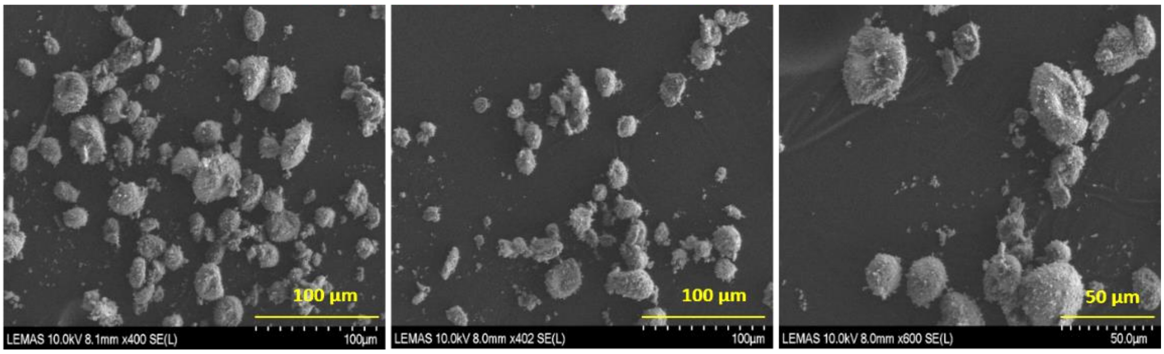

Figure 56 The SEM images of spray-dried granules prepared from drying of 10%wt alumina-coated TiO_2 slurry at IEP and non-IEP conditions. The drying were conducted at 120ºC using an ultrasonic nozzle.

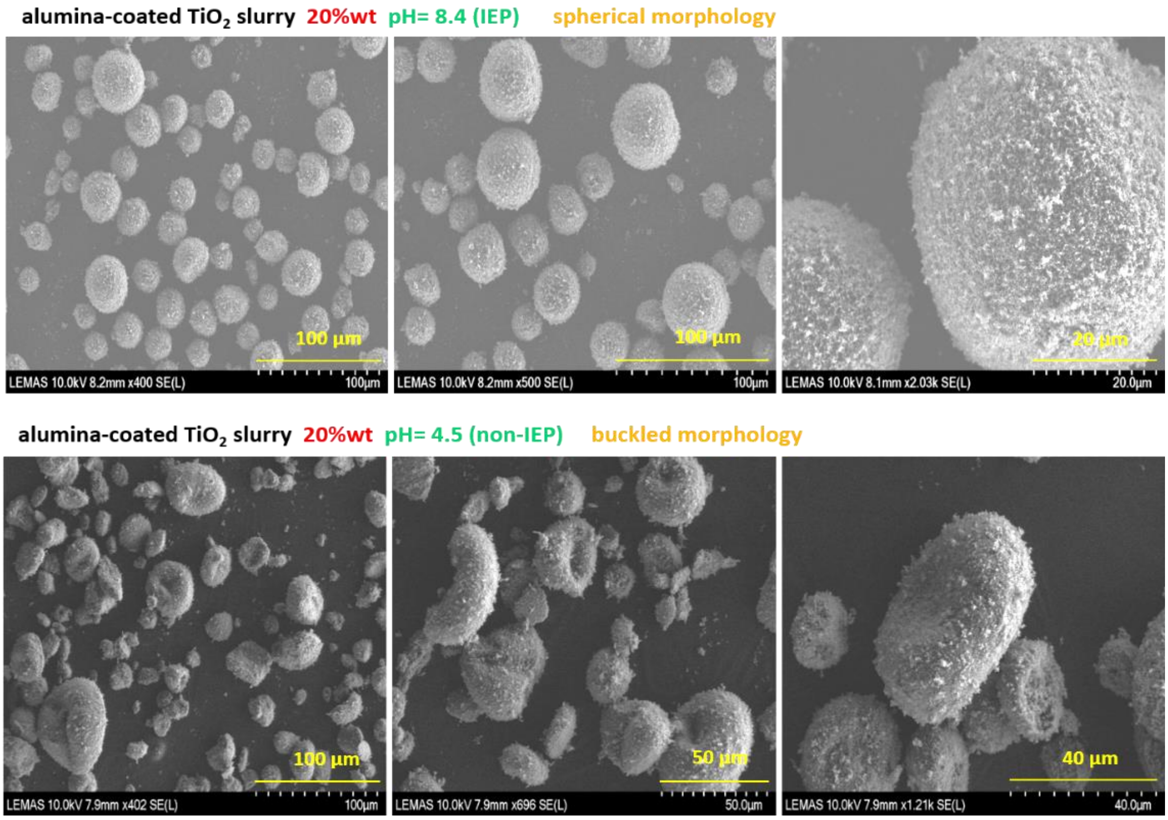

Figure 57 The SEM images of spray-dried granules prepared by drying of 20%wt alumina-coated TiO$_2$ slurry at IEP and non-IEP conditions. The drying were conducted at 120ºC using an ultrasonic nozzle.

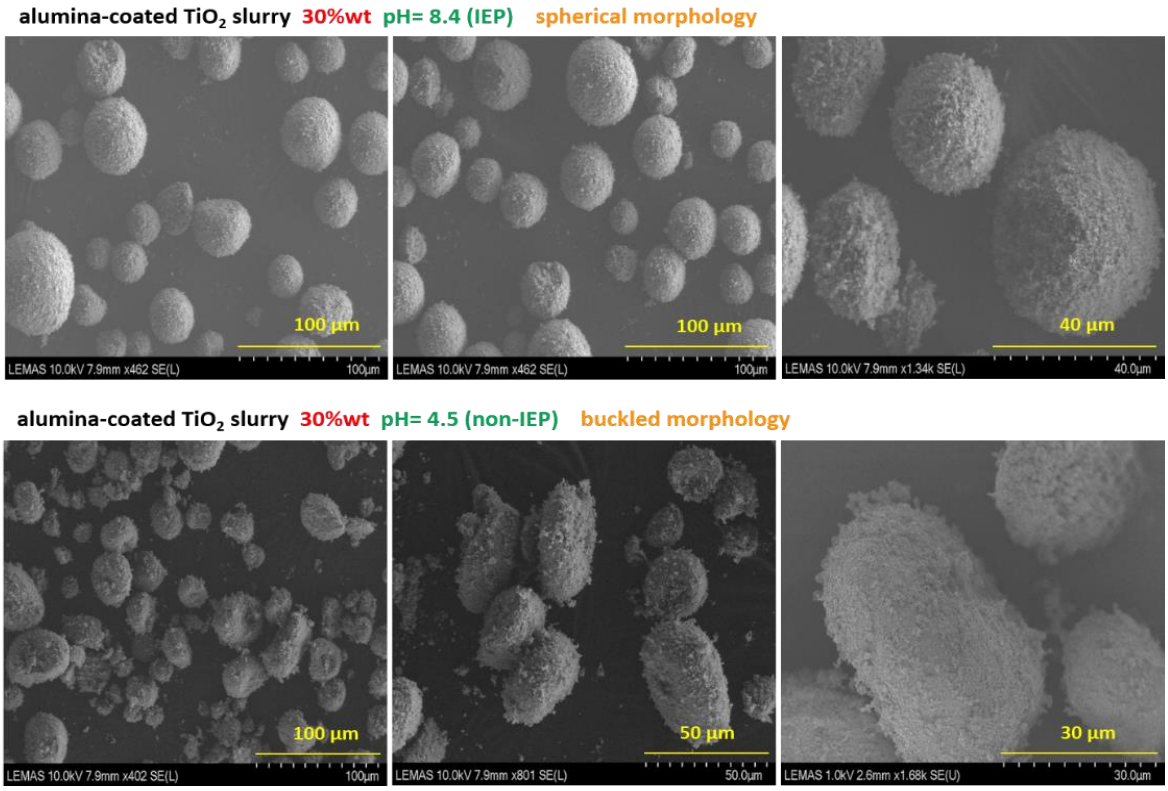

Figure 58 The SEM images of spray-dried granules prepared by drying at of 30%wt alumina-coated TiO_2 slurry at IEP and non-IEP conditions. The drying were conducted at 120ºC using an ultrasonic nozzle.

Figure 59 shows the particle size distribution (PSD) of spray drying formed granules measured by a Morphologi G3S unit. These results were reported in volume-weighted distribution and Circle Equivalent (CE) diameter. The qualitative view of example particles images shown in Figure 59 appears to agree with the SEM observations in Figure 56, Figure 57 and Figure 58. The PSD results demonstrate a size range of 10-100 µm for all drying formed granules regardless of external morphology. Furthermore, the size distribution change caused by 5 bars pressured air was not significant, indicating a similar breakage behaviour for those spherical and buckled granules.

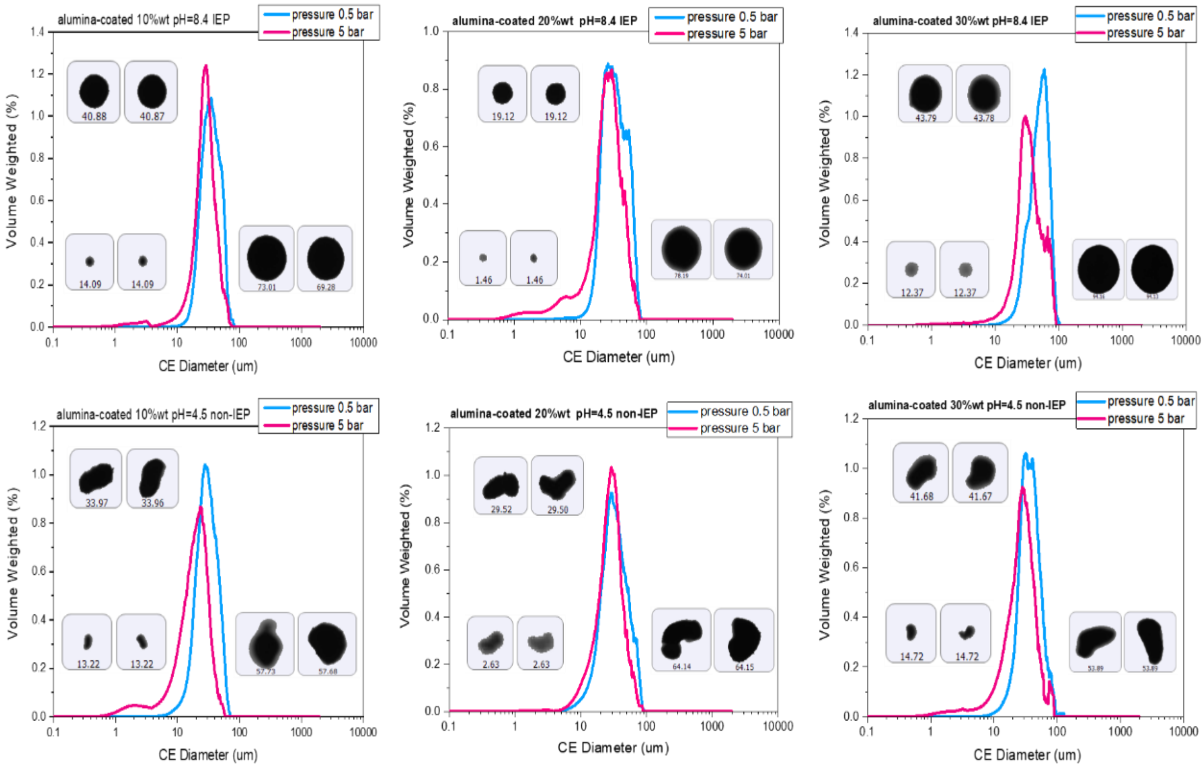

Figure 59 The volume-weighted particle size distribution (PSD) of spray drying formed granules. The top line is PSDs from drying of IEP slurry with 10%wt, 20%wt and 30%wt solid content; the bottom line is PSDs from drying of non-IEP slurry with 10%wt, 20%wt and 30%wt solid content.

4.3.1.2 Non-coated TiO_2 System

The SEM images of granules prepared by spray drying of non-coated TiO_2 slurries with a solid content of 10%wt, 20%wt and 30%wt are shown in Figure 60, Figure 61 and Figure 62 respectively. Neither the slurry concentration nor the pH were proven to have an insignificant effect on morphology as all spray-dried granules showed a spherical morphology. Similar spherical morphology was also reported by other researchers when drying AEROXIDE P-25 (fine-particulate, pure titanium dioxide with a combination of anatase and rutile crystal structure) slurry formulated with polycarboxylate type dispersant. However, the pH effect of slurry on morphology was not investigated in those studies (Faure et al., 2010, Lindeløv and Wahlberg, 2009).

non-coated TiO_2 slurry 10%wt pH= 4.5 (IEP) Spherical Morphology

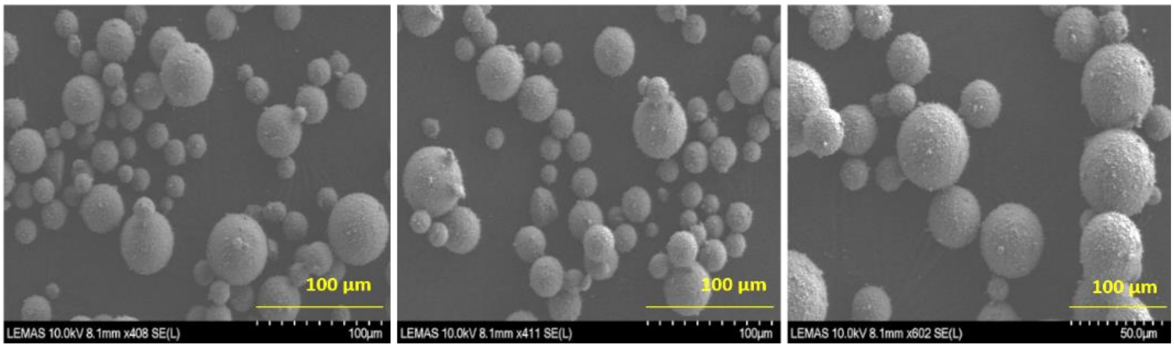

non-coated TiO_2 slurry 10%wt pH= 7.4 (non-IEP) Spherical Morphology

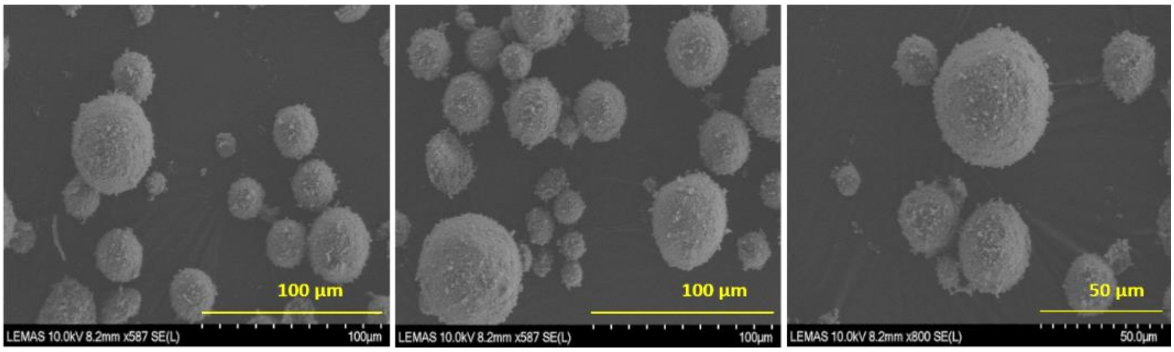

Figure 60 The SEM of spray-dried granules prepared by drying of 10%wt non-coated TiO_2 slurry at IEP and non-IEP conditions. The drying were conducted at 120ºC using an ultrasonic nozzle

non-coated TiO_2 slurry 20%wt pH= 4.5 (IEP) spherical morphology

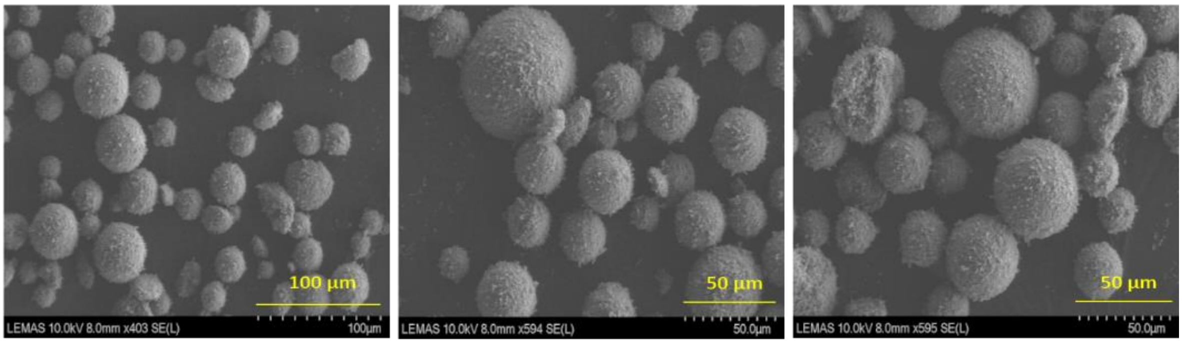

non-coated TiO_2 slurry 20%wt pH= 7.4 (non-IEP) spherical morphology

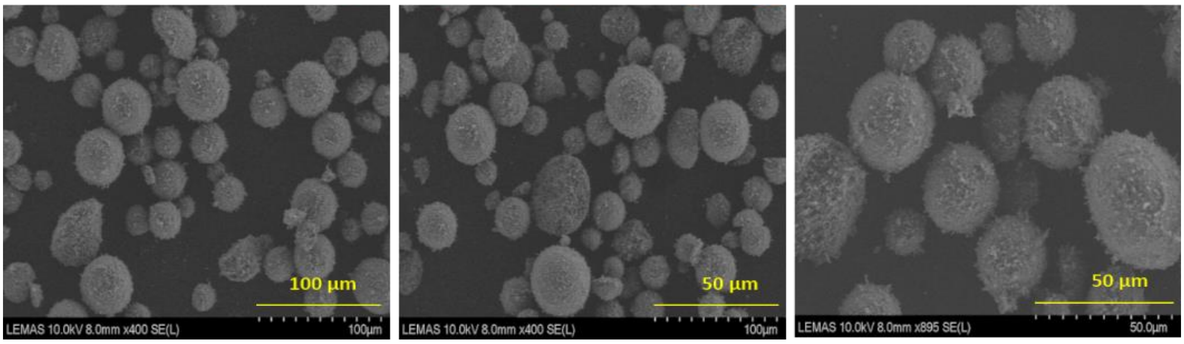

Figure 61 The SEM of spray-dried granules prepared by drying of 20%wt non-coated TiO_2 slurry at IEP and non-IEP conditions. The drying were conducted at 120ºC using an ultrasonic nozzle

non-coated TiO_2 slurry 30%wt pH= 4.5 (IEP) Spherical Morphology

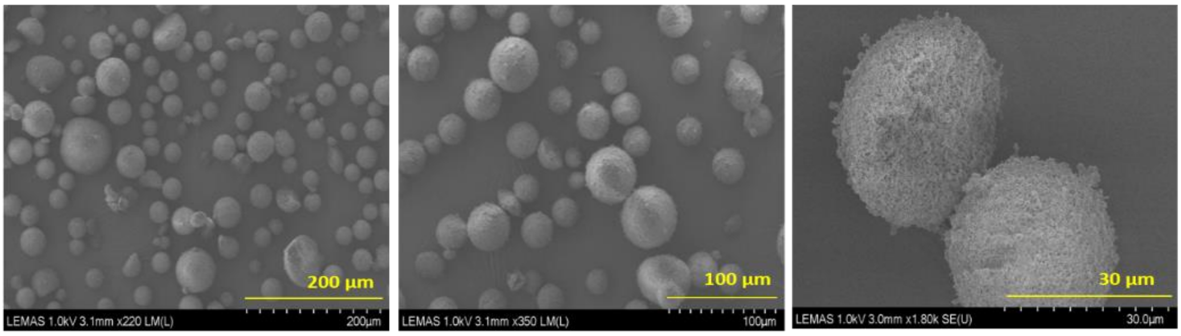

non-coated TiO_2 slurry 30%wt pH= 7.4 (non-IEP) Spherical Morphology

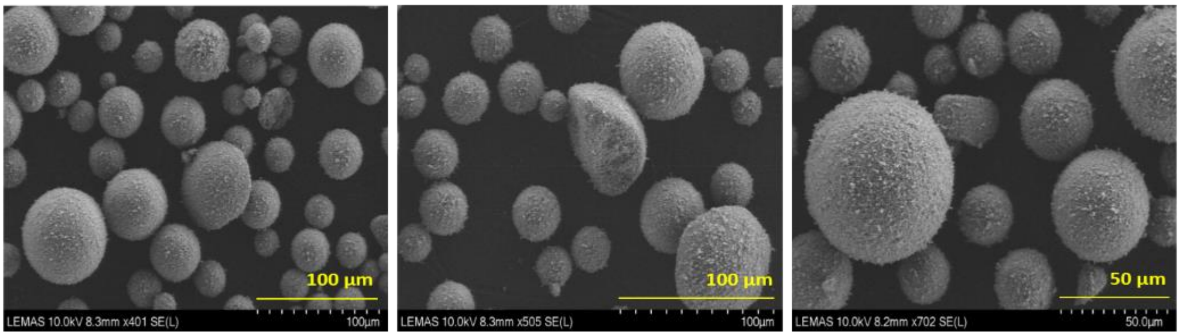

Figure 62 The SEM images of spray-dried granules prepared by drying of 30%wt non-coated TiO_2 slurry at IEP and non-IEP conditions. The drying were conducted at 120ºC using an ultrasonic nozzle

The PSD of spray-dried granules was measured using a Malvern Morphologi G3S and results are shown in Figure 63. These results confirmed the spherical shape for all spray-dried granules, as well as similar PSD at 0.5 bar and at 5 bars. The solid content of liquid feed for spray drying usually contributes to the size of spray-dried formed granules/agglomerates (Masters, 1972). However, in this study the particle size of spry-dried granules was found to be independent of slurry solid content in both alumina-coated and non-coated TiO_2 systems. The mass flow rate of slurry feed was controlled between 2.0 – 2.5 g/min which was recommended by spray dryer supplier ProCepT to ensure an optimal atomisation condition. A higher mass flow rate of 4.0 g/min was attempted to achieve larger granule size. However, this higher mass flow rate led to poor atomisation and undried soggy granules were collected (the result is not shown in this thesis). The capability of a ProCepT ultrasonic nozzle allows production of atomised droplets with narrow size distrubtion (ProCepT, 2014b). Due to same atomisation process condition (when an ultrasonic nozzle was used), the generated droplet size for all assocated drying studies should be more or less same. it is envisaged that a droplet that contains high solid content should have a more compact granular structure than that of one contains low solid content.

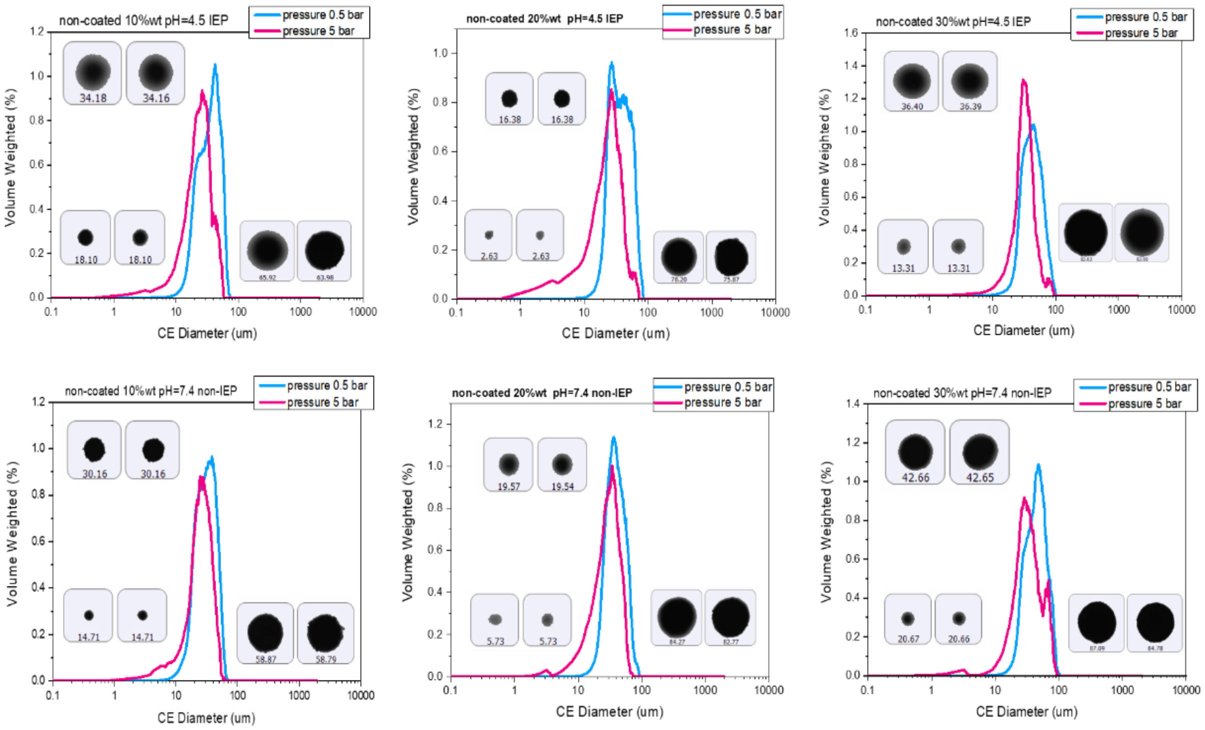

Figure 63 The volume-weighted particle size distribution (PSD) of spray drying formed granules. The top line is PSDs from drying of IEP slurry with 10%wt, 20%wt and 30%wt solid content; the bottom line is PSDs from drying of non-IEP slurry with 10%wt, 20%wt and 30%wt solid content.

4.3.1.3 Thermal Gravimetric Analysis of Product

The residual moisture content of drying formed granules and product yield of spray drying were calculated based on a 300 g powder production campaign for each type of slurries and shown in Table 4. These results demonstrate effective water removal via conducted spray drying process for all productions with similar energy consumption and product yield. Graphical thermal analysis results are shown in Figure 64 and Figure 65.

Table 4 Spray drying production yield and the residual moisture of product. T_{in} and T_{out} are inlet and outlet temperature for each spray drying production.

Materials	Yield %	T_{in}/T_{out} ºC	Residual Moisture %
alumina-coated TiO_2 20%wt pH=4.5 non-IEP	96.0	120/71	0.917
alumina-coated TiO_2 20%wt pH=8.4 IEP	90.6	120/78	0.221
non-coated 20%wt TiO_2 20%wt pH=7.4 non-IEP	87.0	120/74	0.355
non-coated 20%wt TiO_2 20%wtg pH=4.5 IEP	84.0	120/77	0.368

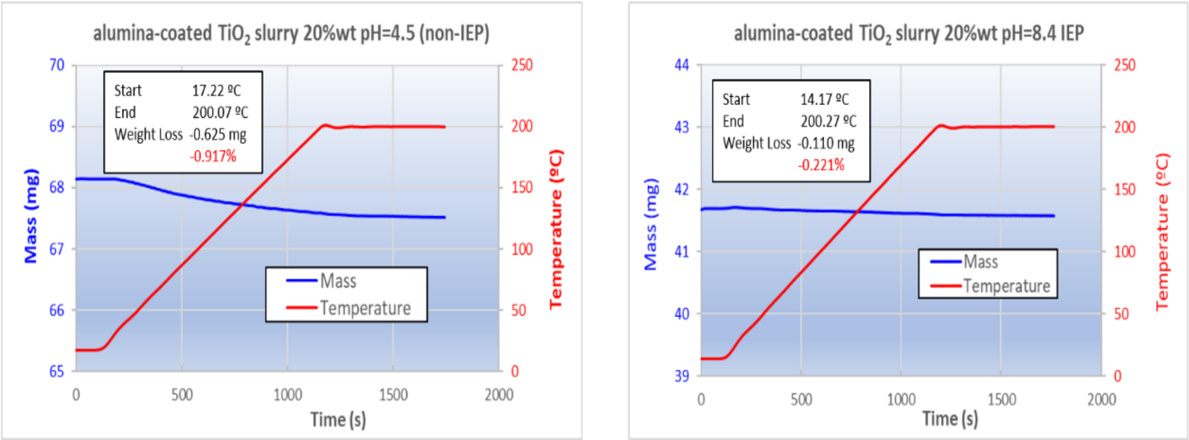

Figure 64 TGA results of drying formed granules via drying of alumina-coated TiO_2 slurry 20%wt at: (left) pH=4.5 non-IEP; (right) pH=8.4 IEP.

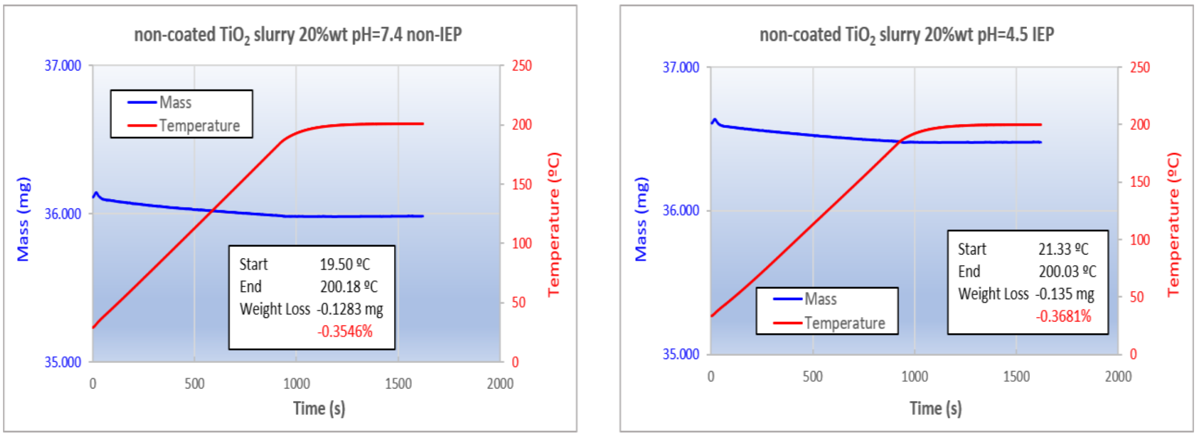

Figure 65 TGA results of drying formed granules via drying of non-coated TiO_2 slurry 20%wt at: (left) pH=7.4 non-IEP; (right) pH=4.5 IEP.

4.3.1.4 Density

The density values of spray drying formed TiO_2 granules are outlined in Table 5. The true density was measured by use of a Pycnomatic ATC unit (from Thermo Fisher Scientific) which is shown in Figure 66 a). This Technique utilises permeation of helium into pores of solids granules for determination of pore volume occupied by gas (ThermoSCIENTIFIC). The tapped density of spray drying formed granules were measured by using a tapping tester from Copley Scientific shown in Figure 66 b). According to ASTM Standard B 527, 100 ± 0.5 g of granules were poured into a 100 cm^3 graduated glass cylinder at ambient. The cylinder was mechanically tapped using this Copley tester until no further decrease in granules volume, and the final volume of powder after tapping was recorded (ASTM, 2008).

The drying formed granular product settling behaviour was expressed by calculating the compressibility index and Hausner Ratio based on tapped density results (Table 5). These two attributes are a reflection of interparticle interactions and are usually correlated to powder flow character based on Table 6 (Carr, 1965, Abdullah and Geldart, 1999). Regardless of external morphology, the alumina-coated TiO_2 granules were found to have low compressibility index % and Hausner Ratio, and were classified to be excellent in free-flowing. This is because of a minor difference between bulk and tapped density, which indicates a less significant interaction between particles. The non-coated TiO_2 granules were rated for good flow character (one grade low than alumina-coated granules) due to slightly low bulk and tapped density values.

a) Thermo Pycnomatic ATC

b) Copley Tapped Density Tester

Figure 66 Instrument image of a) Thermo Pycnomatic ATC unit for true density measurement; b) Copley Tester for tapped density.

Table 5 Summary of different types of density values and calculated compressibility% and Hausner Ratio for spray drying formed granules.

Density (g/cm^3)		TRUE	Bluk	Tapped	Compressibility (%)	Hausner Ratio	Flow Character
alumina-coated TiO_2 20%wt	pH=4.5 non-IEP	4.123 ± 0.005	1.042 ± 0.006	1.142	8.333	1.091	excellent
	pH=8.4 IEP	4.131 ± 0.006	1.025 ± 0.007	1.064	6.000	1.064	excellent
non-coated TiO_2 20%wt	pH=7.4 non-IEP	4.271 ± 0.005	0.965 ± 0.005	1.026	12.857	1.148	good
	pH=4.5 IEP	4.222 ± 0.006	0.862 ± 0.003	0.965	12.648	1.145	good

Table 6 The relationship between compressibility Index %, Hausner Ratio and powder flow character (Carr, 1965).

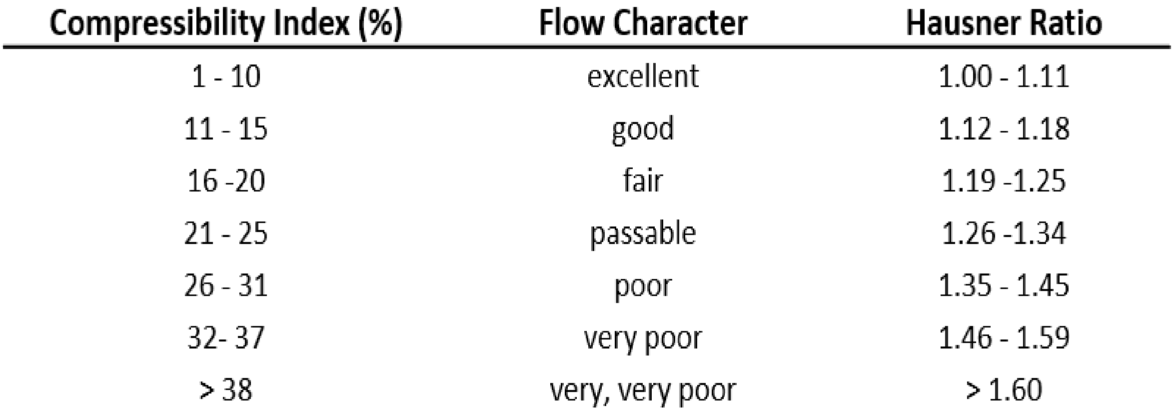

Compressibility Index (%)	Flow Character	Hausner Ratio
1 - 10	excellent	1.00 - 1.11
11 - 15	good	1.12 - 1.18
16 -20	fair	1.19 -1.25
21 - 25	passable	1.26 -1.34
26 - 31	poor	1.35 - 1.45
32- 37	very poor	1.46 - 1.59
> 38	very, very poor	> 1.60

4.3.1.5 Flowability

The flowing ability of drying formed TiO_2 granules was further assessed in a more precise way. The dynamic Angle of Repose (AOR) of dried powder was measured using a robust testing device (Mark 4 Powder AOR tester) which can meet both industrial and academic needs. For sample measurement, 100 g of powder is poured into a metal vibrating chute and flows through a funnel. The powder is subsequently directed by a chute slop and falls onto baseboard to form a pile accumulatively. The AOR is calculated from the height and radius of the formed powder pile (Geldart et al., 2006). The resulting AOR can then be correlated to powder flowability according to pioneers' summary shown in Table 7 (Carr, 1965).

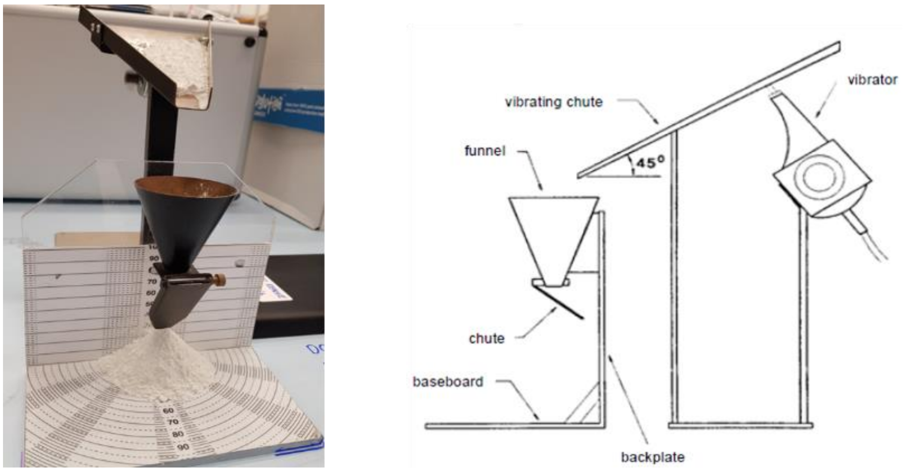

Figure 67 Image of the angle of repose tester and its schematic diagram (Geldart et al., 2006).

Table 7 The relationship between AOR and powder flowability (Geldart et al., 2006, Carr, 1965)

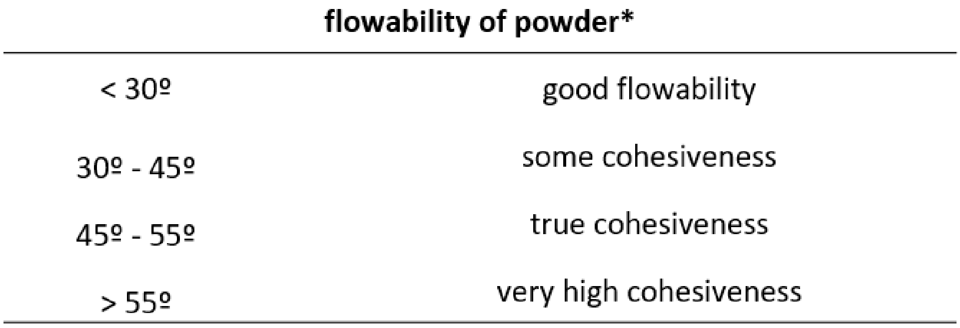

flowability of powder*	
< 30º	good flowability
30º - 45º	some cohesiveness
45º - 55º	true cohesiveness
> 55º	very high cohesiveness

The testing of each type of spray-dried granular product was repeated for 3 times and shown in Table 8. It clearly shows that alumina-coated TiO_2 granules were found to have relatively low AOR with better flow character when compared with non-coated ones. This observation was found to be in good agreement with the Hausner Ratio calculation. Interestingly, the AOR tester was found to have a higher sensitivity to distinguish between granules prepared from drying of non-IEP and IEP slurries in the alumina-coated system. This is thought to be because the spherical morphology for IEP granules has more advantage of powder free-flowing properties when compared with non-spherical and buckled morphology for non-IEP granules (Hassan and Lau, 2009).

Table 8 AOR of spray-dried TiO_2 granules and rated flowability

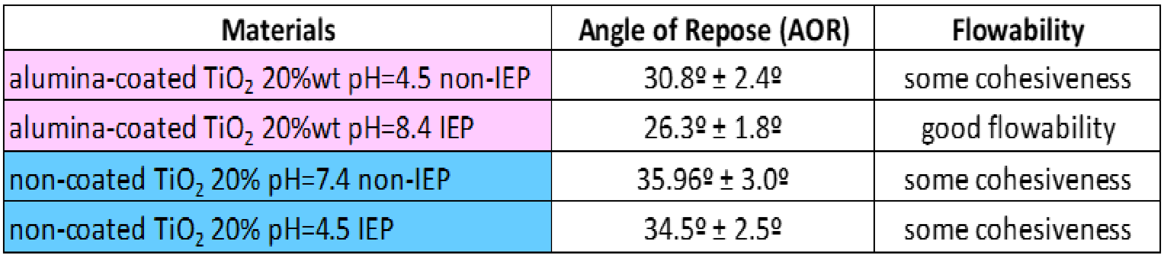

Materials	Angle of Repose (AOR)	Flowability
alumina-coated TiO_2 20%wt pH=4.5 non-IEP	30.8º ± 2.4º	some cohesiveness
alumina-coated TiO_2 20%wt pH=8.4 IEP	26.3º ± 1.8º	good flowability
non-coated TiO_2 20% pH=7.4 non-IEP	35.96º ± 3.0º	some cohesiveness
non-coated TiO_2 20% pH=4.5 IEP	34.5º ± 2.5º	some cohesiveness

4.3.2 Drying Process Conditions Effects on Morphology

4.3.2.1 Alumina-coated TiO_2 Slurry System

Figure 68 and Figure 69 show the SEM of granules prepared from spray drying of alumina-coated TiO_2 slurries at 200ºC using an ultrasonic nozzle and at 120ºC using a 0.6 mm bi-fluids nozzle respectively. The granules prepared from 200ºC drying showed similar morphologies to granules obtained from 120ºC. Drying of a slurry at IEP condition led to a spherical morphology, while a buckled morphology was observed from the drying of a slurry at non-IEP condition (Figure 68). Figure 69 showed a similar morphology trend for these granules prepared using a bi-fluid nozzle at 120ºC. The SEM images also showed a large number of fine particles which were produced by the poor atomisation from the bi-fluid nozzle. More droplets spattering was observed during the bi-fluid nozzle atomisation process when compared with the atomisation performance from the ultrasonic nozzle. These fine particles were not confirmed by the PSD results seen in Figure 70 (bottom line images), because a size filter (< 4 µm) was set before the imaging. This means any particle with a size smaller than 4 µm were filtered and were not shown in PSD results. All these results clearly demonstrate neither a raised drying temperature or a change to atomisation can cause a significant effect on spray-dried morphology.

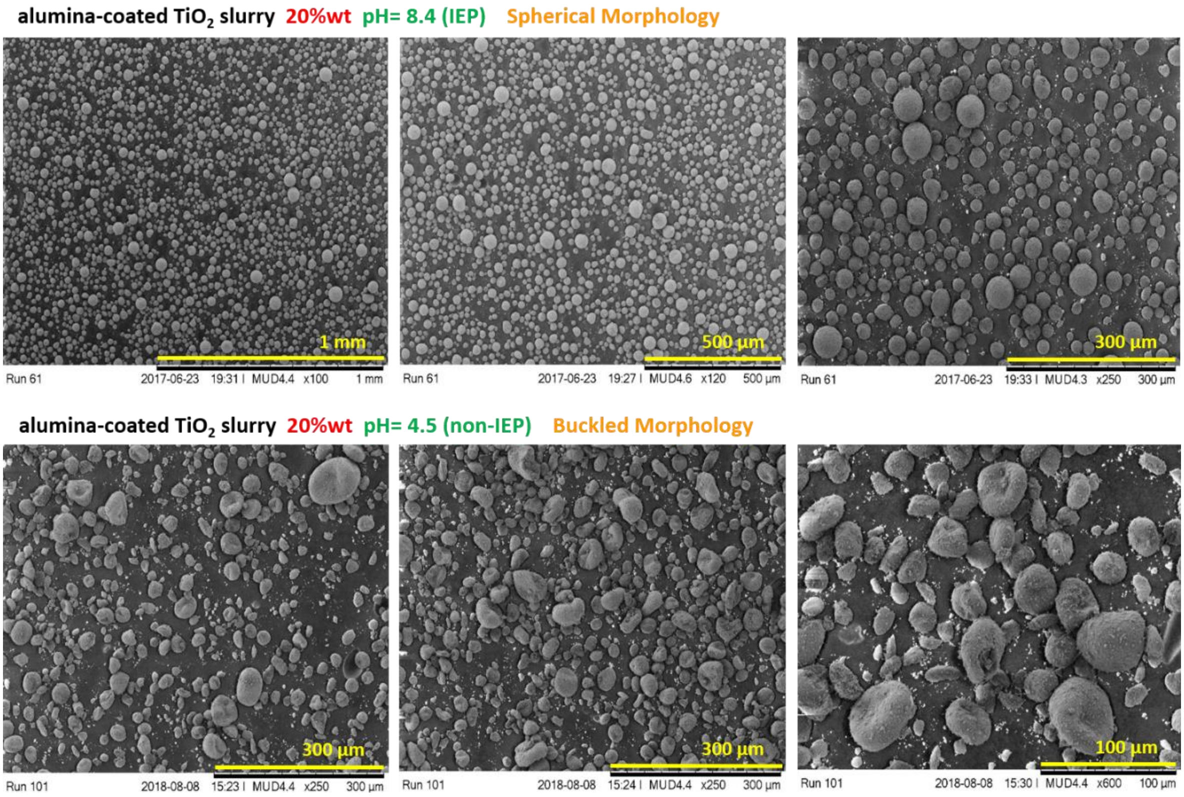

Figure 68 The SEM images of spray-dried granules prepared by drying of 20%wt alumina-coated TiO_2 slurry at IEP and non-IEP conditions. The drying were conducted at 200ºC using an ultrasonic nozzle

alumina-coated TiO_2 slurry 20%wt pH= 8.4 (IEP) Spherical Morphology

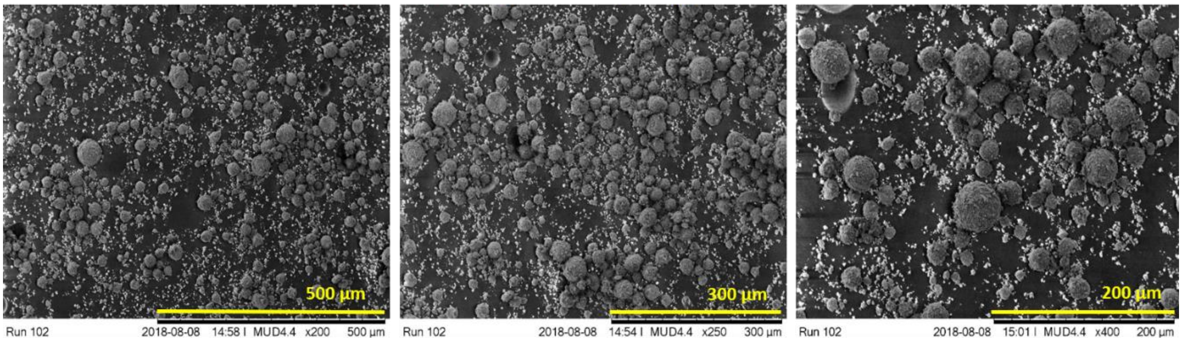

alumina-coated TiO_2 slurry 20%wt pH= 4.5 (non-IEP) Buckled Morphology

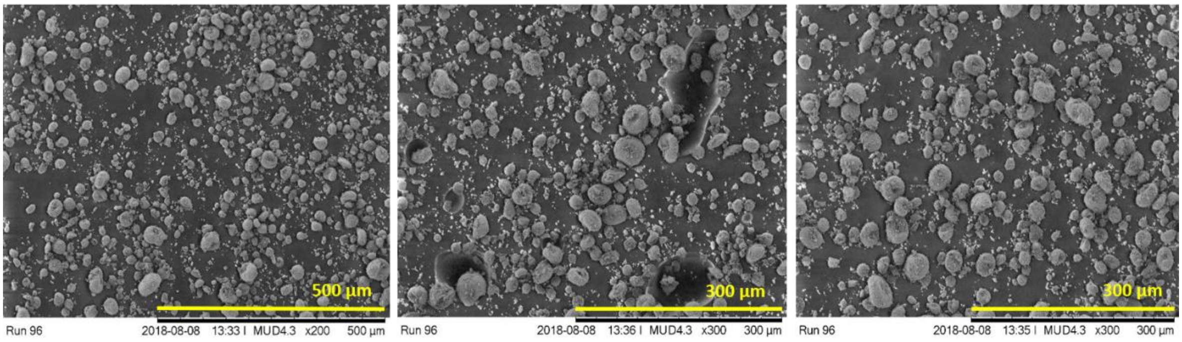

Figure 69 The SEM images of spray-dried granules prepared by drying of 20%wt alumina-coated TiO_2 slurry at IEP and non-IEP conditions. The drying were conducted at 120ºC using a 0.6 mm bi-fluid nozzle

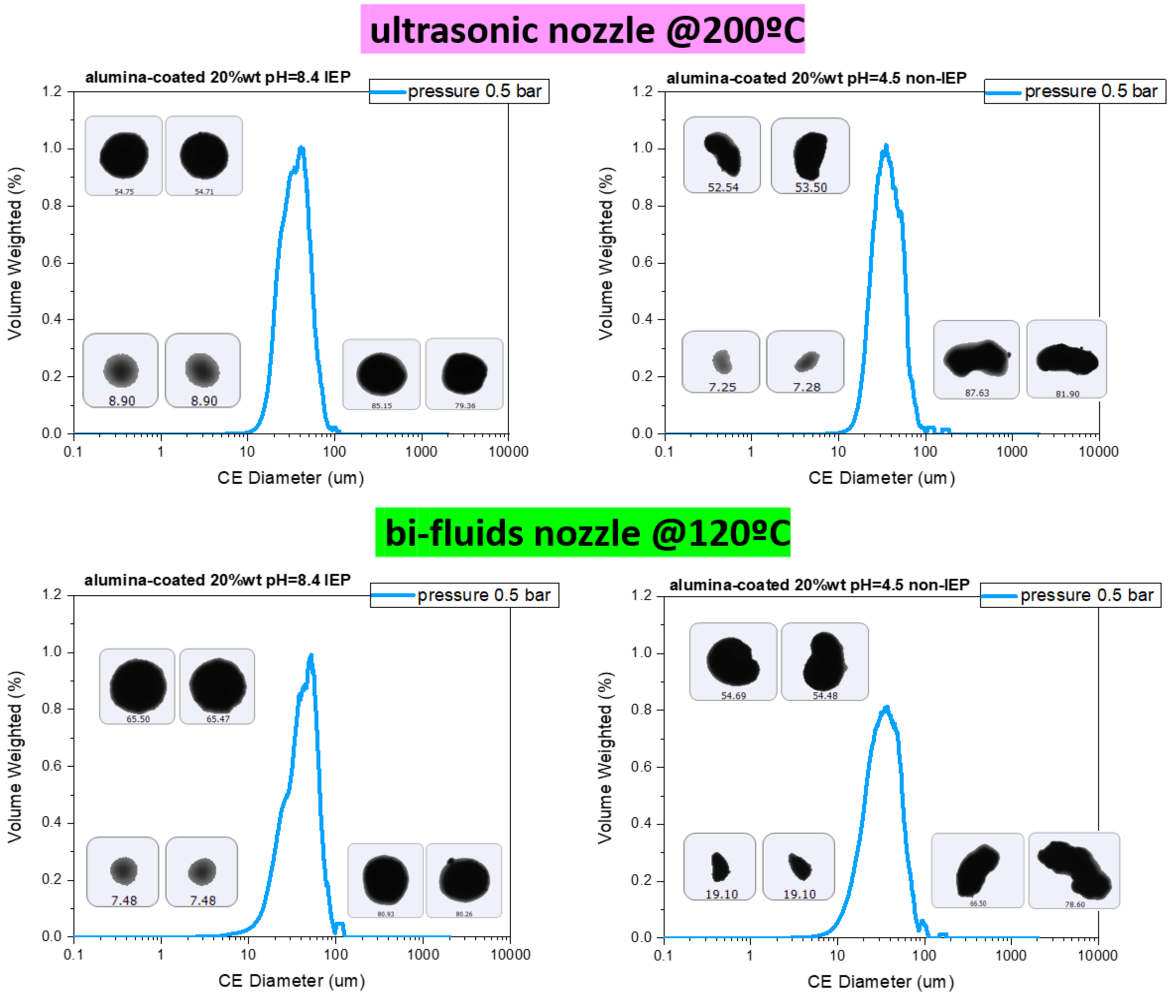

Figure 70 The volume-weighted PSD of spray drying formed alumina-coated TiO_2 granules. The top line is PSDs from drying of IEP and non-IEP slurry with 20%wt solid using an ultrasonic nozzle at 200ºC; the bottom line is PSDs from drying of IEP and non-IEP slurry with 20%wt solid using a bi-fluids nozzle at 120ºC.

4.3.2.2 Non-coated TiO_2 Slurry System

For the non-coated TiO_2 slurry system, the SEM images of spray-dried granules from 200ºC drying using an ultrasonic nozzle and from 120ºC drying using a 0.6 mm bi-fluid nozzle were shown in Figure 71 and Figure 72 respectively. The increased drying temperature and atomisation change were found to have less effect on the morphology. The PSDs of those granules shown in Figure 73 indicated they have similar particle size. The presence of fine particles is also noted in Figure 72. These fines were caused by the poor atomisation from the bi-fluid nozzle. The small particle filter (< 4 µm) set for Morphologi G3 size analysis made these fine particles not shown in PSD results. A methodology improvement is suggested for any future study.

non-coated TiO_2 slurry 20%wt pH= 4.5 (IEP) Spherical Morphology

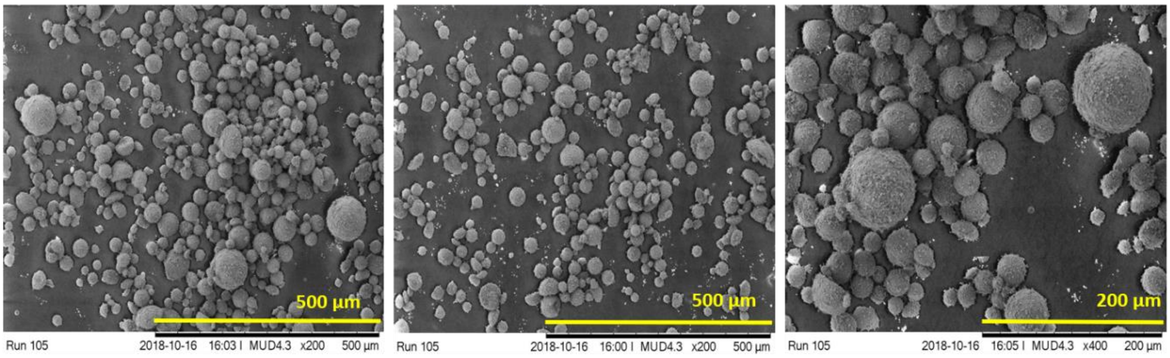

non-coated TiO_2 slurry 20%wt pH= 7.4 (non-IEP) Spherical Morphology

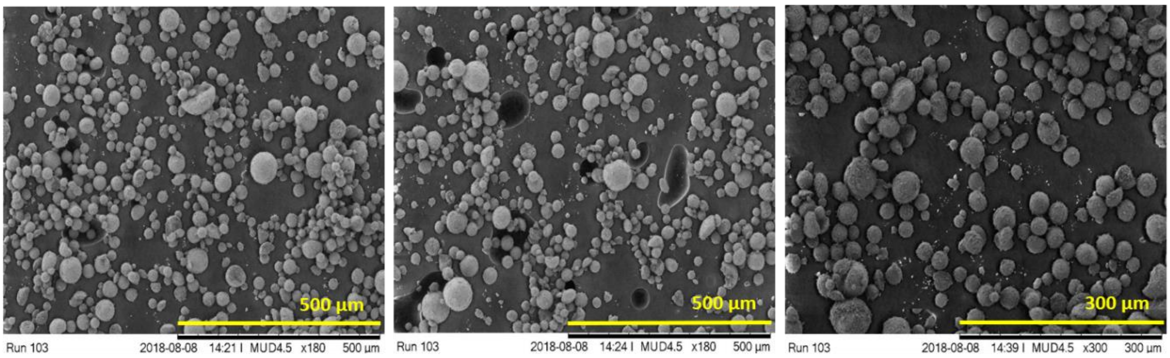

Figure 71 The SEM images of spray-dried granules prepared by drying of 20%wt non-coated TiO_2 slurry at IEP and non-IEP conditions. The drying were conducted at 200ºC using an ultrasonic nozzle

non-coated TiO_2 slurry 20%wt pH= 4.5 (IEP) Spherical Morphology

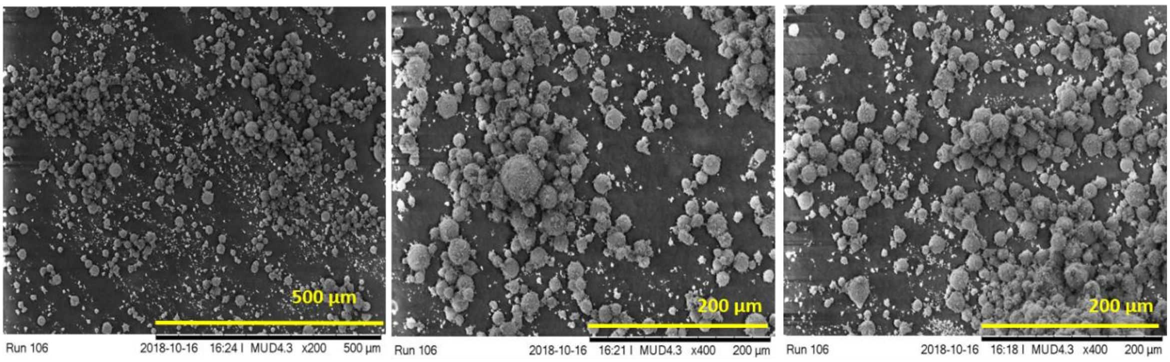

non-coated TiO_2 slurry 20%wt pH= 7.4 (non-IEP) Spherical Morphology

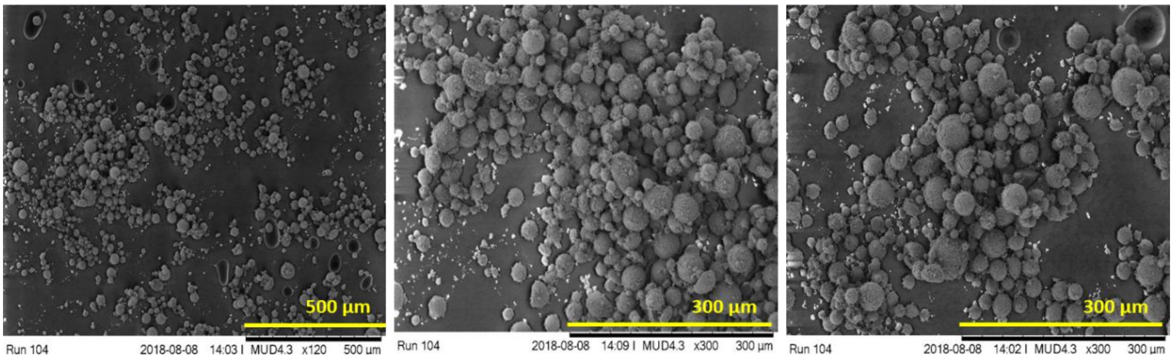

Figure 72 The SEM images of spray-dried granules prepared by drying of 20%wt non-coated TiO_2 slurry at IEP and non-IEP conditions. The drying were conducted at 120ºC using a 0.6 mm bi-fluid nozzle

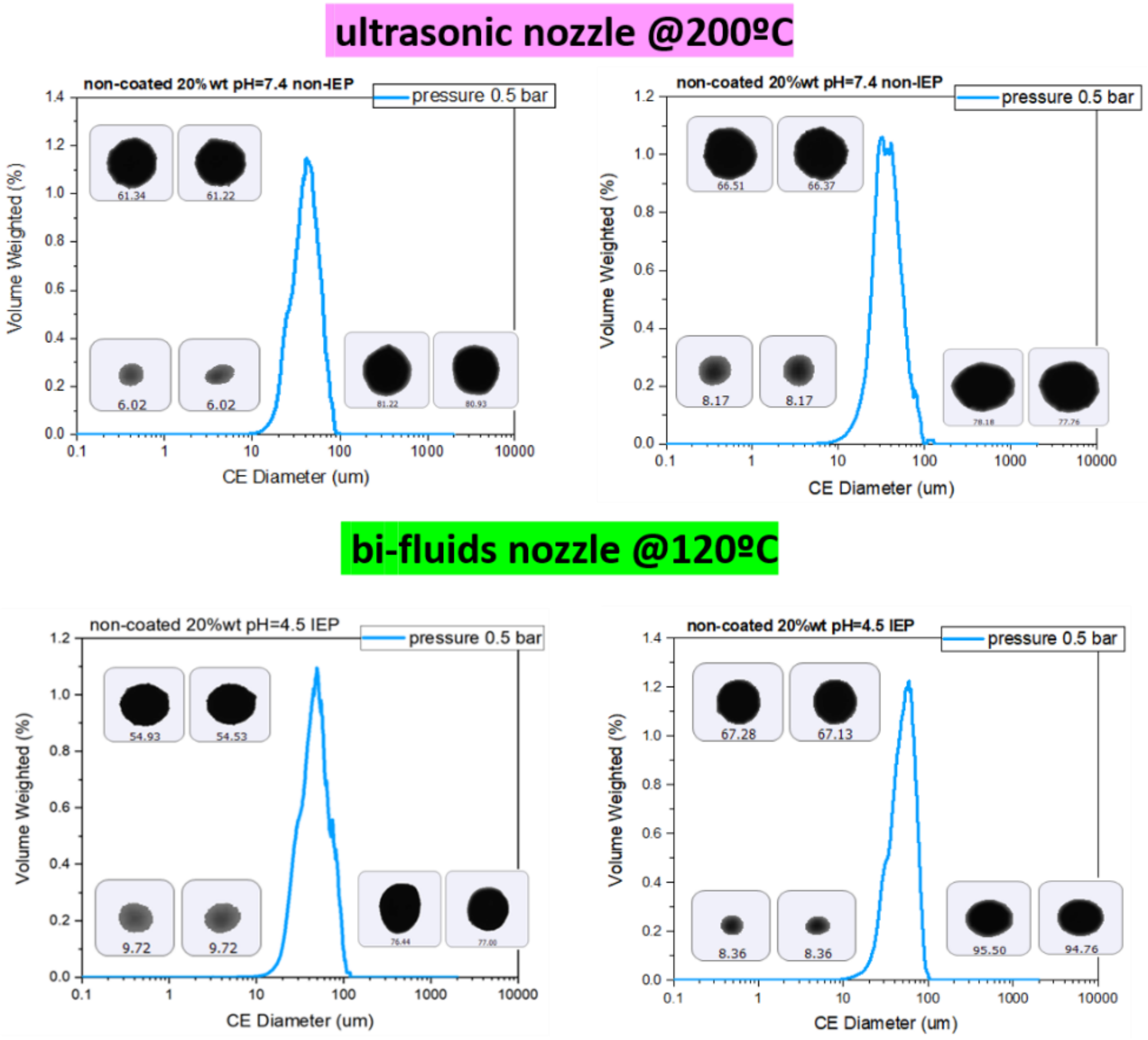

Figure 73 The volume-weighted PSD of spray drying formed non-coated TiO_2 granules. The top line is PSDs from drying of IEP and non-IEP slurry with 20%wt solid using an ultrasonic nozzle at 120ºC; the bottom line is PSDs from drying of IEP and non-IEP slurry with 20%wt solid.

4.4 Conclusions

The initial drying work were performed using a commercial pilot-scale ProCepT spray dryer using a 25 KHz ultrasonic nozzle at 120ºC. For the spray drying of alumina-coated TiO_2 system at all three concentration levels, spherical morphology was found from drying of slurries at IEP condition, whereas a buckled morphology was seen from drying of slurries at non-IEP condition. In addition, some broken granules seen in SEM images indicated a possible solid internal structure for both two morphologies. The image analysis indicated a size range of 10-100 µm for all spray-dried granules, regardless of their external morphology. Furthermore, the buckled and spherical morphology showed similar breakage behaviour when higher sample dispensing pressure was used in

Morphology G3 analysis. It was noted the applied 5 bar pressure did not cause a significant granule breakage.

For the spray drying of non-coated TiO_2 system at all three concentration levels, constant spherical morphology was obtained from drying of slurries at both IEP and non-IEP conditions. In fact, a buckled morphology was expected from the dying of a “well-dispersed” system because the surface charge studies demonstrated a high absolutely zeta-potential for both alumina-coated and non-coated TiO_2 particles at non-IEP condition. The colloidal stability (controlled by pH) was not proved to affect the morphology. This finding is different from conclusion drawn by other researchers who observed a hollow or a distorted structure when drying a flocculated droplet. Interestingly, the spray-dried granules from non-coated TiO_2 system exhibited a similar PSD and breakage behaviour to the granules from alumina-coated TiO_2 system although the two systems had a different primary particle size at both IEP and non-IEP conditions.

The subsequent drying work were conducted at 200ºC using the same ultrasonic nozzle to investigate the temperature effect and also were conducted at 120ºC using a 0.6 mm bi-fluid nozzle to investigate the atomisation effect to the product. For the alumina-coated system, the granules prepared from high-temperature drying showed similar morphologies to granules prepared from 120ºC drying. Drying of a slurry at IEP condition led to a spherical morphology, while a buckled morphology was observed from drying of a slurry at non-IEP condition. Similar morphology trend was observed from the granules prepared using a bi-fluid nozzle which produced a large number of fine particles seen in SEM results. These fine particles were caused by the poor atomisation from the bi-fluid nozzle, more droplets spattering observed during atomisation process when compared with the atomisation performance from an ultrasonic nozzle. These fine particles were not seen in PSD because a size filter (< 4 µm) was set before the size imaging. This means any particle with a size smaller than 4 µm were filtered and not shown in results. The particle sizing methodology needs to be improved to catch the presence of these fines. For non-coated system, neither the increased drying temperature nor the use of bi-fluid atomisation showed any significant effect on morphology, spherical shaped granules were found from drying of slurries at both IEP and non-IEP conditions. The granules prepared from bi-fluid nozzle also contained a large number for dust which is also an indication of poor atomisation.

The granules production campaigns conducted at 120ºC with an ultrasonic nozzle were found to achieve high yield with low residual moisture content for the granules obtained from drying of both non-coated and alumina-coated TiO_2 20%wt slurries at IEP and non-IEP conditions. The powder flow character of these spray-dried granules was also assessed through the calculation of Hausner ratio based on the tapped density measured. Regardless of external morphology, the granules from the drying of alumina-coated system were rated for excellent flow character. A more accurate AOR test was performed to verify the flowability results. The AOR test indicated a good flowability for granules from alumina-coated TiO_2 system, which is consistent with the Hausner ratio assessment. The AOR was also able to distinguish between spherical granules and buckled granules from alumina-coated system. The granules with sphere shape were found to have a better flowability.

Chapter 5 Study of Morphology Control via Single Droplet Drying

5.1 Introduction

In chapter 4, the granular product morphology engineering was studied via a spray drying approach. The morphology was demonstrated to related to the pH in the alumina-coated TiO_2 slurry system. Drying of an aggregated slurry resulted in spherical granules, whereas a buckled structure was observed from the drying of a colloidal stable slurry. Furthermore, similar drying phenomena were reported in the literature about the difference in resultant morphology from drying of a flocculated and a less flocculated colloidal system (Walker et al., 1999, Iskandar et al., 2003, Cho, 2016, Sizgek et al., 1998). In this study, however, the morphology was limited to spherical shape in the drying of non-coated TiO_2 slurry system. Neither the pH nor the drying processing conditions was found to change final product morphology. In addition, none of the above literature shows any clear and convincing conclusion on any factor(s) which can contribute to different morphology as a result of drying. In this chapter, in order to develop a better understanding of different morphology forming mechanism, the drying behaviour was further investigated using a more controlled single droplet drying rig to allow a constant monitor of droplet evolution as a function of drying time.

5.2 Experimental

5.2.1 Materials

For each type of the two TiO_2 slurry systems, 20%wt solid slurry with the addition of 10^{-3} M NaCl electrolyte were prepared at both IEP and non-IEP conditions for single droplet drying work. For the non-coated system, the non-IEP formulation was controlled at pH=7.4 to represent a colloidal stable system, while pH=4.5 to represent a flocculated system. Similarly, pH for non-IEP and IEP was controlled at 8.4 and 4.5 respectively for the alumina-coated system. In the last chapter, the slurry solid content was found not to be responsible for granule morphology and size. Therefore, only 20%wt slurry was considered for the single droplet drying study due to this is the most relevant particle solid content which been using by Venator for their lab-scale spray drying work.

5.2.2 Drying Facility and Method

The schematic diagram of a single droplet drying rig employed for the study is shown in Figure 74. In this setup, a slurry droplet containing particles can be suspended on either a thin a filament or a thermocouple which is positioned in the centre of a cylindrical glass chamber (with an internal diameter of 26.5 mm). The compressed air was heated to 120ºC (to mimic the spray drying condition) with an electrical heater. The heated airflow (at velocity of 0.57 m/s) was subsequently introduced into the glass chamber through a mesh screen for the purpose of flattened air velocity. The droplet drying process was recorded using a Basler Ace USB camera with a resolution of 1280 x 1024. The back illumination of the droplet was provided using high-performance telemetric illuminators (Ebrahim, 2019).

Initial single droplet drying experiment was conducted for validation the morphologies observed from previous spray drying work. Subsequently, the drying study was focused on the understanding of forming behaviour of a droplet with different size. The droplet with varied size/volume of 2.5, 1.0, 0.8, 0.5 and 0.4 µL was controlled and delivered using a single channel micro-pipette respectively. After drying, the dried granular product was carefully removed from filament for structure assessment using a HITACHI benchtop SEM.

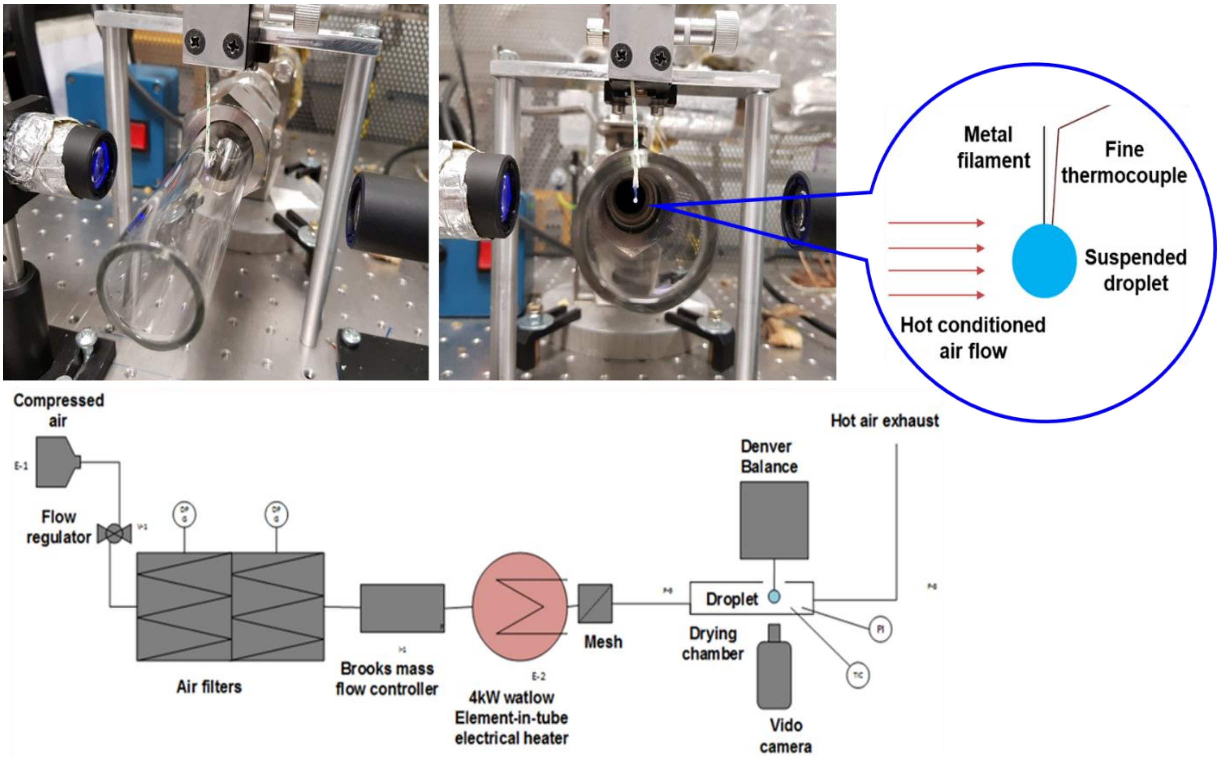

Figure 74 The schematic diagram of a single droplet drying rig (Ebrahim, 2019).

In order to understand the interaction between neighbouring particles suspended in droplet over the drying process, the yield stress of a series of concentrated slurries which are analogous to the surface gelation status of a droplet was estimated. Slurries with a solid content of 40%wt, 50%wt, 60%wt and 70% from each TiO_2 system at non-IEP condition were prepared and characterised using an Anton Paar MCR-301 rheometer with a 1º 70 mm cone and plate geometry. The slurry under test was pre-sheared at 600 s^{-1} for 120 s and then rested for another 120 s prior to starting. The shear rate was ramped from 0.1 s^{-1} to 1000 s^{-1} at ambient in a logarithmical mode over 5 mins.

5.3 Results and Discussions

5.3.1 Single Droplet Drying and Morphology Analysis

5.3.1.1 Alumina-coated TiO_2 system

The evaporation process of a single droplet has been proven to be able to reproduce the main characteristics of a spray drying process. Therefore, such an experiment was commonly used to study the drying mechanism of a colloidal suspension (Lintingre et al., 2016, Perdana et al., 2011a, Yamamoto and Sano, 1992a). Figure 75 shows the evolution of droplet morphology change as a function of drying time for both IEP and non-IEP alumina-coated slurries in a single droplet drying experiment. The corresponding drying curves which indicate the droplet size change as function of drying time are illustrated in Figure 76. For each of the results shown in Figure 75, a montage of droplets was created by extracting the recorded drying video frames at 1-second interval. The created montages for both IEP and non-IEP slurries clearly demonstrated the same spherical droplet morphology prior to the start of drying (t = 0 s). However, these two slurries ended with different granular morphology after drying. Drying of an IEP slurry resulted in a sphere, whereas drying of non-IEP led to a buckled structure. These morphologies obtained from the single droplet drying work were further confirmed by SEM scan and the resulting images are shown in Figure 77. Therefore, the single droplet drying results were found to be in good agreement with observations from the spray drying work completed in the last chapter.

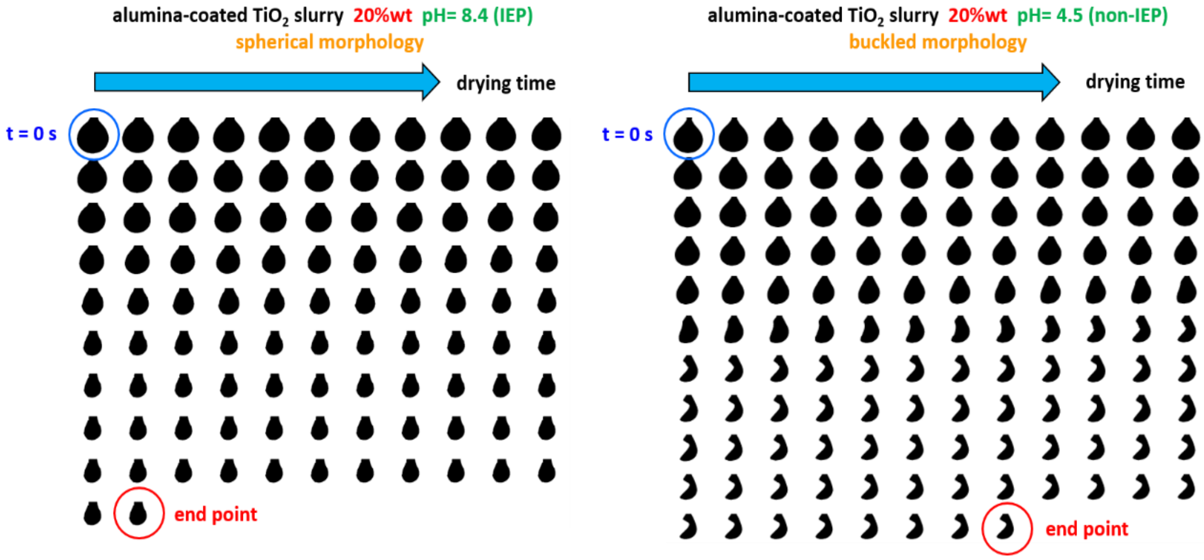

Figure 75 Evolution of droplet change as a function of drying time for alumina-coated TiO_2 slurry at IEP and non-IEP conditions. Each individual frame shot was extracted from a recorded video at an interval of 1 second.

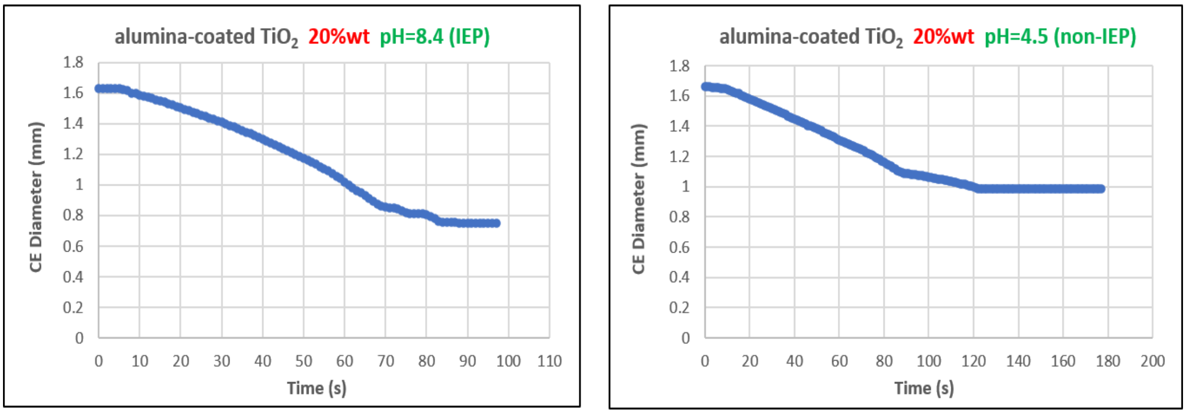

Figure 76 The associated droplet size change as funciton of drying time for alumina-coated TiO_2 system: (left) for IEP condition; (right) for non-IEP condition.

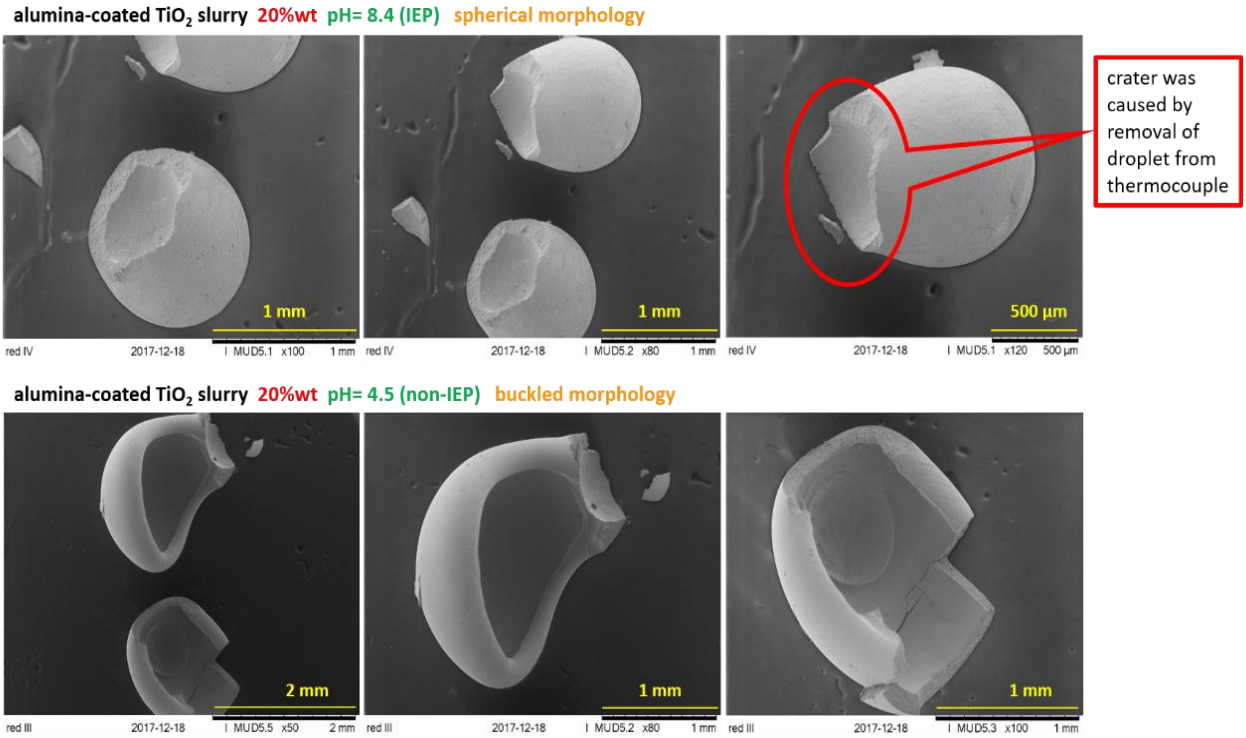

Figure 77 SEM of dried particles from a single droplet drying experiment of alumina-coated TiO_2 slurry at IEP and non-IEP conditions. The damage on the top section of a particle was caused when being removed from the filament.

5.3.1.2 Non-coated TiO_2 system

The spraying drying and single droplet drying experiments of alumina-coated TiO_2 system successfully demonstrated the significant effect of colloidal flocculation on the final product morphology. However, the spray drying of non-coated TiO_2 system drew a different conclusion. The spray dried resultant morphology seemed to be independent of slurry pH or colloidal flocculation. Interestingly, the morphologies obtained from the single droplet drying of non-coated TiO2 system demonstrated different morphology at IEP and at non-IEP conditions. Montage results are shown in Figure 78 and SEM images of collected dried granules shown in Figure 80 distinguished between the morphology formed at IEP and at non-IEP condition. In summary of the drying results of non-coated system, a constant spherical shape was formed in both spray drying and single droplet drying of IEP slurry. However, in the spray drying of non-IEP slurry, the buckled morphology was not observed as expected although this morphology was certainly formed in a single droplet drying experiment.

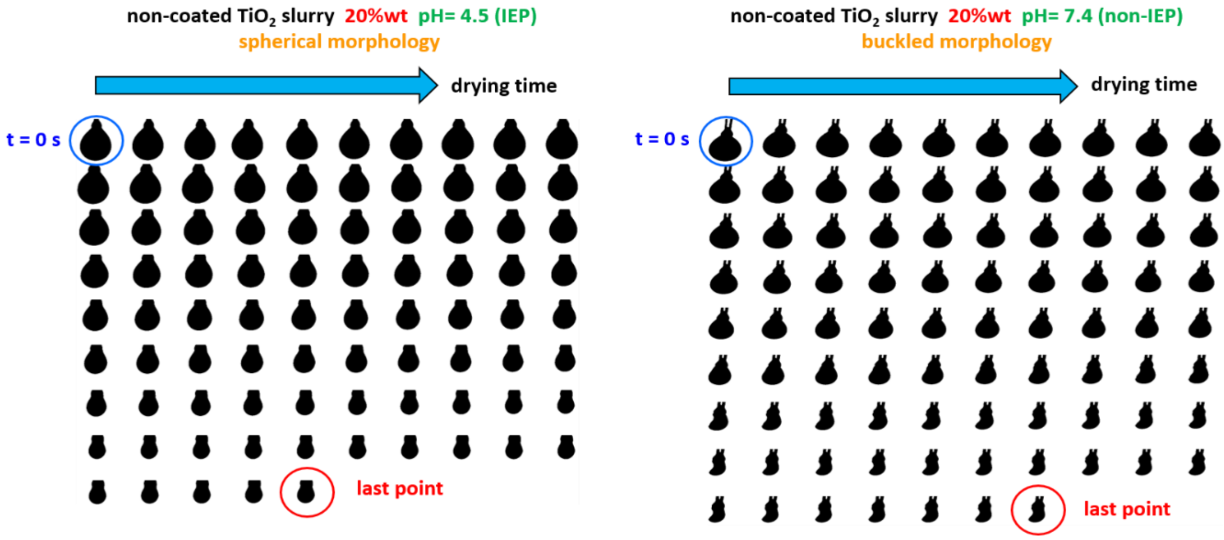

Figure 78 Evolution of droplet change as a function of drying time for non-coated TiO2 slurry at IEP and non-IEP condition. Each individual frame shot was extracted from recorded video in an interval of 1 second.

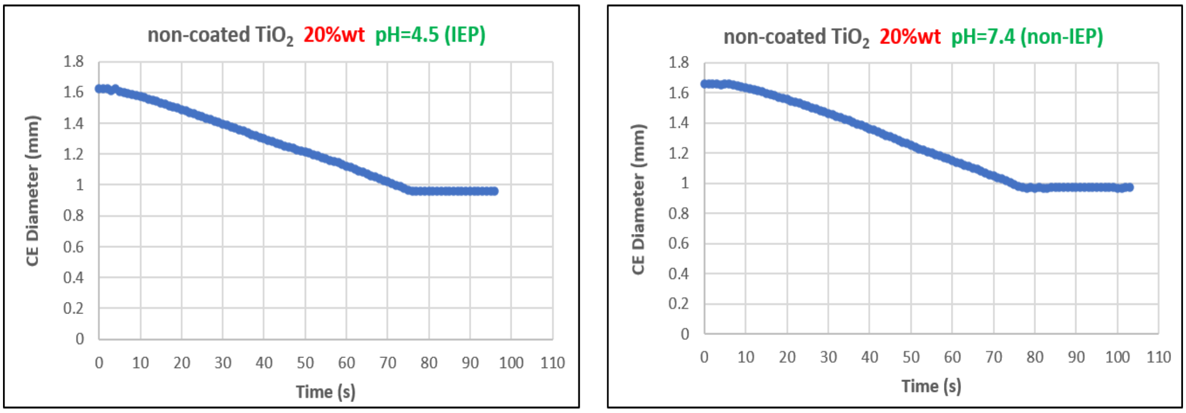

Figure 79 The associated droplet size change as function of drying time for non-coated TiO2 system: (left) for IEP condition; (right) for non-IEP condition.

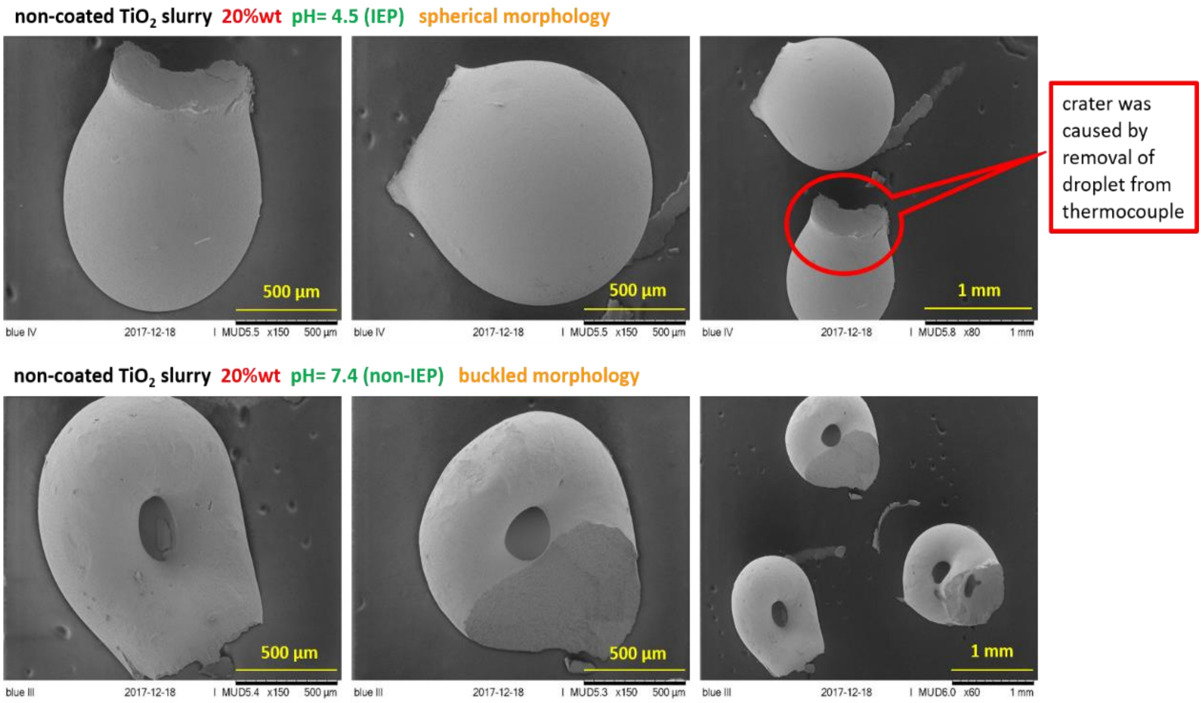

Figure 80 The SEM of dried particles from a single droplet drying experiment of non-coated TiO_2 slurry at IEP and non-IEP condition. The damage on the top section of a particle was caused when being removed from the filament.

5.3.2 Péclet Number and Morphology Formation Mechanism

5.3.2.1 Péclet Number Calculations

In order to develop a better understanding of the inconsistency on morphology forming behaviour, the numerical estimation of dimensionless Péclet was attempted due to many discussions found in the literature about the use of Péclet for morphology prediction (Vehring, 2008, Nandiyanto and Okuyama, 2011, Leong, 1987). The dimensionless Péclet number, *Pe*, which is expressed as the ratio of a droplet evaporation rate to the particle diffusion rate:

$$Pe = \frac{k}{8D} \tag{5.1}$$

The diffusion rate, *D*, can be calculated using the Stokes-Einstein equation. The calculation of the droplet evaporation rate, *k*, is dependent to the drying technique considered. In a real spray drying experiment, the measurement of the atomised droplet size is difficult. In the circumstance of lack of droplet size information, the approximation of *k* was achieved by using a method invented by Vehring

(Vehring, 2008). Whereas, in a single droplet drying experiment, the calculation of *k* is relatively easier due to the droplet size information can be found via camera recording. The calculated Péclet number for two different TiO_2 slurries systems at IEP and non-IEP conditions using the spray drying and using the single droplet drying techniques are shown in Table 9. All calculation details are provided in Appendix sections (Appendix A for the alumina-coated system) and (Appendix B for the non-coated system).

Table 9 Results of Péclet number for spray drying and single droplet drying of two systems

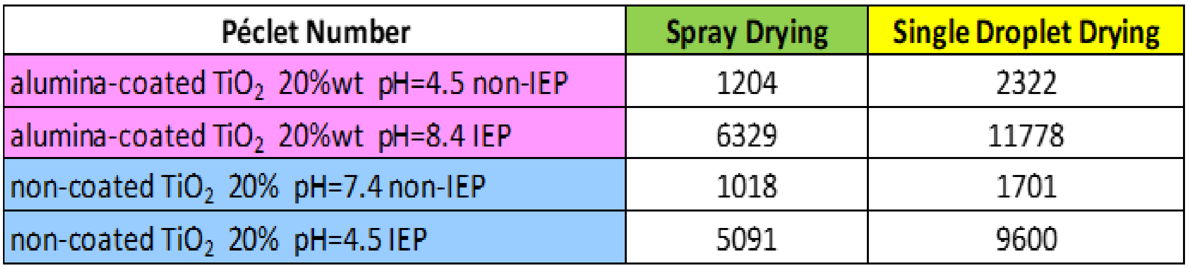

Péclet Number	Spray Drying	Single Droplet Drying
alumina-coated TiO_2 20%wt pH=4.5 non-IEP	1204	2322
alumina-coated TiO_2 20%wt pH=8.4 IEP	6329	11778
non-coated TiO_2 20% pH=7.4 non-IEP	1018	1701
non-coated TiO_2 20% pH=4.5 IEP	5091	9600

The calculated Péclet Numbers from spray drying and single droplet drying were not consistent due to the use of different estimation method as well as difference in drying experiment process conditions, such as drying gas velocity, droplet size and other variations between two techniques. The IEP systems were found to have greater Péclet because of the flocculated particle size contributed to a smaller diffusion rate which further resulted in a larger Péclet. Regardless of the calculation method been used, the Péclet remained much greater than 1 indicating a dominant evaporation phenomenon in both spray drying and single droplet drying process. This finding is in good agreement with arguments discussed in recent reports which concluded the dominance of droplet evaporation in the drying of a typical colloidal suspension. These reports quantitively demonstrated the diffusion rate of suspended particles can be negligible when compared to the significant evaporation rate (Lintingre et al., 2016, Lintingre et al., 2015).

5.3.2.2 Morphology Formation Mechanism

There are many reports discussing the morphology formation of a colloidal system via a spray drying route. Most of those discussions focused on the possible mechanisms for a buckled structure. These arguments mainly focused on the hydrodynamic effect of air to a droplet, the drying temperature, the droplet surface tension versus gravity or the estimation of drying associated Péclet (Cho, 2016, Iskandar et al., 2003, Miglani and Basu, 2015, Sen et al., 2009, Walker et al., 1999). However, recent studies by Lintingre et al. (2015) & (2016) and Tsapis et al. (2005) have demonstrated none of those effects is directly responsible for the buckling instability of a droplet. They identified the spray-dried morphology from a colloidal system is fully determined by the interaction forces between suspended particles in the droplet (Lintingre et al., 2015, Lintingre et al., 2016, Tsapis et al., 2005). Based on the research outcomes from those pioneers, the drying results from this study are further discussed and the mechanisms hypothesised for a buckled and a spherical morphology were fully illustrated in Figure 81.

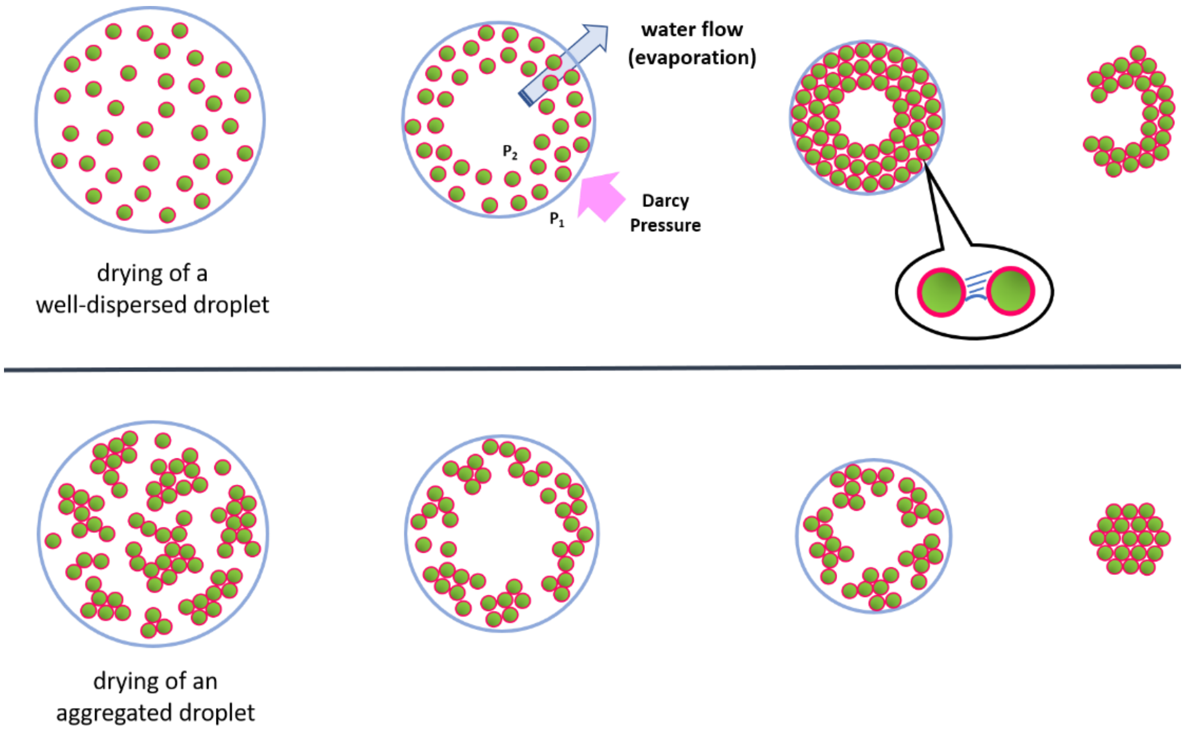

Figure 81 The schematic diagram of granule formation for: (top) buckled morphology; (bottom) spherical morphology. The associated Péclet for both well-dispersed and aggregated droplet are much greater than one

As schematised in Figure 81 (top), in the case of drying of a well-dispersed droplet system, an initial isotropic reduction in droplet size is observed. The droplet evaporation rate is much faster than the particles diffusion rate due to the estimated Péclet is much greater than 1 (Table 9). Therefore, most of the suspended particles are collected at the interface with air due to very rapid evaporation. These accumulated particles can further form a loosely packed shell near the interface. The water flow driven by evaporation through this particles shell is analogue to a fluid through a porous media. This generates a pressure difference across two sides of the shell. According to classic Darcy's law, the pressure difference can be defined as:

$$P_{Darcy} = \frac{\eta\, v}{k} h \tag{5.2}$$

where, P_{Darcy} is Darcy's pressure, η liquid viscosity, v relative velocity between liquid and shell, h shell thickness and k_p permeability of shell (Tsapis et al., 2005, Lintingre et al., 2016). The shell can be compared to a packing of particles with volume fraction $\emptyset_c$. Consequently, the shell permeability k_p can be expressed with the Carmen-Kozeny relation, written as (Tsapis et al., 2005, Lintingre et al., 2016):

$$k_p = \frac{a^2\, (1-\emptyset_c)^3}{45\, \emptyset_c^2} \tag{5.3}$$

where a is the radius of the particle. Remarkably, the permeability k is correlated with dispersed particle size, a (Lintingre et al., 2016). For a well-dispersed suspension, small particle radius leads to a low shell permeability which results in an enhanced Darcy stress which can overcome the electrical repulsive force between stabilised particles. Therefore, those loosely packed particles are compressed into a close-packed solid shell by the Darcy stress. The formation of such solid shell is the critical condition of subsequent buckling phenomenon. As the evaporation further continues, the water between neighbouring particles retracts to form a meniscus which is analogue to a capillary tube. The water capillary pressure across the meniscus can be expressed in Equation (5.4). The derivation of water capillary pressure equation is given in Appendix C.

$$P_{cap} = \frac{2\, \gamma}{R_{pore}} \tag{5.4}$$

where P_{cap} is the water capillary pressure, γ is the water-air interfacial tension and R_{pore} is the radius of the pore exists between neighbouring particles (also known as the radius of capillary curvature). The interfacial tension tends to pull the water outwards, as a result, the neighbouring particles move inwards. At the end of evaporation, the water meniscus is completely replaced with air to achieve a maximum capillary pressure which overcomes the threshold of the solid shell. According to Lintingre et al., the critical instability pressure P_{buckle} above which the solid shell starts to buckle can be estimated using a Zoelly-Van Der Neut formula (Timoshenko and Gere, 2009, Lintingre et al., 2016, Lintingre et al., 2015). Through the calculations based on the drying experimental results of two TiO_2 systems at the non-IEP condition, the maximum capillary pressure was identified to be one order magnitude larger than the critical buckling pressure in both TiO_2 systems (results shown in Table 10). Therefore, the buckling of a solid shell was observed as expected. The calculation details of the maximum capillary and the shell critical instability pressure are shown in Appendix C.

Table 10 Calculation summary of the critical buckling pressure of solid shell and drying associated maximum capillary pressure

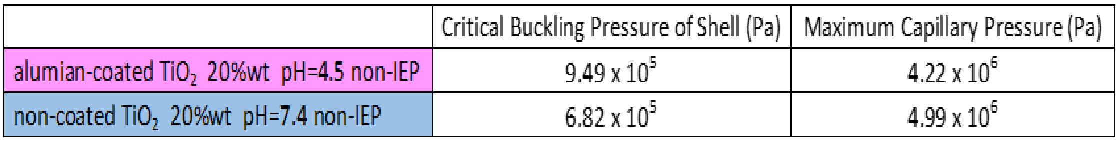

	Critical Buckling Pressure of Shell (Pa)	Maximum Capillary Pressure (Pa)
alumian-coated TiO_2 20%wt pH=4.5 non-IEP	9.49×10^5	4.22×10^6
non-coated TiO_2 20%wt pH=7.4 non-IEP	6.82×10^5	4.99×10^6

As schematised in Figure 81 (bottom), in drying a flocculated droplet system, the aggregated particles also accumulate near the interface due to Pe » 1 (shown in Table 9). However, this loosely packed shell formed from the accumulation of fractal aggregates has an increased permeability k because of its packing of aggregates - larger particle radius a is seen in Carmen-Kozeny relation (5.3). It will be difficult to form a solid and compacted particle shell due to increased permeability (leading to low Darcy pressure which provides less contribution to a solid shell formation). As evaporation continues, the system remains liquid like and the droplet with aggregates can only shrink in an isotropic manner. As a result, all aggreagtes compact to form a sphere progressively at the last stage of drying (Lintingre et al., 2016, Tsapis et al., 2005, Lintingre et al., 2015). It is noted that the use of aggregated suspensions for preparing alumina granules with a solid filled spherical structure was reported in past few years (Walker et al., 1999).

5.3.3 Effect of Droplet Size on Buckling Behaviour

In the last section, the formation mechanisms of spherical and buckled morphologies were illustrated above based on the experimental results and Lintingre's work which demonstrated that drying of a well-dispersed (non-IEP) system will results in a buckled morphology due to the capillary effect at the end of the drying process. However, when drying the non-coated TiO_2 slurry system at non-IEP condition, morphology inconsistency was observed. As outlined in Figure 82 below, a buckled morphology was observed in a single droplet drying experiment, whereas an unexpected spherical morphology was formed in the spray drying of the same slurry formulation. In contrast, a spherical morphology was always formed at IEP condition regardless of the drying technique.

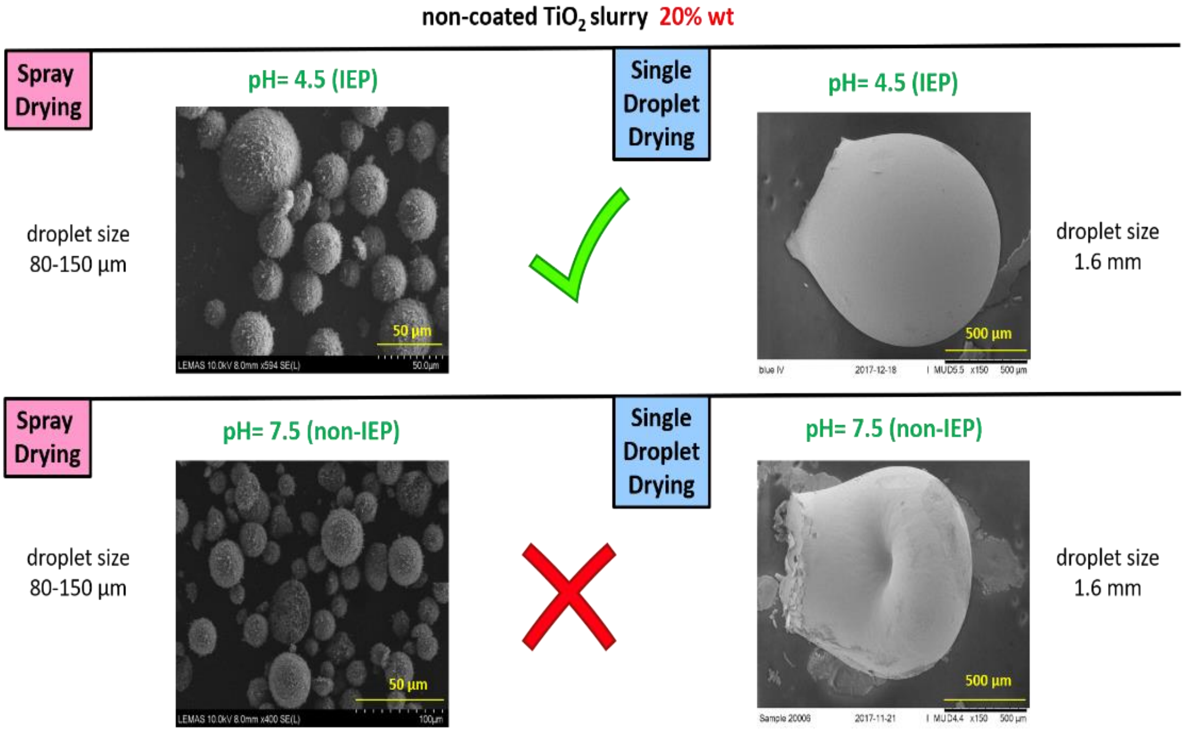

Figure 82 Morphology inconsistency from drying of non-coated TiO_2 slurry at IEP and non-IEP conditions using the spray drying and the single droplet techniques

Majority of morphology formation studies from literatures were conducted using different types of single droplet drying techniques, such as acoustic levitation, aerodynamic levitation, Leidenforsot effect, drying a droplet deposited on a hydrophobic surface or drying a droplet hanged on a filament (Lintingre et al., 2015, Lintingre et al., 2016, Yamamoto and Sano, 1992b, Perdana et al., 2011b, Toei et al., 1978, Yarin et al., 1997, Gandhi et al., 1996). However, none of those single droplet drying techniques is perfect for mimicking a spray drying process because the droplet size involved (in a range from few hundred micrometres to few centimetres) is much larger than the size of the atomised droplet from a real spray dryer (20-150 µm for the ProCepT unit). Apparently, there is a significant difference between the droplet size from a spray dryer and a single droplet drying rig. Therefore, in order to have a better understanding of the inconsistency in morphology forming behaviour at non-IEP condition, the single droplet drying experiment was repeated with varied droplet size (2.5, 1.0, 0.8, 0.5 and 0.4 µL respectively). The droplet size was carefully controlled and delivered by using a micropipette. Figure 83 and Figure 84 exhibit the results of repeated drying of 20%wt slurries at non-IEP condition for both alumina-coated and non-coated TiO_2 systems with varied droplet size. For each of the results, a montage of droplets was created by extracting the recorded drying video frames at 1 s interval. The droplet diameter was estimated using the ImageJ software based on a CE (Circle Equivalent) diameter definition. The initial droplet volume and equivalent diameter (CE diameter) at t = 0 s is marked in box of each image sets.

Figure 83 demonstrates the successful formation of a buckled structure for all droplet size studied. The buckling behaviour of the alumina-coated system was identified to be independent of the droplet size, which was consistent with observations from spray drying studies. In Figure 84, for the non-coated system, a buckled morphology can only be observed with the drying of larger droplets: 2.5, 1.0 and 0.8 µL. The drying of smaller droplets (0.5 and 0.4 µL) was found to end with a spherical granule. The removal of the final granule from filament for SEM assessment was attempted, but unfortunately, it was not successful due to its small size and fragile structure. The effect of droplet size on the morphology forming behaviour was found to be significant for the non-coated system.

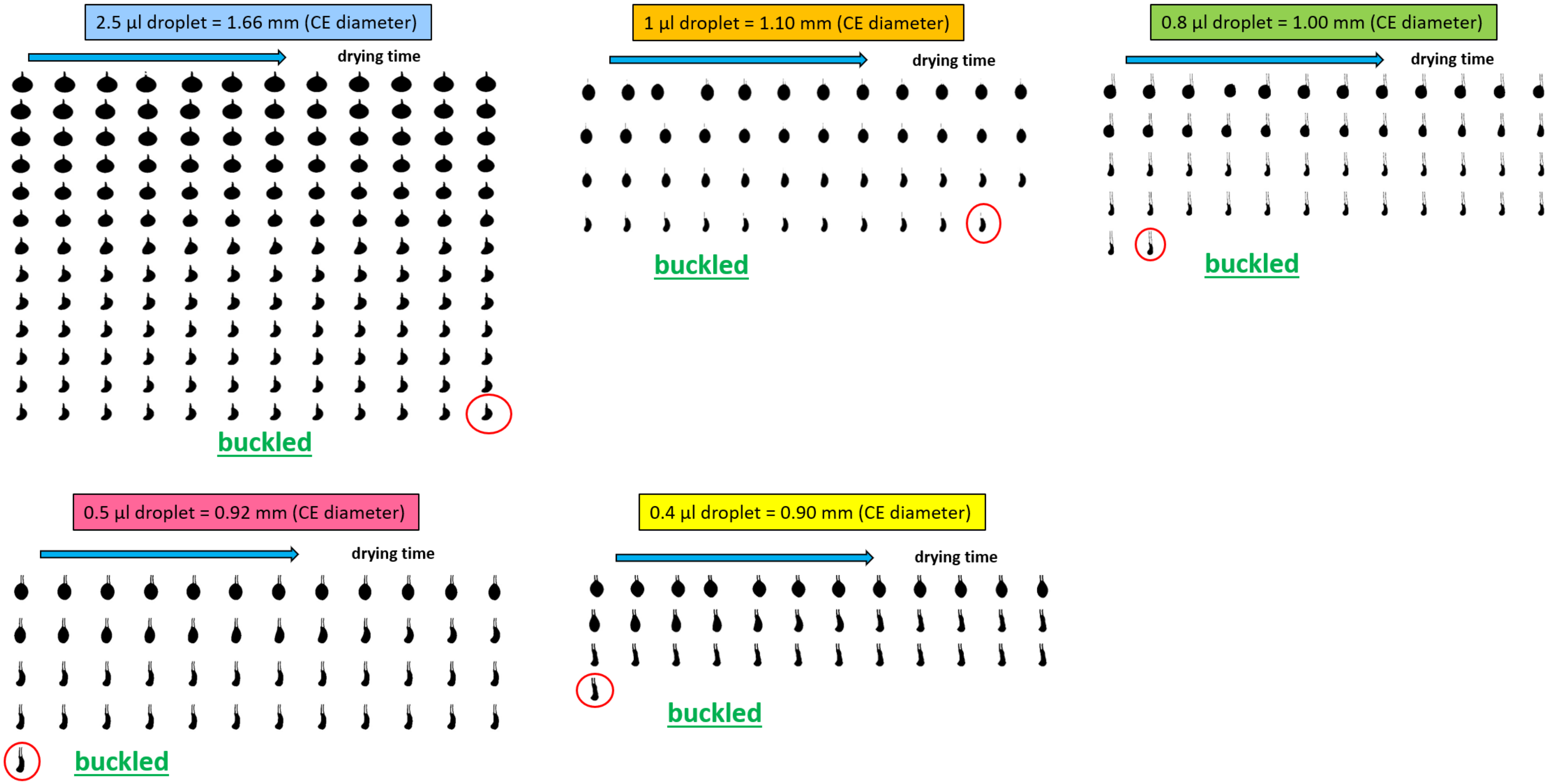

Figure 83 Results of single droplet drying of alumina-coated TiO_2 20%wt slurry at non-IEP condition with different droplet size (2.5 - 0.4 μL). Each individual frame shot was extracted from the recorded video at an interval of 1 second.

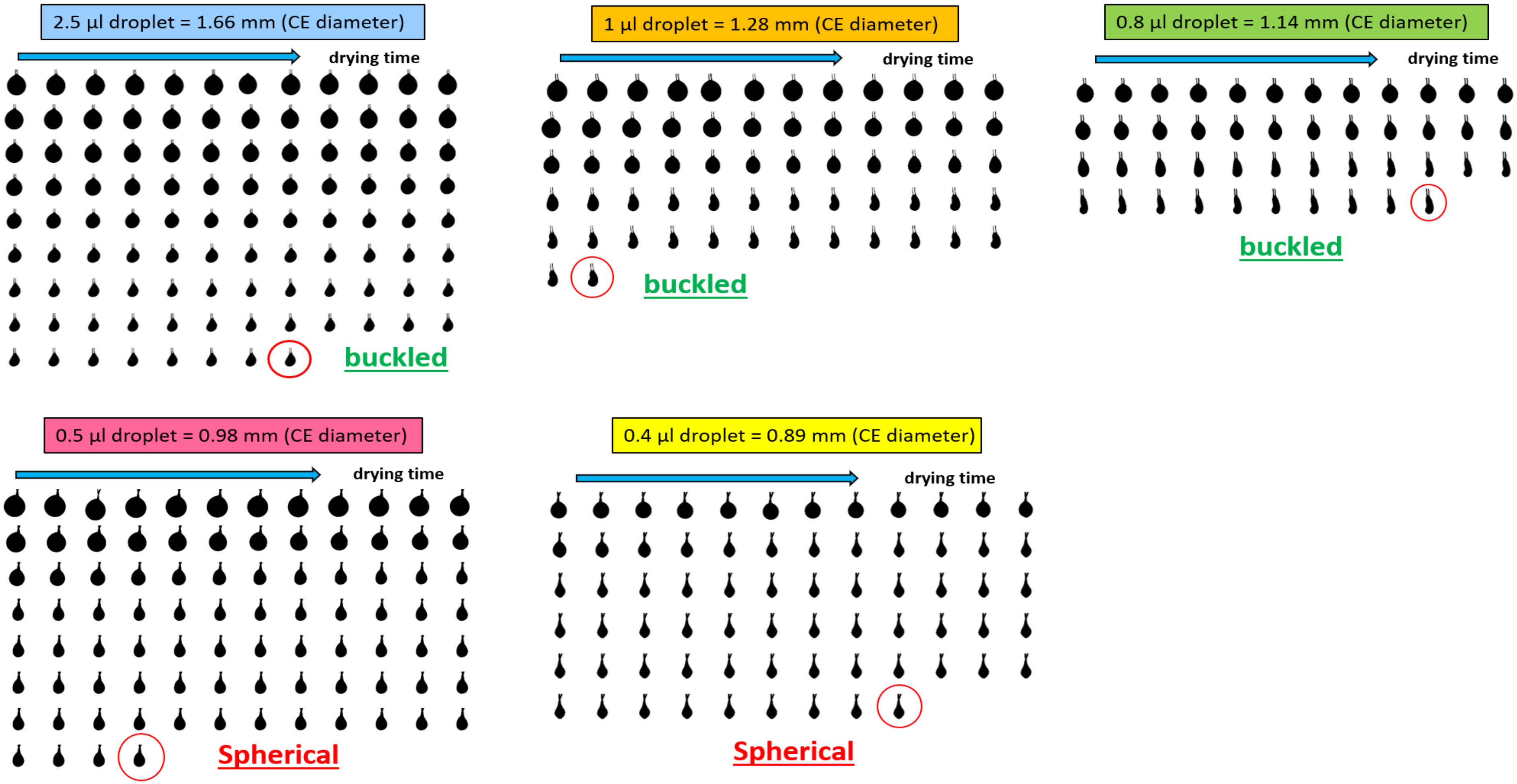

Figure 84 Results of single droplet drying of non-coated TiO_2 20%wt slurry at non-IEP condition with different droplet size (2.5 - 0.4 µL). Each individual frame shot was extracted from the recorded video at an interval of 1 second.

5.3.4 Estimation of Granules Hollowness

In the previous section of this chapter, the successful formation of a solid shell is identified to be the critical condition for subsequent buckling phenomenon. A solid particles shell also indicates the formation of a hollow structure. Therefore, the central void within a droplet can be closely related to the shell buckling. A notional term “Hollowness Index” was invented to quantitively estimate the magnitude of this central void for buckling predication. If a drying formed granule ends with a solid filled structure, the volume of this solid granule (without any central void) can be calculated by the total mass of solid particles in drying droplet divided by the bulk density of final granules (bulk density results can be seen in the Density section of Chapter 4):

$$volume\ of\ solid\ granule\ (without\ void) = \frac{mass\ of\ all\ particles\ in\ a\ droplet}{bulk\ density\ of\ drying\ formed\ granule} \quad (5.5)$$

In reality, as a drying formed granule may have a central void as the result of solid shell formation, the volume of such a granule can be estimated using the following equation:

$$Volume\ of\ granule\ (with\ central\ void) = \frac{4}{3}\pi\, r^3 \quad (5.6)$$

r is either droplet radius at the surface gelation point for a buckled morphology or the droplet/granule radius at the end of drying for a spherical morphology. The surface gelation point is known as the moment right before a droplet starts deforming from a perfect spherical shape. The surface gelation point can be identified from the results of the montage of droplet frames shown in Figure 83 and Figure 84. Examples of a droplet radius *r* determination are illustrated in Figure 85 below. For the buckled morphology (Figure 85 left), the surface gelation point occurred at 15 s. The droplet was found to deform at 16 s of drying time, so the droplet radius at 15 s was taken for its volume calculation. For the spherical morphology (Figure 85 right), the diameter of the last frame (t = 68 s) of montage was taken for value, *r*.

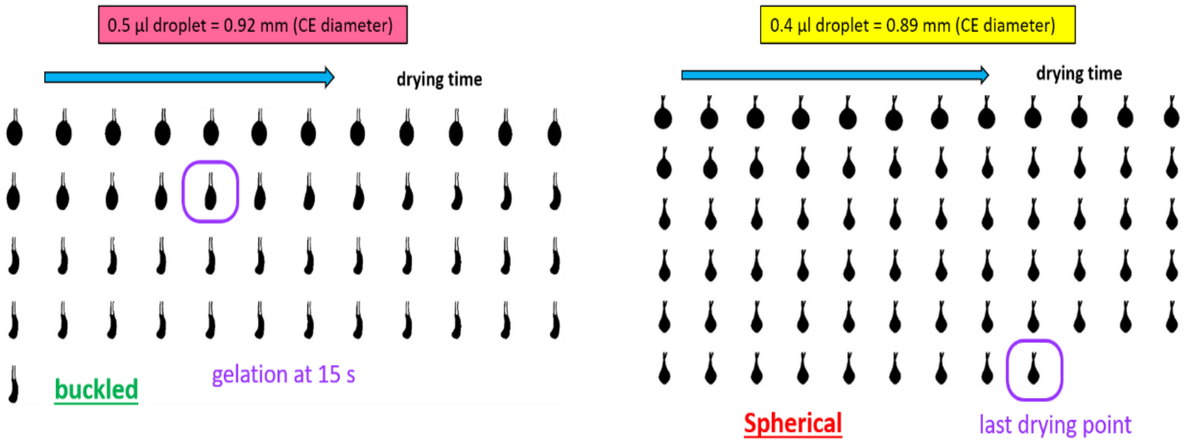

Figure 85 The determination of droplet radius *r* for: (left) a buckled morphology; (right) a spherical morphology.

The Hollowness Index was estimated using the equation shown in Table 11. The calculated Péclet Number and Hollowness Index of different droplet size for both two TiO_2 systems are summarised in Table 11. The associated graphical results that show the relationship between the Péclet Number and the Hollowness Index as a function of the initial droplet size are shown in Figure 86. Both two TiO_2 systems were found to have a clear increment trend in Péclet Number as the increased droplet size. High Péclet (>>1) indicated an accumulation of particles at the water/air interface, which provided a potential condition for shell formation. For the alumina-coated system, the effect of droplet size on the Hollowness Index was found to be minor, which explained the constant buckling phenomena observed from all droplet size. Whereas, very low Hollowness Indexes were seen in 0.4 and 0.5 µL droplet for the non-coated system. This implied an unsuccessful shell formation which further resulted in non-buckling behaviour found in the single droplet drying experiments.

$$Hollowness\ Index = \frac{volume\ of\ granule\ with\ void - volume\ of\ granule\ without\ void}{volume\ of\ granule\ with\ void} \tag{5.7}$$

Table 11 Summary of calculated Péclet Number and Hollowness Index

Initial Droplet Size (µL)	non-coated TiO_2 20%wt pH=7.4 (non-IEP)			alumina-coated TiO_2 20%wt pH=4.5 (non-IEP		
	Péclet	Hollowness Index	Mophology	Péclet	Hollowness Index	Morphology
2.5	1701	0.5151	buckled	2322	0.5666	buckled
1.0	1608	0.4655	buckled	1805	0.5298	buckled
0.8	1511	0.4201	buckled	1582	0.4797	buckled
0.5	612	0.0132	spherical	1514	0.4519	buckled
0.4	594	0.0096	spherical	1301	0.4475	buckled

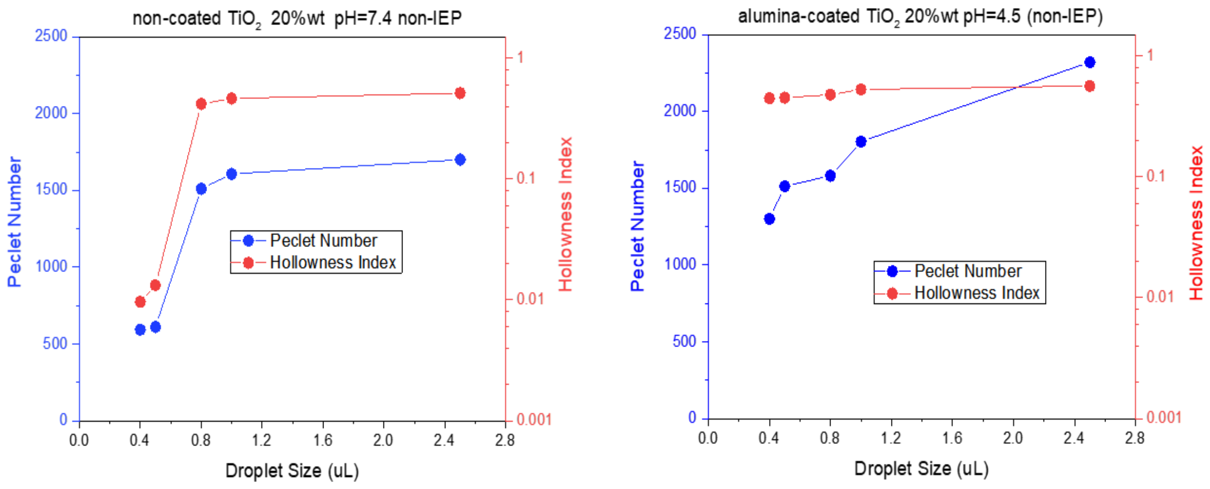

Figure 86 The relationship between Péclet Number and Hollowness Index as a function of droplet size for single droplet drying: (left) for the non-coated system; (right) for the alumina-coated system.

5.3.5 Yield Stress of High Concentrated Slurries

In the above two sections, a droplet buckling instability was identified to be related to its droplet size. Furthermore, the estimation of the Hollowness Index was found to be effective for distinguishing between a buckled and a non-buckled droplet/granule in terms of central void size. Both the experiments and the numerical calculations agreed with the formation of a less hollow structure in the drying of non-coated TiO_2 droplets with small droplet size (0.4 or 0.5 µL). However, in the drying of the alumina-coated TiO_2 system at non-IEP condition, a highly hollow granule was always formed regardless of its droplet size.

To gain a better understanding of the shell formation, rheological yield stress experiments on highly concentrated TiO_2 slurry which is analogous to the surface gelation of a droplet (under drying condition) were executed. The yield stress of slurries with a solid content of 40%wt, 50%wt, 60%wt and 70% from each of TiO_2

systems at non-IEP condition was characterised using an Anton Paar MCR-301 rheometer with a 1º 70 mm cone and plate geometry. The slurry under test was pre-sheared at 600 s^{-1} for 120 s and then rested for another 120 s prior to the test. The shear rate was ramped from 0.1 s^{-1} to 1000 s^{-1} at ambient in a logarithmical mode over 5 mins. The results of alumina-coated and non-coated TiO_2 slurries are shown in Figure 87. The yield stress of measured slurry was determined by plotting corresponding shear stress against the ramped shear rate and finding the intercept of curve on Y-axis (Macosko, 1994, Nguyen and Boger, 1992, Stokes and Telford, 2004).

Figure 88 outlines the measured yield stress value at each solid concentration level for both two TiO_2 systems. It shows that the non-coated system initially had a relatively high yield, but as solid content increased the yield of the alumina-coated system became dominant with a clear increasing trend. For the alumina-coated system, the high yield stress measured at the highest concentration (70%wt) demonstrates when the interface surface becoming enriched, there was a strong interaction between neighbouring particles due to the adhesive gluing effect of alumina coating (Xia et al., 2013). This indicates the formation of a very solid particles shell in the drying of a droplet with any size. In contrast, the non-coated TiO_2 particles accumulated near the interface were weakly associated due to the low yield stress. This may be because the phosphate dispersants anchored on pigment surface tend to re-disperse those accumulated particles. Thus, there was a resistance against the formation of a solid shell in a smaller sized droplet. Whereas, in a larger droplet, it was still possible to accumulate a thick shell containing a central void despite the interactions between particles are not strong. The created central hollowness can provide sufficient support for the subsequent buckling despite there was still a small number of mobile particles existing in the central void. The proposed schematic diagram of the shell formation for both two TiO_2 systems at the non-IEP condition is shown in Figure 89 below.

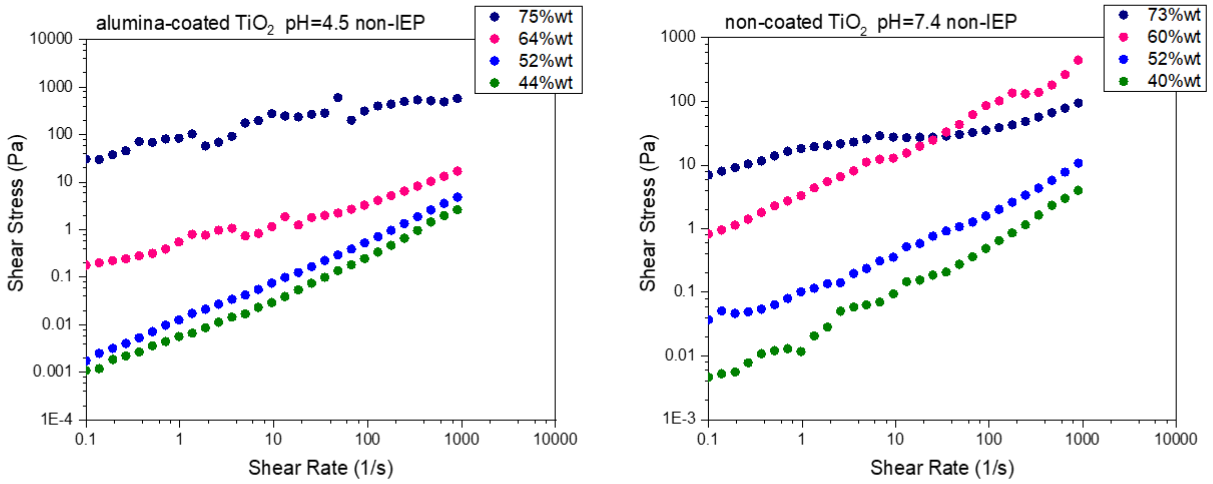

Figure 87 The yield stress measurements of TiO_2 slurries at different solid concentration: (left) alumina-coated system; non-coated system.

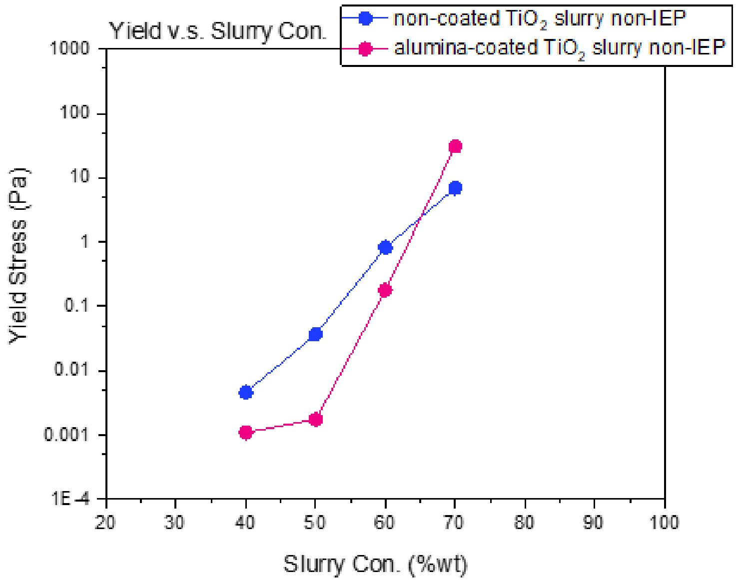

Figure 88 The rheological yield stress as a function of slurry concentration for both non-coated and alumina-coated TiO_2 systems

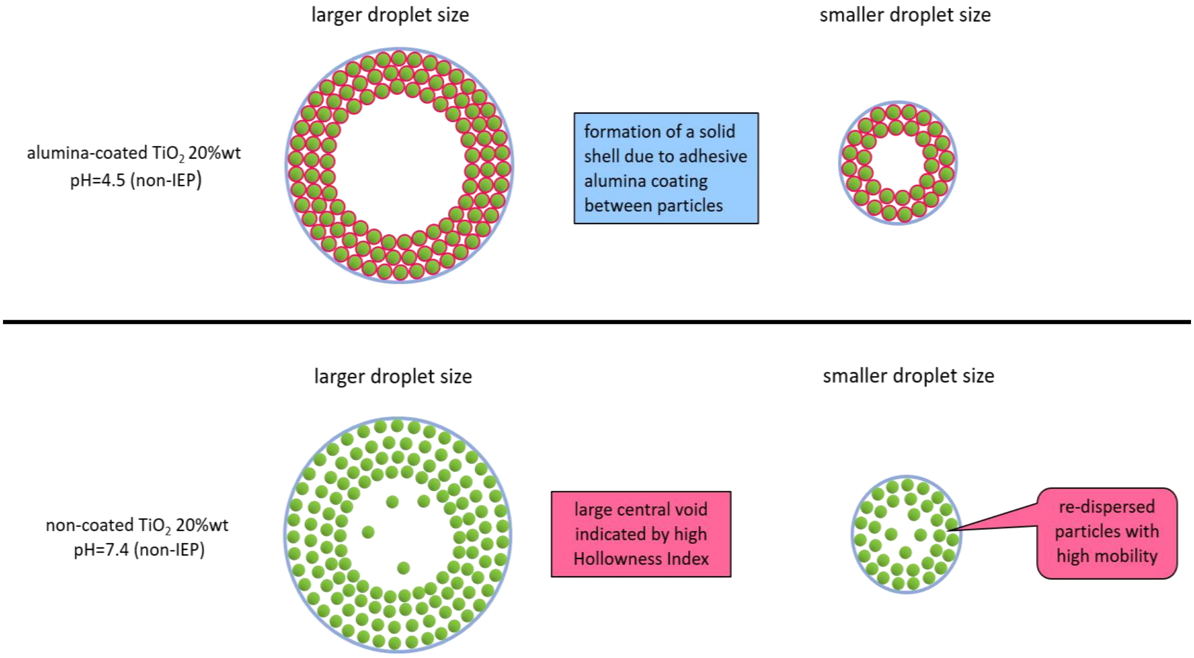

Figure 89 The proposed schematic diagram of the shell formation for both alumina-coated and non-coated TiO_2 systems at non-IEP condition

5.4 Conclusions

The 20%wt slurries at both IEP and non-IEP conditions from two TiO_2 particles systems were dried at 120ºC using a more controlled single droplet drying rig to verify the morphologies from spray drying experiment. For the alumina-coated TiO_2 system, a buckled morphology was found from drying of a droplet with well-dispersed particles, and a sphere was seen from drying of a droplet contained aggregates. These morphologies are consistent with observations from spray drying experiment. In fact, this alumina-coated 20%wt slurry at non-IEP condition contains large aggregates which were caused by the adhesive alumina coating layer. These aggregates in slurry were confirmed by the SEM, TEM and PSD characterisation shown in Chapter 3. However, the sedimentation test demonstrated a low gelation concentration (10%wt) for this system. This means the system is still colloidal stable at 20%wt concentration level due to the networking of gel. For the non-coated TiO_2 system, the trend of morphology formation was different from the observations from spray drying work. The well-dispersed droplet (at non-IEP condition) led to a buckled structure, while the aggregated droplet (at IEP condition). Different morphology was observed from drying of a “well-dispersed” non-coated TiO_2 slurry 20%wt using spray drying and single droplet drying technique. The Péclet number associated with different drying technique was calculated for both two TiO_2 systems. All Péclet numbers were much greater than 1, indicating the formation of the particle shell during the drying process. The structure formation mechanisms for spherical and buckled morphologies were proposed, and the formation of a solid particle shell and high hollowness are found to be the critical condition for structure buckling. Furthermore, the driving force for the shell buckling was numerically proved to be the capillary force. However, the mechanisms outlined cannot fully explain the spheres obtained from spray drying of non-coated TiO_2 slurry at non-IEP condition.

The droplet size effect on morphology was studied by drying the "well-dispersed" slurries (at non-IEP condition) from two TiO_2 systems using single droplet drying rig[1]. The hollowness of spray-dried granules prepared from drying of different droplet size was estimated. It was noted the alumina-coated granule has a high hollowness which implies the buckling is independent of droplet size. The high hollowness was indicated by the solid particle shell formed at Péclet condition (>> 1). The high rheological yield stress implies this solid shell has a strong particle-particle interaction which was also confirmed by the low gelation point of this system (particles in droplet tend to gel when solid content exceeds 10%wt).

For the non-coated system (at non-IEP condition), the hollowness of spray-dried granules is dependent on droplet size. Low hollowness index was found in the drying of smaller droplet (0.5 and 0.4 µL). The granular structure cannot buckle because there was no void formed in granule central which is not complying with the critical condition for buckling. In addition, the lower yield stress and the high gelation point indicated the particle shell formed at high Péclet condition for small-sized droplet had a weak structure. The particles accumulated at droplet interface were weakly associated due to the anchored phosphate dispersants which tend to re-disperse these particles into water and to provide resistance against the formation of a solid shell. A small droplet with a weak shell can only shrink isotropically to end up with spherical morphology. The droplet size generated by the spray dryer atomiser is much smaller than 0.4 µL, thus it was not surprising to see a spherical morphology.

---

[1] The aggregated slurries (at IEP condition) from two TiO_2 systems were not studied due to the consistency in spherical morphology from different drying techniques.

Chapter 6 Granule Structure Analysis and Mechanical Properties

6.1 Introduction

In this chapter, the studies are focused on the characterisation of the spray drying formed TiO_2 granules in terms of their internal structure. The granule internal structure was first analysed through the microtome sectioning, the BET specific surface area, dynamic vapour sorption, and porosity determination. Finally, the granule morphology was correlated with its internal structure and the associated mechanical properties to provide a vision of the overall engineering control though the spray drying approach.

6.2 Experimental

6.2.1 Materials

Granules fabricated from the spray drying of both alumina-coated and non-coated TiO_2 20%wt slurries[1] at IEP and at non-IEP conditions were used for specific surface area analysis, dynamic vapour sorption analysis, porosity and bulk compression tests. These spray-dried granules were named as followings according to the slurry formulation:

- alumina-coated 20%wt non-IEP
- alumina-coated 20%wt IEP
- non-coated 20%wt non-IEP
- non-coated 20%wt IEP

6.2.2 Methods

6.2.2.1 Microtome Sectioning Analysis

A microtome sectioning technique was first employed to explore the internal structure of drying formed products. For sample preparation, an epoxy type resin

---

[1] Granules fabricated from the spray drying of 20%wt were used for characterisations due to this solid content is relevant to Venator's lab-scale spray drying studies.

(25 g) was mixed a hardener (3 g) using an EpoFix kit (Struers Ltd, UK). The resulting mixture was then filled into a safe-lock microcentrifuge tube followed by the addition of a small amount of spray-dried powder. The fast-cure resin polymerised to become solid over 24 hours. The plastic tube was peel-removed and the solid resin block containing embedded granular powder was carefully sectioned using a Reichert Jung Microtome device to allow a SEM access to the cross-section of the embedded granules (setup detail shown in Figure 90).

Figure 90 Images of the EpoxyFix kit and the microtome sectioning setup

6.2.2.2 BET Specific Surface Area Analysis

The specific surface area of spray-dried granules was determined using a Nova 2200 surface analyser from Quantachrome Instruments (Figure 91) based on the popular Brunauer-Emmett-Teller (BET) method. Approximate 0.1 - 0.2 g of powder sample was filled into a long glass tube and weighted out the total mass. The glass tube was placed in a heating mantle for degassing under vacuum at 230ºC for 3 hrs to remove moisture and other contaminants from the sample surface. The sample tube was re-weighted to determine the accurate sample mass after the degassing process. The glass tube with the sample was then transferred to the analysis chamber and cooled to -196ºC using a Dewar with liquid nitrogen-filled in for maximum gas adsorption (gas-solid interaction can be improved at this low temperature). The nitrogen gas was injected/repelled stepwise into/from the glass cell by controlling the partial pressure for the adsorption and the desorption processes. The helium gas was also used for calibrating the dead volume of glass tube due to its non-adsorption behaviour to sample. The specific surface area of sample was calculated from the intercept and slope of the BET plot which was drawn by plugging the isotherm data (over partial pressure range of 0.04 to 0.3) into the classic BET equation. (Barron, 2019, Gardy, 2017, Gregg, 1982, Rouquerol, 2013).

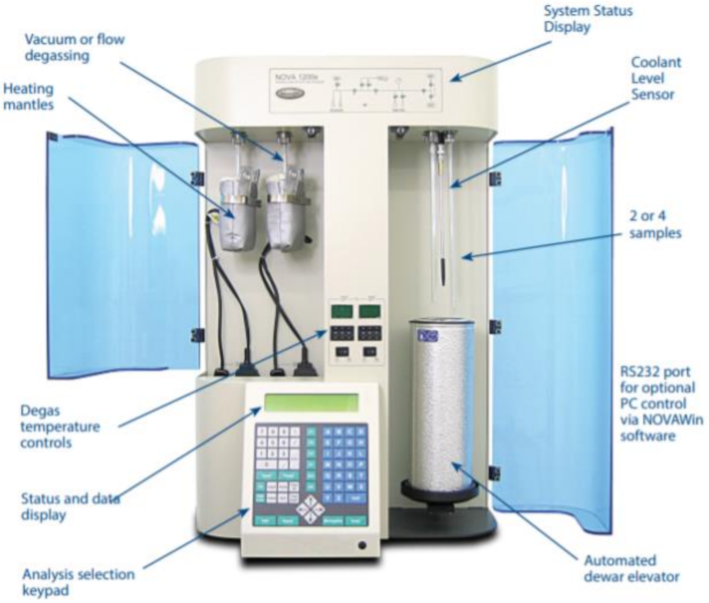

Figure 91 The Quantachrome Instruments Nova-2200 Surface Analyser (QuantachromeInstruments, 2018)

6.2.2.3 Dynamic Vapour Sorption Analysis

The hygroscopicity of the spray-dried granules was determined by using a gravimetric sorption technique – a DVS Advantage Analyser from Surface Measurement Systems, UK (Figure 92). In dynamic vapour sorption (DVS) measurement, the powder sample was placed in a pan which is balanced by another reference pan. Both two pans are connected to an ultra-sensitive microbalance for mass change monitoring. The moisture concentration surrounding the powder was varied precisely by using a dry and saturated (with water) nitrogen gas mixture to achieve a required relative humidity (RH). For the experiment setup, the RH was raised from 0% to 90% in an increment of 5% for the adsorption process. The following desorption process was programmed from 90% back to 0% in a 5% decrement. At each of relative humidity segment, the equilibrium mass change (dm/dt) was set to 0.006 %/min (the threshold for moving onto next RH step). The corresponding sample mass change throughout the adsorption and desorption process was recorded.

Figure 92 The DVS Advantage analyser from Surface Measurement Systems (Surface-Measurement-Systems, 2018)

6.2.2.4 Porosity

A high-resolution Focus Ion Beam Scanning Electron Microscope (FIB-SEM Helios G4 CX Dual Beam) was used to vaporise/mill and exam the porosity of drying formed TiO_2 granules. Due to the high cost for this technique, only granules prepared from spray drying of the TiO_2 slurries at IEP conditions were studied. Prior to the start, the powder sample for analysis was coated with 30 nm thick radium to minimise the charging effect during SEM scanning. The coated sample was subsequently transferred into the instrument chamber for vacuumisation treatment. After that, a 30 µm sized granule was selected (mean size of spray-dried granules, which is representative for the whole population) and marked with a platinum protective coating layer on its surface to ensure a clear cutting edge (Figure 93). A gallium ion beam was used to vaporise/mill half of the granule along the marking line to create access to the cross-section area for SEM scanning.

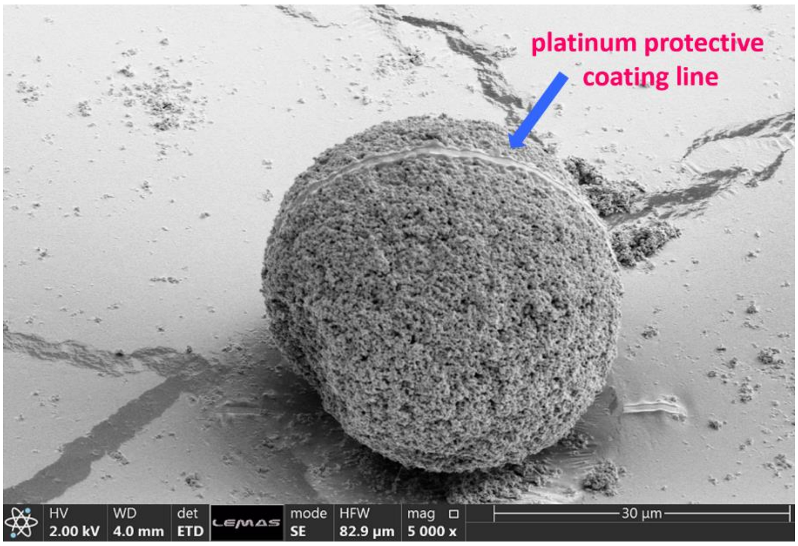

Figure 93 Example of a TiO_2 granule marked with platinum coating line for FIB-SEM

6.2.2.5 Bulk Compression

The compressibility of spray-dried samples was determined by using an INSTRON mechanical universal testing system (INSTRON, UK). The spray drying (of 20%wt slurries) formed powder were carefully filled into a metal die (height: 25 mm; inner diameter: 10 mm) up to the top edge (Figure 94). A 5-Newton load was installed, and the rate of force loading was set to 0.1 mm/min. The piston for compression was lowered to a position where the piston was just about to contact the top layer of powder. The load was balanced to zero prior to the start. After the test, the volume change (ΔV) of power due to the compression was calculated from the extension (powder interface) change and plotted against the applied loading force.

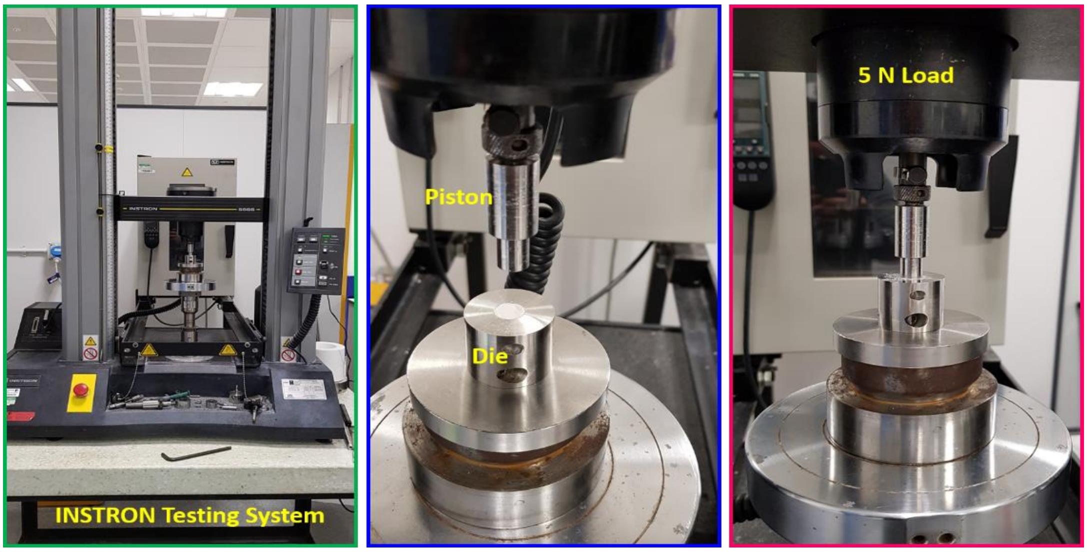

Figure 94 INSTRON Mechanical Universal Testing System

6.3 Results and Discussions

6.3.1 Microtome Sectioning Analysis

The cross-section SEM of the embedded granules from two TiO_2 systems are shown in Figure 95 and Figure 96 respectively. Regardless of the type of TiO_2 system being dried and the external morphology formed, all the spray-dried granules exhibited a solid internal structure. In chapter 5, the morphology forming mechanisms were illustrated in detail: a spherical morphology was caused by the isotropic shrinkage of a droplet; a buckled morphology was initiated with the accumulation of particle shell followed by the structure buckling under the capillary force. In either case, it was clearly illustrated the granule will end with a solid filled structure which was in accordance with the SEM observations on the cross-sections of embedded granules.

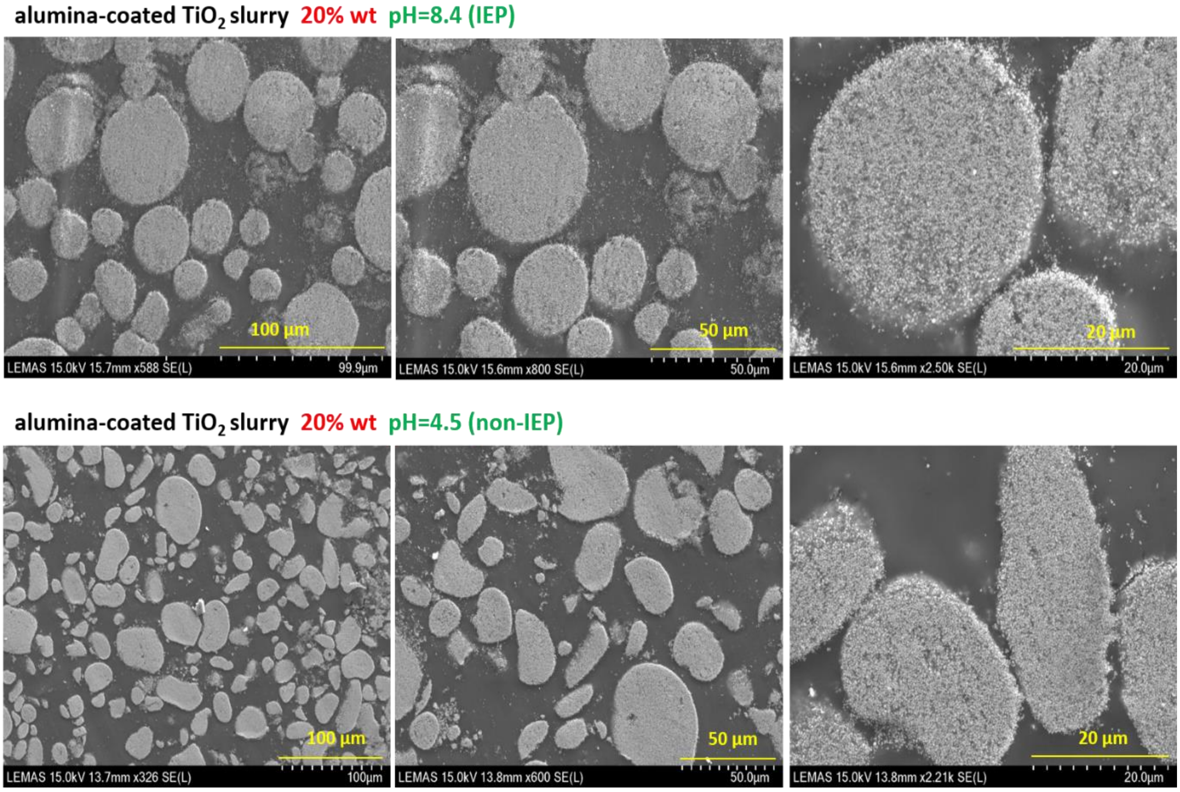

alumina-coated TiO_2 slurry 20% wt pH=8.4 (IEP)

alumina-coated TiO_2 slurry 20% wt pH=4.5 (non-IEP)

Figure 95 The cross-section SEM of the embedded alumina-coated TiO_2 granules: (top line) were fabricated from spray drying of IEP slurry; (bottom line) were fabricated from spray drying of non-IEP slurry.

non-coated TiO_2 slurry 20% wt pH=4.5 (IEP)

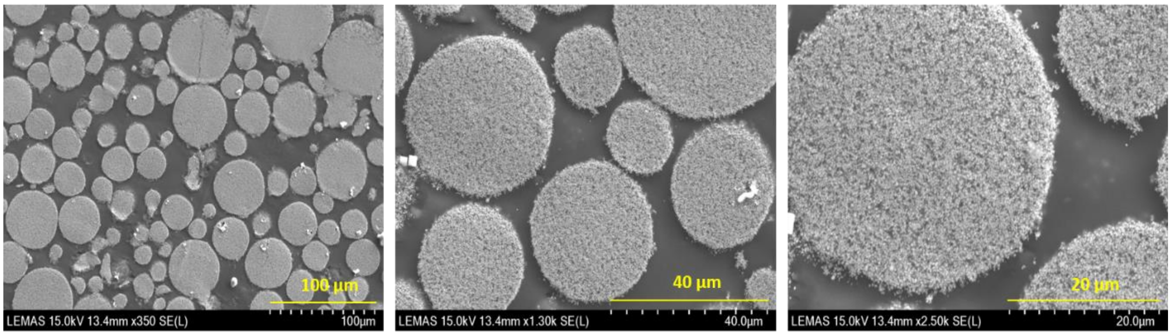

non-coated TiO_2 slurry 20% wt pH=7.4 (non-IEP)

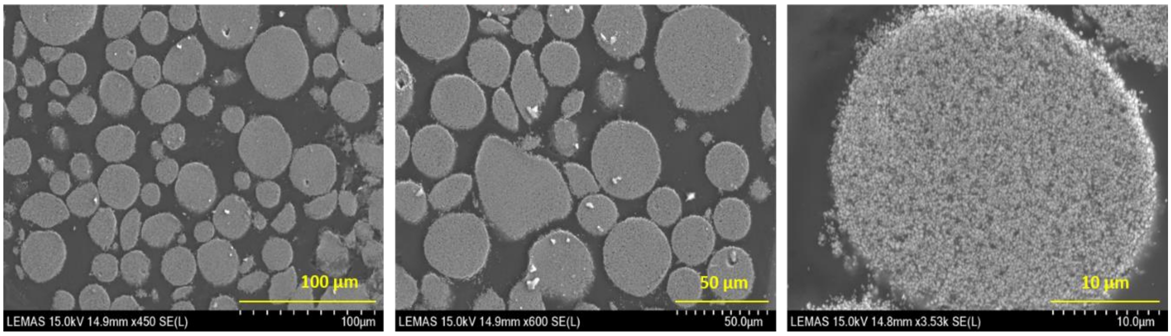

Figure 96 The cross-section SEM of the embedded non-coated TiO_2 granules: (top line) were fabricated from drying of IEP slurry; (bottom line) were fabricated from drying of non-IEP slurry.

6.3.2 Specific Surface Area Analysis

The microtome sectioning studies demonstrated a possible similar solid filled internal structure for the granules prepared from spray drying of the non-coated and the alumina-coated TiO_2 systems. In order to distinguish between the structure from two systems, the BET specific surface area of spray-dried granules was determined through the nitrogen gas adsorption measurements. The relationship between the amount of nitrogen gas adsorbed onto the solid surface as a function of relative pressure is shown in Figure 97. According to the IUPAC (International Union of Pure and Applied Chemistry) classification of gas adsorption (Figure 98), both the alumina-coated and the non-coated granular systems were characterised to be the type III physisorption isotherm which features a concavity shape over the complete P/P_0 range (Rouquerol, 2013, Sing, 1985, Brunauer et al., 1940). This type of isotherm corresponds to multi-layers adsorption. The initial adsorption at small relative pressure region is low due to the weak interaction force (Van der Waals) between the solid adsorbent and the gas adsorbate. Nevertheless, progressive gas adsorption is initiated after the adsorption of first gas molecules onto the solid surface due to the promoted interaction force between gas adsorbates. Thus, a concave-shaped isotherm is formed (Gregg, 1982).

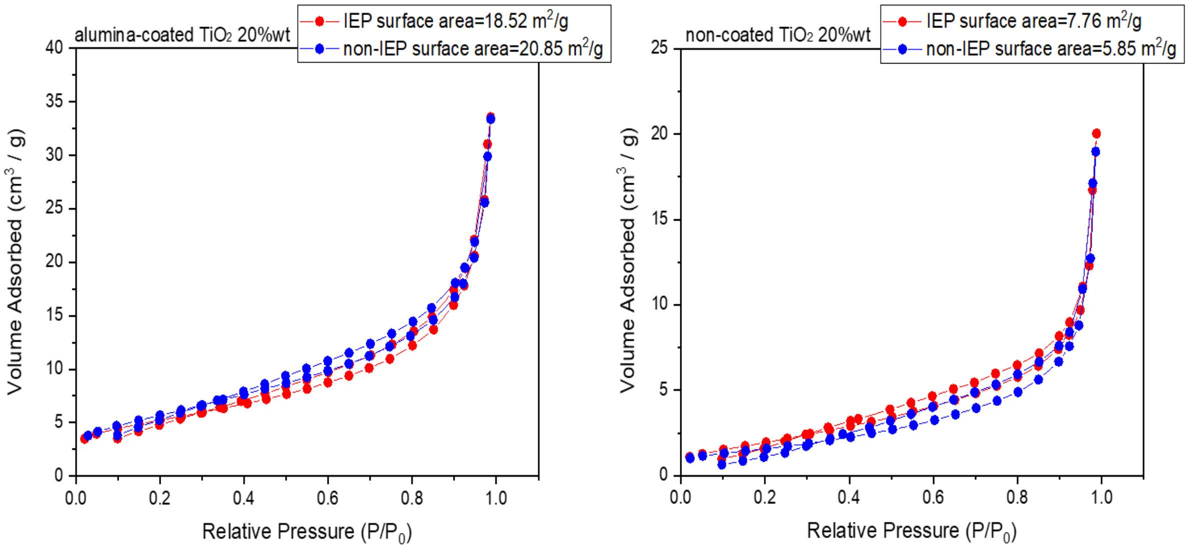

Figure 97 Nitrogen adsorption isotherms of TiO_2 granules: (left) fabricated from spray drying of alumina-coated slurries at IEP and non-IEP; (right) fabricated from spray drying of non-coated slurries at IEP and non-IEP.

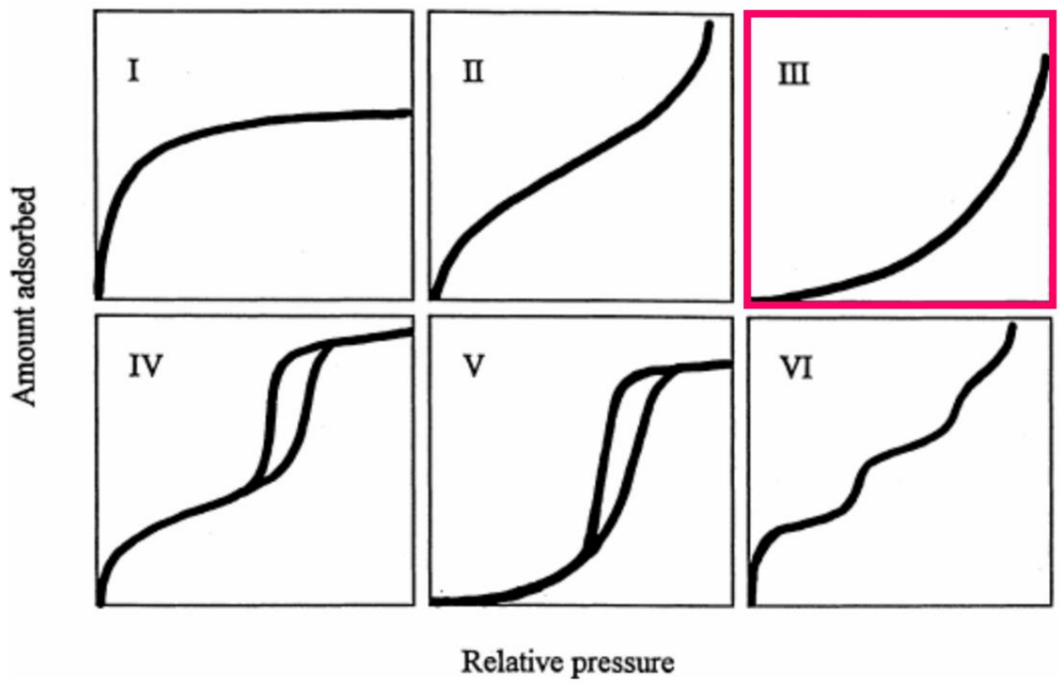

Figure 98 The IUPAC classification of gas adsorption isotherms (Donohue and Aranovich, 1998)

Figure 97 demonstrated low BET specific surface area values (5.85 and 7.76 m^2/g) for those non-coated TiO_2 granules when comparing with the alumina-coated TiO_2 granules (18.52 and 20.85 m^2/g). For any type of TiO_2 systems, the effect of slurry pH on the BET surface area of spray-dried granules was found to be minor. This is because the specific surface area is actually an intrinsic property. It is only related to the material type, but not to the morphology or shape of this material (Rouquerol, 2013). The measured specific surface area values for non-coated system were found to be consistent with the reported results of similar type of TiO_2 materials (Austin, 2019, Patchaiyappan et al., 2016). For the alumina-coated granules, the measured specific surface area values were 18.52 and 20.85 m^2/g (IEP and non-IEP respectively) which were similar to the value of 19 m^2/g from the literature report of 3%wt alumina + 1%wt silica coated TiO_2 granules (Siwinska-Stefanska et al., 2008). This literature report proved the aluminium oxide coating can significantly increase the specific surface area of TiO_2 granules due to the rough surface created by boehmite material. This founding was in a good agreement with the TEM observations of rough boehmite coating on particles surface (shown in Chapter 3).

6.3.3 Dynamic Vapour Sorption Analysis

The DVS isotherms of spray-dried TiO_2 granules are shown in Figure 99. The alumina-coated system was found to have a low moisture uptake (< 2%wt) at the 90% relative humidity level (or relative pressure) when compared against the 4.5%wt moisture uptake for the non-coated system. The low moisture uptake was caused by the boehmite surface coating which was confirmed by the BET surface analysis and the TEM images. In literature, boehmite was reported to have a poor wetting ability (super-hydrophobic property) as its rough surface (a rough surface is usually very hydrophobic) (Ji et al., 2016, Fang et al., 2009). Similar isotherms were found for the IEP and the non-IEP granules, indicating those granules have similar internal structures despite the apparent difference in external morphology.

For the non-coated system, a significant hysteresis loop was seen between 50%-80% relatively humidity (relative pressure) in isotherms for both IEP and non-IEP granules. According to IPUAC, this large hysteresis loop was characterised to be the Type H-1 (or Type A) hysteresis which is symbolic of spheroidal agglomerates with narrow size distribution (Gregg, 1982). The non-coated TiO_2 particles with a rutile crystal structure are hydrophobic in nature, but the phosphate dispersant anchored on the particle surface is hydrophilic with high water affinity. In the adsorption step, sharp water uptake was seen after the formation of a monolayer due to those phosphate dispersants. In the followed desorption step, these hydrophilic species possibly hold water molecules to delay the desorption path. Furthermore, the hysteresis over the range of $P/P_0 = 0.5 - 0.8$ fell into a capillary condensation region where vapour can condense into liquid to form binding to solid surface. This capillary condensation phenomenon may also contribute to the hysteresis loop (Lagoudaki and Demertzis, 1992). In order to verify these possible causes of the hysteresis seen in the isotherms of non-coated system, a further DVS test was performed on the granules prepared from the spray drying of “neat” TiO_2 slurry (TiO_2 particles without any dispersants or coating on surface which is referred as non-coated, undosed TiO_2). The isotherms of non-coated, undosed TiO_2 granules were shown in Figure 100. It exhibited isotherms without any hysteresis for both IEP and non-IEP samples. Therefore, the cause of hysteresis was identified to be the phosphate dispersants anchored on the pigment surface.

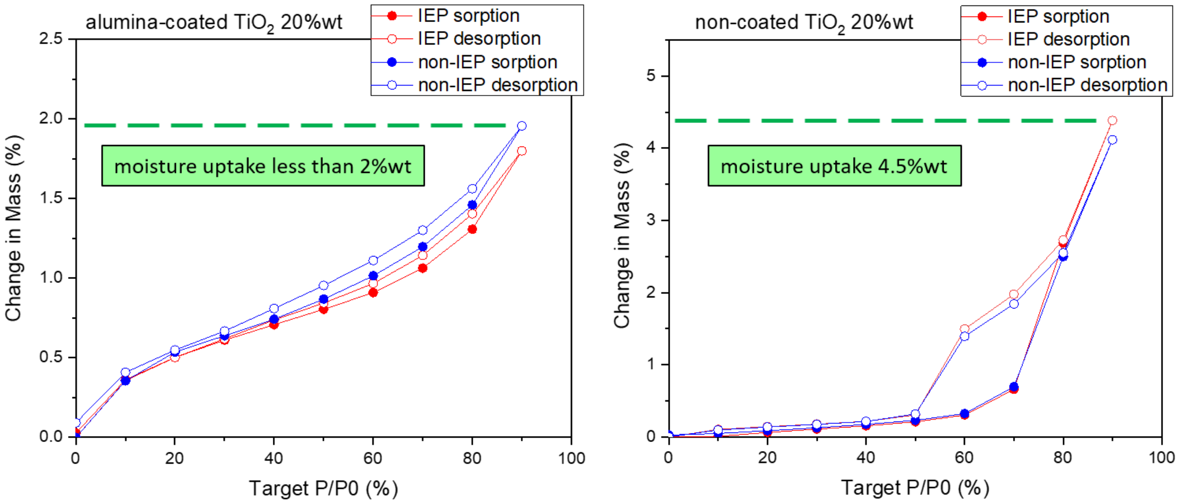

Figure 99 Equilibrium moisture sorption and desorption isotherm of TiO_2 granules: (left) fabricated from spray drying of alumina-coated system; (right) fabricated from spray drying of non-coated system

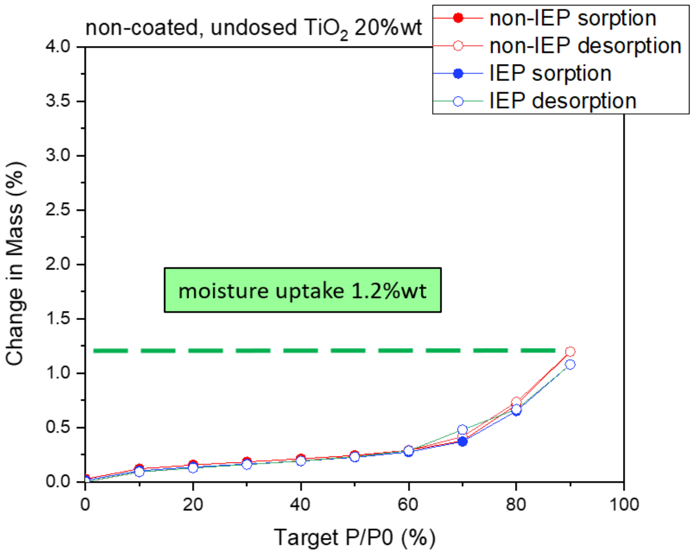

Figure 100 Equilibrium moisture sorption and desorption isotherm of spray-dried non-coated, undosed TiO_2 granules

6.3.4 Porosity

For each type of two TiO_2 systems, the microtome sectioning, BET surface area, and DVS studies have demonstrated a similar internal structure for the IEP and the non-IEP granules. Because of this, only spherical granules fabricated from the spray drying of IEP slurries were used to represent each TiO_2 system. Figure 101 and Figure 102 show the FIB-SEM results of spray-dried TiO_2 granules from the alumina-coated and the non-coated systems respectively. The visual assessment on the cross-section area indicated a similar porosity for the granules from two systems.

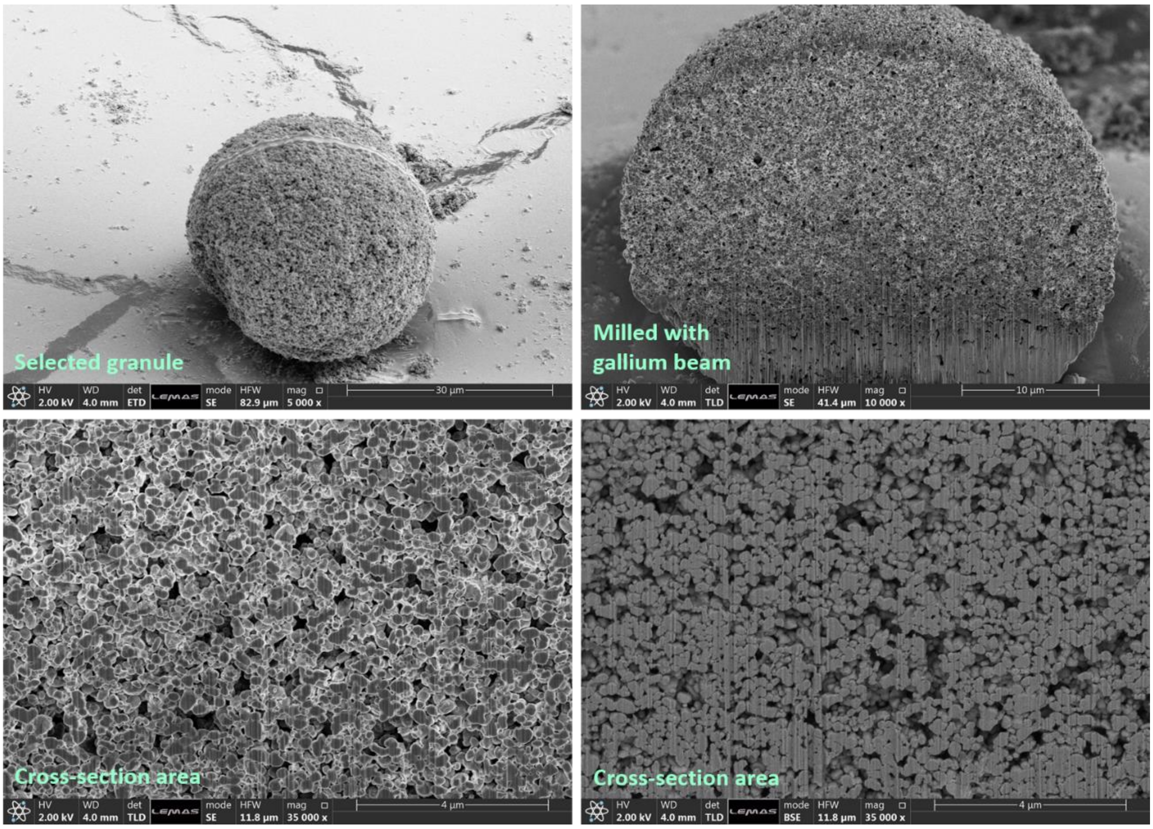

Figure 101 FIB-SEM of spray-dried alumina-coated TiO_2 granule (from drying of IEP slurry)

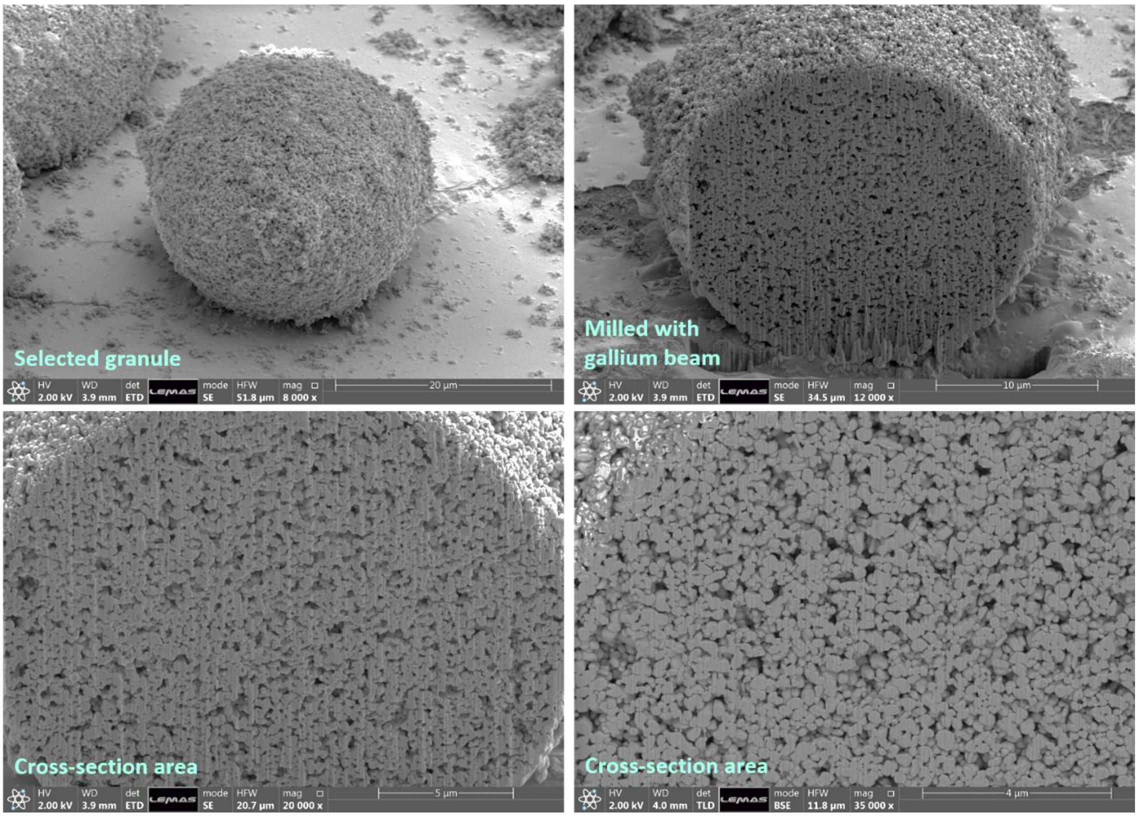

Figure 102 FIB-SEM of spray-dried non-coated TiO_2 granule (from drying of IEP slurry)

6.3.5 Bulk Compression

Figure 103 shows the relationship between the compressed volume (ΔV) and the applied force for spray-dried TiO_2 granules. The non-coated system was found to be more compressible than the alumina-coated system by comparing the slope of curves. The volume change of powder under compression was possibly caused by the rearrangement (voids between particles) and/or the breakage of granules (Patel et al., 2006, Çelik, 2016, Kawakita and Tsutsumi, 1966). In order to verify this, the compressed granules were carefully collected from the top layer of powder in the die for SEM examination. Figure 104 exhibits the SEM images of compressed granules from the INSTRON test. None of those compressed samples were found to have any breakage or cracking. This actually proves the volume change (ΔV) was completely caused by the rearrangement of particles. The resulting compressibility was found to be in good agreement with the compressibility index (%) calculated through tapped density (results given in Chapter 4). Within each system, slurry pH was proved to insignificant effect on the compressibility. Nevertheless, the non-coated system was identified to be more compressible (in bulk) due to its higher cohesiveness which was confirmed by the angle of repose studies shown in Chapter 4.

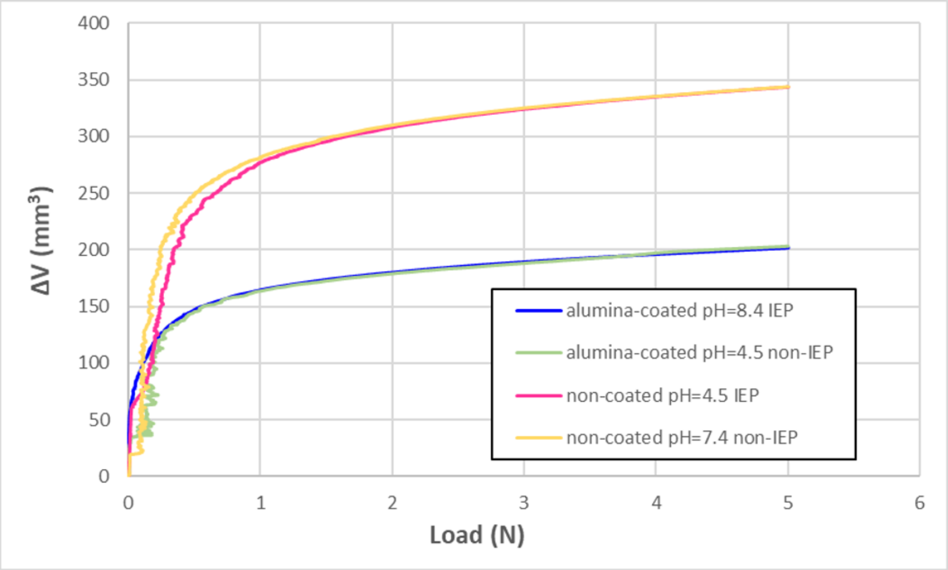

Figure 103 The relationship between the volume change and the applied load for 4 spray-dried TiO_2 samples

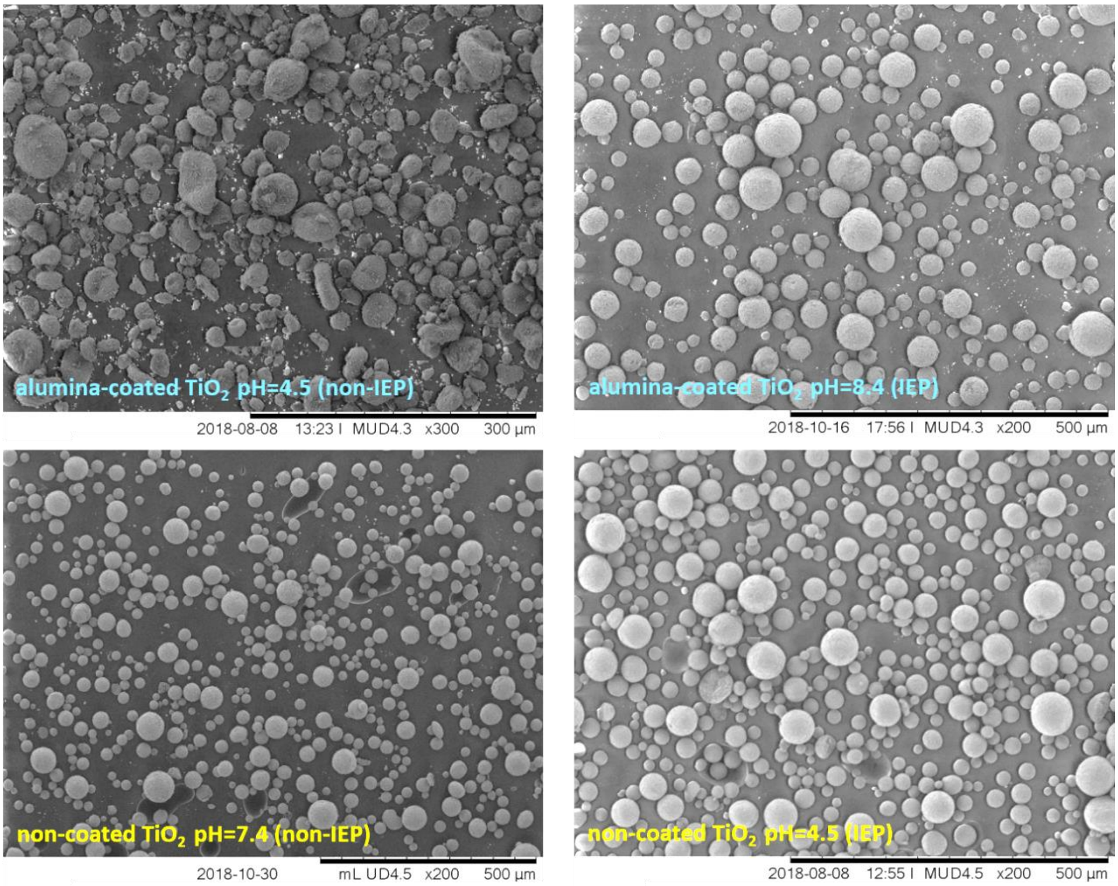

Figure 104 The SEM images of the piston compressed TiO_2 granules

6.3.6 Conclusions

In summary of the granule internal structure analyses discussed in this chapter, the microtome sectioning work demonstrated all spray-dried granules exhibited a similar solid internal structure regardless of TiO_2 type and the external morphology formed. The surface area analysis also confirmed a consistent surface structure for granules from the drying of IEP and non-IEP slurries. The surface structure of a spray-dried granule was proved not affected by its external morphology. The alumina-coated granular system was found to have a higher BET specific surface area due to the rough boehmite coating. Both the alumina-coated and the non-coated granular systems were characterised to be the type III physisorption isotherm which corresponds to multi-layers adsorption. According to IUPAC, this type of isotherm features a weak gas-solid interaction, but a strong lateral interaction between adsorbed gas over the complete P/P_0 range (Gregg, 1982, Rouquerol, 2013).

In DVS studies, the slurry pH was further proved to be less important to the internal structure of spray-dried granules. It was found that both two granular TiO_2 systems had low moisture uptake which indicated a dense particle structure prepared form spray drying. The hydrophilic sodium hexametaphosphate dispersants anchored on pigments surface played an important role in improving the moisture uptake and delaying the water desorption process.

Representative spray-dried granules from each TiO_2 system were cut and examined using a high-resolution FIB-SEM technique. The visual assessment on the cross-section area indicated a similar porosity for the granules from two TiO_2 systems. This finding implies the drying can lead to a similar porosity and internal structure for spray-dried granules from two TiO_2 systems, but the moisture uptake behaviour for non-coated and alumina-coated granules are still slightly different. The sodium hexametaphosphate dispersant on non-coated particle surface can improve the moisture adsorbing and holding abilities. IN the bulk compression test, none of these spray-dried granules was found to have any breakage or cracking, which was confirmed by the SEM examination. This indicates 5 N load was not enough for breaking these granules and also proves the volume change (ΔV) observed from compression curves was completely caused by the rearrangement of particles under compression. The non-coated TiO_2 granules were found more compressible. This was caused by their high cohesiveness which was identified by the AOR test shown in Chapter 5.

Chapter 7 Conclusions and Future Work

7.1 Conclusions

Using a spray drying method to engineer particles with controllable structure has drawn tremendous attention. It is important to understand the correlation between the material colloidal properties, drying process conditions, spray-dried granule morphology and associated structure properties. In particular, there is a need to highlight the key mechanism driving the structural transformation in colloidal droplet. In this study, comprehensive experimental studies have been carried out which covers the colloidal characterisation of different TiO_2 materials, influence of slurry formulation and drying process on the granule properties, morphology control via single droplet drying and spray-dried granule structure analysis.

A comprehensive literature review on topic of TiO_2 pigment manufacture process, particle-particle interaction in a colloidal system, spray drying, structure development during the drying process and morphology control were completed to gain substantial background knowledge and to be clear with the research opportunities for this study.

In summary of slurry characterisation work, The non-coated TiO_2 samples were analysed using X-ray powder diffraction for crystalline phase identification. The peaks obtained in the diffraction pattern confirmed its rutile phase and high sample purity. SEM analysis was used to investigate primary particle size and shape for two TiO_2 systems. The SEM images showed a large portion of primary particles are ellipsoidal shaped with a size range of 300±100 nm (Ferret diameter) for the non-coated TiO_2 particles. By contrast, the alumina-coated TiO_2 pigments are irregularly shaped aggregates with a size range of 2-10 µm under SEM. The observed particle structure from SEM was further confirmed using more powerful TEM. The TEM images also showed the presence of loose flocculant layer on pigment surface. The EDX analysis of elements distribution across the particle surface and the XPS spectra measured by other researchers (Li, et al. 2012) identified the loose surface layer to be boehmite type alumina.

The surface charge measurements indicated the iso-electric point at which particles start to strongly aggregate are pH 4.5 and pH 8.4 for the non-coated and the alumina-coated system respectively. These results provided a guide for manipulating the particle-particle interaction in two colloidal systems. In the non-coated TiO_2 system, pH 4.5 (IEP) was used to represent a well-dispersed slurry and pH 7.4 (non-IEP) was used to represent an aggregated slurry. For alumina-coated TiO_2 system, pH 8.4 (IEP) and pH 4.5 (non-IEP) are selected for a well-dispersed and an aggregated slurry respectively. The purpose of formulating slurries in this way is to distinguish between IEP and non-IEP slurries in terms of colloidal stability.

The particle size distribution (PSD) of non-coated TiO_2 system indicated the presence of large aggregates at IEP with D(50) = 2.3 µm. The formed aggregates were found to break by the applied ultrasonic treatment, resulting in a PSD similar to non-coated particles at non-IEP pH. The particle size D(50) of non-coated TiO_2 at non-IEP was found to be 0.4 µm which was consistent with the size observed from SEM images (300±100 nm). It is also noted the applied ultrasonic treatment is not able to change the PSD at non-IEP condition. This further confirmed the PSD with D(50) of 0.4 µm is the actual size for non-coated TiO_2 particles. For alumina-coated system, the PSD shift a result of applied ultrasonic treatment implies the presence of particle aggregates in both IEP and non-IEP slurries. This finding is consistent with SEM and TEM observations. The formation of aggregates at IEP was caused by the neutralised particle surface charge, while aggregates formed at non-IEP was caused by the adhesive alumina coating layer between particles.

In the non-coated TiO_2 system, at 10%wt concentration level, the particles at IEP condition were found to have a faster settling rate with thicker settled bedding height due to its particle (aggregate) size. As particle concentration exceeds above 20%wt, these particles at IEP condition formed a gel net-working which stabilised the entire structure. Therefore, the particle settling of 20%wt and 30%wt slurries was hindered due to the gelled structure. The non-coated particles at non-IEP condition exhibited an increased sediment bedding height as concentration increased from 10% to 30%wt. The gelation point for this system was found to be high (above 60%wt), but the exact value was difficult to identify as the reading of interface height cannot be taken due to the presence of fine cloud. The particle setting test for non-coated system confirmed the presence of large aggregate at IEP condition shown in PSD measurement.

In the alumina-coated TiO_2 system, it was found the particle at non-IEP condition barely settled at all concentration levels. This was because its gelation point was as low as 10%wt, indicating a strong particle-particle interaction. At the IEP condition, fast particle settling behaviour was found due to large aggregates (confirmed by PSD results). It was also noted there was a diffusive cloud in slurries at IEP condition. This demonstrated the presence of a large portion of fine particles seen in PSD results of alumina-coated particles.

The rheological performance of slurries at non-IEP condition from two TiO_2 systems showed water like Newtonian behaviour. All slurries at IEP condition exhibited higher viscosity due to increased particle size due to aggregation. At IEP condition, the viscosity of 20%wt and 30%wt non-coated slurries were higher than that of alumina-coated slurries. This is caused by increased particle-particle interaction as a result of structure gelation.

The initial drying work was performed using a commercial pilot-plant scale ProCepT spray dryer using a 25 kHz ultrasonic nozzle at 120ºC. For the spray drying of alumina-coated TiO_2 system at all three concentration levels, spherical morphology was found from drying of slurries at IEP condition, whereas a buckled morphology was seen from drying of slurries at non-IEP condition. In addition, some broken granules seen in SEM images indicated a possible solid internal structure for both two morphologies. The image analysis indicated a size range of 10-100 µm for all spray-dried granules, regardless of their external morphology. Furthermore, the buckled and spherical morphology showed similar breakage behaviour when higher sample dispensing pressure was used in Morphologi G3 analysis. It was noted the applied 5 bar pressure did not cause a significant granule breakage.

For the spray drying of non-coated TiO_2 system at all three concentration levels, constant spherical morphology was obtained from drying of slurries at both IEP and non-IEP conditions. In fact, a buckled morphology was expected from the dying of a “well-dispersed” system because the surface charge studies demonstrated a high absolutely zeta-potential for both alumina-coated and non-coated TiO_2 particles at non-IEP condition. The colloidal stability (controlled by pH) was not proved to affect the morphology. This finding is different from the conclusion drawn by other researchers who observed a hollow or a distorted structure when drying a flocculated droplet. Interestingly, the spray-dried granules from non-coated TiO_2 system exhibited a similar PSD and breakage behaviour to the granules from alumina-coated TiO_2 system although the two systems had a different primary particle size at both IEP and non-IEP conditions.

The subsequent drying work was conducted at 200ºC using the same ultrasonic nozzle to investigate the temperature effect and also were conducted at 120ºC using a 0.6 mm bi-fluid nozzle to investigate the atomisation effect to the product. For the alumina-coated system, the granules prepared from high-temperature drying showed similar morphologies to granules prepared from 120ºC drying. Drying of a slurry at IEP condition led to a spherical morphology, while a buckled morphology was observed from drying of a slurry at non-IEP condition. Similar morphology trend was observed from the granules prepared using a bi-fluid nozzle which produced a large number of fine particles seen in SEM results. These fine particles were caused by the poor atomisation from the bi-fluid nozzle, more droplets spattering observed during atomisation process when compared with the atomisation performance from an ultrasonic nozzle. These fine particles were not seen in PSD because a size filter (< 4 µm) was set before the size imaging. This means any particle with a size smaller than 4 µm were filtered and not shown in results. The particle sizing methodology needs to be improved to catch the presence of these fines. For non-coated system, neither the increased drying temperature nor the use of bi-fluid atomisation showed any significant effect on morphology, spherical shaped granules were found from drying of slurries at both IEP and non-IEP conditions. The granules prepared from bi-fluid nozzle also contained a large number for dust which is also an indication of poor atomisation.

The granules production campaigns conducted at 120ºC with an ultrasonic nozzle were found to achieve high yield with low residual moisture content for the granules obtained from drying of both non-coated and alumina-coated TiO_2 20%wt slurries at IEP and non-IEP conditions. The powder flow character of these spray-dried granules was also assessed through the calculation of Hausner ratio based on the tapped density measured. Regardless of external morphology, the granules from the drying of alumina-coated system were rated for excellent flow character. A more accurate AOR test was performed to verify the flowability results. The AOR test indicated a good flowability for granules from alumina-coated TiO_2 system, which is consistent with the Hausner ratio assessment. The AOR was also able to distinguish between spherical granules and buckled granules from alumina-coated system. The granules with sphere shape were found to have a better flowability.

The 20%wt slurries at both IEP and non-IEP conditions from two TiO_2 particles systems were dried at 120ºC using a more controlled single droplet drying rig to verify the morphologies from spray drying experiment. For the alumina-coated TiO_2 system, a buckled morphology was found from drying of a droplet with well-dispersed particles, and a sphere was seen from drying of a droplet contained aggregates. These morphologies are consistent with observations from spray drying experiment. In fact, this alumina-coated 20%wt slurry at non-IEP condition contains large aggregates which were caused by the adhesive alumina coating layer. These aggregates in slurry were confirmed by the SEM, TEM and PSD characterisation shown in Chapter 3. However, the sedimentation test demonstrated a low gelation concentration (10%wt) for this system. This means the system is still colloidal stable at 20%wt concentration level due to the networking of gel. For the non-coated TiO_2 system, the trend of morphology formation was different from the observations from spray drying work. The well-dispersed droplet (at non-IEP condition) led to a buckled structure, while the aggregated droplet (at IEP condition). Different morphology was observed from drying of a “well-dispersed” non-coated TiO_2 slurry 20%wt using spray drying and single droplet drying technique. The Péclet number associated with different drying technique was calculated for both two TiO_2 systems. All Péclet numbers were much greater than 1, indicating the formation of the particle shell during the drying process. The structure formation mechanisms for spherical and buckled morphologies were proposed, and the formation of a solid particle shell and high hollowness are found to be the critical condition for structure buckling. Furthermore, the driving force for the shell buckling was numerically proved to be the capillary force. However, the mechanisms outlined cannot fully explain the spheres obtained from spray drying of non-coated TiO_2 slurry at non-IEP condition.

The droplet size effect on morphology was studied by drying the “well-dispersed” slurries (at non-IEP condition) from two TiO_2 systems using single droplet drying rig[1]. The hollowness of spray-dried granules prepared from drying of different droplet size was estimated. It was noted the alumina-coated granule has a high

---

[1] The aggregated slurries (at IEP condition) from two TiO_2 systems were not studied due to the consistency in spherical morphology from different drying techniques.

hollowness which implies the buckling is independent of droplet size. The high hollowness was indicated by the solid particle shell formed at Péclet condition (>> 1). The high rheological yield stress implies this solid shell has a strong particle-particle interaction which was also confirmed by the low gelation point of this system (particles in droplet tend to gel when solid content exceeds 10%wt).

For the non-coated system (at non-IEP condition), the hollowness of spray-dried granules is dependent on droplet size. Low hollowness index was found in the drying of smaller droplet (0.5 and 0.4 µL). The granular structure cannot buckle because there was no void formed in granule central which is not complying with the critical condition for buckling. In addition, the lower yield stress and the high gelation point indicated the particle shell formed at high Péclet condition for small-sized droplet had a weak structure. The particles accumulated at droplet interface were weakly associated due to the anchored sodium hexametaphosphate dispersants which tend to re-disperse these particles into water and to provide resistance against the formation of a solid shell. A small droplet with a weak shell can only shrink isotropically to end up with spherical morphology. The droplet size generated by the spray dryer atomiser is much smaller than 0.4 µL, thus it was not surprising to see a spherical morphology.

In Chapter 4, broken granules from SEM observations indicated a possible solid internal structure for spray-dried granules. The microtome sectioning studies shown in Chapter 6 confirmed all spray-dried granules from two TiO_2 systems exhibited a similar solid internal structure regardless of TiO_2 type and external morphology formed. The surface area analysis demonstrated the same BET surface area for spray-dried granules from drying of same TiO_2 slurry system. The surface area of a spray-dried granule was proved not affected by its external morphology. The boehmite alumina coating was found to increase the BET specific surface area of spray-dried particles. The spray-dried granules from two TiO_2 systems were characterised to be the type III physisorption isotherm which corresponds to multi-layers adsorption with weak gas-solid interaction characteristics. In DVS studies, the pH of slurry was proved to be not responsible for the internal structure of spray-dried granules. It was also found the isotherm of spray-dried granule was independent of external morphology. The low moisture update by granules prepared from two TiO_2 systems indicated the spray drying formed a dense particle structure. The hydrophilic sodium hexametaphosphate is able to improve the moisture uptake and delay the water desorption process.

Representative spray-dried granules from each TiO_2 system were cut and examined using a high-resolution FIB-SEM technique. The visual assessment on the cross-section area indicated a similar porosity for the granules from two TiO_2 systems. This finding implies the drying can lead to a similar porosity and internal structure for spray-dried granules from two TiO_2 systems, but the moisture uptake behaviour for non-coated and alumina-coated granules are still slightly different. The sodium hexametaphosphate dispersant on non-coated particle surface can improve the moisture adsorbing and holding abilities. In the bulk compression test, none of these spray-dried granules was found to have any breakage or cracking, which was confirmed by the SEM examination. This indicates 5 N load was not enough for breaking these granules and also proves the volume change (ΔV) observed from compression curves was completely caused by the rearrangement of particles under compression. The non-coated TiO_2 granules were found more compressible. This was caused by their high cohesiveness which was identified by the AOR test shown in Chapter 5.

For the overall summary, the results obtained from this research provides an insight of the correlation between the material colloidal properties, drying process conditions, spray-dried granule morphology and associated structure properties. It was found the colloidal stability played an important role in influencing the spray-dried morphology. In this study, the drying temperature, slurry solid concentration and atomisation were not identified as the key variables that can affect morphology. However, due to limitation of spray dryer drying temperature, a higher temperature drying cannot be challenged. Poor atomisation with poly-dispersed droplets was achieved using a bi-fluid type nozzle. The ultrasonic nozzle was found to be more reliable in producing granules with less fine dusts, high product yield and low residual moisture content. However, the size of spray-dried granules was limited to 10-100 µm, the parameters responsible for granule size were not determined and challenges still remained. The key mechanisms driving the droplet structural transformation was identified and the force driving the structure buckling was numerically proved. However, morphologies inconsistency was observed between spray drying and single droplet drying. The morphology was found to be dependent to the droplet size in non-coated TiO_2 system but independent to droplet size in alumina-coated TiO_2 system. This issue was closely related to the colloidal difference between two TiO_2 systems in terms of rheological yield stress, gelation point and stability.

The investigated spray drying conditions cannot affect the porosity, internal structure, surface area, moisture adsorption and desorption, and the density of spray-dried granule, whereas the coating layer on particle surface exhibited a significant effect on these properties. As the colloidal stability was proved to be important to morphology control, it allows a more research gaps for slurry formulation development.

7.2 Future Work

This research provides fundamental understanding of the mechanism driving the structural transformation when drying colloidal droplets. It highlights the correlation between the material colloidal properties, drying process conditions, spray-dried granule morphology and associated structure properties. However, a number for interesting research gaps can still be followed based on work presented in this thesis.

Spray Drying

The drying work performed using the 0.6 mm bi-fluid nozzle showed a poor atomisation with many fine dusts. More effort is needed to investigate an optimal process condition, such as adjust the atomisation gas flow rate, change different nozzle size and adjust the drying gas velocity.

An accurate method of estimating the droplet size for spray dyer is required, as the current models for Péclet calculation relies on many assumptions due to lack of droplet size information. Accurate information about atomised droplet size can help researcher to estimate the spray dryer atomisation performance, droplet drying rate and characteristic drying time.

Single Droplet Drying

The single droplet drying presented in this research only covers the drying of slurries with 20%wt solid content. The ProCepT spray dryer struggles to handle a slurry with higher solid content especially at IEP condition. The viscous material may block the feeding tube of spray dryer. It is not trivial to dry a concentrated slurry using the single droplet drying rig to explore the morphology transformation. In addition, higher temperature drying can also be performed using this rig.

Bulk Compression

The bulk compression tests can be repeated using a heavy load (>> 5 N) to investigate the bulk breakage properties of spray-dried particles. As there is difference between the bulk density and tapped of granules, the particle re-arrangement was observed in breakage curve. It is suggested to use tapped powder for bulk compression test. This can minimise the particle rearrangement issue.

Single Particle Breakage

It is still worthy of assessing the access the mechanical stress of a single particle. As the broad PSD (10-100 µm) for spray-dried particles, a large number of tests on sieved particles will be required. Appropriate techniques include Atomic Force Microscopy (AFM) and nano-indentation test with a suitable piston head.

Internal Structure for Spray-dried Granules

As stated in Chapter 4, there is a possibility for a more compact structure for granule prepared from high concentrated slurry (30%wt) when being compared with granule prepared from low concentrated slurry (10%wt or 20%wt). This can be verified by looking at the difference in porosity (water sorption and desorption), granule internal structure and mechanical strength of granules prepared from 10%wt and 30%wt. In this research, due to the time limitation only granules prepared from 20%wt slurries were characterised (results shown in Chapter 5). It is worthy of compare the compact structure between 10%wt, 20%wt and 30%wt granules to draw a clear conclusion on the effect of slurry solid content on product structure.

Appendixes

7.3 Appendix A

Péclet Number Calculation based on Spray Drying Experiment

The calculation of the Péclet number for alumina-coated TiO_2 particles (in water) at 120ºC drying condition follows the following equation, where *k* is the droplet evaporation rate, and *D* is the diffusion rate of alumina-coated TiO_2 particles within a droplet.

$$Pe = \frac{k}{8D}$$

The calculation of the droplet evaporation rate *k* follows (Vehring 2008):

i) The equilibrium temperature at a droplet surface under 120ºC drying condition can be approximated to its associated wet bulb temperature:

$$T_{wb} = 137 \left(\frac{T_b}{373.15}\right)^{0.68} log\left(T_g\right) - 45$$

T_b liquid phase boiling temperature = 100 ºC = 373.15 K

T_g drying air temperature = 120 ºC = 393.15 K

thus, the wet bulb temperature of droplet, T_{wb} = 310.45 K = 37.30 ºC

ii) The approximation of the water vapour pressure at the droplet surface is calculated using the Antoine Equation:

$$P = 10^{\left(A - \frac{B}{C + T_{wb}}\right)}$$

A, *B* and *C* are Antoine Constant for water: *A* = 8.07131, *B* = 1730.63 and *C* = 233.426;

As T_{wb} = 37.30 ºC

Thus, the water vapour pressure = 47.73 mmHg = 6363.48 Pascal

iii) The water mass fraction at the droplet surface at equilibrium temperature, 37.30ºC follows:

$$Y_s = \frac{water\ vapour\ pressure}{atomospheric\ pressure}$$

as the water vapour pressure = 6363.48 Pascal, and the atmospheric pressure = 101325 Pascal

thus, the water mass fraction at the droplet surface, Y_s = 6363.48 Pascal / 101325 Pascal = 0.0628

iv) The droplet evaporation rate can be calculated using the following equation:

$$k = 8D_g \frac{\rho_g}{\rho_l} (Y_s - Y_\infty)$$

D_g diffusion coefficient of gas phase = water vapour diffusion coefficient at atmospheric pressure at 37.30º C = 2.42 x 10^{-5} m^2/s

ρ_g density of the air at wet bulb temperature, 37.30 ºC = 1.127 Kg/m^3

ρ_l density of the alumina-coated TiO_2 slurry droplet = 1140 Kg/m^3

Y_s mass fraction of water at the droplet surface at 37.30ºC = 0.0628

Y_∞ mass fraction of water far from the droplet surface is estimated close to 0

thus, the droplet evaporation rate, k = 1.2019 x 10^{-8} m^2/s

The diffusion rate of alumina-coated TiO_2 particles in a droplet can be estimated using the following equation (Vehring 2008):

$$D = \frac{K_B\, T}{6\, \pi\, \eta\, a}$$

K_B the Boltzmann's constant = 1.38 x 10^{-23}

η the water viscosity at web bulb temperature, 37.30 ºC = 6.527 x 10^{-4} $N \cdot s/m^2$

T wet bulb temperature = 37.30 ºC = 310.45 K *a* radius of alumina-coated TiO_2 particles = 279 nm (non-IEP) to 1467 nm (IEP) = 2.79×10^{-7} m (non-IEP) to 1.467×10^{-6} m (IEP)

Thus, the calculated particle diffusion rate, $D = 1.2476 \times 10^{-12}$ (non-IEP) to 2.3737×10^{-13} (IEP) m^2/s

Calculation of Péclet number for alumina-coated TiO_2 particles follows:

$$Pe = \frac{k}{8\,D}$$

$k = 1.2019 \times 10^{-8}\ m^2/s$

$D = 1.2476 \times 10^{-12}$ to $2.3737 \times 10^{-13}\ m^2/s$

thus, **Pe = 1204 (non-IEP)** to **6329 (IEP)**

Péclet Calculation based on A Single Droplet Drying Experiment

The calculation of the Péclet number for alumina-coated TiO_2 particles (in water) at 120ºC drying condition follows the following equation, where *k* is the droplet evaporation rate, and *D* is the diffusion rate of alumina-coated TiO_2 particles within a droplet.

$$Pe = \frac{k}{8D}$$

The calculation of the droplet evaporation rate *k* follows (Vehring 2008):

$$D^2(t) = D_0^2 - kt$$

t the drying time at t, take 30 s, t = 30 s

D(t) the droplet diameter at time t = 30 s, D(30s) = 1.5160×10^{-3} m (non-IEP) and 1.4098×10^{-3} m (IEP)

D_0 the initial droplet diameter = 1.6618×10^{-3} m (non-IEP) and 1.6305×10^{-3} m (IEP)

Thus, the droplet evaporate rate, $k = 2.3174 \times 10^{-8}\ m^2/s$ (non-IEP) and $2.23672 \times 10^{-8}\ m^2/s$ (IEP)

The diffusion rate of non-coated TiO_2 particles in a droplet can be estimated using the following equation:

$$D = \frac{K_B\,T}{6\,\pi\,\eta\,a}$$

K_B the Boltzmann's constant = 1.38×10^{-23}

η the water viscosity at web bulb temperature, 37.30 ºC = 6.527×10^{-4} N·s/m^2

T wet bulb temperature = 37.30 ºC = 310.45 K

a radius of alumina-coated TiO_2 particles = 279 nm (non-IEP) and 1467 nm (IEP) = 2.79×10^{-7} m (non-IEP) and 1.467×10^{-6} m (IEP)

Thus, the calculated particle diffusion rate, $D = 1.25 \times 10^{-12}$ m^2/s (non-IEP) and 2.37×10^{-13} (IEP) m^2/s

Calculation of Péclet number for non-coated TiO_2 particles follows:

$$Pe = \frac{k}{8\,D}$$

$k = 2.3174 \times 10^{-8}$ m^2/s (non-IEP) and 2.2367×10^{-8} m^2/s (IEP)

$D = 1.25 \times 10^{-12}$ m^2/s to 2.37×10^{-13} m^2/s

Thus, **Pe = 2322 (at non-IEP)** to **11778 (at IEP)**

7.4 Appendix B

Péclet Number Calculation based on Spray Drying Experiment

The calculation of the Péclet number for non-coated TiO_2 particles (in water) at 120ºC drying condition follows the following equation, where *k* is the droplet evaporation rate, and *D* is the diffusion rate of non-coated TiO_2 particles within a droplet.

$$Pe = \frac{k}{8D}$$

The calculation of the droplet evaporation rate *k* follows (Vehring 2008):

i) The equilibrium temperature at a droplet surface under 120ºC drying condition can be approximated to its associated wet bulb temperature:

$$T_{wb} = 137 \left(\frac{T_b}{373.15}\right)^{0.68} log\left(T_g\right) - 45$$

T_b liquid phase boiling temperature = 100 ºC = 373.15 K

T_g drying air temperature = 120 ºC = 393.15 K

Thus, the wet bulb temperature of droplet, T_{wb} = 310.45 K = 37.30 ºC

ii) The approximation of the water vapour pressure (water in this case) at the droplet surface is calculated using Antoine Equation:

$$P = 10^{\left(A - \frac{B}{C + T_{wb}}\right)}$$

A, *B* and *C* are Antoine Constant for water: *A* = 8.07131, *B* = 1730.63 and *C* = 233.426;

As T_{wb} = 37.30 ºC

Thus, the water vapour pressure = 47.73 mmHg = 6363.48 Pascal

iii) The water mass fraction at the droplet surface at equilibrium temperature, 37.30ºC follows:

$$Y_s = \frac{water\ vapour\ pressure}{atomospheric\ pressure}$$

As the water vapour pressure = 6363.48 Pascal, and the atmospheric pressure = 101325 Pascal

Thus, the water mass fraction at the droplet surface, Y_s = 6363.48 Pascal / 101325 Pascal = 0.0628

iv) The droplet evaporation rate can be calculated using following equation:

$$k = 8D_g \frac{\rho_g}{\rho_l} (Y_s - Y_\infty)$$

D_g diffusion coefficient of gas phase = water vapour diffusion coefficient at atmospheric pressure at 37.30º C = 2.42 x 10^{-5} m^2/s

ρ_g density of the air at wet bulb temperature, 37.30 ºC = 1.127 Kg/m^3

ρ_l density of the non-coated TiO_2 slurry droplet = 1140 Kg/m^3

Y_s mass fraction of water at the droplet surface at 37.30ºC = 0.0628

Y_∞ mass fraction of water far from the droplet surface is estimated close to 0

Thus, the droplet evaporation rate, k = 1.2019 x 10^{-8} m^2/s

The diffusion rate of non-coated TiO_2 particles in a droplet can be estimated using the following equation (Vehring, 2008):

$$D = \frac{K_B\, T}{6\, \pi\, \eta\, a}$$

K_B the Boltzmann's constant = 1.38 x 10^{-23} J/K (Joule per Kelvin)

η the solvent (water) viscosity at web bulb temperature, 37.30 ºC = 6.527 x 10^{-4} N·s/m^2

T wet bulb temperature = 37.30 ºC = 310.45 K

a radius of non-coated TiO_2 particles = 236 nm (non-IEP) and 1180 nm (IEP) = 2.36 x 10^{-7} m (non-IEP) and 1.18 x 10^{-6} m (IEP)

Thus, the calculated particle diffusion rate, *D* = 1.4755 x 10^{-12} (non-IEP) and 2.951 x 10^{-13} (IEP) m^2/s

**note: 1 Joule = 1 Newton Meter

Calculation of Péclet number for non-coated TiO_2 particles follows:

$$Pe = \frac{k}{8\,D}$$

k = 1.2019 x 10^{-8} m^2/s

D = 1.4755 x 10^{-12} and 2.951 x 10^{-13} m^2/s

Thus, **Pe = 1018 (non-IEP)** and **5091 (IEP)**

Péclet Calculation based on A Single Droplet Drying Experiment

The calculation of the Péclet number for non-coated TiO_2 particles (in water) at 120ºC drying condition follows the following equation, where *k* is the droplet evaporation rate, and *D* is the diffusion rate of non-coated TiO_2 particles within a droplet.

$$Pe = \frac{k}{8D}$$

The calculation of the droplet evaporation rate *k* follows (Vehring 2008):

$$D^2(t) = D_0^2 - kt$$

t the drying time at t, take 30 s, t = 30 s

$D(t)$ the droplet diameter at time t = 30 s, D(30s) = 1.4652 x 10^{-3} m (non-IEP) and 1.3967 x 10^{-3} m (IEP)

D_0 the initial droplet diameter = 1.6219 mm (non-IEP) = 1.6219 x 10^{-3} m (IEP)

Thus, the droplet evaporate rate, k = 2.0075 x 10^{-8} m^2/s (non-IEP) and 2.2644 x 1^{-8} m^2/s (IEP)

The diffusion rate of non-coated TiO_2 particles in a droplet can be estimated using the following equation (Vehring 2008):

$$D = \frac{K_B\,T}{6\,\pi\,\eta\,a}$$

K_B the Boltzmann's constant = 1.38 x 10^{-23}

η the solvent (water) viscosity at web bulb temperature, 37.30 ºC = 6.527 x 10^{-4} N·s/m^2

T wet bulb temperature = 37.30 ºC = 310.45 K

a radius of non-coated TiO_2 particles = 236 nm (non-IEP) to 1180 nm (IEP) = 2.36 x 10^{-7} m (non-IEP) to 1.18 x 10^{-6} m (IEP)

Thus, the calculated particle diffusion rate, D = 1.4755 x 10^{-12} (non-IEP) to 2.951 x 10^{-13} (IEP) m^2/s

Calculation of Péclet number for non-coated TiO_2 particles follows:

$$Pe = \frac{k}{8\,D}$$

k = 2.2664 x 10^{-8} m^2/s

D = 1.4755 x 10^{-12} to 2.951 x 10^{-13} m^2/s

Thus, **Pe = 1701 (non-IEP)** to **9600 (IEP)**

7.5 Appendix C

Derivation of the Capillary Pressure Formula

As the evaporation of a droplet continues at the last stage of drying process, the water between two adjacent particles retracts (under evaporation effect) to form a meniscus which is analogue to a capillary rise effect. The derivation of capillary pressure formula of capillary given here based on the illustration of the capillary rise shown in figure below.

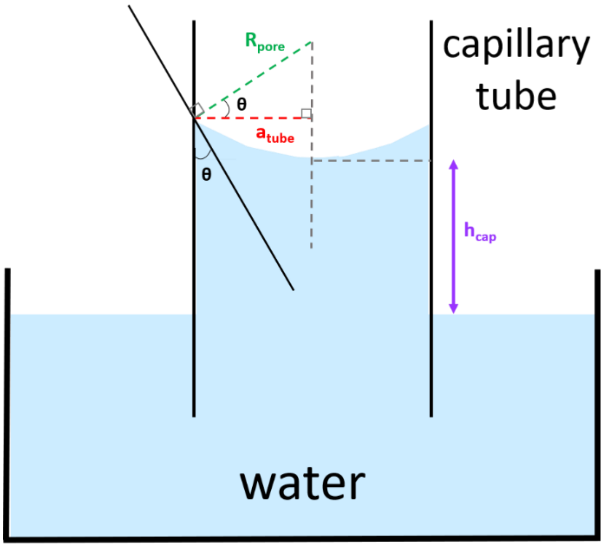

Appendix C Figure: The illustration of capillary rise effect: the end a capillary tube is placed under water, the capillary force pulls the water up the tube

When placing the end of a narrow tube in water, the water will overcome the gravity and flow into tube without assistance any external force. In this capillary rise scenario, the adhesive force between the water molecule and tube surface is greater than the cohesive force between water molecules. Thus,

$$capillary\ force\ =\ adhesion\ force\ -cohesion\ force$$

The capillary force pulls the water up the capillary tube is eventually wetted by water. At capillary equilibrium, the upward force (capillary force) is balanced by the downward force (water gravity). Therefore, the capillary pressure can be derived by the followings (Lintingre et al., 2016, Lintingre et al., 2015):

Calculation of downward water weight:

$$water\ weight\ of\ height\ (h_{cap}) = m_{water}\ g\ = \rho_{water}\, V_{water}\, g\ = \pi\ a_{tube}^{2}\ h_{cap}\ g$$

Where h_{cap} is the height of pulled water in tube, ρ_{water} is density of water, g is the gravity of Earth, and a_{tube} is radius of tube.

Calculation of upward capillary force:

$$water\ surface\ tension\ force\ in\ vertical\ direction = \gamma\ cos\theta$$

Where γ is the air-water interfical tension force and θ is water wetting angle.

As the capillary force exists around the perimeter of capillary tube ($2\pi\ a_{tube}$), the total capillary force acting in the upward direction follows:

$$total\ upward\ capillary\ = \gamma\ cos\theta \times 2\pi\ a_{tube}$$

The upward capillary force = downward water weight, thus,

$$\pi\ a_{tube}^{2}\ h_{cap}\ g\ = \gamma\ cos\theta \times 2\pi\ a_{tube}$$

$$h_{cap}\ \rho_{water}\ g = \frac{2\ \gamma\ cos\theta}{a_{tube}}$$

Because the product of $h_{cap}\ \rho_{water}\ g$ equals to P_{cap} (water capillary pressure). Thus,

$$P_{cap}\ = \frac{2\ \gamma\ cos\theta}{a_{tube}}$$

Because of $a_{tube}\ = R_{pore}\ cos\theta$ (where R_{pore} is the pore radius between adjacent particles or also known as the principle radius of curvature). Thus,

$$P_{cap} = \frac{2\,\gamma}{R_{pore}}$$

Now consider the calculation of critical buckling pressure for two TiO_2 systems respectively:

Calculation of Critical Buckling Pressure of Non-coated TiO_2 System

Calculation of maximum water capillary pressure follows:

$$P_{cap} = \frac{2\,\gamma}{R_{pore}}$$

γ Air-water interfacial tension at 120ºC ≈ 5.89 x 10^{-2} N/m (www.EngineeringToolBox.com, 2019)

R_{pore} Radius of pore in between adjacent two particles. Assuming this pore radius is 10 times smaller than the TiO_2 primary particle size in system based on recommendation by Lintingre et al., (2016). Thus, 10 R_{pore} ≈ a

a Radius of non-coated TiO_2 particles = 236 nm (non-IEP) = 2.36 x 10^{-7} m (non-IEP)

Thus, the maximum water capillary pressure, P_{cap} = 4.99 x 10^{6} Pa (non-IEP)

Calculation of shell thredhold pressure follows:

The critical pressure above which the spherical shell buckles can be estimated using a Zoely-Van Der Neut formula (Timoshenko and Gere 2009, Lintingre et al., 2016):

$$P_{buckle} = \frac{2E}{\left(\frac{R_0}{h}\right)^2 \sqrt{3\,(1-\nu^2)}}$$

E Young's modulus of rutile TiO_2 = 2.8 x 10^{11} Pa (Lukyanov et al., 2016)

υ Poisson's ratio of TiO_2 = 0.28

(https://www.azom.com/properties.aspx?ArticleID=1179, 2002)

a Primary particle radius = 2.36 x 10^{-7} m (non-IEP)

R_0 Initial droplet radius = 3.25 x 10^{-4} m (based on single droplet drying experiment, D_0 = 1.658012 x 10^{-3} m)

h Shell thickness, assuming h = 5a = 5 x 2.36 x 10^{-7} m = 11.8 x 10^{-7} m

Thus, the buckling instability threshold, P_{buckle} ≈ 6.82 x 10^5 Pa

Apparently, as the calculated maximum capillary pressure (4.99 X 10^6 Pa) is one order magnitude larger than critical buckling pressure (6.82 x 10^5 Pa). Therefore, buckling of the solid shell is expected at the end of drying.

Calculation of Critical Buckling Pressure of Alumina-coated TiO_2 System

Same approach is used for alumina-coated system. The calculation of maximum water capillary pressure follows:

$$P_{cap} = \frac{2\,\gamma\, cos\theta}{R_{pore}}$$

γ Air-water interfacial tension at 120ºC ≈ 5.89 x 10^{-2} N/m

(www.EngineeringToolBox.com, 2019)

R_{pore} Radius of pore in between adjacent two particles. Assuming this pore radius is 10 times smaller than the TiO_2 primary particle size in system based on recommendation by Lintingre et al., (2016). Thus, 10 R_{pore} ≈ a

a Radius of alumina-coated TiO_2 particles = 279 nm (non-IEP) = 2.79 x 10^{-7} m (non-IEP)

Thus, the maximum capillary pressure, P_{cap} = 4.22 x 10^6 Pa (non-IEP)

Calculation of shell threshold pressure follows:

The critical pressure above which the spherical shell buckles can be estimated using a Zoely-Van Der Neut formula (Timoshenko and Gere 2009, Lintingre et al., 2016):

$$P_{buckle} = \frac{2E}{\left(\frac{R_0}{h}\right)^2 \sqrt{3\,(1-\nu^2)}}$$

E Young's modulus of alumina-coated TiO_2 = 2.8×10^{11} Pa (assumed same as pure TiO_2)

υ Poisson's ratio of alumina-coated TiO_2 = 0.28 (assumed same as TiO_2)

(https://www.azom.com/properties.aspx?ArticleID=1179, 2002)

a Primary particle radius = 2.79×10^{-7} m (non-IEP)

R_0 Initial droplet radius = 8.31×10^{-4} m (based on single droplet drying experiment, $D_0 = 1.66185 \times 10^{-3}$ m)

h Shell thickness, assuming h = 5a = $5 \times 2.79 \times 10^{-7}$ m = 1.4×10^{-6} m

Thus, the buckling instability threshold, $P_{buckle} \approx 9.49 \times 10^5$ Pa

Apparently, as the calculated maximum capillary pressure (4.22×10^6 Pa) is one order magnitude larger than critical buckling pressure (9.49×10^5 Pa). Therefore, buckling of the solid shell is expected at the end of drying.

References

TiO_2: Manufacture of titanium dioxide.

ABDULLAH, E. C. & GELDART, D. 1999. The use of bulk density measurements as flowability indicators. *Powder technology,* 102**,** 151-165.

ASTM 2008. B527-06 Standard Test Method for Determination of Tap Density of Metallic Powders and Compounds. United States: ASTM International.

AUSTIN, D. 2019. *Physical modeling of milling processes in non-Newtonian systems.* PhD 1st year transfer report, University of Leeds.

BARRON, A. D., C. 2019. *BET Surface Area Analysis of Nanoparticles* [Online]. CHEMISTRY LibreTexts. Available: https://chem.libretexts.org/Bookshelves/Analytical_Chemistry/Book%3A_Physical_Methods_in_Chemistry_and_Nano_Science_(Barron)/02%3A_Physical_and_Thermal_Analysis/02.3%3A_BET_Surface_Area_Analysis_of_Nanoparticles#mjx-eqn-3 [Accessed].

BAYLY, A. 2014. Structure development during drying - a review of the state of the art. *International Fine Particle Research Institute*.

BIGGS, S., TINDLEY, A. & ASME 2009. *THE RHEOLOGY OF OXIDE DISPERSIONS AND THE ROLE OF CONCENTRATED ELECTROLYTE SOLUTIONS,* New York, Amer Soc Mechanical Engineers.

BIRD, R. B. 2002. Transport phenomena. *Applied Mechanics Reviews,* 55**,** R1-R4.

BRAND, J. R. 1982. *Titanium Dioxide Pigment Treated to Suppress Yellowing In Polymers*.

BRUNAUER, S., DEMING, L. S., DEMING, W. E. & TELLER, E. 1940. On a theory of the van der Waals adsorption of gases. *Journal of the American Chemical society,* 62**,** 1723-1732.

CARR, R. L. 1965. Evaluating Flow Properties of Solids. *Chemical Engineering Journal,* 18**,** 163-168.

ÇELIK, M. 2016. *Pharmaceutical powder compaction technology*, CRC Press.

CHARLESWORTH, D. & MARSHALL, W. R. 1960. Evaporation from drops containing dissolved solids. *AIChE Journal,* 6**,** 9-23.

CHO, Y.-S. 2016. Fabrication of Hollow or Macroporous Silica Particles by Spray Drying of Colloidal Dispersion. *Journal of Dispersion Science and Technology,* 37**,** 23-33.

COSGROVE, T. 2005. Colloid Science: Principles. *Methods, and Applications. Blackwell Publishing*.

DE KRETSER, R. G., BOGER, D. V. & SCALES, P. J. J. R. R. 2003. Compressive rheology: an overview. 125-166.

DONOHUE, M. & ARANOVICH, G. 1998. Classification of Gibbs adsorption isotherms. *Advances in Colloid and Interface Science,* 76**,** 137-152.

EBRAHIM, W. 2019. *Single Droplet Drying at High Temperatures.* PhD, University of Leeds.

ELLIOTT, L. N., BEHRA, J. S., HONDOW, N., BOURNE, R. A., HASSANPOUR, A., EDWARDS, J. L., SUTCLIFFE, S. & HUNTER, T. N. 2019. Characterisation of polyphosphate coated aluminium-doped titania nanoparticles during milling. *Journal of colloid and interface science,* 548**,** 110-122.

FANG, X., YU, Z., SUN, X., LIU, X. & QIN, F. J. F. O. C. E. I. C. 2009. Formation of superhydrophobic boehmite film on glass substrate by Sol-Gel method. 3**,** 97-101.

FAURE, B., LINDELOV, J. S., WAHLBERG, M., ADKINS, N., JACKSON, P. & BERGSTROM, L. 2010. Spray drying of TiO2 nanoparticles into redispersible granules. *Powder Technology,* 203**,** 384-388.

FILKOVA, I. & MUJUMDAR, A. S. 1995. Industrial spray drying systems. *Handbook of industrial drying,* 1**,** 263-308.

FINLAY, W. H. 2001. *The mechanics of inhaled pharmaceutical aerosols: an introduction*, Academic press.

FORMULACTION 2009. Stability of Pharmaceutical Products.

FRANKS, G. V., ZHOU, Y., YAN, Y. D., JAMESON, G. J. & BIGGS, S. 2004. Effect of aggregate size on sediment bed rheological properties. *Physical Chemistry Chemical Physics,* 6**,** 4490-4498.

FREITAS, S., MERKLE, H. P. & GANDER, B. 2004. Ultrasonic atomisation into reduced pressure atmosphere—envisaging aseptic spray-drying for microencapsulation. *Journal of controlled Release,* 95**,** 185-195.

FUCHS, N. A. 2013. *Evaporation and droplet growth in gaseous media*, Elsevier.

GANDHI, A., SARAVANAN, A. & JAYARAM, V. 1996. Containerless processing of ceramics by aerodynamic levitation. *Materials Science and Engineering: A,* 221**,** 68-75.

GARDY, J. 2017. *Biodiesel production from used cooking oil using novel solid acid catalysts.* PhD, University of Leeds.

GELDART, D., ABDULLAH, E., HASSANPOUR, A., NWOKE, L. & WOUTERS, I. 2006. Characterization of powder flowability using measurement of angle of repose. *China Particuology,* 4**,** 104-107.

GREGG, S. J. S., K. S. W. 1982. *Adsorption, Surface Area and Porosity,* New York, Academic Press Inc.

HALL, S., COOKE, M., EL-HAMOUZ, A. & KOWALSKI, A. 2011. Droplet break-up by in-line Silverson rotor–stator mixer. *Chemical Engineering Science,* 66**,** 2068-2079.

HANDSCOMB, C. S., KRAFT, M. & BAYLY, A. E. 2009a. A new model for the drying of droplets containing suspended solids. *Chemical Engineering Science,* 64**,** 628-637.

HANDSCOMB, C. S., KRAFT, M. & BAYLY, A. E. 2009b. A new model for the drying of droplets containing suspended solids after shell formation. *Chemical Engineering Science,* 64**,** 228-246.

HASSAN, H. M. & MUMFORD, C. J. 1996. Mechanisms of drylng of skin-forming materials; the significance of skin formation and a comparison between three types of material. *Drying technology,* 14**,** 1763-1777.

HASSAN, M. S. & LAU, R. W. M. 2009. Effect of particle shape on dry particle inhalation: study of flowability, aerosolization, and deposition properties. *Aaps Pharmscitech,* 10**,** 1252.

HESS, W. T., KURTZ, A. & STANTON, D. 1995. Kirk-Othmer encyclopedia of chemical technology. *Kirk-Othmer (Ed.) John Wiley & Sons Ltd., New York*.

HOATH, S. 2016. *Fundamentals of Inkjet Printing: The Science of Inkjet and Droplets*.

HOLDICH, R. G. 2002. *Fundamentals of particle technology*, Midland Information Technology and Publishing.

HTTPS://WWW.AZOM.COM/PROPERTIES.ASPX?ARTICLEID=1179. 2002. *Titanium Dioxide-Titania (TiO2)* [Online]. Available: https://www.azom.com/article.aspx?ArticleID=1179 [Accessed 2020].

HUNTER, R. J. 2001. *Foundations of Colloid Science* Oxford University Press.

ISKANDAR, F. 2009. Nanoparticle processing for optical applications–A review. *Advanced Powder Technology,* 20**,** 283-292.

ISKANDAR, F., GRADON, L. & OKUYAMA, K. 2003. Control of the morphology of nanostructured particles prepared by the spray drying of a nanoparticle sol. *Journal of Colloid and Interface Science,* 265**,** 296-303.

ISKANDAR, F., MIKRAJUDDIN, A. & OKUYAMA, K. 2001. In situ production of spherical silica particles containing self-organized mesopores. *Nano Letters,* 1**,** 231-234.

ISKANDAR, F., NANDIYANTO, A. B. D., WIDIYASTUTI, W., YOUNG, L. S., OKUYAMA, K. & GRADON, L. 2009. Production of morphology-controllable porous hyaluronic acid particles using a spray-drying method. *Acta biomaterialia,* 5**,** 1027-1034.

ISRAELACHVILI, J. N. 2011. Intermolecular and surface forces: revised third edition. *Academic press2011*.

JACKSON, L. S. & LEE, K. 1991. Microencapsulation and the food industry. *Lebensm. Wiss. Technol,* 24**,** 289-297.

JI, W., WANG, Z., MA, J. & GONG, J. 2016. Hydrothermal synthesis of boehmite on alumina membranes for superhydrophobic surfaces. *Surface Engineering,* 32**,** 102-107.

KALEDIN, L. A., TEPPER, F. & KALEDIN, T. G. 2016. Pristine point of zero charge (ppzc) and zeta potentials of boehmite's nanolayer and nanofiber surfaces. *International Journal of Smart and Nano Materials,* 7**,** 1-21.

KALEDIN, L. A., TEPPER, F., VESGA, Y. & KALEDIN, T. G. 2019. Boehmite and Akaganeite 1D and 2D Mesostructures: Synthesis, Growth Mechanism, Ageing Characteristics and Surface Nanoscale Roughness Effect on Water Purification. *Journal of Nanomaterials,* 2019.

KAWAKITA, K. & TSUTSUMI, Y. 1966. A comparison of equations for powder compression. *Bulletin of the Chemical Society of Japan,* 39**,** 1364-1368.

KLAYPRADIT, W. & HUANG, Y.-W. 2008. Fish oil encapsulation with chitosan using ultrasonic atomizer. *LWT-Food Science and Technology,* 41**,** 1133-1139.

KOLESKE, J. 1995. Paint and coating testing manual, Philadelphia: ASTM International.

LAGOUDAKI, M. & DEMERTZIS, P. 1992. Water Sorption Hysteresis in Potato Starch and EGG Albumin. *Developments in Food Science.* Elsevier.

LEONG, K. 1987. Morphological control of particles generated from the evaporation of solution droplets: theoretical considerations. *Journal of Aerosol Science,* 18**,** 511-524.

LI, J., LIU, Y. H., WANG, Y., WANG, W. J., WANG, D. & QI, T. 2012. Hydrous alumina/silica double-layer surface coating of TiO2 pigment. *Colloids and Surfaces a-Physicochemical and Engineering Aspects,* 407**,** 77-84.

LI, X., ANTON, N., ARPAGAUS, C., BELLETEIX, F. & VANDAMME, T. F. J. J. O. C. R. 2010. Nanoparticles by spray drying using innovative new technology: The Büchi Nano Spray Dryer B-90. 147**,** 304-310.

LIDDELL, P. V. & BOGER, D. V. 1994. INFLUENCE OF PROCESSING ON THE RHEOLOGY OF TITANIUM-DIOXIDE PIGMENT SUSPENSIONS. *Industrial & Engineering Chemistry Research,* 33**,** 2437-2442.

LINDELØV, J. S. & WAHLBERG, M. Spray drying for processing of nanomaterials. Journal of Physics: Conference Series, 2009. IOP Publishing, 012027.

LINTINGRE, E., DUCOURET, G., LEQUEUX, F., OLANIER, L., PERIE, T. & TALINI, L. 2015. Controlling the buckling instability of drying droplets of suspensions through colloidal interactions. *Soft Matter,* 11**,** 3660-3665.

LINTINGRE, E., LEQUEUX, F., TALINI, L. & TSAPIS, N. 2016. Control of particle morphology in the spray drying of colloidal suspensions. *Soft Matter,* 12**,** 7435-7444.

LUKYANOV, S. I., BANDURA, A. V. & EVARESTOV, R. A. 2016. Young's modulus and Poisson's ratio for TiO 2-based nanotubes and nanowires: modelling of temperature dependence. *RSC advances,* 6**,** 16037-16045.

LYONNARD, S., BARTLETT, J. R., SIZGEK, E., FINNIE, K. S., ZEMB, T. & WOOLFREY, J. L. 2002. Role of interparticle potential in controlling the morphology of spray-dried powders from aqueous nanoparticle sols. *Langmuir,* 18**,** 10386-10397.

MACOSKO, C. W. 1994. *Rheology: Principles, Measurements and Applications*, Wiley-VCH.

MALVERN Automation in Image Analysis for Particle Size and Shape Measurement.

MALVERN 2015a. Analyzing chocolate with the Morphologi G3 automated image analysis system.

MALVERN 2015b. Zeta Potential - An introduction in 30 minutes.

MASTERS, K. 1972. *Spray Drying: an introduction to principles, operational practice and applications,* London, L. Hill.

MCNULTY, G. S. Production of titanium dioxide. Proceedings of NORM V international conference, Seville, Spain, 2007. Citeseer, 169-189.

MIDDLEMAS, S., FANG, Z. Z. & FAN, P. 2015. Life cycle assessment comparison of emerging and traditional Titanium dioxide manufacturing processes. *Journal of Cleaner Production,* 89**,** 137-147.

MIGLANI, A. & BASU, S. 2015. Sphere to ring morphological transformation in drying nanofluid droplets in a contact-free environment. *Soft Matter,* 11**,** 2268-2278.

MIKULASEK, P., WAKEMAN, R. J. & MARCHANT, J. Q. 1997. The influence of pH and temperature on the rheology and stability of aqueous titanium dioxide dispersions. *Chemical Engineering Journal,* 67**,** 97-102.

MILLER, R., HARSTAD, K. & BELLAN, J. 1998. Evaluation of equilibrium and non-equilibrium evaporation models for many-droplet gas-liquid flow simulations. *International Journal of Multiphase Flow,* 24**,** 1025-1055.

MORRIS, G. E., SKINNER, W. A., SELF, P. G. & SMART, R. S. 1999. Surface chemistry and rheological behaviour of titania pigment suspensions. *Colloids and Surfaces a-Physicochemical and Engineering Aspects,* 155**,** 27-41.

MOSÉN, K., BÄCKSTRÖM, K., THALBERG, K., SCHAEFER, T., KRISTENSEN, H. G. & AXELSSON, A. 2005. Particle formation and capture during spray drying of inhalable particles. *Pharmaceutical development and technology,* 9**,** 409-417.

MUJUMDAR, A. S. 2006. *Handbook of industrial drying*, CRC press.

NANDIYANTO, A. B. D. & OKUYAMA, K. 2011. Progress in developing spray-drying methods for the production of controlled morphology particles: From the nanometer to submicrometer size ranges. *Advanced Powder Technology,* 22**,** 1-19.

NEŠIĆ, S. & VODNIK, J. 1991. Kinetics of droplet evaporation. *Chemical Engineering Science,* 46**,** 527-537.

NGUYEN, Q. & BOGER, D. 1992. Measuring the flow properties of yield stress fluids. *Annual Review of Fluid Mechanics,* 24**,** 47-88.

NIC, M., HOVORKA, L., JIRAT, J., KOSATA, B. & ZNAMENACEK, J. 2005. *IUPAC compendium of chemical terminology-the gold book*, International Union of Pure and Applied Chemistry.

NIESSEN, W. R. 2010. *Combustion and incineration processes: applications in environmental engineering*, CRC Press.

NUZZO, M., MILLQVIST-FUREBY, A., SLOTH, J. & BERGENSTAHL, B. 2015. Surface composition and morphology of particles dried individually and by spray drying. *Drying technology,* 33**,** 757-767.

O'SULLIVAN, J. J., NORWOOD, E.-A., O'MAHONY, J. A. & KELLY, A. L. 2019. Atomisation technologies used in spray drying in the dairy industry: A review. *Journal of food engineering,* 243**,** 57-69.

OKRUSCH, M., HOCK, R., SCHÜSSLER, U., BRUMMER, A., BAIER, M. & THEISINGER, H. 2003. Intergrown niobian rutile phases with Sc-and W-rich ferrocolumbite: An electron-microprobe and Rietveld study. *American Mineralogist,* 88**,** 986-995.

OKUYAMA, K., ABDULLAH, M., LENGGORO, I. W. & ISKANDAR, F. 2006. Preparation of functional nanostructured particles by spray drying. *Advanced Powder Technology,* 17**,** 587-611.

OKUYAMA, K. & LENGGORO, I. W. 2003. Preparation of nanoparticles via spray route. *Chemical Engineering Science,* 58**,** 537-547.

PATCHAIYAPPAN, A., SARAN, S. & DEVIPRIYA, S. P. 2016. Recovery and reuse of TiO 2 photocatalyst from aqueous suspension using plant based coagulant-A green approach. *Korean Journal of Chemical Engineering,* 33**,** 2107-2113.

PATEL, S., KAUSHAL, A. M. & BANSAL, A. K. 2006. Compression physics in the formulation development of tablets. *Critical Reviews™ in Therapeutic Drug Carrier Systems,* 23.

PERDANA, J., FOX, M. B. & SCHUTYSER, M. A. 2011a. Single-droplet experimentation on spray drying: evaporation of a sessile droplet. 34**,** 1151-1158.

PERDANA, J., FOX, M. B., SCHUTYSER, M. A. & BOOM, R. M. 2011b. Single-droplet experimentation on spray drying: evaporation of a sessile droplet. *Chemical Engineering & Technology,* 34**,** 1151-1158.

PÍSECKÝ, J. 2012. *Handbook of milk powder manufacture*, GEA Process Engineering A/S.

PROCEPT 2014a. Installation and Operation Manual - Ultrasonic Nozzle.

PROCEPT 2014b. ProCepT 4M8Trix Installation and Operation Manual.

PROCEPT. 2019. *SD1 Spray Dryer Product Brochure* [Online]. Available: www.procept.be/spray-dryer-chiller [Accessed].

QUANTACHROMEINSTRUMENTS 2018. NOVAe Series Surface Area Analyser Brochure.

RANZ, W. & MARSHALL, W. R. 1952. Evaporation from drops. *Chem. eng. prog,* 48**,** 141-146.

RHODES, M. 2008. *Introduction to Particle Technology*, John Wiley & Sons, Ltd.

ROUQUEROL, J. R., F. ; LLEWELLYN, P ; MAURIN, G. ; SING, K. 2013. *Adsorption by Powders and Porous Solids*, Academic Press.

SAHA, A., BASU, S. & KUMAR, R. 2012. Particle image velocimetry and infrared thermography in a levitated droplet with nanosilica suspensions. *Experiments in fluids,* 52**,** 795-807.

SCHUCK, P., JEANTET, R., BHANDARI, B., CHEN, X. D., PERRONE, Í. T., DE CARVALHO, A. F., FENELON, M. & KELLY, P. 2016. Recent advances in spray drying relevant to the dairy industry: A comprehensive critical review. *Drying Technology,* 34**,** 1773-1790.

SEN, D., MAZUMDER, S., MELO, J., KHAN, A., BHATTYACHARYA, S. & D'SOUZA, S. 2009. Evaporation driven self-assembly of a colloidal dispersion during spray drying: volume fraction dependent morphological transition. *Langmuir,* 25**,** 6690-6695.

SHAW, D. J. 1980. *Introduction to colloid and surface chemistry*, Butterworths.

SING, K. S. 1985. Reporting physisorption data for gas/solid systems with special reference to the determination of surface area and porosity (Recommendations 1984). *Pure and applied chemistry,* 57**,** 603-619.

SIWINSKA-STEFANSKA, K., KRYSZTAFKIEWICZ, A. & JESIONOWSKI, T. 2008. EFFECT OF INORGANIC OXIDES TREATMENT ON THE TITANIUM DIOXIDE SURFACE PROPERTIES. *Physicochemical Problems of Mineral Processing,* 42**,** 141-151.

SIZGEK, E., BARTLETT, J. & BRUNGS, M. 1998. Production of titanate microspheres by sol-gel and spray-drying. *Journal of sol-gel science and technology,* 13**,** 1011-1016.

STOKES, J. & TELFORD, J. 2004. Measuring the yield behaviour of structured fluids. *Journal of Non-Newtonian Fluid Mechanics,* 124**,** 137-146.

SURFACE-MEASUREMENT-SYSTEMS. 2018. *DVS Resolution Dual Vapor Gravimetric Sorption Analyzer* [Online]. Available: https://www.surfacemeasurementsystems.com/products/dynamic-vapor-sorption-instruments/vapor-sorption-analyzer/dvs-resolution/ [Accessed].

SUTCLIFFE, S., EDWARD, J. & LI, Y. 2015. *RE: Personal Communication.*

TAKAHASHI, H., SHINOHARA, N., OKUMIYA, M., UEMATSU, K., JUNICHIRO, T., IWAMOTO, Y. & KAMIYA, H. 1995. INFLUENCE OF SLURRY FLOCCULATION ON THE CHARACTER AND COMPACTION OF SPRAY-DRIED SILICON-NITRIDE GRANULES. *Journal of the American Ceramic Society,* 78**,** 903-908.

THERMOSCIENTIFIC. Pycnomatic ATC For solids and powders density.

TIMOSHENKO, S. P. & GERE, J. M. 2009. *Theory of elastic stability*, Courier Corporation.

TOEI, R., OKAZAKI, M. & FURUTA, T. Drying mechanism of a non-supported droplet. First international symposium on drying, 1978. 53-58.

TSAPIS, N., DUFRESNE, E. R., SINHA, S. S., RIERA, C. S., HUTCHINSON, J. W., MAHADEVAN, L. & WEITZ, D. A. 2005. Onset of buckling in drying droplets of colloidal suspensions. *Physical Review Letters,* 94**,** 4.

VAN OSS, C., ABSOLOM, D. & NEUMANN, A. 1980. Applications of net repulsive van der Waals forces between different particles, macromolecules, or biological cells in liquids. *Colloids and Surfaces,* 1**,** 45-56.

VEHRING, R. 2008. Pharmaceutical particle engineering via spray drying. *Pharmaceutical Research,* 25**,** 999-1022.

VEHRING, R., FOSS, W. R. & LECHUGA-BALLESTEROS, D. 2007. Particle formation in spray drying. *Journal of Aerosol Science,* 38**,** 728-746.

VELEV, O. D., LENHOFF, A. M. & KALER, E. W. 2000. A class of microstructured particles through colloidal crystallization. *Science,* 287**,** 2240-2243.

VERWEY, E. J. W. 1947. Theory of the stability of lyophobic colloids. *The Journal of Physical Chemistry,* 51**,** 631-636.

WALKER, W. J., REED, J. S. & VERMA, S. K. 1999. Influence of slurry parameters on the characteristics of spray-dried granules. *Journal of the American Ceramic Society,* 82**,** 1711-1719.

WALTON, D. E. 2000. The morphology of spray-dried particles a qualitative view. *Drying Technology,* 18**,** 1943-1986.

WALTON, D. E. & MUMFORD, C. J. 1999. The morphology of spray-dried particles - The effect of process variables upon the morphology of spray-dried particles. *Chemical Engineering Research & Design,* 77**,** 442-460.

WINKLER, J. 2003. Titanium dioxide (Hannover: Vincentz Network). ISBN 3-87870-148-9.

WU, H. X., WANG, T. J. & JIN, Y. 2006. Film-coating process of hydrated alumina on TiO2 particles. *Industrial & Engineering Chemistry Research,* 45**,** 1337-1342.

WWW.ENGINEERINGTOOLBOX.COM. 2019. *Surface Tension of Water in contact with Air* [Online]. Available: https://www.engineeringtoolbox.com/water-surface-tension-d_597.html [Accessed].

XIA, Y., ZHANG, L., JIAO, X. & CHEN, D. 2013. Synthesis of γ-AlOOH nanocrystals with different morphologies due to the effect of sulfate ions and the corresponding formation mechanism study. *Physical Chemistry Chemical Physics,* 15**,** 18290-18299.

YAMAMOTO, S. & SANO, Y. 1992a. Drying of enzymes: enzyme retention during drying of a single droplet. 47**,** 177-183.

YAMAMOTO, S. & SANO, Y. 1992b. Drying of enzymes: enzyme retention during drying of a single droplet. *Chemical Engineering Science,* 47**,** 177-183.

YANG, H. G., LI, C. Z., GU, H. C. & FANG, T. N. 2001. Rheological behavior of titanium dioxide suspensions. *Journal of Colloid and Interface Science,* 236**,** 96-103.

YARIN, A., BRENN, G., KELLER, J., PFAFFENLEHNER, M., RYSSEL, E. & TROPEA, C. 1997. Flowfield characteristics of an aerodynamic acoustic levitator. *Physics of fluids,* 9**,** 3300-3314.